Tracing Water Cycling and Variability in Forests and Mountainous Regions with Stable Water Isotopes

by

Phoebe Gabrielle Aron

A dissertation submitted in partial fulfillment
of the requirements for the degree of
Doctor of Philosophy
(Earth and Environmental Sciences)
in the University of Michigan
2020

Doctoral Committee:

Professor Christopher J. Poulsen, Chair
Assistant Professor Gretchen Keppel-Aleks
Associate Professor Naomi E. Levin
Professor Nathan A. Niemi
Assistant Professor Selena Y. Smith

Phoebe Aron

paron@umich.edu

ORCID iD: 0000-0002-4700-5445

Dedication

To my mom, who every day shows me how to be resilient, think creatively, and work hard.
And to Dylan, for whom I never quite have the words, but knows exactly what I'm trying to say.
Without you two, none of this would have been possible.

Acknowledgements

I owe a tremendous debt of gratitude to the many, many people who made this work possible. First, to my advisor Chris Poulsen: thank you for your unwavering support, both personally and professionally. This dissertation is quite a bit different than the one we envisioned five years ago. Thank you for giving me so much independence to pursue these research projects and trusting me to work towards our mutually high expectations. Thank you also to Naomi Levin, who has been much like a second advisor to me. I am very lucky you came to Michigan near the beginning of my PhD and that our labs dovetail so nicely. To my other committee members – Nathan Niemi, Selena Smith, and Gretchen Keppel-Aleks – thank you for your support, feedback, and ideas. Thank you to all five of you for encouraging me to balance the unfortunate ups and downs of life with a very high standard of work. This dissertation was supported by NSF Tectonics Program Award 1550101 and University of Michigan Water Center grants to Chris Poulsen, a Rackham Predoctoral Fellowship, a Rackham International Research Award, the Rackham Graduate Research Awards, University of Michigan Biological (UMBS) graduate student fellowships, and many Scott Turner Awards from the Earth department.

None of this work would have been possible without the support and knowledge of many additional individuals and collaborators. In particular, Rich Fiorella and Ashley Matheny have been extremely helpful and uplifting. Your expertise and encouragement always came at the right time. Thank you to Chris Vogel and Tim Veverica for watching over my equipment at UMBS and helping me run the Picarro analyzers remotely. Thank you to Edgar Garcia Peña, Jose Antonio Luna Zapata, and Sixto Flores Sancho for your creativity and dedication to the rain stations in Peru. Thank you to the staff in Earth and at UMBS, who quite literally opened doors for me. Thank you to the staff in the Randall Business office who worked through my numerous financial requests and never expressed any frustration when I returned from Peru with receipts for hundreds of purchases of a single egg.

If you read far enough in this dissertation, you will make your way through data from more than 3,000 liquid water isotope analyses. I collected fewer than 10% of these samples. Thank you to the hundreds of people who collected water samples for the crowdsource water collection project and the individuals who are still collecting rain samples in Peru. Your enthusiasm, curiosity, and dedication are unmatched. Thank you for reminding me about the power of collaboration and cooperation towards a common goal.

I would also like to acknowledge and thank everyone in the Earth department. My lab mates in the Poulsen Lab, in particular Alex and Sophie, are a constant source of encouragement and comradery, in person and not. Thank you also to everyone in the IPL for letting me weasel my way into your lab group. I have learned so much from you all. Thank you to Becca, Bian, and Naomi for pushing me to think more broadly about graduate student experiences. Thank you to Anne, Chris, Marin, Naomi, Rosie, and many others for working with me to put on events like the writing retreat and writing workshop, recruiting events, and career development panels. Thank you to my friends in the department, in particular Nikita and Sarah, for being the perfect balance of supportive and distracting.

Lastly, thank you to my friends and family, who provide an unending well of support and encouragement. Thank you to Dharni Vasudevan, my undergraduate research advisor at Bowdoin, who saw something in me before I did; to Pam and Fred for being like second parents; to my friends from Maret and Bowdoin, many of whom still think I study dirt; and to Suzanne, Kurt, Paige, Debbi, Taylor, and Sarah, my extended family, for constantly pushing me forward. Thank you to my sister Sophie for your friendship and humor, my dad for being a willing field assistant in Peru, and my mom, for whom there are not enough words or pages to express myself. Finally, to Dylan, my wonderfully patient, supportive, and flexible husband. You keep me grounded and with a sense of perspective when I am tired or hungry or stressed, or the unfortunate combination of all three. For that, and so much more, thank you. Writing the last parts of this dissertation from my childhood bedroom while being socially distanced 6 feet, or many states, away from all of you was unexpected. Thank you for the support and encouragement along the way.

Table of Contents

List of Tables

List of Figures

Abstract

Water is one of the most important substances on Earth and links carbon and energy cycles within the climate system. Global precipitation is predicted to increase as the atmosphere continues to warm, but the rate, timing, and magnitude of local and regional terrestrial hydrologic change are still uncertain. This dissertation presents new understanding of ecosystem and regional scale water cycling from observations of stable oxygen and hydrogen isotope ratios in water. These ratios, referred to as stable water isotopes, are useful hydrologic tracers because they integrate and record information about processes such as evaporation, transpiration, condensation, crystallization, and hydrologic mixing that drive the water cycle. Understanding stable water isotope variation helps trace these processes and offers insight into how the hydrologic system may respond in warmer conditions.

This dissertation presents new stable water isotope data to study water cycling in deciduous forests (Chapters 2 and 3) and in the central Andes in South America (Chapter 4). Chapter 5 presents and explains variation in the triple oxygen isotope system, which until recently had not been applied to hydrologic problems and can add important information about water cycling. These chapters include new observations of high temporal resolution water vapor isotopes and a global dataset of precipitation and surface water isotope variability that is built on citizen science and crowdsourced sample collection. Results and implications from this dissertation help constrain local and regional scale uncertainties in the terrestrial hydrologic cycle.

Chapters 2 and 3 focus on ecosystem scale forest hydrology and use water vapor isotopes to quantify the role of plants in local and regional water cycles. Chapter 2 presents a comparison of water vapor isotopes in two adjacent deciduous forest sites in northern lower Michigan and shows that structural disturbances in forest canopies can affect boundary layer mixing and increase ecosystem-atmosphere gas exchange. Chapter 3 presents a new technique to measure the isotopic composition of transpired water vapor from trees and quantitatively partition land-atmosphere water fluxes. This method is developed and applied to study forest hydrology and can also be used

in non-forested ecosystems to explain the diurnal variation of water vapor isotopes and estimate land-atmosphere water fluxes from vegetation other than trees.

Chapters 4 and 5 increase the spatial and temporal scales of inquiry and focus on the isotopic composition of precipitation and surface water. Chapter 4 presents a three-year record of bimonthly precipitation isotope data from a network of 19 stations in southern Peru. This chapter shows that precipitation on the western flank of the central Andes is sourced from the Pacific Ocean and that precipitation patterns on the Altiplano and Eastern Cordillera are related to local topography, synoptic-scale convection, and moisture recycling as airmasses move across the Amazon Basin. Chapter 5 presents an introduction to meteoric water triple oxygen isotopes and explains the hydrologic processes in tropical, temperate, and polar regions that drive variation in this isotope system. This chapter serves as a practical guide and point of reference for researchers who might want to use triple oxygen isotope data in hydrologic and paleohydrologic studies. Together, these chapters demonstrate the utility of stable water isotopes to trace terrestrial water cycling and help better understand how forest and mountain hydrology may change in the coming decades.

Chapter 1 Introduction

1.1 Overview and motivation

The water cycle plays a critical role in nearly every part of the Earth system and is linked to climate conditions through carbon and energy budgets. As the atmosphere continues to warm in the coming decades, climate models predict that global mean precipitation will increase with a wet-get-wetter and dry-get-drier spatial pattern (Allan et al., 2010; Donat et al., 2016; Held and Soden, 2006; Trenberth, 2011). This pattern is already beginning to emerge over the oceans (Jia et al., 2019), but the details of local and regional hydrologic change over land are still highly uncertain (Byrne and O'Gorman, 2015; Myhre et al., 2017). Understanding the processes that drive terrestrial hydrologic cycling is critical to predict how the hydrologic system will respond in warmer conditions and to support the human and ecological communities that depend on the water cycle. This dissertation focuses largely on water cycling in deciduous forests and the central Andes in South America because these environments are currently undergoing hydrologic change but are hampered by a lack of observations, uncertainties about the rate of change, and disagreement among predictions of future hydrologic conditions (Espinoza et al., 2020; McDowell et al., 2020; Pabón-Caicedo et al., 2020).

Forests cover nearly one third of the global land area and account for approximately 50% of the land-atmosphere water flux through evaporation (from the soil and from intercepted or condensed water on leaves) and transpiration, the process through which water evaporates from plants (Schlesinger and Jasechko, 2014; Xiao et al., 2018). However, studying these fluxes can be challenging because hydrologic exchange between soil, plants, and the atmosphere is complex and boundary layer mixing within forests is rarely straightforward. This dissertation addresses two aspects of forest hydrology in particular: structural disturbances that alter land-atmosphere water exchange and new techniques to measure transpiration. Forests are susceptible to structural disturbances from wildfire, drought, windthrow, ecological succession, pest invasion, and human land use, but the biogeochemical effects forest of disturbance are not completely understood (Brodribb et al., 2020; McDowell et al., 2020). Transpiration is driven by the vapor pressure

gradient between a leaf and the atmosphere, and is dependent on the size and conductance of stomata, the availability of incoming solar radiation, and the hydraulic architecture (e.g., the properties that prevent xylem cavitation or embolism) of plants. However, these factors vary spatially, temporally, and between species, which makes transpiration among the most complex terrestrial hydrologic fluxes. A better understanding of forest hydrology and the processes through which water is exchanged between ecosystems and the atmosphere will inform climate and land surface models and improve predictions of local and regional hydrologic change.

Mountains plays a vital role in terrestrial surface water budgets and are very sensitive to climate conditions. In the central Andes, tropical glaciers and other high elevation water sources sustain vast ecological diversity and supply water for human use across one of the largest hydrologic gradients in the world (the Amazon Rainforest to the Atacama Desert). Recent climate model simulations and ground-based observations show that air temperatures in the central Andes are rising (Pabón-Caicedo et al., 2020), especially at high elevations (e.g., Palazzi et al., 2019; Pepin et al., 2015; Rangwala and Miller, 2012), and satellite imagery shows that central Andean glaciers have lost more than 50% of their land cover over the past five decades (ANA, 2014; CONAM 2001; INAIGEM, 2018). However, neither models nor observations paint a consistent pattern of precipitation change in the central Andes. For example, some observations in southern Peru find that precipitation is increasing (e.g., de los Milagros Skansi et al., 2013) while others report that precipitation is decreasing (e.g., Silva et al., 2008). Part of this disagreement arises from sparse precipitation networks across complex high topography and coarse spatial resolution in climate models that cannot capture local and regional topography or important small-scale hydrologic features. Additional hydrologic observations and a more complete understanding of the processes that control precipitation in the central Andes will help manage regional freshwater resources and will inform hydrologic and climate adaptation plans in a region that supports more than 30 million people.

This dissertation presents new observations and applications of stable water isotopes to better understand forest and mountain hydrology. Stable water isotopes are powerful hydrologic tracers because they integrate information about evaporation, transpiration, condensation, crystallization, and mixing as water moves through the environment. The first half of this dissertation shows that forest canopy structure affects the exchange of water between ecosystems and the atmosphere (Chapter 2) and demonstrates that water isotopes can help quantify evaporation

and transpiration fluxes (Chapter 3). The second half identifies the processes that drive precipitation in the central Andes (Chapter 4) and explains a new oxygen isotope system to trace evaporation, moisture recycling, and hydrologic mixing (Chapter 5). Results from this dissertation help constrain local and regional terrestrial hydrologic uncertainty, serve as a baseline from which to assess environmental change, and inform hydrologic and climate models that predict future conditions.

1.2 Stable water isotopes: fundamentals, definitions, and utility

Water molecules are made up of two hydrogen atoms and one oxygen atom. In each of these molecules, every oxygen atom has eight protons and every hydrogen atom has one proton. Most stable oxygen atoms also have eight neutrons (99.76% of oxygen atoms, termed ^{16}O), although some have nine (0.04%, ^{17}O) or ten (0.2%, ^{18}O) neutrons. Most stable hydrogen atoms have zero neutrons (99.98%, ^{1}H), while some have one neutron (0.02%, ^{2}H or D, for deuterium). Atoms with the same number of protons but a differing number of neutrons, described here for oxygen and hydrogen but found in elements throughout the periodic table, are called isotopes.

Based on natural stable isotope abundances, more water molecules contain lighter isotopes ($^{1}H_2{}^{16}O$, 99.73% of all water molecules) and fewer water molecules contain a heavy isotope ($^{1}H_2{}^{18}O$ (0.2%), $^{1}H_2{}^{17}O$ (0.04%), or $^{1}H^{2}H^{16}O$ (0.03%)) (Coplen et al., 2002).[1] Mass differences among these molecules result in slightly different physical properties (e.g., bond energy and molecular diffusivity) and an unequal, mass-dependent partitioning during phase changes. During phase changes, the more (less) condensed phase preferentially gains or retains more molecules with a heavy (light) isotope. Quantification of the ratio of heavy-to-light water molecules provides a method to trace the processes through which water moves in the environment. This unequal partitioning is called fractionation and is expressed with delta (δ) notation,

$$\delta = 1000\left(\frac{R_{sample}}{R_{standard}} - 1\right), \qquad \text{Eq. 1.1}$$

where R is the ratio of heavy-to-light isotopes in a sample or international standard. Typically, the standard is Vienna Standard Mean Ocean Water (VSMOW) (Coplen, 1996). In this dissertation,

[1] Water molecules with multiple heavy isotopes are exceedingly rare and have few practical applications in isotope hydrology research.

the terms ‘water isotopes’ or ‘stable water isotopes’ refer to ratios of stable oxygen and hydrogen isotopes in water.

Water isotopes fractionate during every phase change. When two phases are in isotopic equilibrium, i.e., the rate of isotopic exchange between phases is identical, fractionation is temperature dependent (Horita and Wesolowski, 1994; Majoube, 1971). When the two phases cannot reach isotopic equilibrium, an additional kinetic fractionation occurs because heavier molecules diffuse slower than lighter molecules (Cappa, 2003; Luz et al., 2009; Merlivat, 1978). With a few notable exceptions (e.g., Gonfiantini et al., 2020), equilibrium and kinetic fractionations are generally well understood in theoretical (Craig and Gordon, 1965), experimental (e.g., Gonfiantini et al., 2018), and observational (e.g., Noone, 2012) work, and water isotopes have been applied to a wide range of hydrologic and paleoclimate questions for more than six decades (e.g., Brady et al., 2019; Gat, 1996; Petit et al., 1999; Salati et al., 1979).

Until the early 2000s, modern isotope hydrology research focused primarily on continental-scale precipitation patterns and hemispheric-scale moisture transport. These early studies were mostly limited to monthly precipitation samples, but determined important global relationships among water isotopes (e.g., Craig, 1961; Rozanski et al., 1993) and established water isotopes as faithful hydrologic tracers (e.g, Dansgaard, 1964; Gat et al., 1994; Joussaume et al., 1984; Kendall and Coplen, 2001; Salati et al., 1979). In recent decades, the development of laser absorption spectrometers (O’Keefe and Deacon, 1998; Scherer et al., 1997), satellite-based hydrogen isotope sensors (Frankenberg et al., 2009; Worden et al., 2007), high precision triple oxygen isotope analyses (Barkan and Luz, 2005), and isotope-enabled general circulation models (Brady et al., 2019; Hoffmann et al., 1998; Joussaume et al., 1984) have greatly expanded the scope of isotope hydrology research. With these approaches, researchers can now trace water cycling across a wide range of temporal (seconds to many years) and spatial (a few millimeters to global) scales to gain new understanding of local and regional hydrologic processes.

This dissertation presents new water isotope data from a laser absorption spectrometer and measurements of hydrologic triple oxygen isotopes. Using laser-based water isotope analyzers, researchers have measured the isotopic composition of water vapor and liquid water to identify moisture sources (e.g., Brooks et al., 2010; Galewsky and Samuels-Crow, 2015), trace atmospheric circulation and moisture transport (e.g., Noone et al., 2013; Vuille and Werner, 2005), and quantify land-atmosphere water fluxes (e.g., Jasechko et al., 2013; Welp et al., 2012). The field of

hydrologic triple oxygen isotopes is still emerging, but these measurements can help constrain evaporation (e.g., Landais et al., 2006; Li et al., 2017) and identify hydrologic mixing in the atmosphere and on land (e.g., Landais et al., 2010; Li et al., 2015; Risi et al., 2013). However, many aspects laser-based isotope hydrology and triple oxygen isotope variation remain unexplored. In particular, there are relatively few water vapor isotope observations, a disproportionate focus on precipitation isotope variability in North America and Europe, and only a handful of published hydrologic triple oxygen isotope studies. This dissertation addresses each of these gaps and presents new observations of water vapor, precipitation, surface water, and groundwater isotopes to better understand the processes and fluxes that drive the water cycle.

1.3 Dissertation chapter summaries

The main body of this dissertation (Chapters 2-5) is a compilation of four studies that use water isotopes to explore hydrologic cycling across a variety of spatial (ecosystem to regional) and temporal (a few minutes to interannual) scales. The overall motivation and goal of these chapters is to present new observations of water isotope variation and understanding about forest and mountain hydrology. Results and conclusions from these chapters help constrain local and regional terrestrial hydrologic uncertainty and can inform predictions of future hydrologic change.

Chapters 2 and 3 begin at the ecosystem-scale and focus on forest hydrology. These chapters use water vapor isotopes to quantitatively assess how water is exchanged between the land and the atmosphere at the University of Michigan Biological Station (UMBS) in northern lower Michigan. These chapters present high temporal resolution (a few minutes) water vapor isotope data made with a field-deployable, laser-based water isotope analyzer to link local water cycles with plant biology (e.g., stomatal aperture) and meteorologic conditions. Such high temporal resolution measurements offer new insights into land-atmosphere water fluxes because previous water vapor isotope monitoring techniques were laborious and produced at most a few measurements per day (e.g., Helliker et al., 2002; Lai et al., 2006). Together, these chapters are part of a growing field of ecohydrologic research that uses near-continuous water vapor isotope data to quantify and trace water exchange between terrestrial ecosystems and the atmosphere.

Chapter 2 (published in *Journal of Geophysical Research: Biogeosciences,* Aron et al., 2019), presents a comparison of vertical profiles of water vapor isotopes in two closely located forest sites at UMBS to examine the effects of structural disturbance on forest water cycling. At

one site, all canopy-dominant early successional species were stem girdled (complete removal of a ~20 cm strip of bark around the trunk of a tree) to induce mortality and accelerate senescence. This disturbance mimics structural and species-level changes during rapid ecological succession and some forest management techniques (e.g., forest thinning or selective logging). We find that structural canopy disturbance can have a substantial impact on local and regional water cycling because intact, closed canopies can act as a diffusive boundary layer that modulates the exchange of energy and moisture between the land and the atmosphere. Structural disturbances that create or widen canopy gaps increase surface-atmosphere water vapor mixing and may reduce moisture retention in forests.

Chapter 3 (published in *Ecohydrology*, Aron et al., 2020b) developed from unconstrained or unexplained elements of Chapter 2. In particular, Chapter 2 only looks at the bulk isotopic composition of atmospheric water vapor at UMBS, which includes background vapor (mixed in from the atmosphere above the forest) and vapor added by evapotranspiration (ET). Chapter 3 presents a new technique to measure the isotopic composition of transpired vapor and quantitatively separate background, evaporation, and transpiration fluxes. This type of flux partitioning provides insights into the role that vegetation plays in terrestrial water recycling and links species-specific hydrologic traits with local meteorologic conditions. We find that evaporation and transpiration fluxes vary in unison over the course of a day and propose that isotopic ET partitioning can help quantify water fluxes from ecosystems (e.g., wetlands, tundra, grasslands) and vegetation types (e.g., young trees, shrubs, grasses) that play an important role in ecosystem-atmosphere water exchange but are hydrologically challenging to measure, model, and predict.

Chapters 4 and 5 increase the spatial and temporal scales of inquiry and focus on the isotopic composition of precipitation and surface waters. These chapters explore the regional and continental scale hydrologic processes that drive precipitation in the central Andes (Chapter 4) and the global variability of meteoric water triple oxygen isotopes (Chapter 5). These chapters rely heavily on citizen science and crowdsourced efforts to collect water samples, and refine longstanding assumptions about hydrology in the central Andes and the isotopic variability of meteoric water. While most hydrologic oxygen isotope studies (including Chapters 2 and 3) focus only on ratios of $^{18}O/^{16}O$, Chapters 4 and 5 include triple oxygen isotope (^{16}O, ^{17}O, ^{18}O) data. These data add a degree of freedom ($^{17}O/^{16}O$) to oxygen isotope records and help constrain kinetic

fractionation (e.g., evaporation and moisture recycling) in modern waters (e.g., Li et al., 2017; Luz and Barkan, 2010) and geologic materials (e.g., Passey et al., 2014) that is impossible to do with $^{18}O/^{16}O$ alone. Chapter 4 introduces hydrologic triple oxygen isotope data and demonstrates their utility in one regional study; Chapter 5 expands this work and explains global meteoric water triple oxygen isotope variations. These chapters present substantial new datasets and show how the isotopic composition of precipitation and surface waters can be useful in a variety of hydrologic and paleoclimate applications.

Chapter 4 focuses on the regional to continental scale hydrologic processes that control precipitation in the central Andes. This chapter presents a three-year record of bimonthly precipitation isotope data from 19 stations in southern Peru that extend from the western Peruvian Amazon to near the Pacific coast. This chapter includes the first precipitation isotope data from the Peruvian Altiplano and Western Cordillera, and we find clear evidence of Pacific-sourced moisture in western regions of southern Peru. This moisture source is generally unaccounted for, but may play a critical role managing freshwater resources in the western central Andes where precipitation is infrequent but agriculture and major population centers (Lima and Arequipa) have high water demands. On the Altiplano and Eastern Cordillera, precipitation isotopes record a signal of evapotranspiration as moisture is transported across the Amazon Basin and seasonal variations in convection and airmass mixing that drive precipitation in the central Andes. These results highlight the utility of precipitation isotopes to understand hydrologic processes and provide new isotopic observations from a data-sparse region.

Chapter 5 (in review in *Chemical Geology*, Aron et al., 2020a) is an invited review that explains the global variability of meteoric water triple oxygen isotopes. This chapter is intended as an introduction to what is known about meteoric water triple oxygen isotopes and serves as a practical guide for researchers who might want to use these data in hydrologic and paleoclimate studies. This chapter shows that meteoric water triple oxygen isotope variations are well characterized and are explained by well-known equilibrium and kinetic fractionation effects. These small variations are statistically significant and can help trace modern water cycling or answer an array of questions about paleohydrology or paleoclimate. This chapter includes a new, near-global dataset of surface water triple oxygen isotope data that greatly expands the geographical distribution of observations. Building upon a decade of work, this chapter presents region-specific triple oxygen isotope meteoric water lines that will be used as a point of reference in future studies.

This dissertation ends with Chapter 6, a summary of the most important findings and implications of this work. This concluding chapter includes directions of future work, a number of important but yet unanswered questions, and a brief description of the samples and data collected during my graduate studies that are not included in this dissertation. I believe these data may help answer some of the remaining questions and look forward to continuing to work on these problems.

1.4 References

Allan, R.P., Soden, B.J., John, V.O., Ingram, W., Good, P., 2010. Current changes in tropical precipitation. Environ. Res. Lett. 5, 1–7. https://doi.org/10.1088/1748-9326/5/2/025205

ANA, 2014. Inventario Nacional de Glaciares y lagunas (in Spanish). Autoridad Nacional del Agua, Dirección de Conservación y Planeamiento de Recursos Hídricos. Peru.

Aron, P.G., Levin, N.E., Beverly, E.J., Huth, T.E., Passey, B.H., Pelletier, E.M., Poulsen, C.J., Winkelstern, I.Z., Yarian, D.A., 2020a. Global variations of triple oxygen isotopes in meteoric waters. Chem. Geol., in review

Aron, P.G., Poulsen, C.J., Fiorella, R.P., Matheny, A.M., 2019. Stable Water Isotopes Reveal Effects of Intermediate Disturbance and Canopy Structure on Forest Water Cycling. J. Geophys. Res. Biogeosciences 124, 2958–2975. https://doi.org/10.1029/2019JG005118

Aron, P.G., Poulsen, C.J., Fiorella, R.P., Matheny, A.M., Veverica, T.J., 2020b. An Isotopic Approach to Partition Evapotranspiration in a Mixed Deciduous Forest. Ecohydrolgy, 1–19. https://doi.org/10.1002/eco.229

Barkan, E., Luz, B., 2005. High precision measurements of $^{17}O/^{16}O$ and $^{18}O/^{16}O$ ratios in H_2O. Rapid Commun. Mass Spectrom. 19, 3737–3742. https://doi.org/10.1002/rcm.2250

Brady, E., Stevenson, S., Bailey, D., Liu, Z., Noone, D., Nusbaumer, J., 2019. The Connected Isotopic Water Cycle in the Community Earth System Model Version 1. J. Adv. Model. Earth Syst. 11, 2547–2566. https://doi.org/10.1029/2019MS001663

Brodribb, T.J., Powers, J., Choat, B., 2020. Hanging by a thread? Forests and drought. Science (80-.). 266, 261–266.

Brooks, J.R., Barnard, H.R., Coulombe, R., McDonnell, J.J., 2010. Ecohydrologic separation of water between trees and streams in a Mediterranean climate. Nat. Geosci. 3, 100–104. https://doi.org/10.1038/NGEO722

Byrne, M.P., O'Gorman, P.A., 2015. The response of precipitation minus evapotranspiration to climate warming: Why the "Wet-get-wetter, dry-get-drier" scaling does not hold over land. J. Clim. 28, 8078–8092. https://doi.org/10.1175/JCLI-D-15-0369.1

Cappa, C.D., 2003. Isotopic fractionation of water during evaporation. J. Geophys. Res. 108, 1–10. https://doi.org/10.1029/2003JD003597

CONAM, 2001. National communication of Peru to the United Nations Framework Convention on Climate change (UNFCCC). Lima.

Coplen, T.B., 1996. New guidelines for reporting stable hydrogen, carbon, and oxygen isotope-ratio data. Geochim. Cosmochim. Acta 60, 3359–3360.

Coplen, T.B., Hopple, J. a, Böhlke, J.K., Peiser, H.S., Rieder, S.E., Krouse, H.R., Rosman, K.J.R., Ding, T., Vocke, R.D.J., Révész, K.M., Lamberty, A., Taylor, P., Bièvre, P. De, 2002. Compilation of minimum and maximum isotope ratios of selected elements in naturally occurring terrestrial materials and reagents, USGS.

Craig, H., 1961. Isotopic Variations in Meteoric Waters. Science (80-.). 133, 1702–1703. https://doi.org/10.1126/science.133.3465.1702

Craig, H., Gordon, L.I., 1965. Deuterium and oxygen-18 variations in the ocean and the marine atmosphere, in: Tongiorgi, E. (Ed.), Proceedings of a Conference on Stable Isotopes in Oceanographic Studies and Paleotemperatures. Spoleto, Italy, pp. 9–130.

Dansgaard, W., 1964. Stable isotopes in precipitation. Tellus 16, 436–468. https://doi.org/10.3402/tellusa.v16i4.8993

de los Milagros Skansi, M., Brunet, M., Sigró, J., Aguilar, E., Arevalo Groening, J.A., Bentancur, O.J., Castellón Geier, Y.R., Correa Amaya, R.L., Jácome, H., Malheiros Ramos, A., Oria Rojas, C., Pasten, A.M., Sallons Mitro, S., Villaroel Jiménez, C., Martínez, R., Alexander, L. V., Jones, P.D., 2013. Warming and wetting signals emerging from analysis of changes in climate extreme indices over South America. Glob. Planet. Change 100, 295–307. https://doi.org/10.1016/j.gloplacha.2012.11.004

Donat, M.G., Lowry, A.L., Alexander, L. V., O'Gorman, P.A., Maher, N., 2016. More extreme precipitation in the world's dry and wet regions. Nat. Clim. Chang. 6, 508–513. https://doi.org/10.1038/nclimate2941

Espinoza, J.C., Garreaud, R., Poveda, G., Arias, P.A., Molina-Carpio, J., Masiokas, M., Viale, M., Scaff, L., 2020. Hydroclimate of the Andes Part I: Main Climatic Features. Front. Earth Sci. 8, 1–20. https://doi.org/10.3389/feart.2020.00064

Frankenberg, C., Yoshimura, K., Warneke, T., Aben, I., Butz, A., Deutscher, N., Griffith, D., Hase, F., Notholt, J., Schneider, M., Schrijver, H., Rockmann, T., 2009. Dynamic Processes Governing Lower-Tropospheric HDO/H_2O Ratios as Observed from Space and Ground. Science (80-.). 325, 1374–1377.

Galewsky, J., Samuels-Crow, K., 2015. Summertime moisture transport to the southern South American Altiplano: Constraints from in situ measurements of water vapor isotopic

composition. J. Clim. 28, 2635–2649. https://doi.org/10.1175/JCLI-D-14-00511.1

Gat, J., 1996. Oxygen and hydrogen isotopes in the hydrologic cycle. Annu. Rev. Earth Planet. Sci. 24, 225–262. https://doi.org/10.1146/annurev.earth.24.1.225

Gat, J.R., Bowser, C.J., Kendall, C., 1994. The contribution of evaporation from the Great Lakes to the continental atmosphere: estimate based on stable isotope data. Geophys. Res. Lett. 21, 557–560. https://doi.org/10.1029/94GL00069

Gonfiantini, R., Wassenaar, L.I., Araguas-Araguas, L., Aggarwal, P.K., 2018. A unified Craig-Gordon isotope model of stable hydrogen and oxygen isotope fractionation during fresh or saltwater evaporation. Geochim. Cosmochim. Acta 235, 224–236. https://doi.org/10.1016/j.gca.2018.05.020

Gonfiantini, R., Wassenaar, L.I., Araguas-Araguas, L., 2020. Stable isotope fractionations in the evaporation of water: The wind effect. Hydrol. Process. 1–12. https://doi.org/10.1002/hyp.13804

Held, I.M., Soden, B.J., 2006. Robust responses of the Sahelian hydrological cycle to global warming. J. Clim. 19, 5686–5699. https://doi.org/10.1175/JCLI-D-18-0238.1

Helliker, B.R., Roden, J.S., Cook, C., Ehleringer, J.R., 2002. A rapid and precise method for sampling and determining the oxygen isotope ratio of atmospheric water vapor. Rapid Commun. Mass Spectrom. 16, 929–932. https://doi.org/10.1002/rcm.659

Hoffmann, G., Werner, M., Heimann, M., 1998. Water isotope module of the ECHAM atmospheric general circulation model: A study on timescales from days to several years. J. Geophys. Res. 103, 16871–16896. https://doi.org/10.1029/98JD00423

Horita, J., Wesolowski, D.J., 1994. Liquid-vapor fractionation of oxygen and hydrogen isotopes of water from the freezing to the critical temperature. Geochim. Cosmochim. Acta 58, 3425–3437.

INAIGEM, 2018. Inventario Nacional de Glaciares. Huaraz: INAIGEM.

Jasechko, S., Sharp, Z.D., Gibson, J.J., Birks, S.J., Yi, Y., Fawcett, P.J., 2013. Terrestrial water fluxes dominated by transpiration. Nature 496, 347–50. https://doi.org/10.1038/nature11983

Jia, G., Shevliakova, E., Artaxo, P., De Noblet-Ducoudré, N., Houghton, R., House, J., Kitajima, K., Lennard, C., Popp, A., Sirin, A., Sukumar, R., Verchot, L., 2019. Land–climate interactions, in: Shukla, P.R., Skea, J., Calvo Buendia, E., Masson-Delmotte, V., Pörtner, H.-O., Roberts, D.C., Zhai, P., Slade, R., Connors, S., van Diemen, R., Ferrat, M., Haughey, E., Luz, S., Neogi, S., Pathak, M., J., P., J. Portugal Pereira, P. Vyas, E. Huntley, K. Kissick, M, Belkacemi, J.M. (Eds.), Climate Change and Land: An IPCC Special Report on Climate Change, Desertification, Land Degradation, Sustainable Land Management, Food Security, and Greenhouse Gas Fluxes in Terrestrial Ecosystems.

Joussaume, S., Jouzel, J., Sadourny, R., 1984. A general circulation model of water isotope cycles in the atmosphere. Nature 311, 24–29. https://doi.org/10.1038/311680a0

Kendall, C., Coplen, T.B., 2001. Distribution of oxygen-18 and deuteriun in river waters across the United States. Hydrol. Process. 15, 1363–1393. https://doi.org/10.1002/hyp.217

Lai, C., Ehleringer, J.R., Bond, B.J., Paw, K., 2006. Contributions of evaparation, isotopic non-stedy state transpiration and atmospheric mixing on the $\delta^{18}O$ of water vapour in Pacific Northewest coniferous forests. Plant Cell Environ. 29, 77–94. https://doi.org/10.1111/j.1365-3040.2005.01402.x

Landais, A., Barkan, E., Yakir, D., Luz, B., 2006. The triple isotopic composition of oxygen in leaf water. Geochim. Cosmochim. Acta 70, 4105–4115. https://doi.org/10.1016/j.gca.2006.06.1545

Landais, A., Risi, C., Bony, S., Vimeux, F., Descroix, L., Falourd, S., Bouygues, A., 2010. Combined measurements of 17Oexcess and d-excess in African monsoon precipitation: Implications for evaluating convective parameterizations. Earth Planet. Sci. Lett. 298, 104–112. https://doi.org/10.1016/j.epsl.2010.07.033

Li, S., Levin, N.E., Chesson, L.A., 2015. Continental scale variation in ^{17}O-excess of meteoric waters in the United States. Geochim. Cosmochim. Acta 164, 110–126. https://doi.org/10.1016/j.gca.2015.04.047

Li, S., Levin, N.E., Soderberg, K., Dennis, K.J., Caylor, K.K., 2017. Triple oxygen isotope composition of leaf waters in Mpala, central Kenya. Earth Planet. Sci. Lett. 468, 38–50. https://doi.org/10.1016/j.epsl.2017.02.015

Luz, B., Barkan, E., 2010. Variations of $^{17}O/^{16}O$ and $^{18}O/^{16}O$ in meteoric waters. Geochim. Cosmochim. Acta 74, 6276–6286. https://doi.org/10.1016/j.gca.2010.08.016

Luz, B., Barkan, E., Yam, R., Shemesh, A., 2009. Fractionation of oxygen and hydrogen isotopes in evaporating water. Geochim. Cosmochim. Acta 73, 6697–6703. https://doi.org/10.1016/j.gca.2009.08.008

Majoube, M., 1971. Oxygen-18 and deuterium fractionation between water and steam. J. Chem. Phys. 68, 1432–1436.

McDowell, N.G., Allen, C.D., Anderson-Teixeira, K., Aukema, B.H., Bond-Lamberty, B., Chini, L., Clark, J.S., Dietze, M., Grossiord, C., Hanbury-Brown, A., Hurtt, G.C., Jackson, R.B., Johnson, D.J., Kueppers, L., Lichstein, J.W., Ogle, K., Poulter, B., Pugh, T.A.M., Seidl, R., Turner, M.G., Uriarte, M., Walker, A.P., Xu, C., 2020. Pervasive shifts in forest dynamics in a changing world. Science 368, 1–10. https://doi.org/10.1126/science.aaz9463

Merlivat, L., 1978. Molecular diffusivities of $H_2{}^{16}O$, $HD^{16}O$, and $H_2{}^{18}O$ in gases. J. Chem. Phys.

69, 2864–2871. https://doi.org/10.1063/1.436884

Myhre, G., Forster, P.M., Samset, B.H., Hodnebrog, Sillmann, J., Aalbergsjø, S.G., Andrews, T., Boucher, O., Faluvegi, G., Fläschner, D., Iversen, T., Kasoar, M., Kharin, V., Kirkevag, A., Lamarque, J.F., Olivié, D., Richardson, T.B., Shindell, D., Shine, K.P., Stjern, C.W., Takemura, T., Voulgarakis, A., Zwiers, F., 2017. PDRMIP: A precipitation driver and response model intercomparison project-protocol and preliminary results. Bull. Am. Meteorol. Soc. 98, 1185–1198. https://doi.org/10.1175/BAMS-D-16-0019.1

Noone, D., 2012. Pairing measurements of the water vapor isotope ratio with humidity to deduce atmospheric moistening and dehydration in the tropical midtroposphere. J. Clim. 25, 4476–4494. https://doi.org/10.1175/JCLI-D-11-00582.1

Noone, D., Risi, C., Bailey, A., Berkelhammer, M., Brown, D.P., Buenning, N., Gregory, S., Nusbaumer, J., Schneider, D., Sykes, J., Vanderwende, B., Wong, J., Meillier, Y., Wolfe, D., 2013. Determining water sources in the boundary layer from tall tower profiles of water vapor and surface water isotope ratios after a snowstorm in Colorado. Atmos. Chem. Phys. 13, 1607–1623. https://doi.org/10.5194/acp-13-1607-2013

O'Keefe, A., Deacon, D.A.G., 1998. Cavity ring-down optical spectrometer for absorption measurements using pulsed laser sources pulsed laser sources. Rev. Sci. Instrum. 59, 2544–2551. https://doi.org/10.1063/1.1139895

Pabón-Caicedo, J.D., Arias, P.A., Carril, A.F., Espinoza, J.C., Borrel, L.F., Goubanova, K., Lavado-Casimiro, W., Masiokas, M., Solman, S., Villalba, R., 2020. Observed and Projected Hydroclimate Changes in the Andes. Front. Earth Sci. 8, 1–29. https://doi.org/10.3389/feart.2020.00061

Palazzi, E., Mortarini, L., Terzago, S., von Hardenberg, J., 2019. Elevation-dependent warming in global climate model simulations at high spatial resolution. Clim. Dyn. 52, 2685–2702. https://doi.org/10.1007/s00382-018-4287-z

Passey, B.H., Hu, H., Ji, H., Montanari, S., Li, S., Henkes, G.A., Levin, N.E., 2014. Triple oxygen isotopes in biogenic and sedimentary carbonates. Geochim. Cosmochim. Acta 141, 1–25. https://doi.org/10.1016/j.gca.2014.06.006

Pepin, N., Bradley, R.S., Diaz, H.F., Baraer, M., Caceres, E.B., Forsythe, N., Fowler, H., Greenwood, G., Hashmi, M.Z., Liu, X.D., Miller, J.R., Ning, L., Ohmura, A., Palazzi, E., Rangwala, I., Schöner, W., Severskiy, I., Shahgedanova, M., Wang, M.B., Williamson, S.N., Yang, D.Q., 2015. Elevation-dependent warming in mountain regions of the world. Nat. Clim. Chang. 5, 424–430. https://doi.org/10.1038/nclimate2563

Petit, J.R., Jouzel, J., Raynaud, D., Barnola, J.M., Basile, I., Bender, M., Chappellaz, J., Davis, M., Delaygue, G., Delmotte, M., Kotlyakov, V.M., Legrand, M., Lipenkov, V.Y., Loriu, C., Pepin, L., Ritz, C., Saltzman, E., Stievenard, M., 1999. Climate and atmospheric history of the past 420,000 years from the Vostok ice core, Antarctica. Nature 3, 429–436.

https://doi.org/https://doi.org/10.1038/20859

Rangwala, I., Miller, J.R., 2012. Climate change in mountains: A review of elevation-dependent warming and its possible causes. Clim. Change 114, 527–547. https://doi.org/10.1007/s10584-012-0419-3

Risi, C., Landais, A., Winkler, R., Vimeux, F., 2013. Can we determine what controls the spatio-temporal distribution of d-excess and ^{17}O-excess in precipitation using the LMDZ general circulation model? Clim. Past 9, 2173–2193. https://doi.org/10.5194/cp-9-2173-2013

Rozanski, K., Araguás-Araguás, L., Gonfiantini, R., 1993. Isotopic Patterns in Modern Global Precipitation, in: Swart, P.K., Lohmann, K.C., Mckenzie, J., Savin, S. (Eds.), Climate Change in Continental Isotopic Records Geophysical Monograph Series, (Vol. 78). American Geophysical Union, Washington, DC, pp. 1–36. https://doi.org/10.1029/GM078p0001

Salati, E., Dall'Olio, A., Matsui, E., Gat, J.R., 1979. Recycling of water in the Amazon Basin: An isotopic study. Water Resour. Res. 15, 1250–1258. https://doi.org/10.1029/WR015i005p01250

Scherer, J.J., Paul, J.B., O'Keefe, A., Saykally, R.J., 1997. Cavity ringdown laser absorption spectroscopy: History, development, and application to pulsed molecular beams. Chem. Rev. 97, 25–51. https://doi.org/10.1021/cr930048d

Schlesinger, W.H., Jasechko, S., 2014. Transpiration in the global water cycle. Agric. For. Meteorol. 189–190, 115–117. https://doi.org/10.1016/j.agrformet.2014.01.011

Silva, Y., Takahashi, K., Chávez, R., 2008. Dry and wet rainy seasons in the Mantaro river basin (Central Peruvian Andes). Adv. Geosci. 14, 261–264. https://doi.org/10.5194/adgeo-14-261-2008

Trenberth, K.E., 2011. Changes in precipitation with climate change. Clim. Res. 47, 123–138. https://doi.org/10.3354/cr00953

Vuille, M., Werner, M., 2005. Stable isotopes in precipitation recording South American summer monsoon and ENSO variability: Observations and model results. Clim. Dyn. 25, 401–413. https://doi.org/10.1007/s00382-005-0049-9

Welp, L.R., Lee, X., Griffis, T.J., Wen, X.F., Xiao, W., Li, S., Sun, X., Hu, Z., Val Martin, M., Huang, J., 2012. A meta-analysis of water vapor deuterium-excess in the midlatitude atmospheric surface layer. Global Biogeochem. Cycles 26, 1–12. https://doi.org/10.1029/2011GB004246

Worden, J., Noone, D., Bowman, K., Beer, R., Eldering, A., Fisher, B., Gunson, M., Goldman, A., Herman, R., Kulawik, S.S., Lampel, M., Osterman, G., Rinsland, C., Rodgers, C., Sander, S., Shephard, M., Webster, C.R., Worden, H., 2007. Importance of rain evaporation and continental convection in the tropical water cycle. Nature 445, 528–532.

https://doi.org/10.1038/nature05508

Xiao, W., Wei, Z., Wen, X., 2018. Evapotranspiration partitioning at the ecosystem scale using the stable isotope method—A review. Agric. For. Meteorol. 263, 346–361. https://doi.org/10.1016/j.agrformet.2018.09.005

Chapter 2 Stable Water Isotopes Reveal Effects of Intermediate Disturbance and Canopy Structure on Forest Water Cycling[2]

Co-authors: Christopher J. Poulsen, Richard P. Fiorella, and Ashley M. Matheny

2.1 Abstract

Forests play an integral role in the terrestrial water cycle and link exchanges of water between the land surface and the atmosphere. To examine the effects of an intermediate disturbance on forest water cycling, we compared vertical profiles of stable water vapor isotopes in two closely located forest sites in northern lower Michigan. At one site, all canopy-dominant early successional species were stem-girdled to induce mortality and accelerate senescence. At both sites, we measured the isotopic composition of atmospheric water vapor at six heights during three seasons (spring, summer, and fall), and paired vertical isotope profiles with local meteorology and sap flux. Disturbance had a substantial impact on local water cycling. The undisturbed canopy was moister, retained more transpired vapor, and at times was poorly mixed with the free atmosphere above the canopy. Differences between the disturbed and undisturbed sites were most pronounced in the summer when transpiration was high. Differences in forest structure at the two sites also led to more isotopically stratified vapor within the undisturbed canopy. Our findings suggest that intermediate disturbance may increase mixing between the surface layer and above-canopy atmosphere and alter ecosystem-atmosphere gas exchange.

2.2 Introduction

Forests cover one-third of Earth's surface and play important roles regulating carbon storage, freshwater, and climate (FAO, 2015). As part of the terrestrial water cycle, forests promote rainfall, cool surface temperatures, transport water across vast landscapes, and regulate water

[2] Published as: Aron, P.G., Poulsen, C.J., Fiorella, R.P., Matheny, A.M., (2019) Stable Water Isotope Reveal Effects of Intermediate Disturbance and Canopy Structure on Forest Water Cycling, Journal of Geophysical Research: Biogeosciences, 124, doi: 10.1029/2019JG005118. Data associated with this chapter are accessible from the Yale University Stable Water Vapor Isotopes Database (SWVID) (https://vapor-isotope.yale.edu/).

supplies (Ellison et al., 2017). Globally, vegetation recycles a tremendous amount of water to the atmosphere via transpiration; forests account for approximately 50% of this flux (Schlesinger & Jasechko, 2014; Xiao, Wei, & Wen, 2018). However, as the frequency of environmental disturbances from natural and anthropogenic forces accelerate, forest hydrological cycles may change (Ellison et al., 2017; Pan et al., 2011). Accordingly, changes in forest cover may affect rainfall and water availability, water transport, and local and global temperatures (Debortoli et al., 2017; Ellison et al., 2017; Hesslerová, Pokorný, Brom, & Rejšková-Procházková, 2013; Jasechko et al., 2013). Understanding the links between forest structure and water cycling is necessary to better predict future temperature and precipitation patterns and to manage freshwater resources.

Forest disturbances range from complete stand-clearing events to subtle changes that target select species or affect the canopy irregularly. Intermediate disturbances, which do not trigger complete stand replacement, occur naturally though pest infestations (Herms & McCullough, 2014; Logan, Régnière, & Powell, 2003), ecological succession (Gough et al., 2013; Hardiman, Bohrer, Gough, & Curtis, 2013), or extreme weather events such as fire, ice storms, strong winds, or drought (Anderegg et al., 2018; He & Mladenoff, 1999; Mcdowell et al., 2008; Mitchell, 2013; Trugman, Medvigy, Anderegg, & Pacala, 2018). Intermediate disturbances can also be anthropogenically driven by selective logging (Asase, Asiatokor, & Ofori-Frimpong, 2014; Asner, Keller, Pereira, Zweede, & Silva, 2004), prescribed fire management (Parsons & DeBenedetti, 1979; Stephens et al., 2009), arson or accidental human fire ignition (Ganteaume et al., 2013), or human land use (Schulte, Mladenoff, Crow, Merrick, & Cleland, 2007). Each of these mechanisms alters forest canopy function through changes in the vertical distribution of solar radiation (Hardiman et al., 2013), soil moisture (He et al., 2013), evapotranspiration partitioning (Matheny et al., 2014), air temperature, humidity, wind speed, and turbulent mixing (Maurer, Hardiman, Vogel, & Bohrer, 2013), and thus affect the microclimate and water cycle within the canopy (Baldocchi, Wilson, & Gu, 2002; Chen et al., 1999).

Forest structure and water cycling are linked through exchanges of mass and energy. Photosynthesis, transpiration, respiration, and stomatal conductance depend on temperature, relative humidity, and light. The physical arrangement of trees in a forest creates drag and turbulence (Maurer et al., 2013), intercepts and scatters light (Atkins, Fahey, Hardiman, & Gough, 2018; Hardiman et al., 2018), and modulates heat received by soil and leaves (Baldocchi & Meyers, 1998). In turn, energy evaporates water, either from the soil or through transpiration, and

generates sensible heat. Although forests are susceptible to an array of intermediate disturbances, potential changes of mass and energy exchanges following changes to canopy structure are not completely understood. Here, we use stable water isotopes to study water cycling at two forest sites, one disturbed and one undisturbed, and examine the effects of an intermediate disturbance on canopy moisture and forest water cycling.

Stable water isotopes are tracers of hydrologic processes and may be used to better understand ecosystem-atmosphere water exchange. Phase changes of water preferentially partition heavy isotopologues into the liquid or solid phase while light isotopologues remain in the higher energy vapor phase (Gat, 1996). At equilibrium, this fractionation is temperature dependent (Horita & Wesolowski, 1994). When the two phases are not in equilibrium, an additional kinetic fractionation arises due to differences in the diffusivities among isotopologues. The difference in diffusivity between $H_2{}^{18}O/H_2{}^{16}O$ is larger than that for $HDO/{}^1H_2O$, which results in a stronger kinetic effect on oxygen isotopes than hydrogen isotopes (Cappa, 2003; Luz, Barkan, Yam, & Shemesh, 2009; Merlivat, 1978). The degree of kinetic fractionation is often quantified using deuterium excess ($d = \delta D - 8*\delta^{18}O$ (Dansgaard, 1964)), which is a measure of deviation from the global meteoric water line (GMWL, $\delta D = 8*\delta^{18}O + 10‰$ (Craig, 1961)).

Advances in laser-based, high-resolution, near-continuous water isotope analyzers have revolutionized water vapor isotope monitoring and greatly broadened the scales of hydrologic spatiotemporal variability that can be studied. At the boundary layer and surface level, isotope ratios of water vapor have been measured to investigate moisture sources (Delattre, Vallet-Coulomb, & Sonzogni, 2015; Fiorella, Poulsen, & Matheny, 2018; Galewsky & Samuels-Crow, 2015; Noone et al., 2013; Steen-Larsen et al., 2015), quantify entrainment and evapotranspiration (ET) (He & Smith, 1999; Huang & Wen, 2014; Lai & Ehleringer, 2011; Simonin et al., 2014; Welp et al., 2012), and partition the ET flux (Aemisegger et al., 2014; Good et al., 2014; Xiao et al., 2018). Together, this work demonstrates the utility of water vapor isotope measurements as a tool to study water fluxes between ecosystems and the atmosphere. The high temporal resolution of vapor isotope measurements from laser-based analyzers captures rapid, sub-diurnal (minutes to hours) changes in water cycling and links surface hydrology with biotic cycles and atmospheric conditions.

Isotope ratios of water vapor can expand our current understanding of forest hydrology because the fluxes and processes that act to dry or moisten canopies – entrainment, evaporation,

and transpiration – have distinct isotopic signatures. During clear conditions, entrainment tends to dry canopy air with vapor that is isotopically more depleted than air within the canopy (Welp et al., 2012). Evaporation moistens canopy air with vapor that is relatively depleted in heavy isotopes and has a high *d* due to the high degree of kinetic fractionation associated with the phase change from soil water to water vapor (Barnes & Allison, 1984). The isotopic signature of transpiration is more complicated and depends on timescale, vegetation type, and microclimates within the canopy. Over timescales greater than leaf-water turnover times, the isotopic composition of transpired vapor must equal that of source water taken up at the roots since plants generally do not fractionate soil water during root uptake (Ehleringer & Dawson, 1992). However, on shorter timescales, the isotopic composition of transpired vapor may deviate from source water (Cernusak, Pate, & Farquhar, 2002; Harwood, Gillon, Griffiths, & Broadmeadow, 1998; Simonin et al., 2013; Welp et al., 2008).

In this study, we measured vertical profiles of water vapor isotopes in two closely located forest sites in northern Michigan. The control site is representative of forests in the northern Great Lakes region; at the experimental site, an intermediate disturbance was prescribed to test the effects of this disturbance on forest processes. Our objectives were to: 1) quantify the temporal variation of vapor $\delta^{18}O$ and δD at the two sites, 2) use the isotopic composition of water vapor to compare water cycling at disturbed and undisturbed sites, and 3) identify patterns and controls on canopy moisture. The sites in this study are hydrologically and meteorologically well studied (e.g. He et al., 2013; Matheny et al., 2014; Maurer et al., 2013). Therefore, an additional goal is to explore how vapor isotope profiles and flux tower measurements complement each other or provide similar information about water cycling. This goal may inform future vapor isotope studies that are not collocated with flux towers or sap flux networks. The addition of isotope measurements at these field sites improves our understanding of forest hydrologic responses to intermediate disturbance and expands the use of water vapor isotopes to study land-atmosphere interactions.

2.3 Materials and methods

2.3.1 Site description

This study was conducted at two field sites at the University of Michigan Biological Station (UMBS) in northern lower Michigan, USA. Mean annual temperature at UMBS is 6.8°C and the site receives an average 805 mm of precipitation annually (Matheny et al., 2014). Soils are well

drained Haplorthods of the Rubicon, Blue Lake, or Cheboygan series and consist of 92.2% sand, 6.5% silt, and 0.6% clay (Nave et al., 2011). Water isotope measurements were conducted at two adjacent UMBS sites (~1.2 km apart) with collocated eddy covariance towers. Both flux towers are affiliated with the AmeriFlux network (http://ameriflux.lbl.gov/).

The forest surrounding the control site (45°35'35" N, 84°41'48" W, AmeriFlux database site-ID US-UMB), hereafter referred to as the undisturbed site, is dominated by early successional bigtooth aspen (*Populus grandidentata*) and paper birch (*Betula papyrifera*), but is transitioning to a mixed composition of mid-successional red oak (*Quercus rubra*), red maple (Acer rubrum), white pine (*Piuns strobus*), American beech (*Fagus grandifolia*), and sugar maple (*Acer saccharum*). The tight arrangement of trees and closed, broadleaf canopy cover at this site is representative of many forests in the northern Great Lakes region. This site has remained undisturbed since the region was extensively logged in the early twentieth century. The tower at the disturbed site (45°33'45" N, 84°41'51" W, AmeriFlux database site-ID US-UMd) is located within the Forest Accelerated Succession ExperimenT (FASET) plot, hereafter referred to as the disturbed site. In 2008, all aspen and birch in a 39 ha stand around the disturbed site's tower were stem girdled to induce mortality of early successional species and evaluate the effects of ecologic succession. Additional information about the FASET experiment and site details are available in Gough et al. (2013).

Prior to the disturbance, forest composition, structure, and meteorological conditions were similar at the undisturbed and disturbed sites. Persistent differences in forest structure and water cycling (He et al., 2013; Matheny et al., 2014) have developed since the disturbance as a result of a younger, more open, structurally complex canopy at the disturbed site (Hardiman et al., 2013; Maurer et al., 2013). As a result of the girdling treatment, the disturbed canopy has more deep gaps and clumped vegetation than the undisturbed canopy.

2.3.2 Water vapor isotope measurements

We deployed cavity ring-down spectrometers (CRDS) in temperature-controlled sheds near both eddy covariance towers. At the undisturbed site, a Picarro L2120-i was installed on April 16, 2016. A Picarro L2130-i was installed at the disturbed site on April 25, 2016. Both analyzers were removed on October 1, 2016. Two liquid internal laboratory standards (−8.33‰ and −55.86‰ (heavy standard) and −23.81‰ and −181.35‰ (light standard) for $\delta^{18}O$ and δD,

respectively) were measured approximately every 12 hours to monitor for drift and calibrate isotope data to the VSMOW–SLAP scale (Bailey, Noone, Berkelhammer, Steen-Larsen, & Sato, 2015). Standards were introduced as a continuous stream using a Standard Delivery Module (SDM) and high precision vaporizer (A0110) maintained at 140°C and ambient pressure. A Drierite (26800) column was used to dry ambient air for standards analysis. Laboratory standards were measured at water vapor concentrations between 10,000 and 30,000 ppmv.

We used version 1.2 of the University of Utah vapor processing scripts (Fiorella, Bares, Lin, Ehleringer, & Bowen, 2018) to calibrate ~1 Hz isotope data and determine instrument precision. We found that isotope values varied with humidity. As a result, we varied the SDM delivery rate of liquid standards and measured isotopic compositions from 2,000 to 30,000 ppm to develop equations and correct for this apparent humidity bias. We measured both internal standards at each injection rate for 20 minutes, but only analyzed measurements from the last 10 minutes of each humidity level to avoid memory effects between different standards or injection rates. Within a humidity range (here 15,000-25,000 ppm) where the response between cavity humidity and isotopic composition was minimal, we calculated the deviation of measured isotopic compositions from the true isotopic composition. We then developed and applied correction equations, determined by a linear regression of the deviation between measured and true isotopic compositions against the inverse of cavity humidity within the 15,000-25,000 ppm range, to correct isotope data for the dependence on cavity humidity. Additional details on this cavity humidity correction are provided in the supplementary information. Instrument precision also depended on cavity humidity. We present the 1σ uncertainty at 5,000 ppmv, the lowest measured vapor mixing ratio during our sampling campaign, and 15,000 ppmv, near the average mixing ratio across all three sampling periods. For *d*, we assume oxygen and hydrogen errors are independent. At the undisturbed site, 1σ uncertainty ranged from 0.43‰ for $\delta^{18}O$, 1.51‰ for δD, and 3.73‰ for *d* at 5,000 ppmv to 0.24‰, 0.74‰, and 2.02‰ (for oxygen, hydrogen, and *d*, respectively) at 15,000 ppm. At the disturbed site, 1σ uncertainty ranged from 0.20‰, 0.68‰, and 1.73‰ at 5,000 ppmv to 0.11‰, 0.35‰, and 0.94‰ (oxygen, hydrogen, and *d*, respectively) at 15,000 ppm.

Each eddy covariance tower was equipped with a vapor sampling manifold that included intake lines at five heights within the canopy and one above the canopy. Within-canopy vapor was sampled at 2, 5, 10, 15, and 20 m above the forest floor. Above-canopy vapor was sampled at 32 m (disturbed site) and 34 m (undisturbed site). The above-canopy sampling port was collocated

with meteorological and flux measurements from the towers. A diaphragm pump operated at ~5 L/min on each sampling manifold to ensure continual airflow and minimize memory effects between samples. Sampling lines were constructed with Bev-A-Line tubing to prevent fractionation (Simonin et al., 2013), encased in insulation, and wrapped with a warm wire to prevent condensation.

Each CRDS was setup to control a multi-position valve (VICI/Valco EMT2SD6MWE) to switch between sampling heights. Each port was measured for 5 minutes; we omit the first 2 minutes of each measurement to account for memory effects from switching positions and used the mean of the last 3 minutes of each measurement for analysis (Aemisegger et al., 2012). We measured 48 vertical profiles of vapor isotopes each day. Within each profile, the 3-minute average of isotopic measurements from each sampling port is assumed to represent the isotopic composition at that height for the full 30-minute profile.

We focus on three time periods during the 2016 growing season: May 10-31 (spring, DOY 131-151), June 7-30 (summer, DOY 159-182), and September 21-30 (fall, DOY 265-274). For convenience we refer to the three time periods as spring, summer, and fall, respectively. We do not include winter measurements because we expect canopy structure to have little effect on water fluxes when trees are bare and dormant. Missing records are due to equipment malfunction and electrical problems at the field sites. In August 2016, the analyzer from the disturbed site was temporarily moved to a different location for another study.

2.3.3 Meteorological, sap flux, and eddy covariance measurements

Temperature and relative humidity (HMP45g, Vaisala, Helsinki, Finland) were measured at 2 m and above the canopy at 32 or 34 m (disturbed and undisturbed sites, respectively) at each site. The 2 m meteorological towers were located approximately 60 m from each flux tower. Temperature and relative humidity sensors were removed from the disturbed site in the late summer. Replacement equipment was installed 1 m above the forest floor near the disturbed site flux tower, but only recorded temperature. Surface pressure (PTB101B, Vaisala, Helsinki Finland) was measured at ground level at the undisturbed site. Sap flux, which was measured as a proxy for transpiration, was continuously measured in 60 trees at each site with Granier-style (Granier, 1987) thermal dissipation probes. Additional details about sap flux measurements at UMBS are available in Matheny et al. (2014). Eddy covariance CO_2 and H_2O fluxes were measured above the canopies at 32 and 34 m. The latent heat flux was measured at high resolution (10 Hz) using the eddy

covariance approach: water vapor and CO_2 concentrations were measured using closed-path infrared gas analyzers (LI7000, LI-COR Biosciences, Lincoln, NE, USA); wind velocity and temperature were measured with a 3-D ultrasonic anemometer (CSAT3, Campbell Scientific, Logan, UT, USA). Details about eddy flux data processing are available in Gough et al. (2013) and Matheny et al. (2014). Above-canopy variables and 1 m temperature measurements were reported as 30-minute averages. Sap flux and 2 m meteorological measurements were collected every minute and averaged to 30-minute time steps to facilitate analysis with isotopic measurements. Daily precipitation amount was measured approximately 4 miles east of UMBS at the Pellston Regional Airport and accessed from the NOAA Climate Data Online archive (Network ID USW00014841).

2.4 Results

2.4.1 Seasonal variability

All $\delta^{18}O$ and δD vapor values are plotted in Figure 2.1. Isotopic compositions cluster around the GMWL during all three seasons with a consistent, slightly shallower slope than the global meteoric water line. In general, isotopic trends were similar for oxygen and hydrogen; therefore, we show and discuss only $\delta^{18}O$ throughout this section.

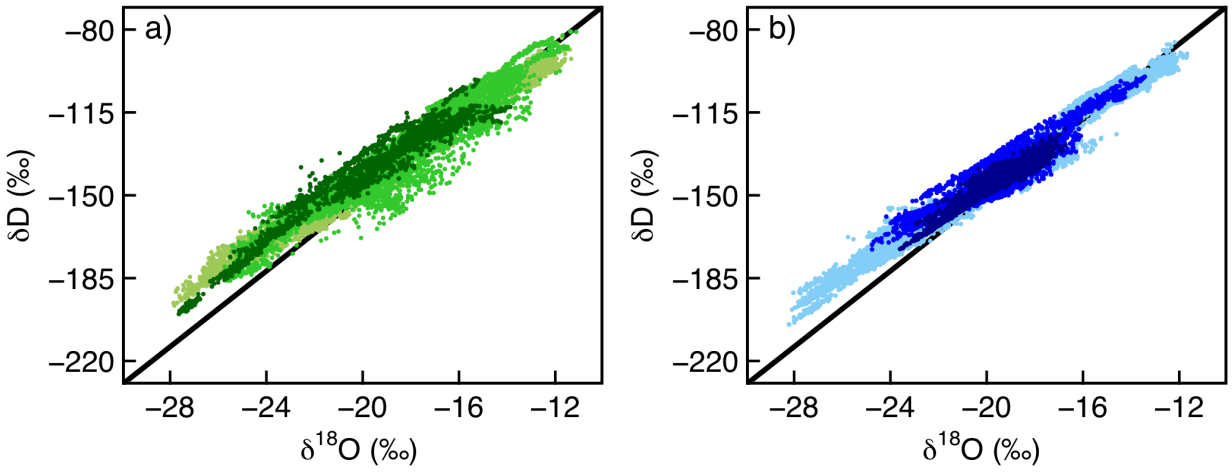

Figure 2.1 $\delta^{18}O$ (‰) and δD (‰) of water vapor measured during all three sampling periods at a) the undisturbed site (green) and b) the disturbed site (blue). Color intensity increases for each seasonal period from spring (pale) to fall (dark). For reference, the GMWL is plotted as a black line.

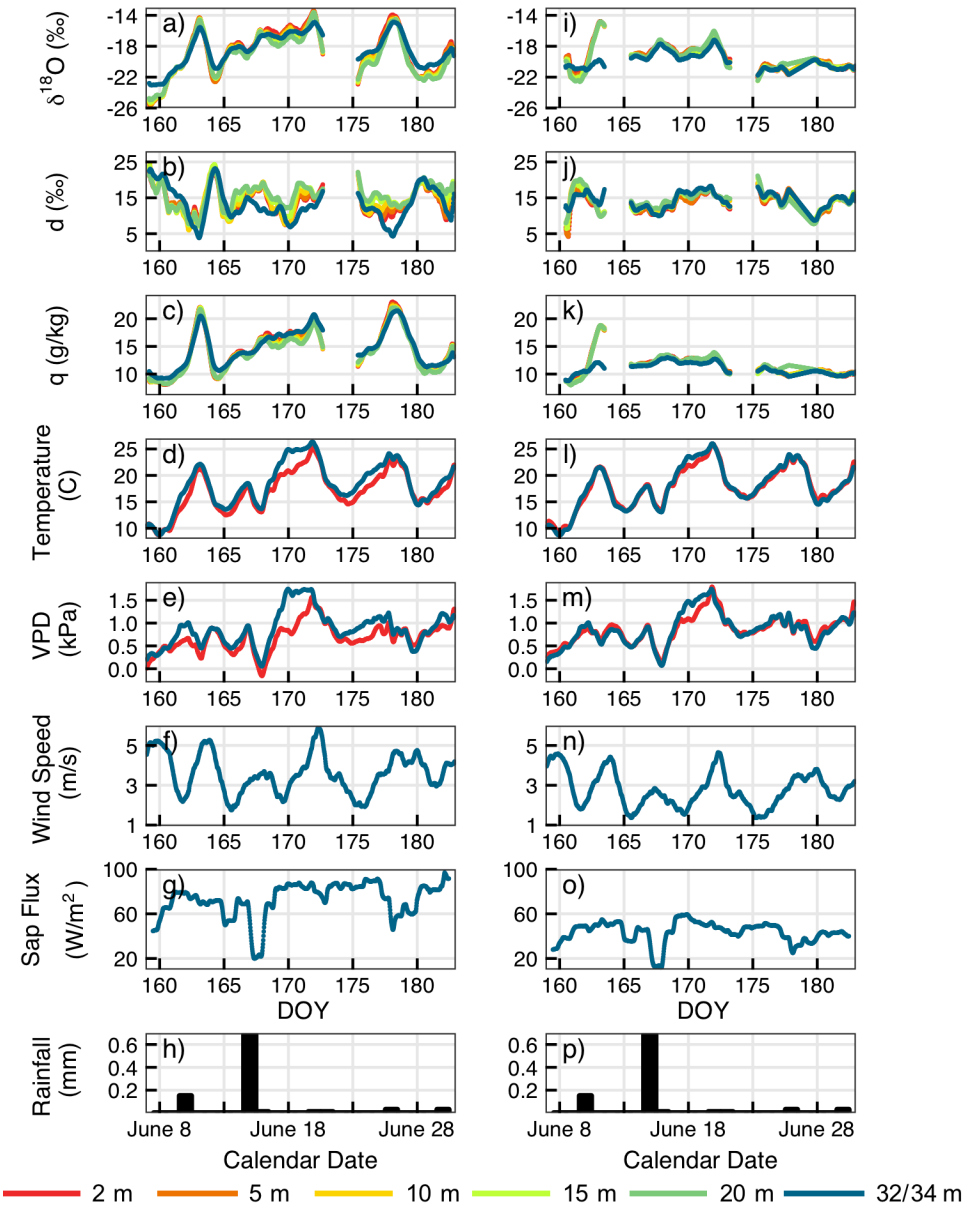

Figure 2.2 Timeseries of moving 24-hour average of summer isotopic compositions, meteorological data, and sap flux at the undisturbed (left) and disturbed (right) sites. a,i) vapor $\delta^{18}O$ (‰); b,j) *d* (‰); c,k) specific humidity (*q*, g/kg); d,l) temperature (°C); e,m) vapor pressure deficit (VPD, kPa); f,n) wind speed (m/s); g,o) sap flux (W/m^2); h,p) daily precipitation amount (mm). Isotopes and specific humidity are shown for all 6 heights from low (red) to high (blue). Meteorology is shown at 2 m (red) and above-canopy (blue).

On timescales longer than a day, isotopic and meteorologic trends were similar at the disturbed and undisturbed sites (Figures 2.2 and S2.11-S2.12). Seasonal comparisons between the two sites were generally consistent across the spring, summer, and fall measurement periods, so

we focus primarily on summer conditions and include additional information about spring and fall conditions in the supplementary information. Vapor $\delta^{18}O$ varied between −14 and −26‰ at both sites and was typically greater at the surface and lower in the upper canopy (10-20 m) (Figures 2.2 and S2.11-S2.12 a and i). On average, vapor $\delta^{18}O$, specific humidity (q), temperature, and vapor pressure deficit (VPD) were highest in the summer and lower in the spring and fall (Figures 2.2 and S2.11-S2.12 a,c,d,e and i,k,l,m). Sap flux increased through the spring sampling period, was at a maximum in the summer, and was at a minimum in the fall (Figures 2.2 and S2.11-S2.12 g and o). The seasonal magnitudes of sap flux are consistent with leaf area index (LAI) trends as canopies at both sites leafed out during the spring sampling period, were at their maximum extent during the summer, and were in decline in the fall. Wind speed did not vary on seasonal timescales, but rather, associated with the passing of synoptic scale weather systems, meandered on a 2-4 day timescale with very few excursions beyond a small range (1-5 m/s) (Figures 2.2 and S2.11-S2.12 f and n).

Despite the general coherence between isotopes, meteorology, and ecohydrology on seasonal timescales at UMBS, differences emerged between the disturbed and undisturbed sites (Figure 2.3, Table 2.1). During the spring and summer, vapor at the disturbed site was generally more depleted in heavy isotopes than at the undisturbed site (Figures 2.3a and 2.3i). This difference was more pronounced in the summer (1-2‰ difference) than in the spring (~0.4‰). Within the canopies, mean spring and summer d was ~0.3‰ greater at the undisturbed site (Figures 2.3b and 2.3j). Although the magnitude of between-site d differences was greater in the summer than in the spring, this difference is not statistically significant. In the fall, the disturbed site was generally more depleted in heavy isotopes than the undisturbed site (Figure 2.3q) and d was 4-8‰ greater at the undisturbed site (Figure 2.3r). In all three seasons the disturbed site was drier than the undisturbed site (Figures 2.3c, 2.3k, and 2.3s). Above the canopy, air temperature was ~0.4 °C warmer at the undisturbed site (Figures 2.3d, 2.3l, and 2.3t) while VPD was nearly identical (< 0.04 kPa difference, Figures 2.3e, 2.3m, and 2.3u). Near the surface (2 m), air temperature was ~0.6 °C cooler (Figures 2.3d, 2.3l, and 2.3t) and VPD ~0.15 kPa lower at the undisturbed site (Figures 2.3e, 2.3m, and 2.3u). Mean wind speed was ~1 m/s greater at the undisturbed site than the disturbed site (Figures 2.3f, 2.3n, and 2.3v), and sap flux was almost always greater at the undisturbed site than the disturbed site (Figures 2.3g, 2.3o, and 2.3w). Mean seasonal differences

of isotopes, meteorology, and sap flux are presented in Table 2.1 with significant differences ($p < 0.05$) between the disturbed and undisturbed sites highlighted.

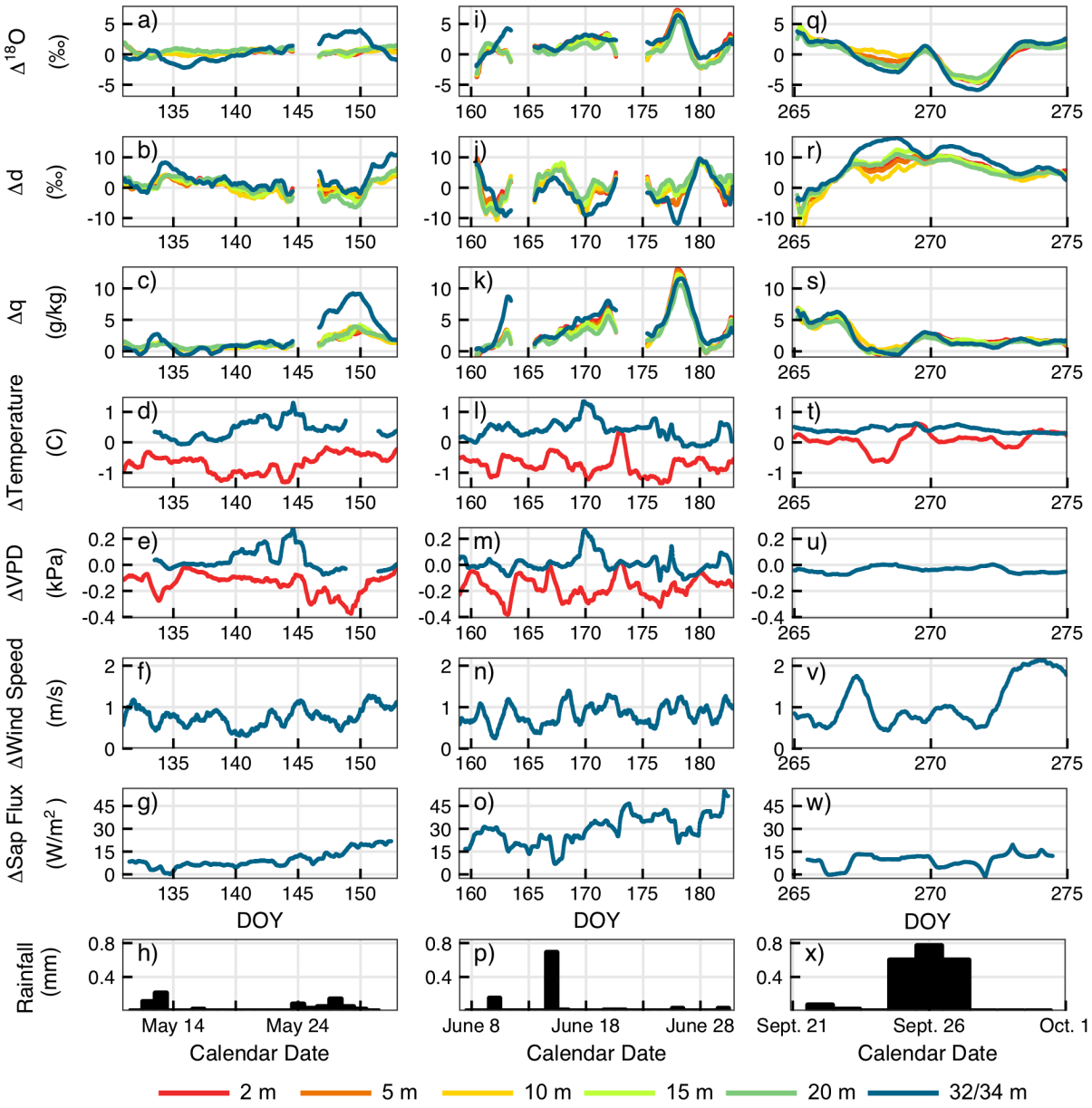

Figure 2.3 Differences (Δ, undisturbed – disturbed) between the undisturbed and disturbed sites in the spring (a-h), summer (i-p), and fall (q-x). a,i,q) vapor $\delta^{18}O$ (‰); b,j,r) *d* (‰); c,k,s) specific humidity (*q*, g/kg); d,l,t) temperature (°C); e,m,u) vapor pressure deficit (VPD, kPa); f,n,v) wind speed (m/s); g,o,w) sap flux (W/m^2). Panels h, p, and x show total daily precipitation amount (mm). Differences of isotopes and specific humidity are shown for all 6 heights from low (red) to high (blue). Where measured, meteorological differences are shown at 2 m (red) and above-canopy (blue).

Table 2.1 Isotopic, meteorologic, and sap flux differences between the undisturbed and disturbed sites. Statistical significance ($p < 0.05$) is indicated by bolded values.

SPRING						
	2 m	5 m	10 m	15 m	20 m	32/34 m
$\delta^{18}O$ (‰)	0.33	0.46	0.36	0.51	0.60	**0.45**
d (‰)	**0.60**	**0.16**	**0.34**	**0.17**	**0.45**	**2.47**
q (g/kg)	**1.26**	**1.31**	**1.28**	**1.35**	**1.40**	**2.38**
Temperature (°C)	**–0.68**					**0.42**
VPD (kPa)	**–0.14**					**0.04**
Wind Speed (m/s)						**0.77**
Sap Flux (W/m^2)						**9.76**
SUMMER						
	2 m	5 m	10 m	15 m	20 m	32/34 m
$\delta^{18}O$ (‰)	**1.48**	**1.34**	**1.29**	**1.19**	**0.84**	**2.00**
d (‰)	**–0.13**	**–0.05**	**–0.23**	**0.68**	**1.19**	**–2.10**
q (g/kg)	**3.71**	**3.56**	**3.43**	**3.45**	**3.01**	**4.34**
Temperature (°C)	**–0.74**					**0.40**
VPD (kPa)	**–0.17**					0.01
Wind Speed (m/s)						**0.83**
Sap Flux (W/m^2)						**29.36**
FALL						
	2 m	5 m	10 m	15 m	20 m	32/34 m
$\delta^{18}O$ (‰)	**–0.52**	–0.20	0.12	**–0.32**	**–0.44**	**-0.61**
d (‰)	**5.75**	**5.18**	**4.29**	**6.31**	**5.54**	**8.62**
q (g/kg)	**2.17**	**2.08**	**2.14**	**2.13**	**1.78**	**2.08**
Temperature (°C)	0.06					**0.42**
VPD (kPa)						**–0.04**
Wind Speed (m/s)						**1.11**
Sap Flux (W/m^2)						**9.25**

The two sites also exhibited isotopic differences with height. While $\delta^{18}O$ was generally greater near the surface than in the upper canopy, vertical gradients of $\delta^{18}O$ within the canopies were larger at the undisturbed site than at the disturbed site (Figure 2.4). Summer and fall $\delta^{18}O$ gradients within the undisturbed canopy (2 – 20 m) were pronounced at night (0.70‰ and 0.95‰ in the summer and fall, respectively) but dissipated through the day (Figure 2.4 a-d). The disturbed site did not exhibit the same stratified nighttime isotopic compositions and was relatively well mixed with vertical gradients generally less than 0.25‰ (Figure 2.4 e-h). Within each season, *q* ratios exhibited little variation at any of the sampling heights (Figure S2.13).

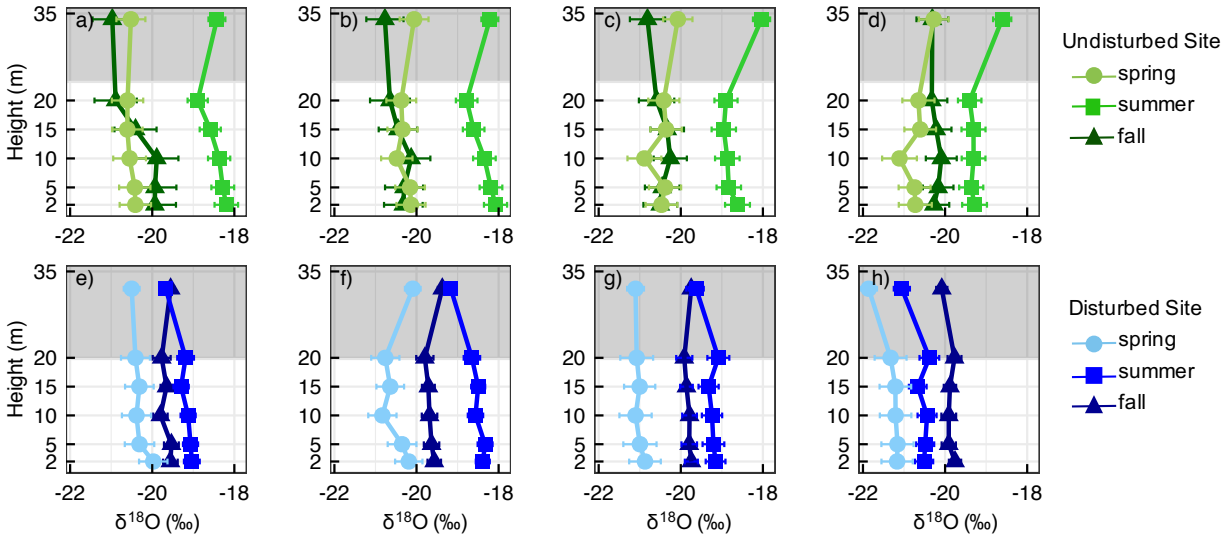

Figure 2.4 Mean profiles of water vapor $\delta^{18}O$ (‰) from the undisturbed (green) and disturbed (blue) sites during the spring, summer, and fall. Shown here are profiles from four time slices: nighttime (00:00 to 03:00, a and e), sunrise (06:00 to 09:00, b and f), midafternoon (14:00 to 17:00, c and g), and sunset (18:00 to 21:00, d and h). Grey shading indicates heights above the canopy. Error bars show standard error.

2.4.2 Synoptic variability

Passing weather systems drove relatively large shifts of isotopes, meteorology, and sap flux within a few days. We focus on a summer storm (DOY 166-171) and examine how isotopes, sap flux, and eddy covariance data reveal information about the hydrologic fluxes associated with this event. 0.69 mm of rain fell on DOY 167. We include one day of pre-storm conditions (DOY 166) and define the end of the storm as the day during which VPD at the undisturbed site was at a maximum following the rainfall event. We calculated the isotopic composition of the ET flux ($\delta^{18}O_{ET}$) at 20 m with a Keeling mixing model (Keeling, 1958; Yakir & Sternberg, 2000), and followed the methods described by Williams et al. (2004) to partition the transpiration component of ET (defined here as T/ET) from sap flux and eddy covariance measurements.

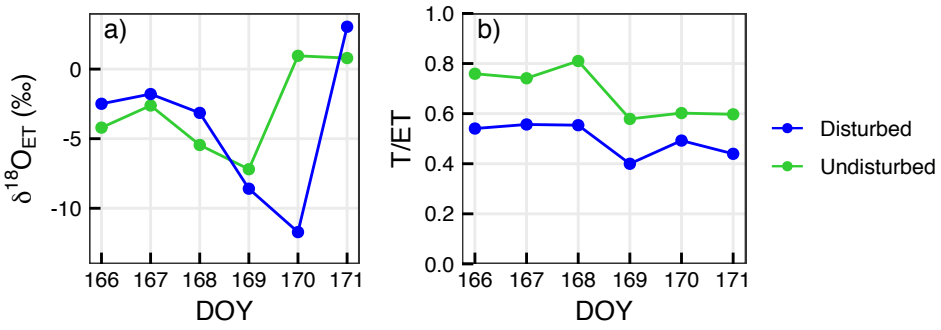

Figure 2.5 a) $\delta^{18}O_{ET}$ and b) T/ET at the disturbed (blue) and undisturbed (green) sites during the summer storm (DOY 166-171). Rain fell during the day on DOY 167.

Prior to the storm, conditions at the disturbed and undisturbed site were similar but reflect the consistent seasonal differences at the two sites: sap flux was greater, $\delta^{18}O$ higher, and air moister at the undisturbed site than at the disturbed site (Figure 2.5). Transpiration accounted for a greater proportion of the ET flux at the undisturbed site (~70%) than the disturbed site (~50%) (Figure 2.5b). Rain fell from 10:00 to 17:00 on DOY 167. During the event, sap flux and VPD decreased to nearly zero while q and $\delta^{18}O$ increased (Figure 2.6). Immediately after the storm (DOY 168) increases in VPD, sap flux, and T/ET drove $\delta^{18}O_{ET}$ and $\delta^{18}O$ of ambient vapor to higher values. By DOY 169 and 170, sap flux and VPD returned to pre-storm values and were similar at the disturbed and undisturbed sites (Figure 2.5 c-d and g-h). At the same time, isotopic differences emerged at the two sites (Figure 2.5a Figures 2.6 a-b and e-f).

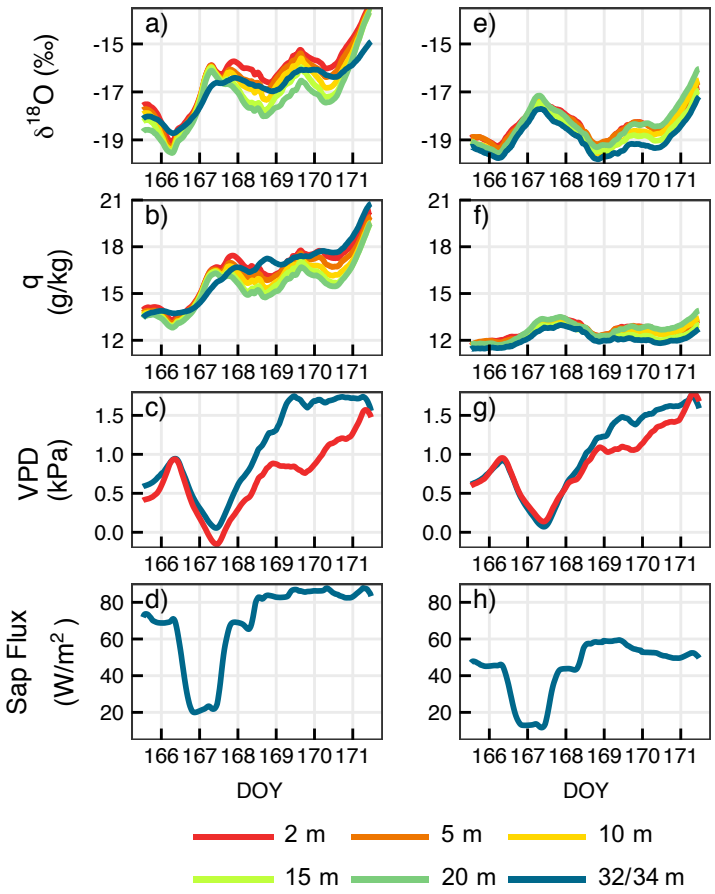

Figure 2.6 Time series of moving 24-hour average of summer storm (DOY 166-171). Rain fell on DOY 167. a,e) vapor $\delta^{18}O$ (‰); b,f) specific humidity (*q*, g/kg); c,g) vapor pressure deficit (VPD, kPa); d,h) sap flux (W/m^2) at the undisturbed (left) and disturbed (right) sites. Isotopes and specific humidity are shown for all 6 heights from low (red) to high (blue). Meteorology is shown at 2 m (red) and above-canopy (blue).

2.4.3 Diurnal cycles

Vapor $\delta^{18}O$ and *d* generated clear diurnal cycles at both the disturbed and undisturbed sites (Figure 2.7). Diurnal cycles emerged in the spring, were most pronounced during the summer, and decreased in amplitude in the fall. Generally, $\delta^{18}O$ increased slightly just after sunrise to an early-morning peak, decreased through the day to a late afternoon minimum, and increased in the early evening before sunset (Figure 2.7, top row). Nighttime $\delta^{18}O$ values exhibited little variation. The diurnal *d* cycle was apparent in all three seasons and at both sites (Figure 2.7, second row). *d* was relatively constant at night, decreased briefly just after sunrise, increased in the morning to a mid-day maximum, and decreased rapidly in the late afternoon. In all three seasons, the timing of the

diurnal *d* cycle was consistent between sites but the amplitude and rate of change differed. *q* exhibited very little diurnal variation (Figure 2.7, third row).

Diurnal temperature generally peaked in the mid-afternoon and was at a minimum just before sunrise (Figure 2.7, fourth row); relative humidity exhibited the opposite diurnal cycle with the greatest values just before sunrise and the lowest values in the mid-afternoon (Figure 2.7, fifth row). Like temperature, diurnal vapor pressure deficit (VPD) increased in the morning and decreased in the afternoon (Figure 2.7, sixth row). In the spring and summer, diurnal wind speed exhibited a distinct cycle with maximum values in the mid-afternoon and minimum values around sunrise. There was no clear diurnal cycle of wind speed in the fall at either site (Figure 2.7, seventh row). At both sites, sap flux began at sunrise, reached a maximum in the early afternoon, and was nearly zero by sunset (Figure 2.7, eighth row). The shape of the diurnal sap flux cycle was consistent throughout all three seasons, but the maximum summer diurnal sap flux was approximately two times greater than sap flux in the spring or fall periods (Figure 2.7, eighth row).

Isotopic, meteorologic, and sap flux differences also emerged at the disturbed and undisturbed sites on diurnal timescales. In the summer and fall, the early morning $\delta^{18}O$ peak was more pronounced at the undisturbed site than at the disturbed site (Figure 2.7 q,ag and y,ao). In addition, although the magnitude of diurnal *d* cycles was similar at the two sites (~12, 20, and 8 ‰ in the spring, summer, and fall, respectively), daytime patterns differed (Figure 2.7, second row). In all three seasons, *d* increased rapidly in the undisturbed canopy in the early morning and maintained a high plateau through the day. In contrast, at the disturbed site, *d* increased gradually through the early morning and mid-afternoon and peaked in the late afternoon. Vertical gradients of meteorological conditions between the surface and 32/34 m were greater at the undisturbed site than the disturbed site (Figure 2.7, fourth and fifth rows). Similarly, diurnal wind speed and sap flux were greater at the undisturbed site than the disturbed site (Figure 2.7, rows seven and eight, respectively).

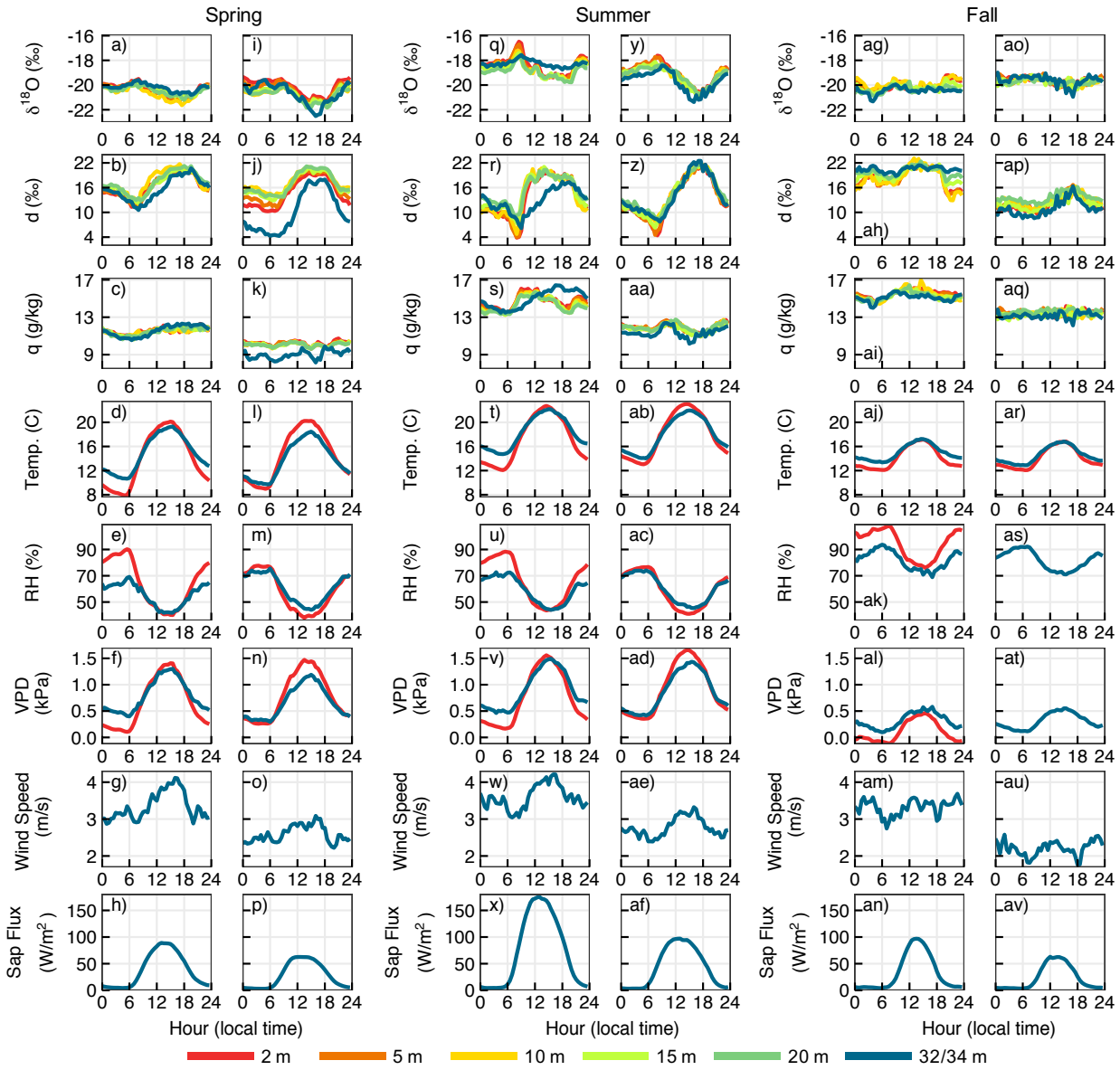

Figure 2.7 Diurnal isotopic, meteorologic, and sap flux cycles at all sampling heights in the spring (a-p), summer (q-af), and fall (ag-av). Diurnal cycles were calculated by removing the background isotopic composition at 15 m. In each season, diurnal cycles at the undisturbed site are shown on the left (a-h, q-x, and ag-an) and diurnal cycles from the disturbed site are to the right (i-p, y-af, and ao-av). $\delta^{18}O$ (‰), (a,i,q,y,ag,ao); *d* (‰), (b,j,r,z,ah,ap); *q* (g/kg), (c,k,s,aa,ai,aq); temperature (°C), (d,l,t,ab,aj,ar); relative humidity (%), (e,m,u,ac,ak,as); vapor pressure deficit (VPD, kPa), (f,n,v,ad,al,at); wind speed (m/s), (g,o,w,ae,am,au); and sap flux (W/m^2), (h,p,x,af,an,av) are shown for both sites and all three seasons. Heights of isotope measurements vary along a spectrum from low (red) to high (blue) height. Meteorological variables were measured near the surface (red) and above the canopy (blue).

2.5 Discussion

2.5.1 Seasonal variability

Observed seasonal isotopic shifts reflect changes in large-scale circulation and seasonal wind patterns, which we expect to be similar at the disturbed and undisturbed sites (Gat, Bowser, & Kendall, 1994). In northern Michigan, air advected from the north is drier and has experienced colder temperatures along its trajectory than air from the south (Rasmusson, 1968). As a result, at UMBS the boundary layer was cooler, drier, and more depleted in heavy isotopes in the spring and fall than was observed in the summer. Sap flux trends point to seasonal variability of transpiration at UMBS (Figures 2.2 and S2.11-S2.12 g and o). Sap flux increased through the spring as the canopies leafed out and hydrologic cycling intensified during the beginning of the growing season, was greatest during the summer when the canopies were fully developed, and was low in the fall when transpiration was in decline at the end of the growing season.

Seasonal $\delta^{18}O$ differences between the disturbed and undisturbed site may be explained by canopy structure, the magnitude of local water fluxes, and different species-specific ecohydrological strategies that have previously been observed at UMBS (Matheny et al., 2014, 2016; Thomsen et al., 2013). The 2008 girdling treatment altered the spatial arrangement of vegetation and increased gaps between trees at the disturbed site. As a result, light reaches deeper (Hardiman et al., 2013), the evaporation flux is greater (Matheny et al., 2014), and canopy roughness is more variable (Maurer et al., 2013) at the disturbed site than at the undisturbed site. On seasonal timescales, mass balance dictates that the isotopic composition of transpired vapor must equal that of source water. On this relatively long timescale, we expect that the isotopic composition of transpired vapor was enriched in heavy isotopes relative to background vapor and that the greater transpiration flux at the undisturbed site pushed $\delta^{18}O$ within the canopy to higher values than at the disturbed site. Due to the fractionation associated with the evaporation of soil water that preferentially partitions lighter isotopologues into the vapor phase, more evaporation at the disturbed site depressed vapor $\delta^{18}O$ relative to the undisturbed site. Maurer et al. (2013) demonstrated that the structural rearrangement at the disturbed site altered the surface roughness parameters and increased surface drag, turbulent eddies, and vertical mixing. Although analysis of surface roughness did not continue past 2011, the lower observed $\delta^{18}O$ at the disturbed site suggests that between-site differences in vertical mixing persist at UMBS.

Species-specific hydrologic strategies may also have contributed to observed isotopic differences. Aspen transpire a majority of the water at the undisturbed site; absent this species at the disturbed site, oak and pine account for a much larger proportion of sap flux (Matheny et al., 2014). At UMBS, oak have a relatively deep rooting depth and access a deeper soil water pool that is more depleted in heavy isotopes than near-surface soil water (Matheny et al., 2016). Therefore, more transpiration from oak at the disturbed site may have contributed more isotopically negative vapor into the disturbed canopy than the undisturbed canopy. Differences in stomatal regulation may also control vapor isotopes because oak at UMBS are anisohydric while maple and aspen are isohydric (Matheny et al., 2016; Thomsen et al., 2013). While these species-specific hydrologic strategies may affect vapor isotopes, the trees at the two sites generally share much of the same physiology. Therefore, we focus on structural differences between the disturbed and undisturbed sites because the differences between the sites are greater.

2.5.2 Synoptic variability

Isotope, sap flux, and eddy covariance data from the DOY 166-171 storm reveal synoptic scale differences in water cycling between the disturbed and undisturbed sites. Following the rainfall event, precipitation moved quickly through the porous sandy UMBS soil, was rapidly taken up by trees, and transpired to the atmosphere (He et al., 2013; Matheny et al., 2014; Nave et al., 2011). At the undisturbed site where transpiration dominates the ET flux (Figure 2.5b and Matheny et al., 2014), T/ET, vapor $\delta^{18}O$, and $\delta^{18}O_{ET}$ increased after the storm. Due to increased light penetration and a more open canopy structure, evaporation played a larger role in the ET flux at the disturbed site. Accordingly, T/ET remained nearly unchanged immediately after the storm. At both sites soil evaporation contributed more to the ET flux a few days after the storm and likely drove T/ET, $\delta^{18}O$, and $\delta^{18}O_{ET}$ to lower values. $\delta^{18}O_{ET}$ was most similar at the two sites during (DOY 167) and immediately after (DOY 168) the storm when evaporation of intercepted precipitation, which was likely the same at the two sites, contributed to $\delta^{18}O_{ET}$ (Figure 2.5a). Following DOY 168 and likely the complete evaporation of intercepted water, differences in vegetation, canopy structure, and the relative magnitudes of evaporation and transpiration fluxes caused $\delta^{18}O_{ET}$ to diverge at the two sites.

Measurements of additional water pools would greatly improve an isotopic understanding of synoptic scale water cycling and are suggested for future studies. We assume that rainwater had

a lower *d* and higher $\delta^{18}O$ than background vapor (Gat, 1996), but without an exact value of the isotopic composition of precipitation it is difficult to diagnose the shift in vapor $\delta^{18}O$ due to transpiration after a rain storm. Similarly, without knowledge of the isotopic composition of soil water, it is difficult to estimate the decrease in vapor isotopes from evaporation. Additionally, isotopic measurements of xylem water would clarify questions of rooting depth and the timescales over which trees access recent precipitation. Matheny et al. (2014 and 2016) have previously reported on the rapid ET response to rain at UMBS. Following a storm, isotopic measurements of precipitation, soil, and xylem water would enable a similar assessment of forest water cycling. Future synoptic-scale vapor isotope studies, especially those without sap flux or eddy covariance data, should consider these additional measurements imperative to fully understand vapor isotope data and forest water cycling.

2.5.3 Vertical variability

Vertical isotope gradients within the canopies demonstrate the effects of entrainment and local ET at the disturbed and undisturbed sites (Figure 2.4). Local above-canopy temperature, relative humidity, and wind speed were similar at the two sites (Figures 2.3 and Figure 2.7), therefore we attribute differences in vertical gradients to forest structure. To this end, we compared isotope gradients at four time slices through the day (Figure 2.4): in the middle of the night (a and e) and mid-afternoon (c and g) when local meteorological and atmospheric conditions were relatively stable and in the early morning (b and f) and late afternoon (d and h) when conditions changed rapidly. When transpiration was low at night, atmospheric mixing shifted vapor *d* ($\delta^{18}O$) to higher (lower) values. In all three seasons, vertical isotope gradients were larger at the undisturbed site than the disturbed site and more pronounced at night when water fluxes were relatively low. With higher water fluxes and more turbulence through the day, entrained and transpired vapor was mixed through the canopies so that by sunset vertical isotopic gradients dissolved away (Figures 2.4d and 2.4h). This pattern was most pronounced during the summer sampling period and more distinguishable within the thick, spatially homogenous, undisturbed canopy that is prone to stratification than within the open, disturbed canopy that has many gaps that promote mixing.

Differences in forest structure at the two sites also contributed to gradients of diurnal temperature, relative humidity, and VPD between the surface (2 m) and above the canopies (Figure

2.7). In general, these gradients were greater at the undisturbed site than at the disturbed site. At the undisturbed site, nighttime conditions near the surface were generally moister than at 34 m due to the thick canopy that slowed the advection of moisture from within the canopy to the free atmosphere above. In contrast, during the day at the disturbed site, the surface was slightly warmer and drier than conditions above the canopy. There, open gaps among the trees allowed more solar radiation to reach the forest floor and promoted vertical mixing (Hardiman et al., 2013).

2.5.4 Diurnal isotope variations

Diurnal water vapor isotope cycles have been widely reported and generally appear to be independent of continentality or vegetation type. Diurnal cycles of $\delta^{18}O$ and *d* at UMBS are similar to those observed in coastal New Haven (Lee, Kim, & Smith, 2007; Lee, Smith, & Williams, 2006), above a wheat field (Zhang, Sun, Wang, Yu, & Wen, 2011) and arid oasis cropland (Huang & Wen, 2014) in North China, in a coniferous forest in the Pacific Northwest (Lai & Ehleringer, 2011), above a Mediterranean coastal wetland (Delattre et al., 2015), in an evergreen forest in Northern California (Simonin et al., 2014), and in an isotope enabled large-eddy simulation of the atmospheric boundary layer (Lee, Huang, & Patton, 2012). Welp et al. (2012) reported on water vapor *d* from six sites in the United States and China, including a broadleaf deciduous forest site in Borden, Ontario near UMBS. While local water fluxes affect the magnitude of diurnal isotope cycles, characteristic patterns of diurnal $\delta^{18}O$ and *d* variation emerged in all of these locations. Taken together, these cycles reflect competing influences of boundary layer entrainment and local ET on near surface water vapor.

Generally, entrainment and evaporation mix vapor with high *d* and low $\delta^{18}O$ into a forest canopy. *q* helps differentiate these two processes as evaporation moistens canopy air and entrainment dries canopy air. On short (sub-hourly) timescales, the isotopic composition of transpired vapor depends on leaf and xylem water storage and local meteorological conditions. On diurnal timescales, relative humidity changes cause vapor *d* to increase in the morning and decrease in the evening (Simonin et al., 2014). As morning relative humidity decreases and evaporation increases, the degree of kinetic fractionation increases and acts to increase vapor *d*. This kinetic effect is driven by the diffusivity difference between isotopologues during evaporation (Cappa, 2003; Merlivat, 1978). Environmental conditions are the opposite in the evening and, following the same logic that explains equilibrium and kinetic fractionation factors in the morning,

tend to decrease vapor *d* late in the day as relative humidity increases. As a result of daytime transpiration, leaf water undergoes an isotopic enrichment and is expected to have a low *d* by the late afternoon. During the late afternoon and evening when relative humidity is high and transpiration likely occurs closer to equilibrium, stored leaf water with low *d* may also decrease vapor *d*.

A few features of the diurnal $\delta^{18}O$ and *d* cycles are consistent between sites, seasons, and heights and reflect the dominant hydrologic processes in the UMBS canopies. In the early morning, transpiration drove a small increase of $\delta^{18}O$ and decrease of *d* (Figure 2.7). These isotopic shifts began just after sunrise and coincided with a VPD increase and the initiation of diurnal sap flux. In the mid-morning *d* increased rapidly as sap flux increased, temperature increased, and relative humidity decreased. As temperature and relative humidity changed in the late afternoon and evening, *d* decreased as expected. At night, when sap flux and VPD were at minima, entrainment was low and *d* was generally consistent, the isotopic composition of canopy vapor was predominantly governed by equilibrium fractionation. We did not observe characteristic isotope patterns of dew formation at either site, perhaps due to the relatively thick canopy and high LAI ($3\ m^2\ m^{-2}$) of the UMBS forest. Unlike some open-canopy forests (e.g. a ponderosa pine forest in central Colorado (Berkelhammer et al., 2013)), at UMBS dew formation did not impart a distinct signature on the isotopic composition of near surface water vapor.

At UMBS, transpiration dominates ET at the undisturbed site; evaporation accounts for a larger fraction of ET at the disturbed site (Matheny et al., 2014). In addition, due to differences in canopy structure, we expect that more entrained vapor was mixed into the disturbed canopy than into the undisturbed canopy (Maurer et al., 2013). At the undisturbed site, the early increase of summer *q* and *d* suggest that transpiration supplied most of the morning vapor within that canopy. The morning *q* increase was absent at the disturbed site because there was less transpiration at that site and more entrainment of dry air from above the canopy. By mid-day, higher wind speeds and warmer surface temperatures increased mechanical turbulence and buoyant convection and entrained vapor was mixed into both canopies. Entrainment tended to depress $\delta^{18}O$ of vapor within the disturbed canopy. It is likely that evaporation also decreased $\delta^{18}O$ at the disturbed site, but it is difficult to disentangle evaporation and entrainment because the variations of *q* were so small.

We further examined the controls on diurnal isotopic compositions with a $\delta^{18}O$-δD plot of diurnal summer water vapor measurements (Figure 2.8). In this dual isotope space, diurnal vapor

isotopic measurements produce a hysteretic loop that readily demonstrates when equilibrium and kinetic fractionation dominated in the UMBS canopies and highlights hydrologic differences at the disturbed and undisturbed sites. In the early morning, transpiration briefly drove $\delta^{18}O$ and δD higher and likely shifted vapor isotopes toward the isotopic composition of xylem water. This feature of the $\delta^{18}O$-δD hysteric loop is more pronounced at the undisturbed site where the transpiration flux was greater and the thicker canopy initially retained transpired vapor and slowed the intrusion of entrained vapor. *d* increased through the morning at both sites, but the kinetic effect was stronger (compare the slope between ~9 am and just before noon) at the disturbed site, which is consistent with a greater contribution of evaporated vapor. At noon, $\delta^{18}O$ values were ~ –19‰ at the two sites. Through the afternoon, entrainment and ET pushed isotopic compositions to lower values, although this effect was greater at the disturbed site (–2‰) than at the undisturbed site (–1‰) likely due to differences in canopy structure. In the late afternoon and evening, transpiration dragged isotopic compositions up to similar nighttime values (~ –19‰). The evening shift from decreasing isotope values to increasing isotope values occurred approximately three hours later at the undisturbed site than at the disturbed site (compare the direction of the hysteric loop after 6 pm). The thick, closed undisturbed canopy was slow to change and retained daytime characteristics well into the evening. Alternatively, the open, disturbed canopy responded rapidly to changing atmospheric and meteorological conditions.

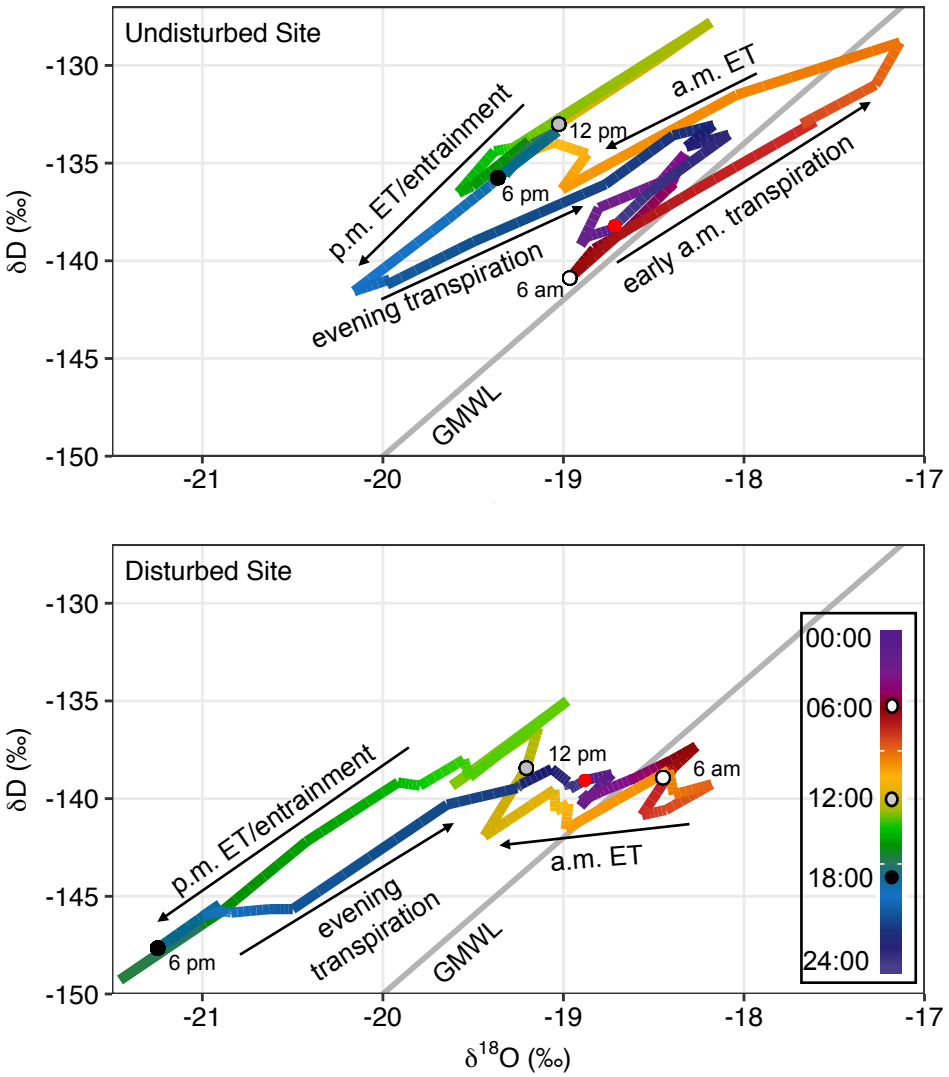

Figure 2.8 15 m interpolated diurnal summer $\delta^{18}O$ and δD from the undisturbed (top) and disturbed (bottom) sites. Each diurnal $\delta^{18}O$ and δD value was interpolated to a five-minute time step to demonstrate the hysteretic loop of water vapor $\delta^{18}O$ and δD throughout the day. Color indicates time and varies from midnight (navy) to morning, afternoon, and night (yellow, green, and blue, respectively). White, grey, and black circles indicate 6 am, 12 pm, and 6 pm, respectively. The red circle indicates midnight. Arrows indicate hydrologic processes that drive the isotopic composition of water vapor within the canopies and point in the direction that each process pushes isotope values. The global meteoric water line (GMWL) is included for reference.

2.5.5 Summertime surface-atmosphere vapor mixing

Finally, we focus on summertime meteorological and isotopic differences within and above the disturbed and undisturbed canopies and examine the implications of intermediate disturbance on forest hydrology. We concentrate on the summer period because differences in canopy structure

at the two sites were most pronounced during this time. At the disturbed site, summer temperature, VPD, and vapor isotopic compositions were nearly identical within and above the canopy (Figure 2.2 i-m). Alternatively, when vertical temperature and relative humidity gradients emerged at the undisturbed site, for example during DOY 161-163, 166-173, and 175-179, isotopic gradients emerged as well (Figure 2.2a-f). In particular, above-canopy *d* deviated from within-canopy *d* during these times (Figure 2.2c). The timing of summer vertical meteorological and isotope gradients suggests that, at times, air above the undisturbed canopy was incompletely mixed with air within the canopy. During the summer, air at the disturbed site generally remained well mixed from the surface to at least 32 m.

Diurnal summer isotopes and meteorology at the undisturbed site also point to a decoupling between water vapor within the canopy and vapor above the canopy. Above the undisturbed canopy, *d* and *q* exhibited similar diurnal patterns and were strongly correlated (Pearson's $r > 0.8$, Figures 2.7r and 2.7s). The coherence between diurnal *d* and *q* was unique to the 34 m observations at the undisturbed site, and points to a measurable influence of canopy structure on forest water cycling. The correlation between *d* and *q* was low ($r < 0.5$) at all other sampling locations. In addition, the disturbance muted diurnal vertical meteorological gradients (Figure 2.7), and suggests that forest structure affects mixing within the canopy. Broadly, this suggests that the assumption of well-coupled canopy-atmosphere interactions (e.g. Ewers & Oren, 2000) may be violated in the case of thick, homogeneous forest canopies.

2.5.6 Implications of intermediate disturbance on forest hydrology

Since its initiation in 2008, the FASET disturbance has proven to be a fruitful experiment to examine and better understand forest biogeochemical responses to intermediate disturbances such as forest thinning management or rapid ecological succession. Following the treatment, carbon, nitrogen, and water cycles changed rapidly in the disturbed plot. Carbon (Gough et al., 2013) and nitrogen (Nave et al., 2011) cycles returned to pre-treatment levels within a few years; changes to boundary layer turbulence (Maurer et al., 2013), forest structure (Hardiman et al., 2013) and the water cycle (He et al., 2013; Matheny et al., 2014) have persisted. Here we use water vapor isotopes to demonstrate that intermediate disturbances that open canopy gaps can alter vapor mixing within and above a forest canopy. Our results also show that forest canopy structure modulates the timescale over which moisture is returned to the atmosphere, as closed canopies can act like a diffusive boundary layer and return energy and moisture to the atmosphere more slowly

than open canopies. Greater vapor mixing between the surface layer and the above-canopy layer may increase moisture transport as surface layer moisture is mixed into the drier above-canopy air and advected away, and therefore may influence the timing and amount of downstream moisture. At the local scale, increased surface-atmosphere water vapor mixing may reduce forest moisture retention and further influence forest composition (Fotis et al., 2018). Many of these inferences can be made from eddy covariance, sap flux, or vapor isotope measurements. However, only isotopes offer insights into the particular processes, both during the day and at night, that generate water fluxes.

Importantly, forest intermediate disturbances do not proceed in isolation. Instead, over the next few decades, many forests will experience higher atmospheric CO_2 and warmer temperatures. It is therefore prudent to consider disturbance alongside the broad suite of pressures that may affect forests. Independent of atmospheric CO_2, changes in vertical mixing modulated by canopy structure can increase VPD and impact stomatal regulation, transpiration, and photosynthesis (Novick et al., 2016). Under higher atmospheric CO_2, decreased stomatal conductance may increase intrinsic water-use efficiency (Frank et al., 2015). Under higher CO_2 conditions, many climate models suggest that transpiration will decrease or remain stable (Lemordant, Gentine, Swann, Cook, & Scheff, 2018; Skinner, Poulsen, Chadwick, Diffenbaugh, & Fiorella, 2017). Although many changes to forest water cycles, including stomatal behavior, forest moisture gradients, and soil wetness, are yet unknown, higher water-use efficiency and increased canopy openness may reinforce each other to further dry forest environments. If the transpiration rate remains stable as canopies transition from closed to open, more canopy moisture may be lost to the atmosphere, which may increase the flux of water from forests to downstream regions.

2.6 Conclusions

We compared meteorology, sap flux, and vertical profiles of water vapor stable isotopes in two closely located forest sites in northern Michigan to assess the effects of intermediate disturbance and canopy structure on local hydrologic cycling. Records from both the disturbed and undisturbed sites reflect seasonality and are imprinted with storm events. On diurnal timescales, we found that differences in water vapor isotope cycles reflect differences in canopy structure, the relative influence of entrainment and ET, and the hydrologic mixing both within the canopy and between the surface layer and the atmosphere. These differences were most pronounced during the summer when the canopies were fully developed and transpiration was high. Vertical water vapor

isotope measurements revealed stratified canopy vapor at night at the undisturbed site and relatively well mixed canopy air at the disturbed site. Generally, meteorological, sap flux, and isotopic measurements complement each other: eddy covariance gives the net water flux and isotopes reveal the hydrologic processes that generate that flux. This work helps expand our understanding of water vapor isotopes in forests and improves predictions of water fluxes between the land and atmosphere and associated changes to regional climate and water cycles.

Acknowledgements and funding

We thank Chris Vogel for assistance running the isotope analyzers and collecting field data. This work was funded by the University of Michigan Water Center. Funding for AmeriFlux data resources was provided by the U.S. Department of Energy's Office of Science. Funding for this study was provided by U.S. Department of Energy's Office of Science, Office of Biological and Environmental Research, Terrestrial Ecosystem Sciences Program Award No. DE-SC0007041 and the AmeriFlux Management program under Flux Core Site Agreement No. 7096915 through Lawrence Berkeley National Laboratory. PGA received funding from a departmental fellowship from the University of Michigan Department of Earth and Environmental Sciences and NSF Tectonics Program award 1550101. RPF received funding from NSF Graduate Research Fellowship 2011094378. Funding for AMM was provided by National Science Foundation Hydrological Science grant 1521238. Vapor isotope data are available from the Yale University Stable Water Vapor Isotopes Database (SWVID) at https://vapor-isotope.yale.edu/.

2.7 References

Aemisegger, F., Pfahl, S., Sodemann, H., Lehner, I., Seneviratne, S. I., & Wernli, H. (2014). Deuterium excess as a proxy for continental moisture recycling and plant transpiration. *Atmospheric Chemistry and Physics*, *14*(8), 4029–4054. https://doi.org/10.5194/acp-14-4029-2014

Aemisegger, F., Sturm, P., Graf, P., Sodemann, H., Pfahl, S., Knohl, A., & Wernli, H. (2012). Measuring variations of $\delta^{18}O$ and $\delta^{2}H$ in atmospheric water vapour using two commercial laser-based spectrometers: an instrument characterisation study. *Atmospheric Measurement Techniques*, *5*, 1491–1511. https://doi.org/10.5194/amt-5-1491-2012

Anderegg, W. R. L., Konings, A. G., Trugman, A. T., Yu, K., Bowling, D. R., Karp, D., et al. (2018). Hydraulic diversity of forests regulates ecosystem resilience during drought. *Nature*, *561*(7724), 537–541. https://doi.org/10.1038/s41586-018-0539-7

Asase, A., Asiatokor, B. K., & Ofori-Frimpong, K. (2014). Effects of selective logging on tree diversity and some soil characteristics in a tropical forest in southwest Ghana. *Journal of Forestry Research*, *25*(1), 171–176. https://doi.org/10.1007/s11676-014-0443-4

Asner, G. P., Keller, M., Pereira, R., Zweede, J. C., & Silva, J. N. M. (2004). Canopy damage and recovery following selective logging in an Amazon forest: Integrating field and satellite studies. *Ecological Applications*, *14*(4), 280–298. https://doi.org/https://doi.org/10.1890/01-6019

Atkins, J. W., Fahey, R. T., Hardiman, B. H., & Gough, C. M. (2018). Forest Canopy Structural Complexity and Light Absorption Relationships at the Subcontinental Scale. *Journal of Geophysical Research: Biogeosciences*, *123*(4), 1387–1405. https://doi.org/10.1002/2017JG004256

Bailey, A., Noone, D., Berkelhammer, M., Steen-Larsen, H. C., & Sato, P. (2015). The stability and calibration of water vapor isotope ratio measurements during long-term deployments. *Atmospheric Measurement Techniques*, *8*(10), 4521–4538. https://doi.org/10.5194/amt-8-4521-2015

Baldocchi, D. D., & Meyers, T. (1998). On using eco-physiological, micrometeorological and biogeochemical theory to evaluate carbon dioxide, water vapor and trace gas fluxes over vegetation: a perspective. *Agricultural and Forest Meteorology*, *90*, 1–25. https://doi.org/10.1016/S0168-1923(97)00072-5

Baldocchi, D. D., Wilson, K. B., & Gu, L. (2002). How the environment, canopy structure and canopy physiological functioning influence carbon, water and energy fluxes of a temperate broad-leaved deciduous forest - An assessment with the biophysical model CANOAK. *Tree Physiology*, *22*(15–16), 1065–1077. https://doi.org/10.1093/treephys/22.15-16.1065

Barnes, C. J., & Allison, G. (1984). The distribution of deuterium and ^{18}O in dry soils: 3. Theory for non-isothermal water movement. *Journal of Hydrology*, *74*, 119–135. https://doi.org/10.1016/0022-1694(84)90144-6

Berkelhammer, M., Hu, J., Bailey, A., Noone, D. C., Still, C. J., Barnard, H., et al. (2013). The nocturnal water cycle in an open-canopy forest. *Journal of Geophysical Research Atmospheres*, *118*(17), 10225–10242. https://doi.org/10.1002/jgrd.50701

Cappa, C. D. (2003). Isotopic fractionation of water during evaporation. *Journal of Geophysical Research*, *108*(D16), 4525. https://doi.org/10.1029/2003JD003597

Cernusak, L. A., Pate, J. S., & Farquhar, G. D. (2002). Diurnal variation in the stable isotope composition of water and dry matter in fruiting Lupinus angustifolius under field conditions. *Plant, Cell and Environment*, *26*, 893–907. https://doi.org/10.1046/j.1365-3040.2002.00875.x

Chen, J., Saunders, S. C., Crow, T. R., Naiman, R. J., Kimberley, D., Mroz, G. D., et al. (1999). Microclimate in Forest Ecosystem and Landscape Ecology. *BioScience*, *49*(4), 288–297. https://doi.org/10.2307/1313612

Craig, H. (1961). Isotopic Variations in Meteoric Waters. *Science*, *133*(3465), 1702–1703. https://doi.org/10.1126/science.133.3465.1702

Dansgaard, W. (1964). Stable isotopes in precipitation. *Tellus*, *16*(4), 436–468. https://doi.org/10.3402/tellusa.v16i4.8993

Debortoli, N. S., Dubreuil, V., Hirota, M., Filho, S. R., Lindoso, D. P., & Nabucet, J. (2017). Detecting deforestation impacts in Southern Amazonia rainfall using rain gauges. *International Journal of Climatology*, *37*(6), 2889–2900. https://doi.org/10.1002/joc.4886

Delattre, H., Vallet-Coulomb, C., & Sonzogni, C. (2015). Deuterium excess in the atmospheric water vapour of a Mediterranean coastal wetland: Regional vs. local signatures. *Atmospheric Chemistry and Physics*, *15*(17), 10167–10181. https://doi.org/10.5194/acp-15-10167-2015

Ehleringer, J. R., & Dawson, T. E. (1992). Water uptake by plants: perspectives from stable isotope composition. *Plant, Cell and Environment*, *15*, 1073–1082. https://doi.org/10.1111/j.1365-3040.1992.tb01657.x

Ellison, D., Morris, C. E., Locatelli, B., Sheil, D., Cohen, J., Murdiyarso, D., et al. (2017). Trees, forests and water: Cool insights for a hot world. *Global Environmental Change*, *43*, 51–61. https://doi.org/10.1016/j.gloenvcha.2017.01.002

Ewers, B. E., & Oren, R. A. M. (2000). Analyses of assumptions and errors in the calculation of stomatal conductance from sap flux measurements. *Tree Physiology*, *20*, 579–589.

Fiorella, R. P., Bares, R., Lin, J. C., Ehleringer, J. R., & Bowen, G. J. (2018). Detection and variability of combustion-derived vapor in an urban basin. *Atmospheric Chemistry and Physics*, *18*(12), 8529–8547. https://doi.org/10.5194/acp-18-8529-2018

Fiorella, R. P., Poulsen, C. J., & Matheny, A. M. (2018). Seasonal Patterns of Water Cycling in a Deep, Continental Mountain Valley Inferred From Stable Water Vapor Isotopes. *Journal of Geophysical Research: Atmospheres*, *123*(14), 7271–7291. https://doi.org/10.1029/2017JD028093

Fotis, A. T., Morin, T. H., Fahey, R. T., Hardiman, B. S., Bohrer, G., & Curtis, P. S. (2018). Forest structure in space and time: Biotic and abiotic determinants of canopy complexity and their effects on net primary productivity. *Agricultural and Forest Meteorology*, *250–251*(June 2017), 181–191. https://doi.org/10.1016/j.agrformet.2017.12.251

Frank, D. C., Poulter, B., Saurer, M., Esper, J., Huntingford, C., Helle, G., & Treydte, K. (2015). Water-use efficiency and transpiration across European forests during the Anthropocene. *Nature Climate Change*, *5*, 579–584. https://doi.org/10.1038/NCLIMATE2614

Galewsky, J., & Samuels-Crow, K. (2015). Summertime moisture transport to the southern South American Altiplano: Constraints from in situ measurements of water vapor isotopic composition. *Journal of Climate*, *28*(7), 2635–2649. https://doi.org/10.1175/JCLI-D-14-00511.1

Ganteaume, A., Camia, A., Jappiot, M., San-Miguel-Ayanz, J., Long-Fournel, M., & Lampin, C. (2013). A review of the main driving factors of forest fire ignition over Europe. *Environmental Management*, *51*(3), 651–662. https://doi.org/10.1007/s00267-012-9961-z

Gat, J. (1996). Oxygen and hydrogen isotopes in the hydrologic cycle. *Annual Review of Earth and Planetary Sciences*, *24*, 225–262. https://doi.org/10.1146/annurev.earth.24.1.225

Gat, J. R., Bowser, C. J., & Kendall, C. (1994). The contribution of evaporation from the Great Lakes to the continental atmosphere: estimate based on stable isotope data. *Geophysical Research Letters*, *21*(7), 557–560. https://doi.org/10.1029/94GL00069

Good, S. P., Soderberg, K., Guan, K., King, E. G., Scanlon, T. M., & Caylor, K. K. (2014). δ^2H isotopic flux partitioning of evapotranspiration over a grass field following a water pulse and subsequent dry down. *Water Resources Research*, *50*, 1410–1432. https://doi.org/10.1002/2013WR014333

Gough, C. M., Hardiman, B. S., Nave, L. E., Bohrer, G., Maurer, K. D., Vogel, C. S., et al. (2013). Sustained carbon uptake and storage following moderate disturbance in a Great Lakes forest. *Ecological Applications*, *23*(5), 1202–1215. https://doi.org/10.1890/12-1554.1

Granier, A. (1987). Evaluation of transpiration in a Douglas-fir stand by means of sap flow measurements. *Tree Physiology*, *3*(4), 309–320. https://doi.org/10.1093/treephys/3.4.309

Hardiman, B. S., Bohrer, G., Gough, C. M., & Curtis, P. S. (2013). Canopy structural changes following widespread mortality of canopy dominant trees. *Forests*, *4*(3), 537–552. https://doi.org/10.3390/f4030537

Hardiman, B. S., LaRue, E. A., Atkins, J. W., Fahey, R. T., Wagner, F. W., & Gough, C. M. (2018). Spatial variation in canopy structure across forest landscapes. *Forests*, *9*(8). https://doi.org/10.3390/f9080474

Harwood, K. G., Gillon, J. S., Griffiths, H., & Broadmeadow, M. S. J. (1998). Diurnal variation of $\Delta^{13}CO_2$, $\Delta^{18}O^{16}O$ and evaporative site enrichment of $\delta H_2{}^{18}O$ in Piper aduncum under field conditions in Trinidad. *Plant, Cell and Environment*, *21*(3), 269–283. https://doi.org/10.1046/j.1365-3040.1998.00276.x

He, H. S., & Mladenoff, D. J. (1999). Spatially Explicit and Stochastic Forest Landscape Model of Fire Disturbance and Succession. *Ecology*, *80*(1), 81–99. https://doi.org/10.2307/176981

He, H., & Smith, R. B. (1999). Stable isotope composition of water vapor in the atmospheric

boundary layer above the forests of New England. *Journal of Geophysical Research Atmospheres*, *104*(D9), 11657–11673. https://doi.org/10.1029/1999JD900080

He, L., Ivanov, V. Y., Bohrer, G., Thomsen, J. E., Vogel, C. S., & Moghaddam, M. (2013). Temporal dynamics of soil moisture in a northern temperate mixed successional forest after a prescribed intermediate disturbance. *Agricultural and Forest Meteorology*, *180*, 22–33. https://doi.org/10.1016/j.agrformet.2013.04.014

Herms, D. A., & McCullough, D. G. (2014). Emerald Ash Borer Invasion of North America: History, Biology, Ecology, Impacts, and Management. *Annual Review of Entomology*, *59*(1), 13–30. https://doi.org/10.1146/annurev-ento-011613-162051

Hesslerová, P., Pokorný, J., Brom, J., & Rejšková-Procházková, A. (2013). Daily dynamics of radiation surface temperature of different land cover types in a temperate cultural landscape: Consequences for the local climate. *Ecological Engineering*, *54*, 145–154. https://doi.org/10.1016/j.ecoleng.2013.01.036

Horita, J., & Wesolowski, D. J. (1994). Liquid-vapor fractionation of oxygen and hydrogen isotopes of water from the freezing to the critical temperature. *Geochimica et Cosmochimica Acta*, *58*(16), 3425–3437. Retrieved from papers2://publication/uuid/F9BCD32F-8569-4ACF-81AF-08518BF40A32

Huang, L., & Wen, X. (2014). Temporal variations of atmospheric water vapor δD and $\delta^{18}O$ above an arid artifical oasis cropland in the Heihe River Basin. *Journal of Geophysical Research: Atmospheres*, *119*, 11,456-11,476. https://doi.org/10.1002/2014JD021891

Jasechko, S., Sharp, Z. D., Gibson, J. J., Birks, S. J., Yi, Y., & Fawcett, P. J. (2013). Terrestrial water fluxes dominated by transpiration. *Nature*, *496*(7445), 347–350. https://doi.org/10.1038/nature11983

Keeling, D. (1958). The concentration and isotopic abundances of atmospheric carbon dioxide in rural areas. *Geochimica et Cosmochimica Acta*, *13*, 322–334.

Lai, C. T., & Ehleringer, J. R. (2011). Deuterium excess reveals diurnal sources of water vapor in forest air. *Oecologia*, *165*(1), 213–223. https://doi.org/10.1007/s00442-010-1721-2

Lee, X., Huang, J., & Patton, E. G. (2012). A Large-Eddy Simulation Study of Water Vapour Boundary Layer, 229–248. https://doi.org/10.1007/s10546-011-9631-3

Lee, X., Kim, K., & Smith, R. (2007). Temporal variations of the $^{18}O/^{16}O$ signal of the whole-canopy transpiration in a temperate forest, *21*(August), 1–12. https://doi.org/10.1029/2006GB002871

Lee, X., Smith, R., & Williams, J. (2006). Water vapour $^{18}O/^{16}O$ isotope ratio in surface air in New England, USA. *Tellus B: Chemical and Physical Meteorology*, *58*(4), 293–304. https://doi.org/10.1111/j.1600-0889.2006.00191.x

Lemordant, L., Gentine, P., Swann, A. S., Cook, B. I., & Scheff, J. (2018). Critical impact of vegetation physiology on the continental hydrologic cycle in response to increasing CO_2. *Proceedings of the National Academy of Sciences*, *115*(16), 4093–4098. https://doi.org/10.1073/pnas.1720712115

Logan, J. A., Régnière, J., & Powell, J. A. (2003). Assessing the impacts of global warming on forest pest dynamics. *Frontiers in Ecology and the Environment*, *1*(3), 130–137. https://doi.org/110.1890/1540-9295(2003)001[0130:ATIOGW]2.0.CO;2

Luz, B., Barkan, E., Yam, R., & Shemesh, A. (2009). Fractionation of oxygen and hydrogen isotopes in evaporating water. *Geochimica et Cosmochimica Acta*, *73*(22), 6697–6703. https://doi.org/10.1016/j.gca.2009.08.008

Matheny, A. M., Bohrer, G., Vogel, C. S., Morin, T. H., He, L., Frasson, R. P. D. M., et al. (2014). Species-specific transpiration responses to intermediate disturbance in a northern hardwood forest. *Journal of Geophysical Research: Biogeosciences*, *119*, 2292–2311. https://doi.org/10.1002/2014JG002804

Matheny, A. M., Fiorella, R. P., Bohrer, G., Poulsen, C. J., Morin, T. H., Wunderlich, A., et al. (2016). Contrasting strategies of hydraulic control in two codominant temperate tree species. *Ecohydrology*, *10*(3), 1–16. https://doi.org/10.1002/eco.1815

Maurer, K. D., Hardiman, B. S., Vogel, C. S., & Bohrer, G. (2013). Canopy-structure effects on surface roughness parameters: Observations in a Great Lakes mixed-deciduous forest. *Agricultural and Forest Meteorology*, *177*, 24–34. https://doi.org/10.1016/j.agrformet.2013.04.002

McDowell, N., Pockman, W. T., Allen, C. D., Breshears, D. D., Cobb, N., Kolb, T., et al. (2008). Mechanisms of Plant Survival and Mortality during Drought : Why Do Some Plants Survive while Others Succumb to Drought? *New Phytologist*, *178*(4), 719–739. https://doi.org/10.1111/j.1469-8137.2008.02436.x

Merlivat, L. (1978). Molecular diffusivities of $H_2{}^{16}O$, $HD^{16}O$, and $H_2{}^{18}O$ in gases. *The Journal of Chemical Physics*, *69*(6), 2864–2871. https://doi.org/10.1063/1.436884

Mitchell, S. J. (2013). Wind as a natural disturbance agent in forests: A synthesis. *Forestry*, *86*(2), 147–157. https://doi.org/10.1093/forestry/cps058

Nave, L. E., Gough, C. M., Maurer, K. D., Bohrer, G., Hardiman, B. S., Le Moine, J., et al. (2011). Disturbance and the resilience of coupled carbon and nitrogen cycling in a north temperate forest. *Journal of Geophysical Research: Biogeosciences*, *116*(4), 1–14. https://doi.org/10.1029/2011JG001758

Noone, D., Risi, C., Bailey, A., Berkelhammer, M., Brown, D. P., Buenning, N., et al. (2013). Determining water sources in the boundary layer from tall tower profiles of water vapor and

surface water isotope ratios after a snowstorm in Colorado. *Atmospheric Chemistry and Physics*, *13*(3), 1607–1623. https://doi.org/10.5194/acp-13-1607-2013

Novick, K. A., Ficklin, D. L., Stoy, P. C., Williams, C. A., Bohrer, G., Oishi, A. C., et al. (2016). The increasing importance of atmospheric demand for ecosystem water and carbon fluxes. *Nature Climate Change*, *6*(September), 1023–1027. https://doi.org/10.1038/NCLIMATE3114

Forest and Agriculty Organization (2015). *Global Forest Resources Assessment 2015* (2nd ed.). Rome. Retrieved from http://www.fao.org/forestry/fra2005/en/

Pan, Y., Chen, J. M., Birdsey, R., McCullough, K., He, L., & Deng, F. (2011). Age structure and disturbance legacy of North American forests. *Biogeosciences*, *8*(3), 715–732. https://doi.org/10.5194/bg-8-715-2011

Parsons, D. J., & DeBenedetti, S. H. (1979). Impact of fire suppression on a mixed conifer forest. *Forest Ecology and Management*, *2*, 21–33.

Rasmusson, E. M. (1968). Atmospheric Water Vapor Transport and the Water Balance of North America. *Monthly Weather Review*, *96*(10), 720–734. https://doi.org/10.1175/1520-0493(1968)096<0720:AWVTAT>2.0.CO;2

Schlesinger, W. H., & Jasechko, S. (2014). Transpiration in the global water cycle. *Agricultural and Forest Meteorology*, *189–190*, 115–117. https://doi.org/10.1016/j.agrformet.2014.01.011

Schulte, L. A., Mladenoff, D. J., Crow, T. R., Merrick, L. C., & Cleland, D. T. (2007). Homogenization of northern U.S. Great Lakes forests due to land use. *Landscape Ecology*, *22*(7), 1089–1103. https://doi.org/10.1007/s10980-007-9095-5

Simonin, K. A., Link, P., Rempe, D., Miller, S., Oshun, J., Bode, C., et al. (2014). Vegetation induced changes in the stable isotope composition of near surface humidity. *Ecohydrology*, *7*(3), 936–949. https://doi.org/10.1002/eco.1420

Simonin, K. A., Roddy, A. B., Link, P., Apodaca, R., Tu, K. P., Hu, J., et al. (2013). Isotopic composition of transpiration and rates of change in leaf water isotopologue storage in response to environmental variables. *Plant, Cell and Environment*, *36*(12), 2190–2206. https://doi.org/10.1111/pce.12129

Skinner, C. B., Poulsen, C. J., Chadwick, R., Diffenbaugh, N. S., & Fiorella, R. P. (2017). The Role of Plant CO2 Physiological Forcing in Shaping Future Daily-Scale Precipitation. *Journal of Climate*, *30*(7), 2319–2340. https://doi.org/10.1175/JCLI-D-16-0603.1

Steen-Larsen, H. C., Sveinbjörnsdottir, A. E., Jonsson, T., Ritter, F., Bonne, J., Sodemann, H., et al. (2015). Moisture sources and synoptic to seasonal variability of North Atlantic water vapor isotopic composition. *Journal Geophysical Research Atmospheres*, *120*, 5757–5774.

https://doi.org/10.1002/2015JD023234

Stephens, S. L., Moghaddas, J. J., Edminster, C., Fiedler, C. E., Haase, S., Harrington, M. G., et al. (2009). Fire Treatment Effects on Vegetation Structure, Fuels, and Potential Fire Severity in Western U.S. Forests. *Ecological Applications*, *19*(2), 305–320. https://doi.org/10.1890/07-1755.1

Thomsen, J. E., Bohrer, G., Matheny, A. M., Ivanov, V. Y., He, L., Renninger, H. J., & Schäfer, K. V. R. (2013). Contrasting hydraulic strategies during dry soil conditions in Quercus rubra and Acer rubrum in a sandy site in Michigan. *Forests*, *4*(4), 1106–1120. https://doi.org/10.3390/f4041106

Trugman, A. T., Medvigy, D., Anderegg, W. R. L., & Pacala, S. W. (2018). Differential declines in Alaskan boreal forest vitality related to climate and competition. *Global Change Biology*, *24*(3), 1097–1107. https://doi.org/10.1111/gcb.13952

Welp, L. R., Lee, X., Griffis, T. J., Wen, X. F., Xiao, W., Li, S., et al. (2012). A meta-analysis of water vapor deuterium-excess in the midlatitude atmospheric surface layer. *Global Biogeochemical Cycles*, *26*(3), 1–12. https://doi.org/10.1029/2011GB004246

Welp, L. R., Lee, X., Kim, K., Griffis, T. J., Billmark, K. A., & Baker, J. M. (2008). $\delta^{18}O$ of water vapour, evapotranspiration and the sites of leaf water evaporation in a soybean canopy. *Plant, Cell and Environment*, *31*(9), 1214–1228. https://doi.org/10.1111/j.1365-3040.2008.01826.x

Williams, D. G., Cable, W., Hultine, K., Hoedjes, J. C. B., Yepez, E. A., Simonneaux, V., et al. (2004). Evapotranspiration components determined by stable isotope, sap flow and eddy covariance techniques. *Agricultural and Forest Meteorology*, *125*, 241–258. https://doi.org/10.1016/j.agrformet.2004.04.008

Xiao, W., Wei, Z., & Wen, X. (2018). Evapotranspiration partitioning at the ecosystem scale using the stable isotope method—A review. *Agricultural and Forest Meteorology*, *263*(November 2017), 346–361. https://doi.org/10.1016/j.agrformet.2018.09.005

Yakir, D., & Sternberg, S. L. (2000). The use of stable isotopes to study ecosystem gas exchange, *123*(January), 297–311.

Zhang, S., Sun, X., Wang, J., Yu, G., & Wen, X. (2011). Short-term variations of vapor isotope ratios reveal the influence of atmospheric processes. *Journal of Geographical Sciences*, *21*(3), 401–416. https://doi.org/10.1007/s11442-011-0853-6

2.8 Supplementary information

Introduction

The isotopic composition of water vapor measured on laser-based cavity ringdown spectrometers is dependent on cavity humidity. Here we describe the correction we applied to correct for this apparent bias. Figures S2.1 and S2.3 show the humidity-dependent isotopic offset for oxygen; Figures S2.2 and S2.4 show the humidity-dependent isotopic offset for hydrogen. These offsets were used to correct measured isotopic compositions for the cavity humidity bias.

We used the 95% confidence interval of the regression relationships to generate uncertainty of our isotopic measurements. We focus on cavity humidity as the dominant source of measurement uncertainty. We do not independently consider uncertainty from measurements of liquid standards because they add no additional uncertainty (the R^2 of the two-point calibration was close to 1). Standards are subject to the same humidity bias as samples, but we extended the humidity correction to standards and samples so we expect no additional uncertainty to arise. We show the estimated 1-sigma (1σ) uncertainty as a function of cavity humidity for $\delta^{18}O$ (Figures S2.5 and S2.8), δD (Figures S2.6 and S2.9), and d (Figures S2.7 and S2.10). For d, we assume $\delta^{18}O$ and δD errors are independent.

Cavity humidity correction

The isotopic composition of water vapor measured on laser-based cavity ringdown spectrometers is dependent on cavity humidity (Aemisegger et al., 2012; Fiorella, Bares, Lin, Ehleringer, & Bowen, 2018). Therefore, as part of the calibration to the VSMOW-SLAP scale, it is necessary to correct these data for humidity dependence. To do so, we follow the methods described in Fiorella et al. (2018). For each analyzer, we varied the rate of standard liquid injection from the Picarro Standard Delivery Module (SDM) and measured the isotopic composition as cavity humidity ranged from 2,000 to 30,000 ppm. We then calculated the isotopic bias as the deviation between measured and true isotope values when cavity humidity was between 15,000 and 25,000 ppm. We chose these values because the response between cavity humidity and isotopic composition was minimal in this range and because this range overlaps with the range in which standards were measured during the field deployment. Humidity correction data were not uniformly distributed across the 2,000-30,000 ppm range, so we sorted the values into 500 ppm

bins to ensure that all humidity values were weighted equally. We then used a Deming regression to describe the relationship between isotopic composition and $1/[H_2O]$ ($[H_2O]$ in ppm). Here we present the best fit and 95% confidence interval offset equations below:

Picarro L2130-i (disturbed site)

$\Delta^{18}O_{offset} = 0.185 - 4270.00/[H_2O]$ (best fit)

$\Delta^{18}O_{offset} = 0.311 - 2908.93/[H_2O]$ (upper 95% CI)

$\Delta^{18}O_{offset} = 0.059 - 5631.07/[H_2O]$ (lower 95% CI)

$\Delta D_{offset} = 0.090 - 1121.81/[H_2O]$ (best fit)

$\Delta D_{offset} = 0.462 - 3849.46/[H_2O]$ (upper 95% CI)

$\Delta D_{offset} = -0.283 - 6093.08/[H_2O]$ (lower 95% CI)

Picarro L2120-i (undisturbed site)

$\Delta^{18}O_{offset} = 0.503 - 7513.12/[H_2O]$ (best fit)

$\Delta^{18}O_{offset} = 0.782 - 4640.83/[H_2O]$ (upper 95% CI)

$\Delta^{18}O_{offset} = 0.022 - 10385.42/[H_2O]$ (lower 95% CI)

$\Delta D_{offset} = 2.733 - 51785.75/[H_2O]$ (best fit)

$\Delta D_{offset} = 3.443 - 40247.47/[H_2O]$ (upper 95% CI)

$\Delta D_{offset} = 2.026 - 63324.02/[H_2O]$ (lower 95% CI).

We corrected for the humidity bias by subtracting the humidity-dependent offset from the measured isotopic composition:

$\delta X_{humidity\_corrected} = \delta X_{measured} - \Delta X_{offset}$*(humidity).

The magnitude of humidity-dependent offset was related to $1/[H_2O]$ for both oxygen (Figures S2.1 and S2.3) and hydrogen (Figures S2.2 and S2.4).

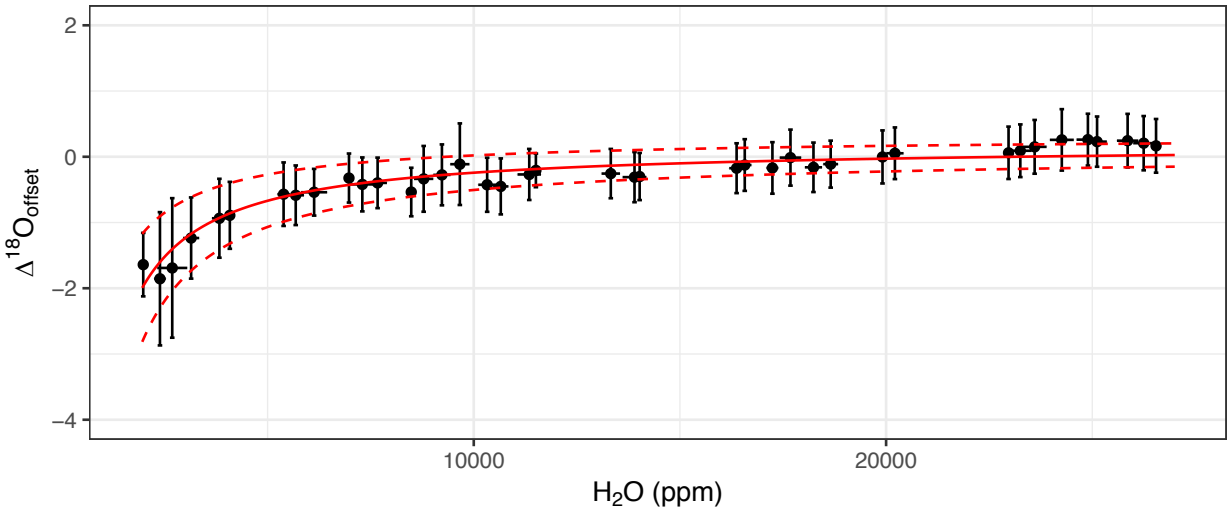

Figure S2.1 L2130-i (disturbed site) $\Delta^{18}O_{offset}$ with 95% confidence intervals for each humidity bin.

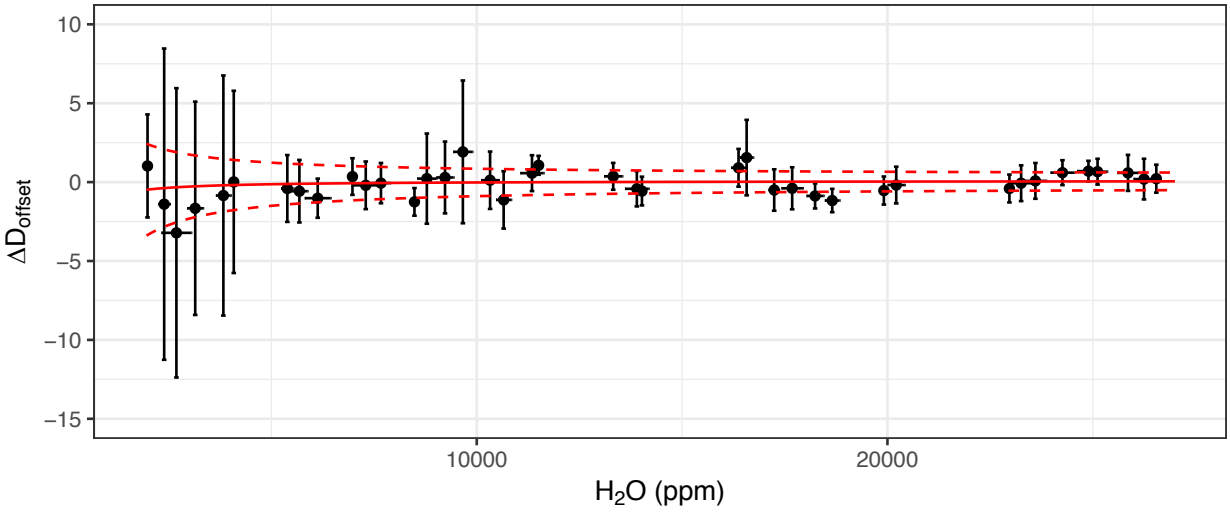

Figure S2.2 L2130-i (disturbed site) ΔD_{offset} with 95% confidence intervals for each humidity bin.

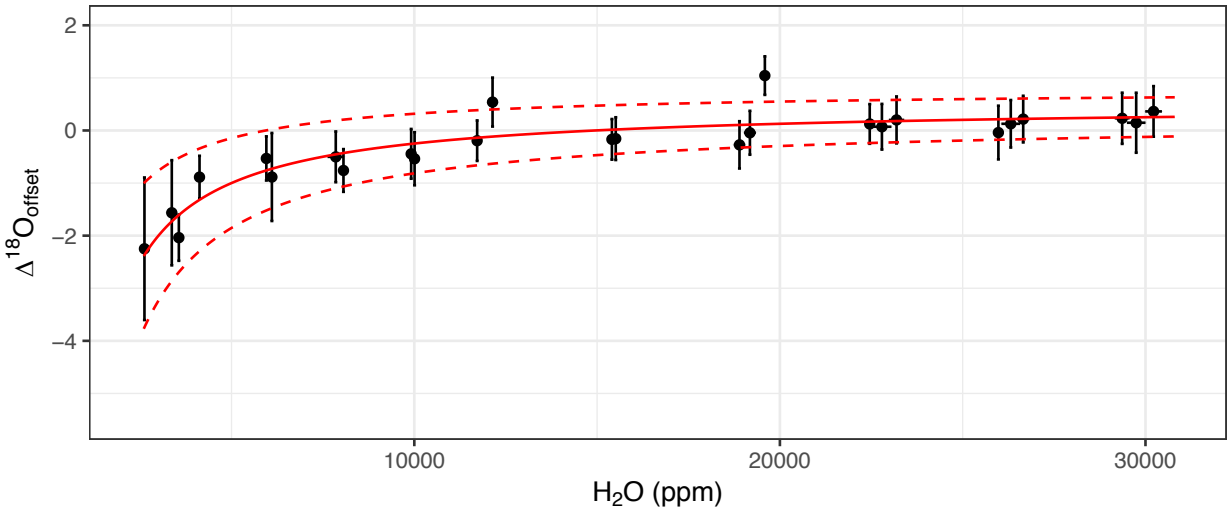

Figure S2.3 L2120-i (undisturbed site) $\Delta^{18}O_{offset}$ with 95% confidence intervals for each humidity bin.

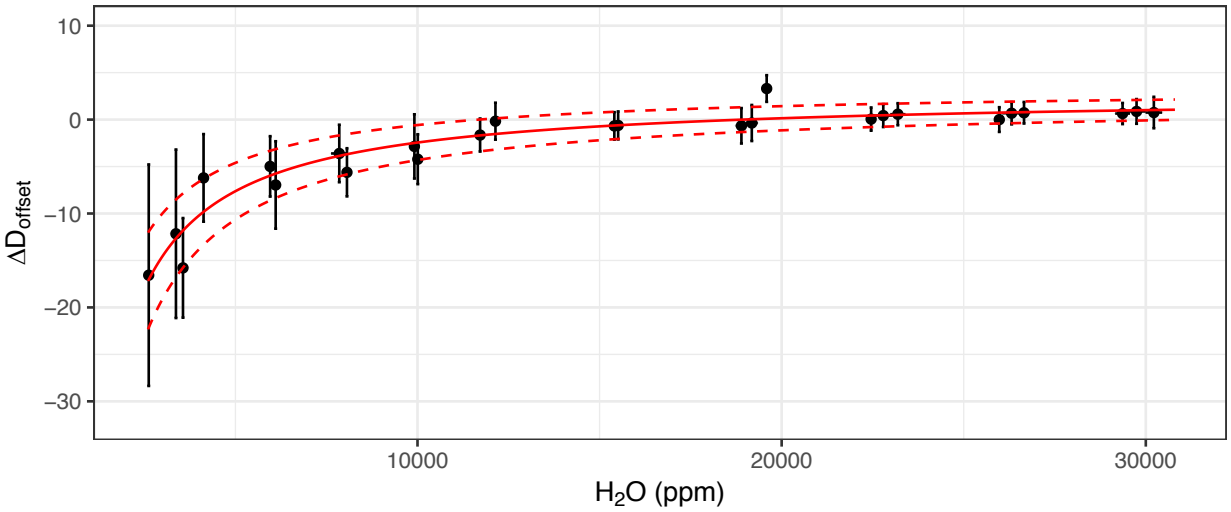

Figure S2.4 L2120-i (undisturbed site) ΔD_{offset} with 95% confidence intervals for each humidity bin.

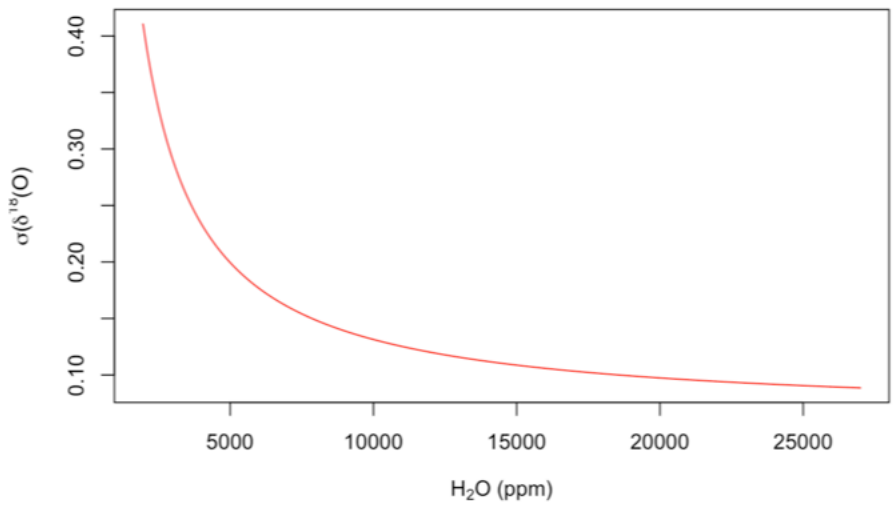

Figure S2.5 L2130-i (disturbed site) 1-sigma uncertainty of $\delta^{18}O$ as a function of cavity humidity.

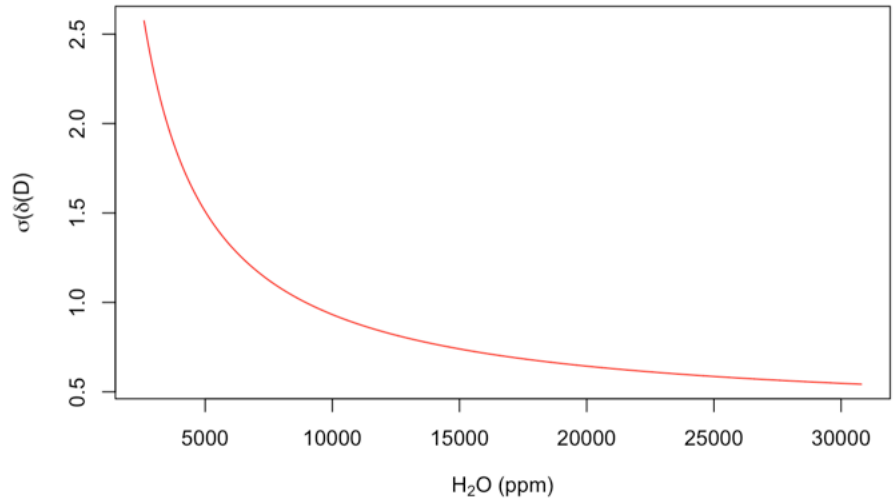

Figure S2.6 L2130-i (disturbed site) 1-sigma uncertainty of δD as a function of cavity humidity.

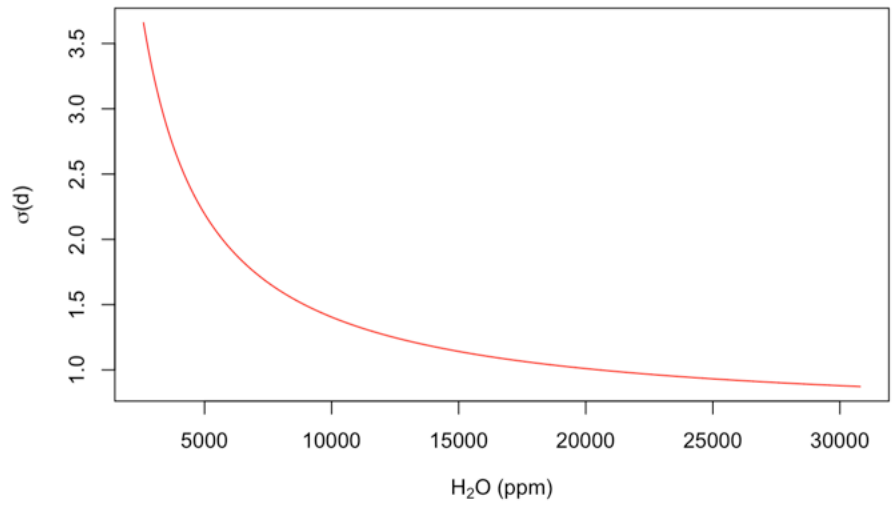

Figure S2.7 L2130-i (disturbed site) 1-sigma uncertainty of *d* as a function of cavity humidity.

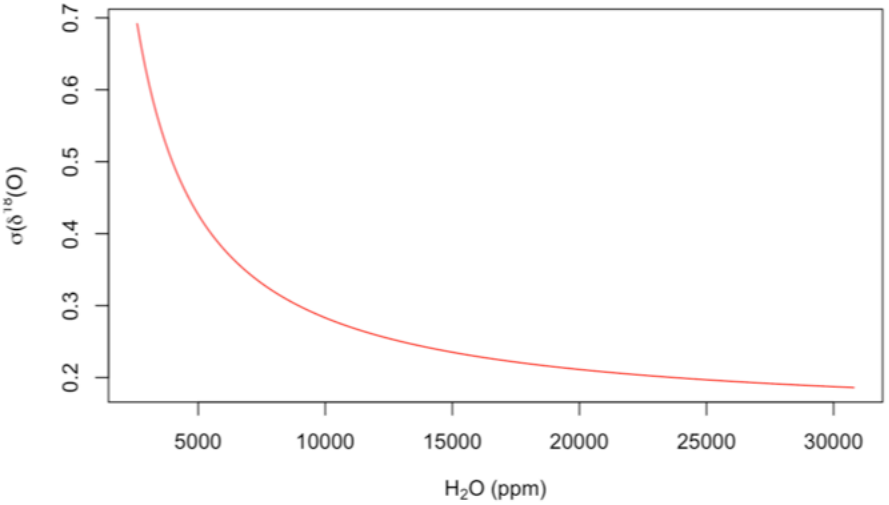

Figure S2.8 L2120-i (undisturbed site) 1-sigma uncertainty of $\delta^{18}O$ as a function of cavity humidity.

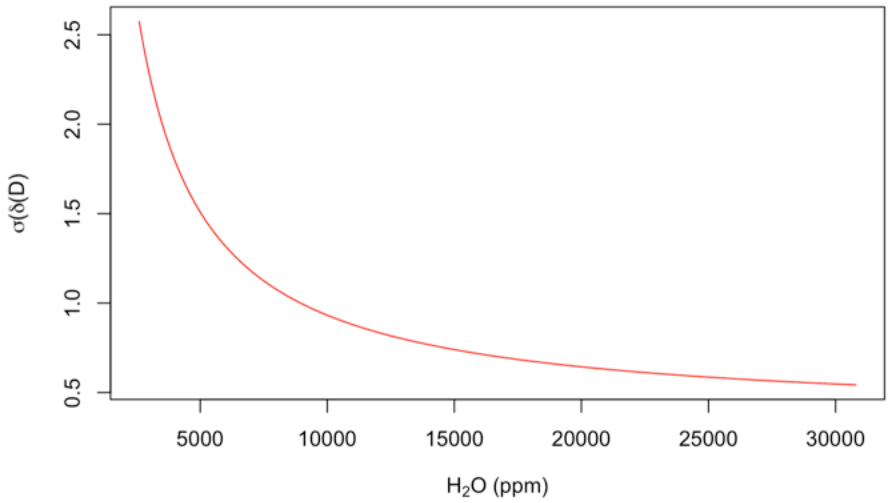

Figure S2.9 L2120-i (undisturbed site) 1-sigma uncertainty of δD as a function of cavity humidity.

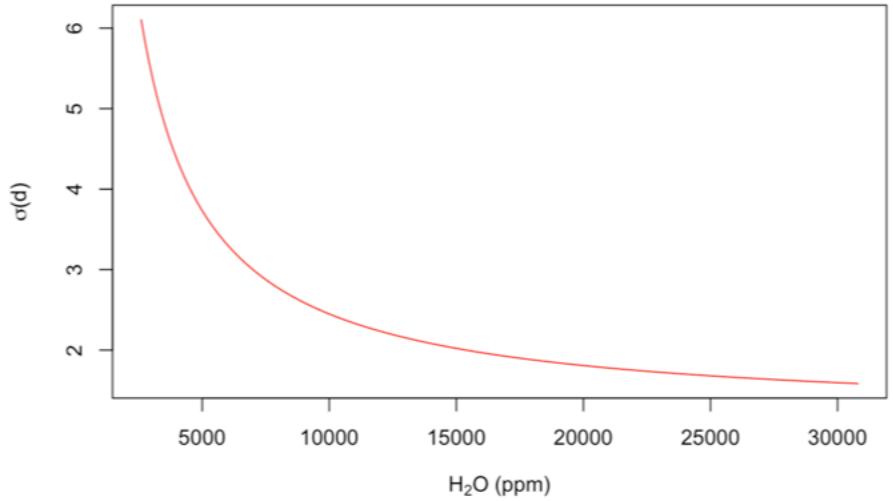

Figure S2.10 L2120-i (undisturbed site) 1-sigma uncertainty of *d* as a function of cavity humidity.

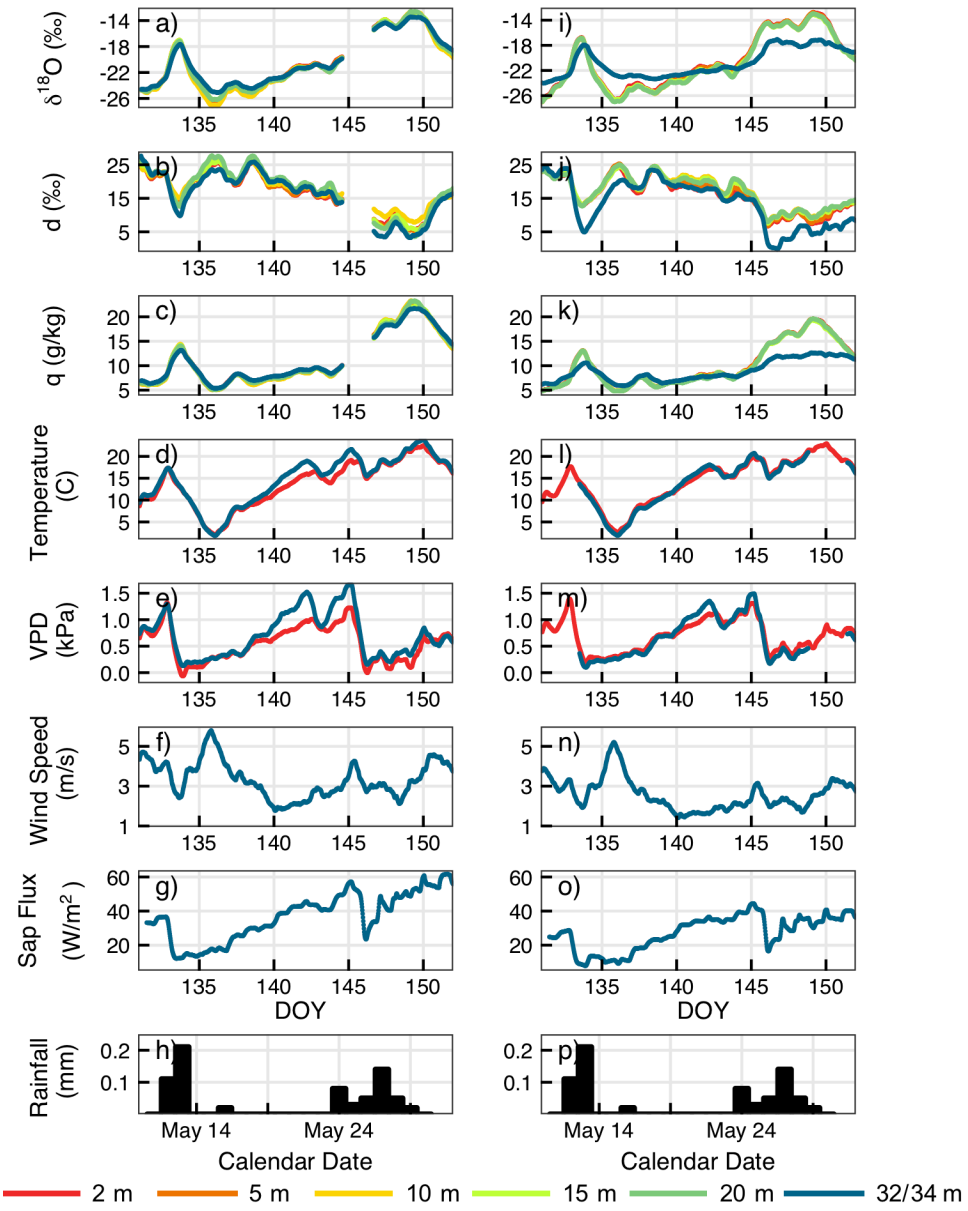

Figure S2.11 Time series of moving 24-hour average of spring isotopic compositions, meteorological data, and sap flux at the undisturbed (left) and disturbed (right) sites. a,i) vapor $\delta^{18}O$ (‰); b,j) *d* (‰); c,k) specific humidity (*q*, g/kg); d,l) temperature (°C); e,m) vapor pressure deficit (VPD, kPa); f,n) wind speed (m/s); g,o) sap flux (W/m^2); h,p) daily precipitation amount (mm). Isotopes and vapor mixing ratios are shown for all 6 heights from low (red) to high (blue). Meteorology is shown at 2m (red) and above-canopy (blue).

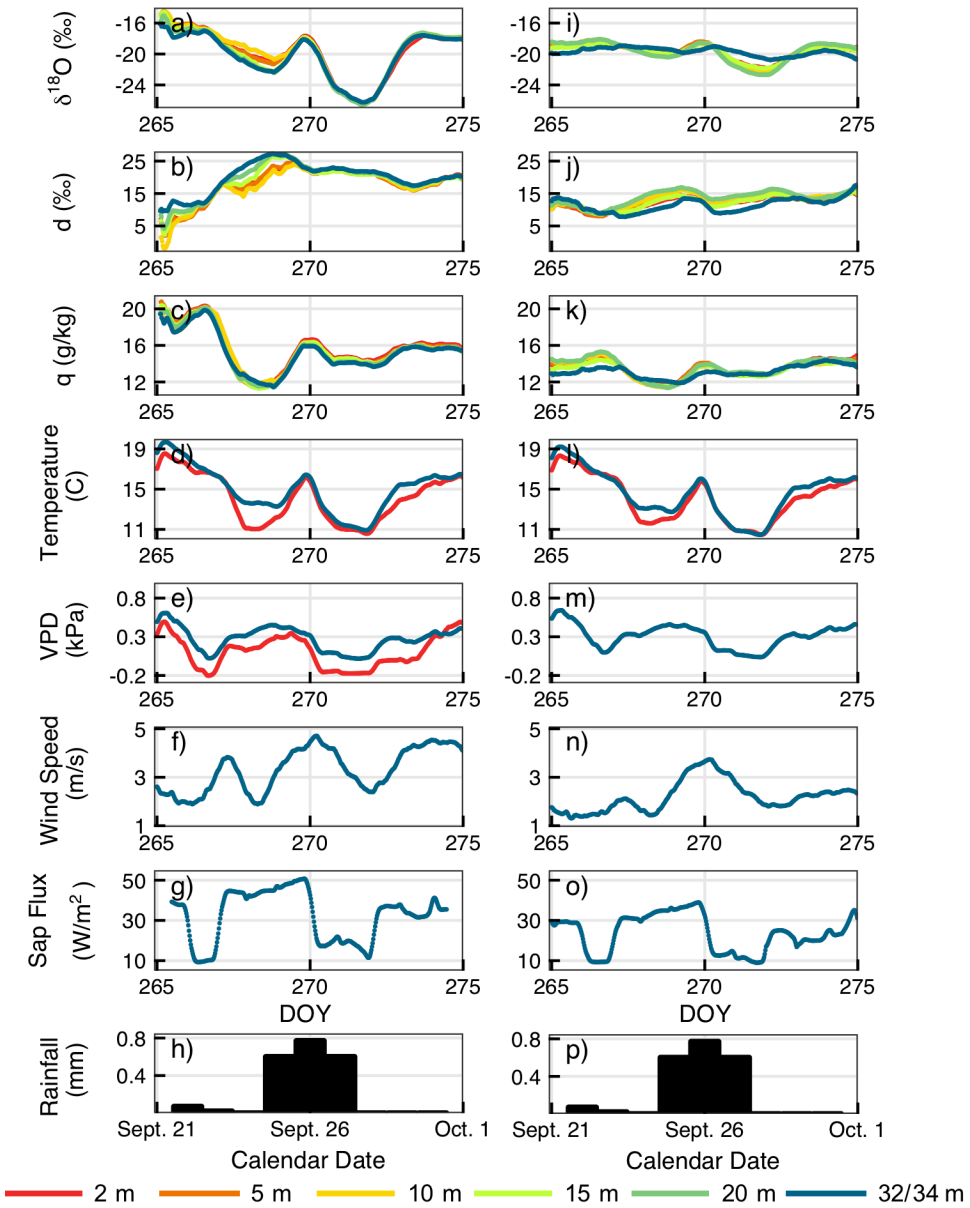

Figure S2.12 Time series of moving 24-hour average of fall isotopic compositions, meteorological data, and sap flux at the undisturbed (left) and disturbed (right) sites. a,i) vapor $\delta^{18}O$ (‰); b,j) *d* (‰); c,k) specific humidity (*q*, g/kg); d,l) temperature (°C); e,m) vapor pressure deficit (VPD, kPa); f,n) wind speed (m/s); g,o) sap flux (W/m^2); h,p) daily precipitation amount (mm). Isotopes and vapor mixing ratios are shown for all 6 heights from low (red) to high (blue). Meteorology is shown at 2m (red) and above-canopy (blue).

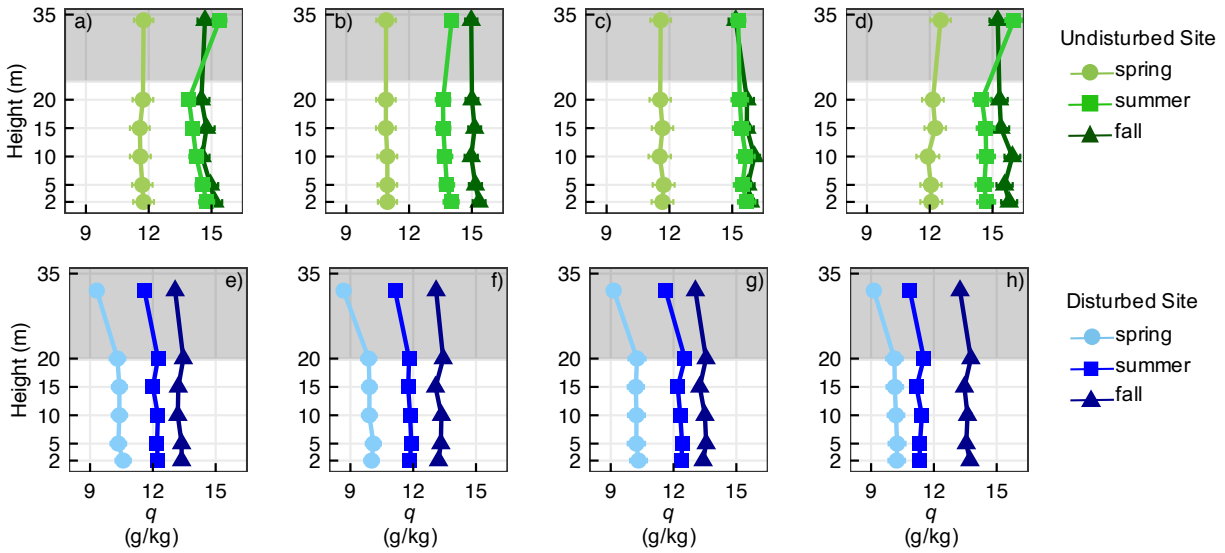

Figure S2.13 Mean profiles of specific humidity (q) from the undisturbed (green) and disturbed (blue) sites during the spring, summer, and fall. Shown here are profiles from four time slices: a and e) nighttime (00:00 to 03:00; b and f) sunrise (06:00 to 09:00), c and g) midafternoon (14:00 to 17:00); *d* and h) sunset (18:00 to 21:00). Grey shading indicates heights above the canopy. Error bars show standard error.

References

Aemisegger, F., Sturm, P., Graf, P., Sodemann, H., Pfahl, S., Knohl, A., & Wernli, H. (2012). Measuring variations of $\delta^{18}O$ and $\delta^{2}H$ in atmospheric water vapour using two commercial laser-based spectrometers: an instrument characterisation study. *Atmospheric Measurement Techniques*, *5*, 1491–1511. https://doi.org/10.5194/amt-5-1491-2012

Fiorella, R. P., Bares, R., Lin, J. C., Ehleringer, J. R., & Bowen, G. J. (2018). Detection and variability of combustion-derived vapor in an urban basin. *Atmospheric Chemistry and Physics*, *18*(12), 8529–8547. https://doi.org/10.5194/acp-18-8529-2018

Chapter 3 An Isotopic Approach to Partition Evapotranspiration in a Mixed Deciduous Forest[3]

Co-authors: Christopher J. Poulsen, Richard P. Fiorella, Ashely M. Matheny, and Timothy J. Veverica

3.1 Abstract

Transpiration (T) is perhaps the largest fluxes of water from the land surface to the atmosphere and is susceptible to changes in climate, land use, and vegetation structure. However, predictions of future transpiration fluxes vary widely and are poorly constrained. Stable water isotopes can help expand our understanding of land-atmosphere water fluxes, but are limited by a lack of observations and a poor understanding of how the isotopic composition of transpired vapor (δ_T) varies. Here, we present isotopic data of water vapor, terrestrial water, and plant water from a deciduous forest to understand how vegetation affects water budgets and land-atmosphere water fluxes. We measured sub-diurnal variations of $\delta^{18}O_T$ from three tree species, and use water isotopes to partition T from ET to quantify the role of vegetation in the local water cycle. We find that $\delta^{18}O_T$ deviated from isotopic steady-state during the day but find no species-specific patterns. The ratio of T to ET varied from 53% to 61%, and was generally invariant during the day, indicating that diurnal evaporation and transpiration fluxes respond to similar atmospheric and micrometeorological conditions at this site. Finally, we compared the isotope-inferred ratio of T to ET with results from another ET partitioning approach that uses eddy covariance and sap flux data. We find broad mid-day agreement between these two partitioning techniques, in particular the absence of a diurnal cycle, which should encourage future ecohydrological isotope studies.

[3] Published as: Aron, P.G., Poulsen, C.J., Fiorella, R.P., Matheny, A.M., Veverica, T.J. (2020) An Isotopic Approach to Partition Evapotranspiration in a Mixed Decidous Forest, Ecohydrology, doi: 10.1002/eco.229. Data associated with this study are available from Mfield, the University of Michigan Research and Data Hub (https://mfield.umich.edu/).

Isotope-inferred estimates of transpiration can inform land surface models and improve our understanding of land-atmosphere water fluxes.

3.2 Introduction

Evapotranspiration (ET) connects the water and carbon cycles and plays an important role maintaining terrestrial energy balance (Dunn & Mackay, 1995; Ellison et al., 2017; Swann et al., 2012; Worden et al., 2007). Despite its broad significance, estimates of terrestrial water fluxes from reanalysis, upscaled observations, and land surface models (LSMs) differ by up to 50% and predicting future land-atmosphere water fluxes remains a challenge (Mao et al., 2015; Mueller et al., 2013; Vinukollu et al., 2011). Central to this uncertainty are yet unresolved responses of plants to climate and land use change (Frank et al., 2015; Jackson et al., 2001; Massmann et al., 2019; Schlesinger & Jasechko, 2014). In a higher CO_2 world, some predict changes to leaf area index (LAI), stomatal conductance, soil moisture, and terrestrial runoff will intensify the water cycle (Brutsaert, 2017; Ohmura & Wild, 2002; Zeng et al., 2018; Zhang et al., 2016); others anticipate these vegetation-induced changes will decrease water cycling (Gedney et al., 2006; Labat et al., 2004). Consequently, a growing body of ecohydrological research is aimed at studying terrestrial water fluxes to better understand what drives water exchange between the land and the atmosphere, how terrestrial hydrology may change in the future, and how plants regulate freshwater resources.

ET is comprised of ecosystem evaporation (E, including surface evaporation and evaporation of canopy-intercepted water) and plant transpiration (T). The ratio of T to ET, hereafter referred to as F_T, provides insight into the role that vegetation plays in terrestrial water recycling and links plant hydrology with climate and meteorological conditions (Stoy et al., 2019). A complete understanding of this ratio is an important step towards predicting how plants will respond to land use and climate changes and how hydrologic balance may change in the future. To date, there is no consensus about the values of global, regional, and ecosystem F_T (Anderegg et al., 2019; Bowen et al., 2019; Stoy et al., 2019). In particular, estimates of T and F_T from LSMs and remote sensing algorithms, which rely on ecosystem-scale information, do not currently agree with ground-based observations of T and F_T that can vary on spatial scales of less than a kilometer (Good et al., 2015; Talsma et al., 2018; Wei et al., 2017). Most LSMs and remote sensing data cannot capture sub-grid cell variations of lateral water flow (Chang et al., 2018; Ji et al., 2017; Maxwell & Condon, 2016), plant water stress (Fang et al., 2017; Matheny, Bohrer, Stoy, et al.,

2014), and micrometeorological forcing (Badgley et al., 2015) that are necessary to accurately model F_T. Further complicating our understanding of land-atmosphere water exchange, some ground-based observations of ET may not actually capture conditions at the transpiring or evaporating surfaces. For example, near-surface gradients of water vapor concentrations and vapor pressure deficits can make it difficult to relate ET measurements, most of which are made using eddy covariance above canopies, to leaf and soil fluxes within canopies (Aron et al., 2019; Jarvis & McNaughton, 1986; Kauwe et al., 2017). Therefore, additional leaf- and soil-level flux measurements are needed to improve estimates of F_T and predictions of terrestrial water fluxes.

Stable water isotopes can improve our understanding of water fluxes from the land to the atmosphere because the component processes, evaporation and transpiration, have distinct isotopic signatures (Yakir & Sternberg, 2000). Evaporation causes a large fractionation that enriches vapor in the lighter isotope. Because plants generally do not fractionate water during uptake and a vast amount of water passes through plants without fractionating, transpiration generally adds vapor with a higher proportion of heavy isotopes to the atmosphere (Ehleringer & Dawson, 1992). Using these fingerprints, many researchers have use water isotopes to measure F_T and learn about land-atmosphere water exchange (Xiao et al., 2018 and references therein).

Isotopic ET partitioning requires knowledge of the isotope ratios associated with evapotranspiration (δ_{ET}), evaporation (δ_E), and transpiration (δ_T). Until recently, isotope-inferred estimates of evapotranspiration were limited to a low temporal resolution (day-to-annual timescales). As a result, the isotopic composition of transpired vapor was not measured and instead was assumed to be in isotopic steady-state (equal to that of source water) (Haese et al., 2013). However, observations from high-resolution laser absorption spectrometers now enable estimates of δ_T and show that transpiration can deviate from isotopic steady-state when periods of stable environmental conditions are too short to allow δ_T to reach the isotopic composition of source water (Dubbert et al., 2013, 2017; Dubbert, Cuntz, et al., 2014; Dubbert, Piayda, et al., 2014; Simonin et al., 2013). These δ_T observations may improve estimates of land-atmosphere water fluxes and our understanding of the role plants play in the water cycle. However, thus far studies of δ_T have focused only on a small subset of species and environments, and it is still quite challenging to model short term (sub-diurnal) variations of δ_T (Dubbert, Cuntz, et al., 2014) or incorporate non-steady-state transpiration into isotope-enabled land surface models (Wong et al., 2017). Additional observations of δ_T from a wide variety of species and environments can inform

estimates of F_T and may help reconcile F_T differences between observations and LSMs or remote sensing.

Forests play a critical role in land-atmosphere water exchange, but very few studies have directly used water isotopes to partition forest ET (Lai, Ehleringer, Bond, & Paw, 2006; Lee, Kim, & Smith, 2007; Moreira et al., 1997). Instead, most isotopic ET partitioning studies are based in croplands or grasslands where water management is easy to control and canopy cover is low, uniform, and continuous (e.g., Aouade et al., 2016; Lu et al., 2017; Wu et al., 2017). To address this gap, we measured the isotopic composition of transpired vapor from three tree species, bigtooth aspen (*Populus grandidentata*), red oak (*Quercus rubra*), and red maple (*Acer rubrum*), in a mixed deciduous forest in northern lower Michigan. We then use δ_T measurements to estimate forest F_T. Our objectives are to: 1) quantify the temporal and species-specific variability of δ_T, 2) use water isotopes to estimate forest F_T, and 3) evaluate whether measurements of non-steady-state δ_T improve isotopic ET partitioning. Finally, we compare our results from the isotopic ET partitioning with results from another partitioning technique that uses eddy covariance and sap flux data. Taken together, these objectives examine whether water isotopes provide accurate quantitative estimates of forest ET fluxes. If so, isotope-inferred F_T and δ_T may inform isotope-enabled LSMs and improve predictions of land-atmosphere water exchange. Broadly, this work builds upon a growing field of high-resolution isotope ecohydrology studies that seek to understand the role of vegetation in local, regional, and global water budgets.

3.3 ET partitioning

3.3.1 Theoretical isotopic ET flux partitioning

The isotopic two-source model is commonly used to partition evapotranspiration (ET) because evaporation (E) and transpiration (T) fluxes have distinct isotopic compositions. In this framework, ET is defined as

$$ET = E + T. \quad \text{Eq. 3.1}$$

Following isotopic mass balance and using delta (δ) notation, Eq. 3.1 can be expressed as

$$\delta_{ET}ET = \delta_E E + \delta_T T \quad \text{Eq. 3.2}$$

where δ_{ET}, δ_E, and δ_T are the isotopic compositions of evapotranspiration, evaporation, and transpiration, respectively. A list of all symbols and abbreviations used in this study is presented in Table 3.1. Throughout this manuscript, we use δ notation in per mil (‰), where R is the ratio of the heavy isotope to the light isotope ($\delta = (R_{sample} / R_{standard} - 1)*1000$) and the standard is Vienna Standard Mean Ocean Water (VSMOW) (Coplen, 1996; Gat, 1996). Combining Eq. 3.1 and Eq. 3.2 yields F_T, the ratio of T to ET:

$$F_T = \frac{T}{ET} = \frac{\delta_{ET} - \delta_E}{\delta_T - \delta_E}. \quad \text{Eq. 3.3}$$

This linear, two-source mixing model has been used in a number of previous studies to partition water fluxes of evapotranspiration (e.g., Wang and Yakir, 2000; Xiao et al., 2018; Yakir and Sternberg, 2000).

We determined δ_{ET} with a Keeling mixing model (Keeling, 1958; Yakir and Sternberg, 2000), where δ_{ET} is estimated as the y-intercept of a linear regression between the isotopic composition of atmospheric water vapor (δ_a) and the reciprocal of the water vapor concentration.

The isotopic composition of transpired vapor (δ_T) is calculated from leaf chamber measurements following Wang et al. (2012). Using this approach, δ_T is defined as

$$\delta_T = \frac{q_m\delta_m - q_a\delta_a}{q_m - q_a} \quad \text{Eq. 3.4}$$

where *q* is the water vapor concentration, $_m$ refers to measurements when the chamber was closed around a leaf, and $_a$ refers to measurements when the chamber was open to ambient vapor (Wang et al., 2012).

The isotopic composition of soil evaporation (δ_E) is estimated using the Craig and Gordon (1965) model:

$$\delta_E = \frac{\alpha_{eq}^{-1}\delta_s - h\delta_a - \varepsilon_{eq} - (1-h)\varepsilon_k}{(1-h) + 10^{-3}(1-h)\varepsilon_k} \quad \text{Eq. 3.5}$$

using meteorological measurements and isotopic values of soil water (δ_s) and atmospheric vapor (δ_a). Here α_{eq} (> 1) is the temperature dependent equilibrium fractionation factor (Majoube, 1971), ε_{eq} is calculated as $(1 - 1/\alpha_{eq}) \times 10^3$, ε_k is the kinetic fractionation term, and h is the relative humidity at the temperature of the evaporating surface.

Table 3.1 Description of symbols and subscripts used in this chapter.

Symbol	Description	Subscript	Description
α_{eq}	equilibrium fractionation factor	a	Atmospheric vapor
α_k	kinetic fractionation factor	E	Evaporation
δ	Delta notation, stable isotope value (‰)	ET	Evapotranspiration
$\delta^{18}O$	Oxygen isotope value (‰)	g	Groundwater
$\delta^{2}H$	Hydrogen isotope value (‰)	l	Leaf
d or d-excess	Deuterium-excess	lake	Lake
E	Evaporation	m	Closed leaf chamber vapor
ET	Evapotranspiration	p	Precipitation
F_T	Transpiration/Evapotranspiration	s	Soil
h	Relative humidity	T	Transpiration
q	Specific humidity	x	Xylem
R	Isotope ratio (e.g., $^{18}O/^{16}O$)		
T	Transpiration		

3.3.2 ET partitioning from sap flux and eddy covariance data

ET partitioning from sap flux and eddy covariance measurements follows the approach described by Williams et al. (2004). In this technique, the latent heat-derived ET is separated into biotic (T) and abiotic (E) components using eddy covariance estimates of latent energy and direct measurements of sap flux. To partition ET, we assumed that transpiration accounted for nearly all of the ET flux on the driest days during the growing season and derived a scaling equation to estimate the ratio of T to ET on days when evaporation was not negligible (Kool et al., 2014). Additional details on this scaling are provided in the supplementary information.

3.4 Methods

3.4.1 Site description

This study was conducted at the 46 m AmeriFlux-affiliated eddy covariance tower site at the University of Michigan Biological Station (UMBS) in northern lower Michigan (45.59°N, 84.70°W, AmeriFlux database site-ID US-UMB). The forest at this site has been dominated by bigtooth aspen (*Populus grandidentata*) and paper birch (*Betula papyrifera*), but is currently transitioning to a mixed composition dominated by red oak (*Quercus rubra*), red maple (*Acer rubrum*), white pine (*Pinus strobus*), American beech (*Fagus grandifolia*), and sugar maple (*Acer saccharum*). As a result of heavy logging in the early 20th century, the forest has a relatively uniform age and canopy structure. Mean canopy height is ~ 22 m and mean peak LAI is 3.9 m^2/m^2. The site receives 766 mm of precipitation annually and the mean annual temperature is 5.5°C (Matheny et al., 2017). Soils at the UMBS site are well drained Haplorthods of the Rubicon, Blue Lake, or Cheboygan series and consist of ~ 95% sand and ~ 5% silt (Nave et al., 2011). Additional site details are available in Matheny et al. (2017) and Gough et al. (2013).

3.4.2 Isotope measurements

3.4.2.1 Surface waters

We collected a variety of surface waters and shallow groundwaters during the 2017 growing season to characterize the isotopic composition of potential source waters for trees and to examine seasonal hydrologic variability near our study site. We collected event-scale precipitation at the tower site in a plastic bucket lined with mineral oil to prevent evaporation (Friedman et al., 1992; Scholl et al., 1996). We used a needle point syringe to extract precipitation and avoid transferring any oil to the collection vial. The sampling bucket was cleaned, dried, and given a fresh layer of oil between samples. From April to October, we collected monthly samples from the edge of a nearby lake and from the mouth of a groundwater spring. The groundwater spring originates from a seep at the bottom of the lake (Hendricks et al., 2016). We collected shallow (within 3 m of the surface) groundwater in April, June, and November from 15 wells near the mouth of the spring. All liquid water samples were collected in HDPE vials (Wheaton Industries, 986716) and analyzed within a few weeks of collection, so we do not expect any fractionation

between the plastic HDPE collection containers and the sampled water (Spangenberg, 2012). We used a Picarro L2130-i cavity ringdown spectrometer (CRDS) with an A0211 high-precision vaporizer and attached autosampler to measure $\delta^{18}O$ and $\delta^{2}H$ of liquid water samples. We used Picarro ChemCorrect software to monitor samples for organic contamination. For liquid samples, precision was better than 0.1‰ and 0.3‰ for $\delta^{18}O$ and $\delta^{2}H$, respectively.

3.4.2.2 Vapor

To analyze water vapor isotopes, we deployed two cavity ringdown spectrometers, a Picarro L2120-i and a Picarro L2130-i, in a temperature-controlled shed located next to the 46 m eddy covariance tower. We used a Picarro Standard Delivery Module (SDM, A0101) to deliver liquid laboratory standards to monitor for drift and calibrate isotope data to the VSMOW–SLAP scale (Bailey et al., 2015). Each SDM was setup with a Drierite (26800) column and a Picarro high precision vaporizer (A0211) maintained at 140°C and ambient pressure. We analyzed standards at night in order to minimize interference with data collection during the day when transpiration was higher.

Cavity ringdown spectrometers are known to exhibit an isotope-ratio bias due to changes in cavity humidity (Aemisegger et al., 2012). To correct for this bias, we used version 1.2 of the University of Utah vapor processing scripts to derive cavity-humidity correction equations and instrument precision (Fiorella et al., 2018). We present the 1σ uncertainty at 10,000 ppmv, the lowest measured vapor mixing ratio, and 25,000 ppmv, near the highest measured mixing ratio. For d-excess ($d = \delta^{2}H - 8*\delta^{18}O$ (Dansgaard, 1964)), we assume oxygen and hydrogen errors are independent. 1σ uncertainty on the L2120-i ranged from 0.28‰ for $\delta^{18}O$, 0.93‰ for $\delta^{2}H$, and 2.45‰ for *d* at 10,000 ppmv to 0.20‰, 0.59‰, and 1.68‰ (for oxygen, hydrogen, and d, respectively) at 25,000 ppm. On the L2130-i, 1σ uncertainty ranged from 0.13‰ for $\delta^{18}O$, 0.43‰ for $\delta^{2}H$, and 1.14‰ for *d* at 10,000 ppmv to 0.09‰, 0.29‰, and 0.78‰ (for oxygen, hydrogen, and d, respectively) at 25,000 ppm. Additional information about the cavity humidity correction equations is available in the supplementary information.

We installed a vapor sampling manifold on the eddy covariance tower and selected three similarly-sized nearby trees – a bigtooth aspen, a red oak, and a red maple – for transpiration measurements. We chose these species because together they account for more than 70% of the LAI and a majority of the sap flux at the site (Figure 3.1). Leaves and branches from the aspen and

oak were accessible from a platform on the eddy covariance tower 15 m above the ground. No maple branches were accessible directly from the eddy covariance tower, so we built a small 5 m tower a few meters from the base of the eddy covariance tower to reach a maple tree. The uppermost extent of all three sampled trees reached the upper canopy and was exposed to full sunlight.

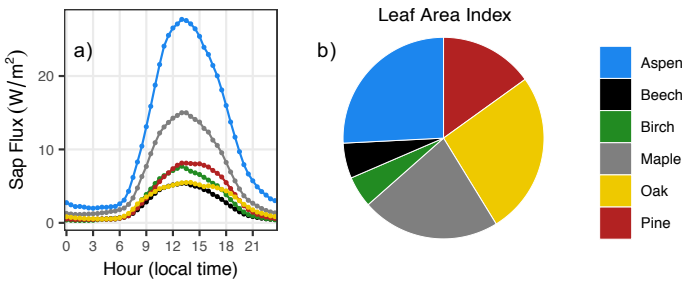

Figure 3.1 a) Mean diurnal sap flux (W/m^2) and b) leaf area index (LAI) by species during the 2017 growing season (May to October).

We built two transparent flow-through sampling chambers following the description in Wang et al. (2012) to make δ_T measurements at 5 and 15 m. Each chamber was approximately 20 cm long, 15 cm wide, and 5 cm tall. This size accommodated large (up to ~15 cm) oak leaves but was kept small to minimize lag or memory effects between switching samples. Just before a closed-chamber transpiration measurement, we manually inserted a live leaf (still attached to the tree) into the chamber and sealed the chamber. Each chamber had two small (~2 cm) openings to pull in ambient vapor during closed-chamber measurements. The chamber hung from the tree for the duration of each transpiration measurement period. Occasionally we had to reorient the chamber to prevent the leaf from touching the side of the chamber because any contact points between the leaf and the chamber promoted condensation. Every closed-chamber measurement was made on a different leaf. At the end of the transpiration measurement period, we opened the chamber, removed the leaf, and measured ambient vapor from the open chamber.

Sampling lines extended from the chambers to the Picarro analyzer. The 5 m chamber had two sampling lines, one to measure vapor when the chamber was closed around a leaf and another to measure vapor when the chamber was open. The 15 m chamber had three sampling lines, one for closed oak measurements, one for closed aspen measurements, and one for open chamber

measurements. A final ambient-only sampling line extended above the canopy and was collocated adjacent to 34 m meteorological and flux measurements from the eddy covariance tower. All sampling lines were constructed from non-fractionating Bev-A-Line tubing (Simonin et al., 2013), encased in insulation, and wrapped with a warm wire to prevent condensation. The whole sampling manifold was held below ambient pressure by a diaphragm pump that operated at ~5 L/min to maintain constant airflow and minimize memory effects between samples.

Each Picarro analyzer controlled a multi-position valve (VICI/Valco EMT2SD6MWE) to switch between sampling locations. We measured each ambient vapor for 5 minutes and transpired (closed chamber) vapor for 10 minutes. We define a cycle of isotopic measurements as a loop through each port on the multi-position valve, and assume that the average isotopic composition at each sampling location represents the isotopic composition at that location for the full cycle of measurements.

Initially we planned to use the L2120-i to analyze ambient vapor and the L2130-i to analyze transpired vapor. This setup was designed to measure the highest possible temporal resolution of δ_T. However, the L2130-i analyzer malfunctioned after the June sampling campaign, which forced us to reconfigure our approach and use the L2120-i to measure all six locations in August and October. We measured vapor isotopes during three periods in 2017: June 19 (DOY 170); August 14 (DOY 226), August 15 (DOY 227), and August 16 (DOY 228); and October 6 (DOY 279) and October 9 (DOY 282). These days were selected to study transpiration during periods when water fluxes were high (June and August) and low (October). Missing days in October (DOY 280 and 281) are due to technical issues with the Picarro analyzers, poor weather, and other logistical difficulties at the field site.

3.4.2.3 Terrestrial and biological waters

We used a soil auger to collect soil from the top 10 cm around noon on June 19, August 16, and October 6. Xylem samples were collected mid-day at breast height using an increment borer on August 16, October 6, and October 9. To avoid disrupting the hydraulics of the trees that were monitored for transpiration, we collected xylem samples from trees near the eddy covariance tower. We collected leaves from the transpiration-monitored trees because leaves from other trees were out of reach and the removal of a few leaves from a fully leafed-out tree was not expected to significantly affect plant hydraulics. Leaf samples were collected around 8am, 11am, 2pm, and

5pm on August 15, August 16, October 6, and October 9. To collocate measurements of leaf water and transpired vapor, we collected maple leaves at 5 m and oak and aspen leaves at 15 m. Soil, xylem, and leaf samples were stored in a refrigerator after collection.

Waters from soil, xylem, and leaf matrices were extracted on a cryogenic vacuum distillation line following the methods of West et al. (2006). The midrib was not removed from leaves prior to the distillation. Distilled soil waters were analyzed for oxygen and hydrogen isotopes on a Picarro L2130-i as described earlier. Due to complications arising from the presence of organic compounds (West et al., 2010), leaf and xylem waters were analyzed for $\delta^{18}O$ and $\delta^{2}H$ using a Thermo Scientific Delta V gas isotope ratio mass spectrometer (TC/EA-IRMS hereafter) that does not suffer from organic contamination. The TC/EA-IRMS was interfaced with a Thermo Scientific FlashIRMS elemental analyzer running in pyrolysis mode. A 0.5 uL aliquot of distilled water was injected into a glassy carbon furnace maintained at 1450°C. The product gases were separated chromatographically on a Restek Molesieve 5A column (60/80 mesh, 2m x 2 mm ID isothermal at 50°C) and were introduced to the IRMS by means of a continuous flow open-split interface (Conflo IV) optimized to each gas for linearity and sensitivity. Each gas was normalized to an injection of internal reference gas, and each batch of samples was then normalized to VSMOW by means of complementary analysis of known standards under these same conditions. Precision of TC/EA-IRMS analyses was better than 0.4‰ for $\delta^{18}O$ and 2.4‰ for $\delta^{2}H$.

3.4.3 Sap flux

Sap flux is considered a proxy for transpiration (Granier & Loustau, 1994; Phillps & Oren, 1998). We used a network of custom-built Granier (1987) style thermal dissipation probes in 60 trees to continuously monitor sap flux at our field site. For this project, we installed six additional sap flux probes in the maple and oak trees that were used to measure transpiration to ensure they were hydrologically similar to others at the site. Sap flux measurements were made every minute and reported as 30-minute averages. Additional details about the sap flux sensors and network are available in Matheny et al. (2014b) and Matheny et al. (2017).

3.4.4 Meteorological and eddy covariance measurements

Temperature and relative humidity (HMP45g, Vaisala, Helsinki, Finland) were measured at 3, 15, and 34 m from the eddy covariance tower. 3 m measurements were reported every minute;

15 and 34 m measurements were reported as 30-minute averages. To facilitate comparison with other meteorological and eddy covariance data, 3 m temperature and relative humidity were averaged to common 30-minute timesteps. Daily precipitation amount was measured approximately 6 km east of our field site at the Pellston Regional Airport. These data are available from the National Oceanic and Atmospheric Administration Climate Data Online archive (Network ID USW00014841).

Eddy covariance CO_2 and H_2O fluxes were measured above the canopy at 34 m. The latent heat flux was measured at high resolution (10 Hz) using the eddy covariance approach: water vapor and CO_2 concentrations were measured using a closed-path infrared gas analyzer (LI7000, LI-COR Biosciences, Lincoln, NE, USA); wind velocity and temperature were measured with a 3-D ultrasonic anemometer (CSAT3, Campbell Scientific, Logan, UT, USA). The latent heat flux was corrected by the Webb-Pearman-Leuning correction to account for density fluctuations in water vapor fluxes (Webb et al., 1980). A complete description of the eddy covariance data processing is available in Gough et al. (2013). All eddy covariance variables were reported as 30-minute averages. Spikes in the eddy covariance data were identified using a median filter (Starkenburg et al., 2016) and removed.

3.4.5 Data processing: δ_T calculations and ET partitioning

All isotopic, meteorologic, and eddy covariance data were processed to a common time-step to facilitate analysis. The common time of δ_T measurements was rounded to the nearest half hour of the closed-chamber measurements. Following Eq. 3.4, $\delta^{18}O_T$ was calculated from isotope and humidity measurements when the chamber was open (measuring ambient vapor) and closed (measuring transpired vapor). The Picarro simultaneously measures isotopic compositions and specific humidity; no additional parameters or measurements are needed to calculated δ_T (Wang et al., 2012). We omit the first 2 minutes of each measurement period to minimize memory effects from switching sampling ports and used the average of measurements from minutes 3-5 for the $\delta^{18}O_T$ calculation (Aemisegger et al., 2012). Although the closed-chamber measurements continued for 10 minutes, we chose not to use transpired vapor measurements from minutes 5-10 because we observed that condensation occasionally built up in the chambers after 5 minutes.

Air within the canopy is usually poorly mixed (Aron et al., 2019), so we used above-canopy measurements for the Keeling regression to derive ecosystem-scale δ_{ET}. In contrast, δ_T

measurements are separated by species (e.g., $\delta_{T,maple}$, $\delta_{T,aspen}$, and $\delta_{T,oak}$). At UMBS, maple, aspen, and oak account for ~ 22%, 26%, and 26%, respectively, of the total LAI (Figure 3.1b). To ensure we did not overpredict the transpiration flux from these three species, we scaled $\delta_{T,maple}$, $\delta_{T,aspen}$, and $\delta_{T,oak}$ values by the percentage of total LAI accounted for by each species. This approach can produce species-specific values of F_T, although that is not our focus in this study because similar measurements are already done at UMBS from sap flux data (Figure 3.1a). Instead, in this study, we combine transpiration fluxes from maple, oak, and aspen trees to approximate an ecosystem-wide flux. We refer to F_T calculated from the scaled δ_T measurements as non-steady-state F_T.

To test the effects of assumed steady-state transpiration on isotope-inferred F_T, we compare non-steady-state F_T with F_T estimated with two steady-state δ_T assumptions: a source water assumption that uses the Craig and Gordon (1965) leaf water model and defines δ_T as xylem water (δ_x) and a precipitation assumption that sets δ_T as δ_p. A summary of the various techniques and assumptions we use to estimate F_T is presented in Table 3.2. δ_s and δ_x can vary spatially across a landscape (Brooks et al., 2010; McDonnell, 2014) and mostly likely reflect a mixture of water from past precipitation events and other incoming surface and groundwater flows (Barbour, 2007). Preferential flow paths through the porous (> 90% sand) UMBS soil may also bias the isotopic composition of available soil water (Brooks et al., 2010). Neither the source water nor the precipitation assumptions consider these environmental complexities, and a detailed assessment of soil hydrology is beyond the scope of this study. Instead, the steady-state assumptions used in this study are our best attempt to capture a representative transpiration flux from the forest.

Table 3.2 Summary of F_T methods, species, assumptions, and results.

Method	Species	Assumptions	F_T Explanation	F_T
δ_T measurements (non-steady-state)	Aspen, maple, oak		Direct leaf-level measurements of δ_T	37 ± 2%
Source water assumption (steady-state δ_T)	Aspen, maple, oak	$\delta_x = \delta_T$	δ_T scaled to LAI of aspen, maple, oak	36 ± 2%
Aspen, maple, oak ecohydrologic	Aspen, maple, oak		Sap flux scaled to LAI of aspen, maple, oak	43 ± 9% (40 ± 7% midday)
Precipitation assumption (steady-state δ_T)	Aspen, beech, birch, maple, oak, pine	$\delta_p = \delta_T$	δ_T scaled to LAI of all non-oak species + $\delta_{x,oak}$ scaled to the LAI of oak*	53 ± 3%,
Plot-level ecohydrologic	Aspen, beech, birch, maple, oak, pine		Total plot level sap flux	65 ± 12% (61 ± 8% midday)

* Matheny et al. (2017) demonstrated that oak at our study site have a deeper rooting structure and can access soil water that is more depleted in heavy isotopes than other tree species at the site. As a result, F_T from the precipitation assumption is calculated from the sum of δ_p scaled to the LAI of all non-oak species plus $\delta_{x,oak}$ scaled to the LAI of oak.

3.5 Results

3.5.1 Seasonal and synoptic scale variability

Seasonal variations of local meteorology, sap flux, and latent heat flux are shown in Figure 3.2. Temperature, specific humidity, sap flux, and latent heat flux increased through the spring, reached a maximum in the summer, and decreased in the fall. Soil moisture was greatest in the spring when the soil was moist from winter snowmelt and decreased through the growing season as water percolated through the soil or returned to the atmosphere via evapotranspiration (Figure 3.2f). Soil moisture increased rapidly after precipitation events, but due to the high sand content, limited storage potential, and increased ET fluxes after rain, decreased quickly after each storm pulse (Figure 3.2f). Sap flux and latent heat were positively correlated (Pearson's $r > 0.75$) throughout the growing season and moderately well correlated with above-canopy VPD ($r > 0.53$) (Figures 3.2d and 3.2e). Imprinted on this seasonal variation, meteorological, eddy covariance, and sap flux measurements varied on 3-4 day timescales as weather systems passed through the

study region (Figure 3.2). Daily precipitation totals varied from 0 to 1.18 cm (Figure 3.2f). In general, on rainy days, temperature, sap flux, and latent heat were lower and specific humidity was higher.

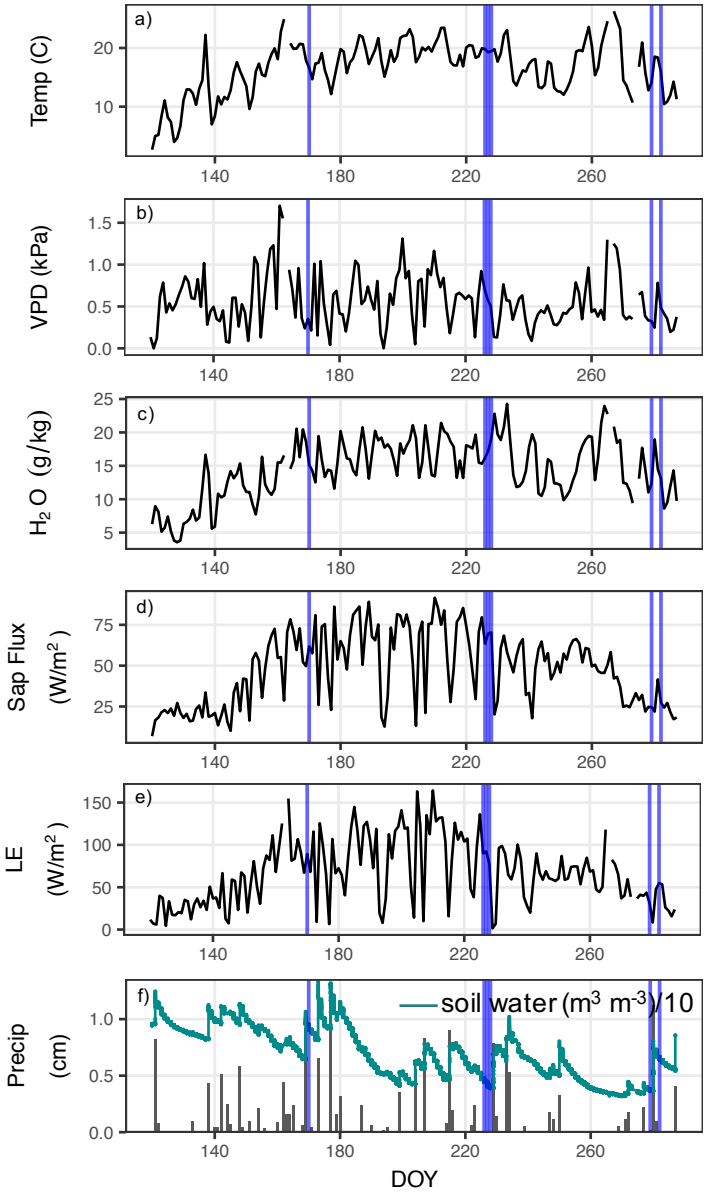

Figure 3.2 Above-canopy mean daily (a) temperature, (b) vapor pressure deficit, (c) specific humidity, (d) sap flux, (e) latent heat flux, and (f) total daily precipitation and mean daily soil moisture through the growing season. The vertical blue lines indicate days on which we measured transpiration isotopes.

Monthly variability of terrestrial (rain, lake, soil, and ground) and plant (xylem and leaf) waters $\delta^{18}O$ and $\delta^{2}H$ are shown in Figure 3.3. Precipitation, surface water, and shallow groundwater cluster around the global meteoric water line (GMWL, $\delta^{2}H = 8*\delta^{18}O + 10‰$ (Craig, 1961)). The local meteoric water line (LMWL, $\delta^{2}H = 7.9*\delta^{18}O + 13.6‰$) at UMBS has a slope close to the that of the GMWL and an intercept that reflects the high degree of moisture recycling downwind of Lake Michigan (Bowen et al., 2012; Putman et al., 2019). The isotopic compositions of soil (δ_s), xylem (δ_x), and leaf (δ_l) waters generally fall below the GMWL along lines with shallow slopes (~2.5‰‰$^{-1}$) and very low intercepts (~–37‰), indicative of evaporative enrichment.

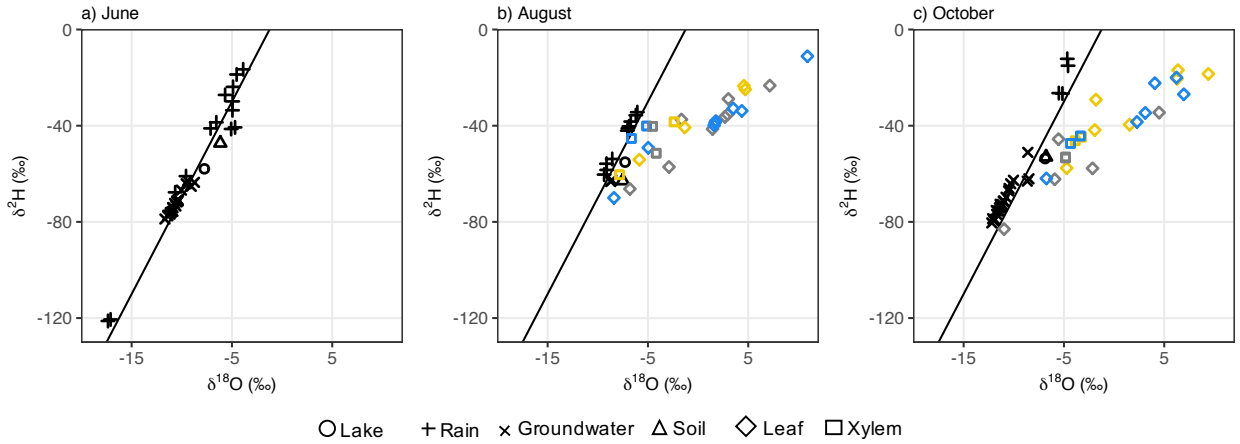

Figure 3.3 $\delta^{18}O$ and $\delta^{2}H$ of various waters pools at or near the study site. Leaf (diamonds) and xylem (squares) isotopes are color coded by species (maple is grey, aspen is blue, and oak is yellow). Lake, rain, ground, and soil water are differentiated by symbology but are all colored black. The black line is the global meteoric water line.

Timeseries of meteoric water isotopes through the 2017 growing season are shown in Figure 3.4. Event-scale $\delta^{18}O_p$ generally varied between –4 to –12‰ (–10 to –80‰ for $\delta^{2}H$), although a large (~1.2 cm) storm in late June had a particularly low isotopic composition (–17.1 and –120.6‰ for oxygen and hydrogen, respectively, Figure 3.4a). Precipitation d-excess (~13‰) was relatively consistent from May to October, with the exception of three mid-summer storms that had low d-excess (< 6.1‰, Figure 3.4b). $\delta^{18}O$ of the lake and groundwater spring, which flows from a seep at the bottom of the lake, increased 1.2‰ and 0.3‰, respectively, through the growing season (Figure 3.4a). Together, these trends indicate that some lake water evaporated during the growing season. $\delta^{18}O$ and $\delta^{2}H$ of groundwater was almost always less than that of surface water.

The groundwater spring ($\delta^{18}O$ –9.1‰ to –8.5‰) was therefore likely a mixture of lake water ($\delta^{18}O$ –8.1‰ to –6.9‰) and shallow groundwater ($\delta^{18}O$ –12.2‰ to –8.1‰). The seasonal trends in $\delta^{18}O$ and d-excess of the spring suggest that the contribution of groundwater to the spring decreased through the growing season.

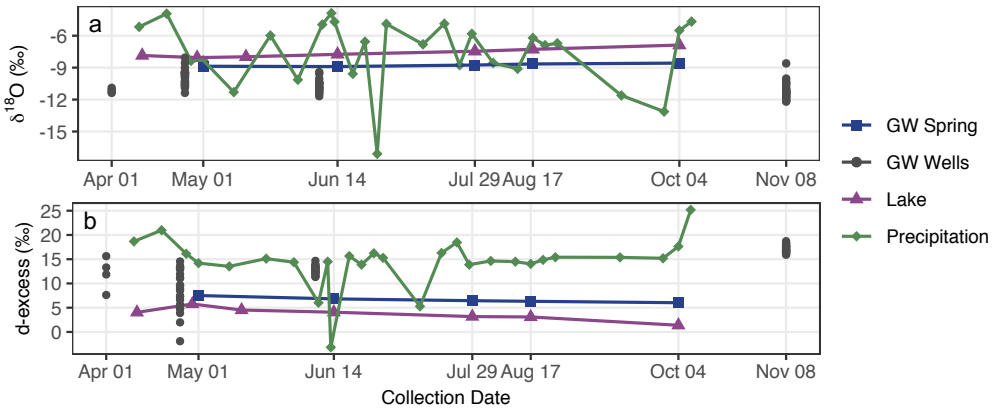

Figure 3.4 Timeseries of a) $\delta^{18}O$ and b) d-excess of precipitation (green diamond), lake (purple triangle), groundwater well (gray circle), and groundwater spring (blue square) from April to November 2017.

3.5.2 Diurnal isotope variability

Soil and xylem waters were evaporatively enriched relative to precipitation on all the days we measured these pools (Figure 3.5). In August, $\delta^{18}O_p$ of the rain event just before the measurement period (–9.1 ‰) was less than that of $\delta^{18}O_x$ for maple, aspen, and oak (–4.2, –6.7, –7.8‰, respectively) (Figures 3.5a and 3.5b). Similarly, on October 6, $\delta^{18}O_p$ (–5.5‰) was lower than $\delta^{18}O_x$ (–4.8, –4.3, and –3.9‰, maple, aspen, and oak, respectively, Figure 3.5c); on October 9 $\delta^{18}O_p$ (–4.7‰) was lower than or nearly equal to $\delta^{18}O_x$ (–4.9, –3.4, and –3.3‰, maple, aspen, and oak, respectively, Figure 3.5d). Precipitation d-excess in August, October 6, and October 9 was higher (14.5, 17.6, and 25.2‰, respectively) than d-excess of xylem water, suggesting that the difference between $\delta^{18}O_x$ and $\delta^{18}O_p$ is likely related to evaporative enrichment prior to uptake (Figures 3.5e-3.5h). $\delta^{18}O_s$ was never equal to $\delta^{18}O_p$, which suggests that soil water experienced fractionation by post-depositional processes (likely evaporation), was a mixture of water from multiple previous rain events, and/or was fed by other nearby sources (Figures 3.5a-3.5d). Near

surface soil water d-excess was lower than that of precipitation, indicating that soil water was also evaporatively enriched relative to the most recent precipitation (Figures 3.5e-3.5h).

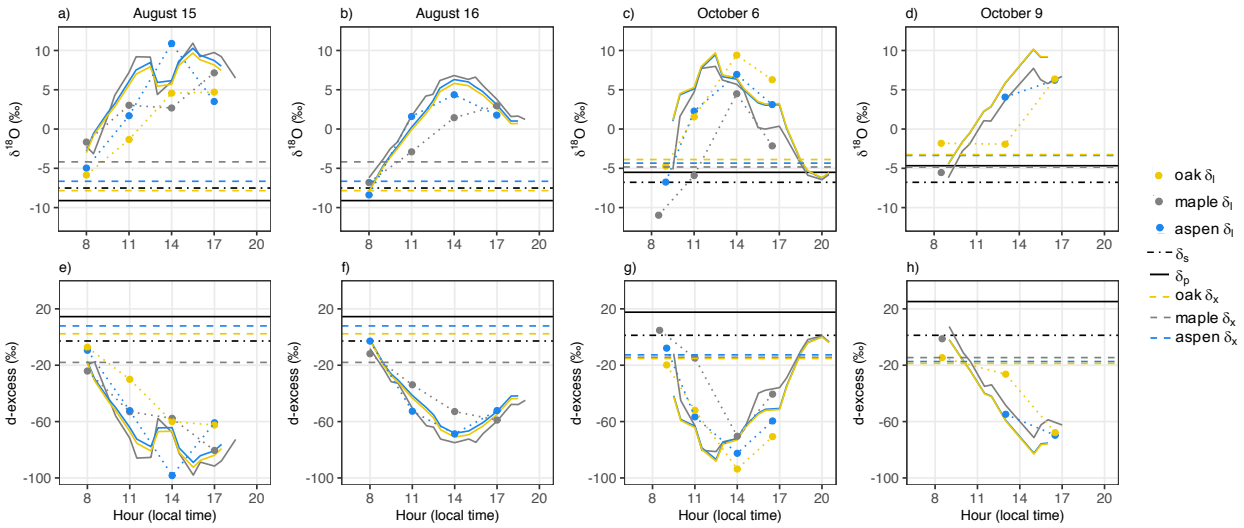

Figure 3.5 Diurnal $\delta^{18}O$ (a-d) and d-excess (e-h) of leaf water (circles), xylem (dashed lines), precipitation (solid black line), and soil water (black dotted dashed line). Color differentiates species: maple is grey, aspen is blue, and oak is yellow. The solid colored lines are expected steady state $\delta^{18}O_l$ and d-excess$_l$ estimated from the Craig and Gordon (1965) using values of the kinetic fractionation factor from Merlivat (1978). Values of δ_x on August 15 are assumed to be the same as those measured on August 16.

Observed $\delta^{18}O_l$ of all three species exhibited a pronounced (> 10‰) daily pattern with the most evaporative enrichment (highest $\delta^{18}O_l$ values) in the afternoon when temperature was at a maximum, relative humidity was at a minimum, and sap flux was high (Figures 3.5a-3.5d). As expected, d-excess of leaf water exhibited the opposite diurnal pattern with the greatest values in the morning and the lowest values in the mid-afternoon (Figures 3.5e-3.5h). Observed $\delta^{18}O_l$ are generally lower than estimated steady-state $\delta^{18}O_l$, which may result from a discrepancy between observed $\delta^{18}O_l$, which includes midrib and vein water, and modeled $\delta^{18}O_l$, which estimates water at the evaporation sites. Alternatively, the offset between observed and estimated $\delta^{18}O_l$ may suggest that, even at midday when the transpiration flux was high (Figure 3.1a) and leaf-water turnover time was quickest, leaves were not at isotopic steady-state (Figures 3.5a-3.5d).

Although the diurnal pattern of leaf water isotopes was consistent between maple, oak, and aspen, the magnitude of diurnal δ_l change and values of $\delta^{18}O_l$ and $\delta^{18}O_x$ varied between species.

For example, in August morning (8am) $\delta^{18}O_x$ and $\delta^{18}O_l$ of oak were lower than $\delta^{18}O_x$ and $\delta^{18}O_l$ of either maple or aspen (Figure 3.5a). Additionally, minimum morning $\delta^{18}O_l$ varied on consecutive sampling days, with lower $\delta^{18}O_{l,maple}$ and $\delta^{18}O_{l,aspen}$ on August 16 than August 15 (Figures 3.5a and 3.5b). In contrast, October $\delta^{18}O_{x,maple}$, $\delta^{18}O_{x,oak}$, and $\delta^{18}O_{x,aspen}$ were within 1‰ of each other (~–4‰), but $\delta^{18}O_{l,maple}$ was ~5‰ lower than $\delta^{18}O_{l,oak}$ and $\delta^{18}O_{l,aspen}$ (Figures 3.5c and 3.5d).

$\delta^{18}O_T$ varied between –15 and 6‰ and frequently deviated from $\delta^{18}O_x$, $\delta^{18}O_s$, or $\delta^{18}O_p$, indicating that transpiration was not at isotopic steady state on sub-diurnal timescales (Figure 3.6). In general, $\delta^{18}O_T$ was lower in the morning when relative humidity was high and increased through the day as transpiration increased. $\delta^{18}O_T$ was always greater than $\delta^{18}O_a$ (–23.6 to –16.7‰, Figure 3.6) and therefore pushed the isotopic composition of atmospheric water vapor to higher values. No consistent species-specific $\delta^{18}O_T$ trend emerged, and $\delta^{18}O_{T,aspen}$, $\delta^{18}O_{T,oak}$, and $^{18}O_{T,maple}$ varied considerably day-to-day and on sub-diurnal timescales (Figure 3.6). $\delta^{18}O_E$ varied between –38.3 and –31.2‰ and pushed $\delta^{18}O_a$ to lower values (Figure 3.6).

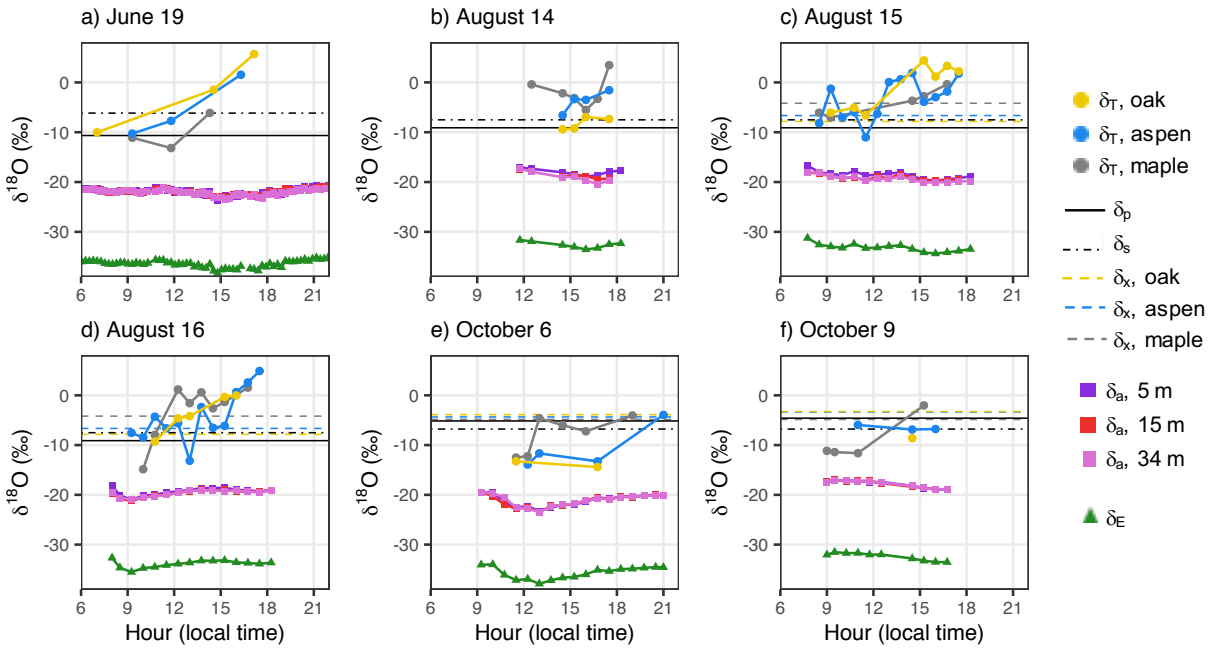

Figure 3.6 Diurnal δ_T (circles), δ_a (squares), and δ_E (triangles) on six days of measurements. For δ_T, maple is grey, aspen is blue, and oak is yellow. For δ_a, 5 m is purple, 15 m is red, and 34 m is pink. Horizontal lines indicate δ_p (solid black) of recent precipitation, δ_s (dotted dash black), and δ_x (dashed, maple is yellow, aspen is blue, and oak is gray).

3.5.3 Diurnal ET partitioning

A summary of ET partitioning results is presented in Table 3.2. Using Eq. 3.3 and the measured values of $\delta^{18}O_T$, transpiration from maple, oak, and aspen accounted for 37 ± 2% of the ET flux. This value, referred to as non-steady-state F_T, did not exhibit a consistent diurnal cycle (Figure 3.7). We compare non-steady-state F_T with F_T calculated from two steady-state isotope assumptions: that δ_T is equal to xylem water (source water assumption) and that δ_T is equal to δ_p of the most recent storm event (precipitation assumption). The precipitation assumption, which assumes that the only available source water is recent precipitation, allows us to estimate a transpiration flux from all species in the forest, including ones from which we did not measure δ_x. The precipitation assumption is our best attempt to quantitively estimate a plot-level transpiration flux; it does not address the timescale over which plants access available soil water or the complexities of preferential flow paths through soils, both of which affect δ_x and δ_T (Allen et al., 2018; Brooks et al., 2010; Evaristo et al., 2015).

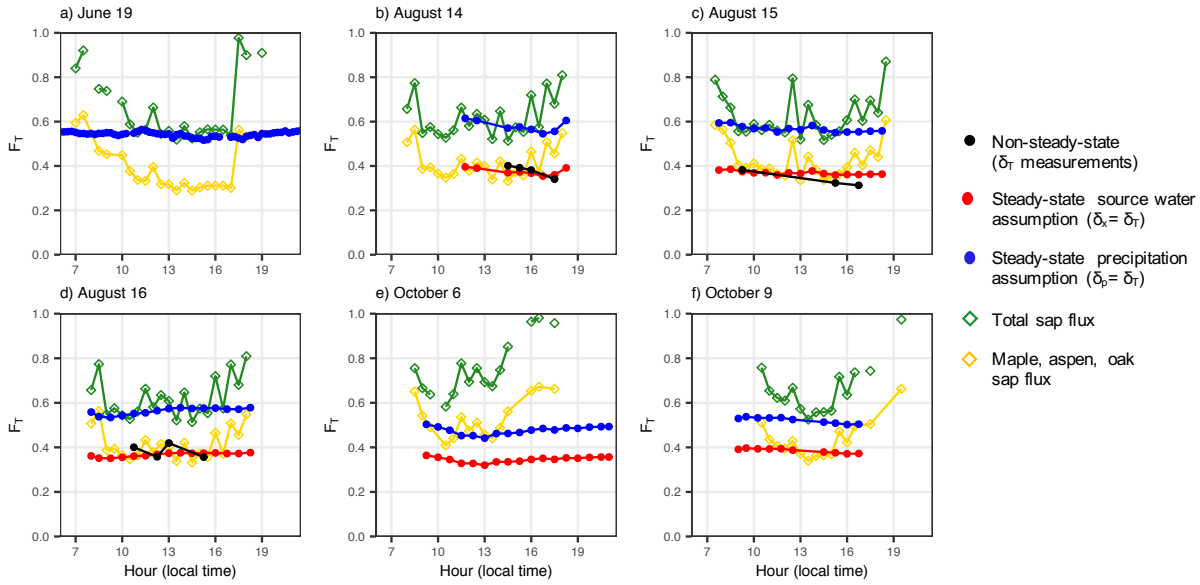

Figure 3.7 Isotopic (filled circles) and ecohydrologic (open diamonds) F_T on six days of measurements. F_T estimated with non-steady-state measurements (black), the source water assumption (red), and sap flux scaled to include only medium maple, large oak, and large aspen (yellow) only capture the transpiration flux from a subset of trees. F_T from the precipitation assumption (blue) and plot level sap flux (green) capture the transpiration flux from all species and size classes in the forest.

F_T estimated from the source water assumption (36 ± 2%, Figure 3.7) is nearly identical to non-steady-state F_T. The precipitation assumption produces a higher estimate of F_T (53 ± 3%, Figure 3.7). The offset between these F_T values arises because the precipitation assumption includes a water flux from all tree species at the site while the source water assumption only includes only the species from which we measured δ_x (maple, oak, and aspen) and accounts for ~70% of the site LAI. Correcting for this LAI discrepancy (scaling F_T results from the precipitation assumption to include only 70% of the trees) and assuming that each species produces a similar amount of transpiration per unit leaf (Jarvis & McNaughton, 1986), we find that the source water assumption (36%) and the precipitation assumption (37%) produce nearly identical estimates of F_T. Agreement between the two steady-state δ_T assumptions suggests that at this site either technique is a precise approach to measuring forest F_T. The plot-level F_T results (53 ± 3%) agree with other estimates of forest F_T (Berkelhammer et al., 2016; Matheny, Bohrer, Vogel, et al., 2014; Sun et al., 2014; Tsujimura et al., 2007; Zhou et al., 2016). Like non-steady-state F_T, F_T calculated using the either source water or precipitation assumptions exhibits no diurnal variation (Figure 3.7).

Finally, we compare isotopic ET partitioning results with F_T estimated using eddy covariance and sap flux data (Figure 3.7). The sap flux network at this site is extensive and, coupled with eddy covariance data, provides a wide range of information about forest water fluxes including an estimate of F_T. For simplicity, we refer to F_T calculated using eddy covariance and sap flux data as the ecohydrologic ET partitioning technique. Plot-level ecohydrologic F_T was 65 ± 12%; ecohydrologic F_T scaled to include only the transpiration flux from maple, oak, and aspen was 43 ± 9% (Figure 3.7). Agreement between the isotopic and ecohydrologic partitioning techniques was stronger midday (10am to 4pm, 61 ± 8% plot-level F_T; 40 ± 7% F_T for maple, oak, and aspen) when water fluxes were high and weaker in the morning and evening when water fluxes were lower. When F_T from the isotopic and ecohydrologic ET partitioning techniques diverged, the ecohydrologic partitioning technique tended to estimate higher F_T than the isotopic technique (Figure 3.7). Neither partitioning approach revealed a consistent or pronounced daytime F_T cycle.

3.6 Discussion

3.6.1 Isotope data as an indicator of local hydrology

3.6.1.1 Observations of non-steady-state δ_T

It has long been recognized that on timescales longer than the plant-water turnover time the isotopic composition of vapor that is transpired from a leaf must equal the water that enters the leaf from the source (Dongmann et al., 1974). Accordingly, most isotope models assume that transpiration is a non-fractionating process, at least on longer timescales (Farquhar & Cernusak, 2005; Flanagan et al., 1991; Haese et al., 2013; Wang & Yakir, 1995). However, on short timescales (sub-diurnal to a few days) recent observations have revealed that δ_T deviates from steady-state conditions because environmental conditions change quicker than the turnover of plant water (Dubbert et al., 2017; Dubbert, Piayda, et al., 2014; Harwood, Gillon, Griffiths, & Broadmeadow, 1998; Simonin et al., 2013; Wang & Yakir, 1995; Yakir, Berry, Giles, & Osmond, 1994). δ_T varies with abiotic and biotic conditions including stomatal conductance, temperature, humidity, and δ_a (Simonin et al., 2013). At the leaf level, δ_T is also controlled by the transpiration rate, stomatal density, and leaf water content (Buckley, 2019; Dubbert et al., 2017). The Craig and Gordon (1965) model predicts that temperature and humidity are correlated with δ_T (Dongmann et al., 1974; Farquhar et al., 1993; Farquhar & Cernusak, 2005; Farquhar & Lloyd, 1993; Farris & Strain, 1978; Flanagan et al., 1991), which Simonin et al. (2013) confirmed in a leaf-cuvette study and we find to be true in naturally varying conditions (Figure 3.6).

We measured δ_T from three broadleaf deciduous trees but did not find consistent species-specific δ_T patterns (Figure 3.6). In contrast, in a controlled greenhouse, Dubbert et al. (2017) measured δ_T from a variety of herbs, shrubs, and trees and linked δ_T variations to species-specific differences in the transpiration rate, stomatal aperture, stomatal density, and leaf water content. At our field site, oak have an extensive rooting structure and can access a deeper, isotopically more depleted soil water pool than maple, which are shallow rooting (Matheny et al., 2017), although these uptake dynamics may be site-specific (Lanning et al., 2020). We therefore expected that the isotopic composition of xylem, leaf, and transpired water from oaks would be less than that from maples and aspen, but this was only true of xylem and leaf water in August when soil moisture was low. Rain storms on October 4 and October 7 moistened the soil and provided near-surface

moisture for the maple, oak, and aspen trees to transpire. When the soil was drier during the August sampling period, the oak favored a more abundant, deeper, isotopically more negative water source (Matheny et al., 2017). Taken together, these results suggest that when broadleaf deciduous trees are not water stressed species-specific effects on local isotope signals are difficult to identify and distinguish. In contrast, when these trees are water stressed, species-specific differences may be evident in water isotope signals.

3.6.1.2 Surface, terrestrial, and biologic water isotope variability

The isotopic composition of precipitation at UMBS reflects the dominant fractionation processes in northern Michigan, Rayleigh distillation and 'lake-effect' precipitation (Bowen et al., 2012). Previous estimates suggest that up to 32% of precipitation in this region is derived from evaporation over Lake Michigan (Bowen et al., 2012; Gat et al., 1994; Machavaram and Krishnamurthy, 1995). This high degree of moisture recycling explains the high (~13‰) observed precipitation d-excess. The seasonal increase (decrease) of $\delta^{18}O_{lake}$ ($d\text{-}excess_{lake}$) indicates that evaporation of local surface water likely also added vapor with a high d-excess to the atmosphere (Figure 3.4).

The dome-shaped pattern of diurnal δ_l has been observed in many studies and is related to the changes in vapor pressure deficit and transpiration rate (Cernusak et al., 2016 and references therein). Among the broadleaf deciduous trees in this study, the shape and magnitude of the diurnal $\delta^{18}O_l$ pattern was independent of species type and are broadly consistent with common isotopic leaf water models (Farquhar & Cernusak, 2005). The initial, morning isotopic composition of $\delta^{18}O_l$ did, however, vary between the three species and is particularly notable on August 16 ($\delta^{18}O_{l,oak}$, Figure 3.5b and 3.5e) and October 6 ($\delta^{18}O_{l,maple}$, Figure 3.5c and 3.5f). These differences may be related to rooting strategy when the soils are dry (Matheny et al., 2017) or may arise due to the high sand content and low moisture retention of soils that can cause high spatial variability of δ_s or δ_x at the site (He et al., 2013; Nave et al., 2011).

3.6.2 ET partitioning

ET partitioning distinguishes the evaporation and transpiration components of the ET flux and helps provide a quantitative understanding of ecological processes within the water cycle (Jasechko et al., 2013; Kool et al., 2014). Isotopic ET partitioning is predicated on E and T fluxes

of distinct isotopic compositions and accurate estimates of $\delta_{ET,}$ $\delta_{E,}$ and δ_T. Currently, there is no consensus on the best approach to measure the isotopic composition of the ET flux, and researchers use either Keeling mixing models or the flux-gradient technique (Good et al., 2012). The flux-gradient method works best over smooth, homogenous surfaces such as lakes and grasses (Xiao et al., 2017); we chose the Keeling approach to avoid complications of canopy turbulence that may limit the flux-gradient method (Good et al., 2012; Yakir & Wang, 1996). Other ET partitioning studies (e.g., Berkelhammer et al., 2016; Sun et al., 2014; Tsujimura et al., 2007) have also successfully used the Keeling method to calculate δ_{ET} in forested environments, which further justifies our approach to estimating δ_{ET}.

We used the Craig and Gordon (1965) model (Eq. 3.5) to calculate δ_E. Here the challenging factors are an accurate and representative value for the isotopic composition of soil water at the evaporation front and the soil kinetic fractionation factor (Wang et al., 2013; Xiao et al., 2018). We collected soil from the top 10 cm and used δ_s from a single location to estimate the evaporative flux over the entire tower footprint. This approach does not capture the spatial heterogeneity of δ_s (Gazis & Feng, 2004; Hsieh et al., 1998), but is a common approach in most ET partitioning studies (e.g., Aouade et al., 2016; Dubbert et al., 2014; Yepez et al., 2005; Zhang et al., 2011). The closed, thick canopy cover at our field site (Aron et al., 2019) likely reduces spatial variation in δ_s. The kinetic fractionation factor in soil evaporation studies has long been a point of debate and varies with soil tortuosity, soil moisture, and atmospheric conditions (Quade et al., 2018; Xiao et al., 2018). In our study, diurnal soil water content was relatively consistent (varied by less the 0.5 % (m^3 m^{-3}) per day) so we elected to use the constant value for ε_k provided by Quade et al. (2018).

Most isotope-based ET studies assume transpiration is in isotopic-steady state and estimate that δ_T is equal to δ_x or δ_s (e.g., Aouade et al., 2016; Wang and Yakir, 2000; Yepez et al., 2003; Zhang et al., 2011). Instead, in this study we measured δ_T using a leaf chamber to 1) observe any non-steady-state transpiration isotope patterns and 2) evaluate whether direct δ_T measurements affect isotopic ET partitioning. The technical and methodological advancements for this type of measurement have only recently been developed (e.g., Wang et al., 2012) and to date only a handful of studies have used a leaf chamber to measure δ_T and partition F_T (Dubbert, Cuntz, et al., 2014; Good et al., 2014; Lu et al., 2017; Wang et al., 2010, 2013; Wu et al., 2017). However,

nearly all of this work has been done in agricultural fields or grasslands, and still relatively little is known about δ_T (Lanning et al., 2020) and isotope-inferred F_T in forests.

The daytime, plot-level values of F_T reported in this study (53% from the precipitation assumption; 61% from the ecohydrologic technique, Figure 3.7) agree well with other estimates of forest F_T. Berkelhammer et al. (2016) and Tsujimura et al. (2007) used water isotopes to calculate forest F_T values of 49-62% and 60-73%, respectively. Non-isotope ET partitioning techniques reveal similar F_T and range from 52% (Zhou et al., 2016) to ~70-80% (Matheny, Bohrer, Vogel, et al., 2014; Sulman et al., 2016) in deciduous broadleaf forest sites. At our field site, Matheny et al. (2014b) and Aron et al. (2019) demonstrated that ET partitioning is sensitive to forest structure and LAI, with a greater transpiration flux from closed forest canopies and a greater evaporation flux from open forest canopies. The positive relationship between LAI and F_T is also observed in a variety of non-forest environments (Scott & Biederman, 2017; Wang, Good, & Caylor, 2014; Wei et al., 2017), although it is poorly parameterized in most LSMs, with estimates of F_T that are typically lower than expected (Bowen et al., 2019).

In this study, mid-day F_T did not exhibit a consistent cycle regardless of species, steady-state assumption, or partitioning technique (Figure 3.7). Because LAI sets F_T, Wang et al. (2014) proposed that F_T should be relatively consistent throughout the growing season. Although F_T can vary with passing weather systems and precipitation (e.g., Aron et al., 2019; Wen et al., 2016), periods of water stress (Good et al., 2014; Matheny et al., 2017), and the removal of biomass (e.g., harvesting or cutting grass) (Wang, Yamanaka, Li, & Wei, 2015), Berkelhammer et al. (2016) demonstrated that forest F_T was generally invariant on seasonal timescales. We come to the same conclusions on sub-diurnal timescales (Figure 3.7), although this observation may be dependent on vegetation type, aridity, and soil moisture. For example, in arid sites with very low soil moisture, diurnal increases in the transpiration flux may not be accompanied by a concurrent evaporation flux and F_T may increase mid-day (Zhou et al., 2018). However, the absence of a diurnal F_T cycle at our broadleaf deciduous forest site suggests that similar ecological processes and environmental conditions drive the component ET fluxes in this environment as both evaporation and transpiration fluxes are controlled by external environmental factors including vapor pressure deficit, incoming solar radiation, temperature, humidity, wind speed, water availability, and ambient CO_2 concentration as well as a number of internal soil or plant factors

(e.g., tortuosity, available surface area, water potential) (Ball, 1988; Cernusak et al., 2016; Penman, 1948; Sperry et al., 2002; Tyree & Zimmerman, 2002).

Finally, we compare F_T from the isotopic and ecohydrologic partitioning techniques. Isotopic and ecohydrologic derived F_T were similar during the day when ET was high, but results from the two techniques diverged in the early morning and late afternoon when water fluxes were lower. The timing of diurnal sap flux is usually well correlated with incoming solar radiation, temperature, and vapor pressure deficit (Ling et al., 2008). It is therefore possible that the high ecohydrologic F_T in the morning and evening reflects differences in the initiation and termination of early morning and late afternoon diurnal evaporation and transpiration fluxes. However, both steady-state isotopic F_T estimates remained invariant during these times (field logistics and low water fluxes prohibited direct δ_T measurements in the early morning and evening), suggesting that the high morning and afternoon ecohydrologic F_T may be an artefact of sap flux or eddy covariance measurements. To this point, sap flux measurements are known to be biased and prone to errors when water fluxes are low (Ewers & Oren, 2000; Granier, 1987). High ecohydrologic F_T may also be explained by the refilling of dehydrated xylem tissues that does not necessarily result in the release of water to the atmosphere at that time. The mid-day agreement between isotopic non-steady-state, isotopic steady-state, and ecohydrologic partitioning techniques highlights the precision of these different approaches. Despite a multitude of assumptions and simplifications, these techniques capture the same water fluxes that are driven by incoming solar radiation, water availability, and plant hydraulics. Additional ET partitioning techniques such as solar-induced fluorescence (SIF) (Lu et al., 2018; Shan et al., 2019) may soon be available at this site and may yield new insights into the divergent partitioning results in the early morning and late afternoon.

3.6.3 Caveats and experimental considerations

Forests play a critical role in the water cycle and imprint a distinct signature on the isotopic composition of local and regional water cycles. However, measuring forest water fluxes is difficult because forests are heterogeneous, turbulent environments. Accordingly, studies of forest δ_T (e.g., Lanning et al., 2020) and isotopic ET partitioning have lagged behind similar studies in greenhouses or homogenous environments such as croplands and grasslands (e.g., Dubbert et al., 2017; Good et al., 2014). While our experimental approach mitigates this gap, this study was affected by field logistics. For example, we were only able to reach three trees for transpiration

measurements. As a result, F_T from δ_T measurements, the source water assumption, and sap flux scaled to include only the transpiration flux from maples, oaks, and aspen are biased low.

Limitations of the experimental setup are also an important consideration. First, direct δ_T calculations require that a leaf be manually inserted and removed from a sampling chamber, which limits the number of measurements. We likely missed water fluxes before and after our measurement periods. Second, the different measurement heights (5 m for maple, 15 m for aspen and oak) may complicate species-specific observations of δ_T. Although vertical light-induced differences in stomatal conductance and leaf temperature can balance each other (Bögelein et al., 2017), even small differences in measurement location and microclimate within the canopy can strongly affect transpiration and δ_T (Baldocchi et al., 2002; Chen et al., 1999; Jarvis & McNaughton, 1986). Third, scaling isotopic ET partitioning from local measurements to a plot or regional scale remains a challenge given soil heterogeneity, diversity of plant ecophysiology, and a variety of vegetative and canopy structures. Sap flux measurements suffer from similar scaling challenges (Schaeffer et al., 2000), however our field site has an unusually robust sap flux network that has been successfully statistically-scaled to plot-level water fluxes (Matheny, Bohrer, Vogel, et al., 2014). Scaling individual soil and tree isotope measurements to the plot-level remains difficult (Sutanto et al., 2014).

3.6.4 Implications and directions of future work

Moving forward, we show that continuous analysis of δ_a and routine measurements of δ_x or δ_p can efficiently record F_T. Researchers should make measurements for the source water (δ_x) or precipitation (δ_p) approaches based on site-specific characteristics such as species distribution, expected δ_s heterogeneity, and the frequency of precipitation events. Neither approach requires laborious leaf chamber measurements and both are founded on a steady-state assumption about δ_T that is valid for mid-day (Figure 3.7) and seasonal (e.g., Wei et al., 2015) isotopic ET partitioning. In contrast, assumptions of steady-state δ_T may not suffice for questions related to isotope and water cycles on sub-diurnal timescales (e.g., Aron et al., 2019; Simonin et al., 2013; Welp et al., 2012). On this relatively short timescale, non-steady-state δ_T measurements inform how transpiration forces the isotopic composition of atmospheric water vapor and may help validate the Craig and Gordon (1965) model that is commonly used to estimate δ_T and δ_E (e.g., Dubbert et al., 2013; Dubbert et al., 2014; Good et al., 2012; Hu et al., 2014). Additionally, studies that

measure and model δ_T can partition species-specific F_T to learn about species-specific hydrology and responses to environmental conditions. Observation of δ_T may also improve the parameterization of kinetic isotope effects during evaporation and transpiration, which remains a major challenge in isotope ecohydrology research (Quade et al., 2018).

Overall, continued efforts to accurately measure and understand local transpiration are critical to expand our knowledge of continental water recycling and understand the role that plants play in regulating water budgets. This study examines forest ET fluxes; additional observations from environments such as wetlands and tundra are still needed to assess how hydrologic processes are represented in land surface models and to monitor how water and energy fluxes respond to climate and land use change. Currently, almost all LSMs underestimate F_T. Recent and ongoing efforts to incorporate water isotopes into land surface models (e.g., Wong et al., 2017) may improve our understanding of land-atmosphere water fluxes, but these models must be validated with measurements of local δ_T and F_T.

3.7 Conclusions

We present direct, species-specific measurements of $\delta^{18}O_T$ from three broadleaf deciduous trees and estimate the contribution of transpiration to the ET flux in a mixed deciduous forest. The methodology to make δ_T measurements in a field setting is new, and these are among the first δ_T results obtained from a forest environment. $\delta^{18}O_T$ deviated from isotopic steady-state on sub-diurnal timescales but did not exhibit a clear species-specific pattern. Using water isotopes, we found that the F_T was invariant during the day, which indicates similar atmospheric and micrometeorologic conditions control evaporation and transpiration fluxes at this site. We find strong mid-day agreement between isotopic steady-state, isotopic non-steady-state, and ecohydrologic (eddy covariance and sap flux) estimates of F_T, which suggests that assumptions of steady-state δ_T may suffice for other forest ET partitioning studies. Agreement between the isotopic and ecohydrologic partitioning techniques, in particular the absence of a diurnal cycle using either approach, should encourage use of the isotopic ET partitioning method in environments where it is impossible or logistically impractical to install sap flux sensors. Transpiration and evapotranspiration remain challenging fluxes to measure, model, and predict, but water isotopes can help improve our understanding of these important hydrological processes. Future work on non-steady-state δ_T will improve the utility water vapor isotopes as a tool to study

land-atmosphere water exchange while steady-state assumptions of δ_T and isotopic ET partitioning can provide insight into the role of plants in terrestrial water cycling.

Acknowledgements and funding

We thank Chris Vogel for assistance running the isotope analyzers; Luke Nave and Katy Hofmeister for collecting groundwater samples; and Molly Cavaleri and Evan Kane for assistance designing the cryodistillation apparatus. Funding for AmeriFlux data resources was provided by the U.S. Department of Energy's Office of Science. Funding for this study was provided by U.S. Department of Energy's Office of Science, Office of Biological and Environmental Research, Terrestrial Ecosystem Sciences Program Award DE- SC0007041, and the AmeriFlux Management program under Flux Core Site Agreement 7096915 through Lawrence Berkeley National Laboratory. PGA received funding from the University of Michigan Department of Earth and Environmental Sciences, University of Michigan Rackham Graduate School, and the University of Michigan Biological Station. CJP received funding from NSF Tectonics Program Award 1550101. RPF received funding from NSF Macrosystems Biology Early Neon Science Award 1802880. AMM received funding from NSF Hydrological Science grant 1521238. Data associated with this study are archived and freely available from the University of Michigan Biological Station Data Repository (http://biostation.lsa.umich.edu/data).

3.8 References

Aemisegger, F., Sturm, P., Graf, P., Sodemann, H., Pfahl, S., Knohl, A., & Wernli, H. (2012). Measuring variations of $\delta^{18}O$ and $\delta^{2}H$ in atmospheric water vapour using two commercial laser-based spectrometers: an instrument characterisation study. *Atmospheric Measurement Techniques*, *5*, 1491–1511. https://doi.org/10.5194/amt-5-1491-2012

Allen, S. T., Kirchner, J. W., & Goldsmith, G. R. (2018). Predicting Spatial Patterns in Precipitation Isotope ($\delta^{2}H$ and $\delta^{18}O$) Seasonality Using Sinusoidal Isoscapes. *Geophysical Research Letters*, *45*(10), 4859–4868. https://doi.org/10.1029/2018GL077458

Anderegg, W. R. L., Trugman, A. T., Bowling, D. R., Salvucci, G., & Tuttle, S. E. (2019). Plant functional traits and climate influence drought intensification and land – atmosphere feedbacks. *Proceedings of the National Academy of Sciences*, *116*(28), 14071–14076. https://doi.org/10.1073/pnas.1904747116

Aouade, G., Ezzahar, J., Amenzou, N., Er-raki, S., Benkaddour, A., & Khabba, S. (2016). Combining stable isotopes, Eddy Covariance system and meteorological measurements for partitioning evapotranspiration, of winter wheat, into soil evaporation and plant transpiration

in a semi-arid region. *Agricultural Water Management*, *177*, 181–192. https://doi.org/10.1016/j.agwat.2016.07.021

Aron, P. G., Poulsen, C. J., Fiorella, R. P., & Matheny, A. M. (2019). Stable Water Isotopes Reveal Effects of Intermediate Disturbance and Canopy Structure on Forest Water Cycling. *Journal of Geophysical Research: Biogeosciences*, 2958–2975. https://doi.org/10.1029/2019JG005118

Badgley, G., Fisher, J. B., Jimenez, C., Tu, K. P., & Vinukollu, R. (2015). On Uncertainty in Global Terrestrial Evapotranspiration Estimates from Choice of Input Forcing Datasets. *Journal of Hydrometeorology*, *16*, 1449–1455. https://doi.org/10.1175/JHM-D-14-0040.1

Bailey, A., Noone, D., Berkelhammer, M., Steen-Larsen, H. C., & Sato, P. (2015). The stability and calibration of water vapor isotope ratio measurements during long-term deployments. *Atmospheric Measurement Techniques*, *8*(10), 4521–4538. https://doi.org/10.5194/amt-8-4521-2015

Baldocchi, D. D., Wilson, K. B., & Gu, L. (2002). How the environment, canopy structure and canopy physiological functioning influence carbon, water and energy fluxes of a temperate broad-leaved deciduous forest - An assessment with the biophysical model CANOAK. *Tree Physiology*, *22*(15–16), 1065–1077. https://doi.org/10.1093/treephys/22.15-16.1065

Ball, J. T. (1988). *An Analysis of Stomatal Conductance*. Stanford University.

Barbour, M. M. (2007). Review: Stable oxygen isotope composition of plant tissue. *Functional Plant Biology*, *34*, 83–94. https://doi.org/10.1071/FP06228

Berkelhammer, M., Noone, D. C., Wong, T. E., Burns, S. P., Knowles, J. F., Kaushik, A., Blanken, P. D., & Williams, M. W. (2016). Convergent approaches to determine an ecosystem's transpiration fraction. *Global Biogeochemical Cycles*, *30*(6), 933–951. https://doi.org/10.1002/2016GB005392

Bögelein, R., Thomas, F. M., & Kahmen, A. (2017). Leaf water ^{18}O and ^{2}H enrichment along vertical canopy profiles in a broadleaved and a conifer forest tree. *Plant, Cell and Environment*, *40*, 1086–1103. https://doi.org/10.1111/pce.12895

Bowen, G. J., Cai, Z., Fiorella, R. P., & Putman, A. L. (2019). Isotopes in the Water Cycle: Regional- to Global-Scale Patterns and Applications. *Annual Reviews*, *47*, 453–479. https://doi.org/10.1146/annurev-earth-053018- 060220

Bowen, G. J., Kennedy, C. D., Henne, P. D., & Zhang, T. (2012). Footprint of recycled water subsidies downwind of Lake Michigan. *Ecosphere*, *3*(6), 1–16. https://doi.org/10.1890/ES12-00062.1

Brooks, J. R., Barnard, H. R., Coulombe, R., & McDonnell, J. J. (2010). Ecohydrologic separation of water between trees and streams in a Mediterranean climate. *Nature Geoscience*, *3*.

https://doi.org/10.1038/NGEO722

Brutsaert, W. (2017). Advances in Water Resources Global land surface evaporation trend during the past half century : Corroboration by Clausius-Clapeyron scaling. *Advances in Water Resources*, *106*, 3–5. https://doi.org/10.1016/j.advwatres.2016.08.014

Buckley, T. N. (2019). How do stomata respond to water status? *New Phytologist*, *224*, 21–36. https://doi.org/10.1111/nph.15899

Cernusak, L. A., Barbour, M. M., Arndt, S. K., Cheesman, A. W., English, N. B., Feild, T. S., Helliker, B. R., Holloway-Phillips, M. M., Holtum, J. A. M., Kahmen, A., Mcinerney, F. A., Munksgaard, N. C., Simonin, K. A., Song, X., Stuart-Williams, H., West, J. B., & Farquhar, G. D. (2016). Stable isotopes in leaf water of terrestrial plants. *Plant Cell and Environment*, *39*(5), 1087–1102. https://doi.org/10.1111/pce.12703

Chang, L., Dwivedi, R., Knowles, J. F., Fang, Y., Niu, G.-Y., Pelletier, J. D., Rasmussen, C., Durcik, M., Barron-Gafford, G. A., & Meixner, T. (2018). Why Do Large-Scale Land Surface Models Produce a Low Ratio of Transpiration to Evapotranspiration? *Journal Geophysical Research Atmospheres*, *123*, 9109–9130. https://doi.org/10.1029/2018JD029159

Chen, J., Saunders, S. C., Crow, T. R., Naiman, R. J., Kimberley, D., Mroz, G. D., Brookshire, B. L., Franklin, J. F., Chen, J., Saunders, S. C., Crow, T. R., Naiman, R. J., Brosofske, K. D., Mroz, G. D., Brookshire, B. L., & Franklin, J. F. (1999). Microclimate in Forest Ecosystem and Landscape Ecology. *BioScience*, *49*(4), 288–297. https://doi.org/10.2307/1313612

Coplen, T. B. (1996). New guidelines for reporting stable hydrogen, carbon, and oxygen isotope-ratio data. *Geochimica et Cosmochimica Acta*, *60*(17), 3359–3360.

Craig, H., & Gordon, L. I. (1965). Deuterium and oxygen-18 variations in the ocean and the marine atmosphere. In E. Tongiorgi (Ed.), *Proceedings of a Conference on Stable Isotopes in Oceanographic Studies and Paleotemperatures* (pp. 9–130).

Craig, Harold. (1961). Isotopic Variations in Meteoric Waters. *Science*, *133*(3465), 1702–1703. https://doi.org/10.1126/science.133.3465.1702

Dansgaard, W. (1964). Stable isotopes in precipitation. *Tellus*, *16*(4), 436–468. https://doi.org/10.3402/tellusa.v16i4.8993

Dongmann, G., Nürnberg, H. W., Forstel, H., & Wagener, K. (1974). On the Enrichment of $H_2{}^{18}O$ in the Leaves of Transpiring Plants. *Radiation and Environmental Biophysics*, *11*, 41–52.

Dubbert, M., Cuntz, M., Piayda, A., Maguás, C., & Werner, C. (2013). Partitioning evapotranspiration – Testing the Craig and Gordon model with field measurements of oxygen isotope ratios of evaporative fluxes. *Journal of Hydrology*, *496*, 142–153. https://doi.org/10.1016/j.jhydrol.2013.05.033

Dubbert, M., Cuntz, M., Piayda, A., & Werner, C. (2014). Oxygen isotope signatures of transpired water vapor: the role of isotopic non-steady-state transpiration under natural conditions. *New Phytologist*, *203*, 1242–1252. https://doi.org/10.1111/nph.12878

Dubbert, M., Kübert, A., & Werner, C. (2017). Impact of Leaf Traits on Temporal Dynamics of Transpired Oxygen Isotope Signatures and Its Impact on Atmospheric Vapor. *Frontiers in Plant Science*, *8*(January), 1–12. https://doi.org/10.3389/fpls.2017.00005

Dubbert, M., Piayda, A., Cuntz, M., Correia, A. C., Silva, F. C. e., Pereira, J. S., & Werner, C. (2014). Stable oxygen isotope and flux partitioning demonstrates understory of an oak savanna contributes up to half of ecosystem carbon and water exchange. *Frontiers in Plant Science*, *5*, 1–16. https://doi.org/10.3389/fpls.2014.00530

Dunn, S. M., & Mackay, R. (1995). Spatial variation in evapotranspiration and the influence of land use on catchment hydrology. *Journal of Hydrology*, *171*, 49–73.

Ehleringer, J. R., & Dawson, T. E. (1992). Water uptake by plants: perspectives from stable isotope composition. *Plant, Cell and Environment*, *15*, 1073–1082. https://doi.org/10.1111/j.1365-3040.1992.tb01657.x

Ellison, D., Morris, C. E., Locatelli, B., Sheil, D., Cohen, J., Murdiyarso, D., Gutierrez, V., Noordwijk, M. van, Creed, I. F., Pokorny, J., Gaveau, D., Spracklen, D. V., Tobella, A. B., Ilstedt, U., Teuling, A. J., Gebrehiwot, S. G., Sands, D. C., Muys, B., Verbist, B., … Sullivan, C. A. (2017). Trees, forests and water: Cool insights for a hot world. *Global Environmental Change*, *43*, 51–61. https://doi.org/10.1016/j.gloenvcha.2017.01.002

Evaristo, J., Jasechko, S., & Mcdonnell, J. J. (2015). Global separation of plant transpiration from groundwater and streamflow. *Nature*, *525*, 91–94. https://doi.org/10.1038/nature14983

Ewers, B. E., & Oren, R. A. M. (2000). Analyses of assumptions and errors in the calculation of stomatal conductance from sap flux measurements. *Tree Physiology*, *20*, 579–589.

Fang, Y., Leung, L. R., Duan, Z., Wigmosta, M. S., Maxwell, R. M., Chambers, J. Q., & Tomasella, J. (2017). Influence of landscape heterogeneity on water available to tropical forests in an Amazonian catchment and implications for modeling drought response. *Journal Geophysical Research Atmospheres*, *122*, 8410–8426. https://doi.org/10.1002/2017JD027066

Farquhar, G. D., & Cernusak, L. A. (2005). On the isotopic composition of leaf water in the non-steady state. *Functional Plant Biology, 32*(1974), 293–303. https://doi.org/10.1071/FP04232

Farquhar, G. D., & Lloyd, J. (1993). Carbon and Oxygen Isotope Effects in the Exchange of Carbon Dioxide between Terrestrial Plants and the Atmosphere. In James R. Ehleringer, A. Hall, & G. D. Farquhar (Eds.), *Stable Isotopes and Plant Carbon-Water Relations* (pp. 47–70). Academic Press, Inc. https://doi.org/10.1016/B978-0-08-091801-3.50011-8

Farquhar, G. D., Lloyd, J., Taylort, J. A., Flanagan, L. B., Syvertsen, J. P., Hubick, K. T., Wong, S. C., & Ehleringerll, J. R. (1993). Vegetation effects on the isotope composition of oxygen in atmospheric CO2. *Nature*, *363*, 439–443.

Farris, F., & Strain, B. R. (1978). The Effects of Water-Stress on Leaf $H_2{}^{18}O$ Enrichment. *Radiation and Environmental Biophysics*, *15*, 167–202.

Fiorella, R. P., Bares, R., Lin, J. C., Ehleringer, J. R., & Bowen, G. J. (2018). Detection and variability of combustion-derived vapor in an urban basin. *Atmospheric Chemistry and Physics*, *18*(12), 8529–8547. https://doi.org/10.5194/acp-18-8529-2018

Flanagan, L. B., Comstock, J. P., Ehleringer, J. R., Flanagan, L. B., Comstock, J. P., & Ehieringer, J. R. (1991). Comparison of Modeled and Observed Environmental Influences on the Stable Oxygen and Hydrogen Isotope Composition of Leaf Water in Phaseolus vulgaris L . *Plant Physiology*, *96*(2), 588–596.

Frank, D. C., Poulter, B., Saurer, M., Esper, J., Huntingford, C., Helle, G., & Treydte, K. (2015). Water-use efficiency and transpiration across European forests during the Anthropocene. *Nature Climate Change*, *5*, 579–584. https://doi.org/10.1038/NCLIMATE2614

Friedman, I., Smith, G. I., Gleason, J. D., Warden, A., & Harris, J. M. (1992). Stable Isotope Composition of Waters in Southeastern California 1. Modern Precipitation. *Journal of Geophysical Research*, *97*(D5), 5795–5812.

Gat, J. (1996). Oxygen and hydrogen isotopes in the hydrologic cycle. *Annual Review of Earth and Planetary Sciences*, *24*, 225–262. https://doi.org/10.1146/annurev.earth.24.1.225

Gat, J. R., Bowser, C. J., & Kendall, C. (1994). The contribution of evaporation from the Great Lakes to the continental atmosphere: estimate based on stable isotope data. *Geophysical Research Letters*, *21*(7), 557–560. https://doi.org/10.1029/94GL00069

Gazis, C., & Feng, X. (2004). A stable isotope study of soil water: evidence for mixing and preferential flow paths. *Geoderma*, *119*, 97–111. https://doi.org/10.1016/S0016-7061(03)00243-X

Gedney, N., Cox, P. M., Betts, R. A., Boucher, O., Huntingford, C., & Stott, P. A. (2006). Detection of a direct carbon dioxide effect in continental river runoff records. *Nature*, *439*, 835–838. https://doi.org/10.1038/nature04504

Good, S. P., Noone, D., & Bowen, G. (2015). Hydrologic connectivity constrains partitioning of global terrestrial water fluxes. *Science*, *349*(6244), 175–178.

Good, S. P., Soderberg, K., Guan, K., King, E. G., Scanlon, T. M., & Caylor, K. K. (2014). δ^2H isotopic flux partitioning of evapotranspiration over a grass field following a water pulse and subsequent dry down. *Water Resources Research*, *50*, 1410–1432. https://doi.org/10.1002/2013WR014333

Good, S. P., Soderberg, K., Wang, L., & Caylor, K. K. (2012). Uncertainties in the assessment of the isotopic composition of surface fluxes: A direct comparison of techniques using laser-based water vapor isotope analyzers. *Journal of Geophysical Research Atmospheres*, *117*(15), 1–22. https://doi.org/10.1029/2011JD017168

Gough, C. M., Hardiman, B. S., Nave, L. E., Bohrer, G., Maurer, K. D., Vogel, C. S., Nadelhoffer, K. J., & Curtis, P. S. (2013). Sustained carbon uptake and storage following moderate disturbance in a Great Lakes forest. *Ecological Applications*, *23*(5), 1202–1215. https://doi.org/10.1890/12-1554.1

Granier, A. (1987). Evaluation of transpiration in a Douglas-fir stand by means of sap flow measurements. *Tree Physiology*, *3*(4), 309–320. https://doi.org/10.1093/treephys/3.4.309

Granier, Andre, & Loustau, D. (1994). Measuring and modelling the transpiration of a maritime pine canopy from sap-flow data. *Agricultural and Forest Meteorology*, *71*, 61–81. https://doi.org/10.1016/0168-1923(94)90100-7

Haese, B., Werner, M., & Lohmann, G. (2013). Stable water isotopes in the coupled atmosphere-land surface model ECHAM5-JSBACH. *Geoscientific Model Development*, *6*(5), 1463–1480. https://doi.org/10.5194/gmd-6-1463-2013

Harwood, K. G., Gillon, J. S., Griffiths, H., & Broadmeadow, M. S. J. (1998). Diurnal variation of $\Delta^{13}CO_2$, $\Delta^{18}O^{16}O$ and evaporative site enrichment of $\delta H_2{}^{18}O$ in Piper aduncum under field conditions in Trinidad. *Plant, Cell and Environment*, *21*(3), 269–283. https://doi.org/10.1046/j.1365-3040.1998.00276.x

He, L., Ivanov, V. Y., Bohrer, G., Thomsen, J. E., Vogel, C. S., & Moghaddam, M. (2013). Temporal dynamics of soil moisture in a northern temperate mixed successional forest after a prescribed intermediate disturbance. *Agricultural and Forest Meteorology*, *180*, 22–33. https://doi.org/10.1016/j.agrformet.2013.04.014

Hendricks, S., Vande Kopple, R., Goodspeed, P., & White, D. (2016). Groundwater Connectivity between Douglas Lake and Carp Creek Based on Fluorescein Dye Studies. *Michigan Academician*, *43*(3), 380–392. https://doi.org/10.7245/0026-2005-43.3.380

Hsieh, J. C. C., Chadwick, O. A., Kelly, E. F., & Savin, S. M. (1998). Oxygen isotopic composition of soil water: Quantifying evaporation and transpiration. *Geoderma*, *82*, 269–293. https://doi.org/10.1016/S0016-7061(97)00105-5

Hu, Z., Wen, X., Sun, X., Li, L., Yu, G., Lee, X., & Li, S. (2014). Partitioning of evapotranspiration through oxygen isotopic measurements of water pools and fluxes in a temperate grassland. *Journal Geophysical Research Biogeosciences*, *119*, 358–371. https://doi.org/10.1002/2013JG002367.Received

Jackson, R. B., Carpenter, S. R., Dahm, C. N., McKnicht, D. M., Naiman, R. J., Postel, S. L., &

Running, S. W. (2001). Water in a Changing World. *Ecological Applications*, *11*(4), 1027–1045.

Jarvis, P. G., & McNaughton, K. G. (1986). Stomatal Control of Transpiration: Scaling Up from Leaf to Region. *Advances in Ecological Research*, *15*, 1–49. https://doi.org/10.1016/S0065-2504(08)60119-1

Jasechko, S., Sharp, Z. D., Gibson, J. J., Birks, S. J., Yi, Y., & Fawcett, P. J. (2013). Terrestrial water fluxes dominated by transpiration. *Nature*, *496*(7445), 347–350. https://doi.org/10.1038/nature11983

Ji, P., Yuan, X., & Liang, X.-Z. (2017). Do Lateral Flows Matter for the Hyperresolution Land Surface Modeling? *Journal Geophysical Research Atmospheres*, *122*, 12077–12092. https://doi.org/10.1002/2017JD027366

Kauwe, M. G. De, Medlyn, B. E., Knauer, J., & Williams, C. A. (2017). Ideas and perspectives: how coupled is the vegetation to the boundary layer ? *Biogeosciences*, *14*, 4435–4453. https://doi.org/10.5194/bg-14-4435-2017

Keeling, D. (1958). The concentration and isotopic abundances of atmospheric carbon dioxide in rural areas. *Geochimica et Cosmochimica Acta*, *13*, 322–334.

Kool, D., Agam, N., Lazarovitch, N., Heitman, J. L., Sauer, T. J., & Ben-gal, A. (2014). A review of approaches for evapotranspiration partitioning. *Agricultural and Forest Meteorology*, *184*, 56–70. https://doi.org/10.1016/j.agrformet.2013.09.003

Labat, D., Godd, Y., Probst, J. L., & Guyot, J. L. (2004). Evidence for global runoff increase related to climate warming. *Advances in Water Resources*, *27*, 631–642. https://doi.org/10.1016/j.advwatres.2004.02.020

Lai, C., Ehleringer, J. R., Bond, B. J., & Paw, K. (2006). Contributions of evaparation, isotopic non-stedy state transpiration and atmospheric mixing on the $\delta^{18}O$ of water vapour in Pacific Northewest coniferous forests. *Plant Cell Environ.*, *29*, 77–94. https://doi.org/10.1111/j.1365-3040.2005.01402.x

Lanning, M., Wang, L., Benson, M., Zhang, Q., & Novick, K. A. (2020). Canopy isotopic investigation reveals different water uptake dynamics of maples and oaks. *Phytochemistry*, *175*(October 2019), 112389. https://doi.org/10.1016/j.phytochem.2020.112389

Lee, X., Kim, K., & Smith, R. (2007). *Temporal variations of the $^{18}O/^{16}O$ signal of the whole-canopy transpiration in a temperate forest*. *21*(August), 1–12. https://doi.org/10.1029/2006GB002871

Ling, M., Ping, L., Ping, Z., Xing-quan, R., Xi-an, C., & Xiao-ping, Z. (2008). Diurnal, daily, seasonal and annual patterns of sap-flux-scaled transpiration from an Acacia mangium plantation in South China. *Annals of Forest Science*, *65*, 402–410.

https://doi.org/10.1051/forest:2008013

Lu, Xiaoliang, Liu, Z., An, S., Miralles, D. G., Maes, W., Liu, Y., & Tang, J. (2018). Potential of solar-induced chlorophyll fluorescence to estimate transpiration in a temperate forest. *Agricultural and Forest Meteorology*, *252*(January), 75–87. https://doi.org/10.1016/j.agrformet.2018.01.017

Lu, Xuefei, Liang, L. L., Wang, L., Jenerette, G. D., Mccabe, M. F., & Grantz, D. A. (2017). Partitioning of evapotranspiration using a stable isotope technique in an arid and high temperature agricultural production system. *Agricultural Water Management*, *179*, 103–109. https://doi.org/10.1016/j.agwat.2016.08.012

Machavaram, M. V, & Krishnamurthy, R. V. (1995). Earth surface evaporative process: A case study from the Great Lakes region of the United States based on deuterium excess in precipitation. *Geochimica et Cosmochimica Acta*, *6*(20), 4279–4283.

Majoube, M. (1971). Oxygen-18 and deuterium fractionation between water and steam. *Journal of Chemical Physics*, *68*, 1432–1436.

Mao, J., Shi, X., Mao, J., Thornton, P. E., Forbes, W. L., Mao, J., Fu, W., Shi, X., Ricciuto, D. M., Fisher, J. B., & Dickinson, R. E. (2015). Disentangling climatic and anthropogenic controls on global terrestrial evapotranspiration trends. *Environmental Research Letters*, *10*(9), 094008. https://doi.org/10.1088/1748-9326/10/9/094008

Massmann, A., Gentine, P., & Lin, C. (2019). When does vapor pressure deficit drive or reduce evapotranspiration? *Journal of Advances in Modeling Earth Systems*, 1–27. https://doi.org/10.1029/2019MS001790

Matheny, A. M., Bohrer, G., Stoy, P. C., Baker, I. T., Black, A. T., Desai, A. R., Dietze, M. C., Gough, C. M., Ivanov, V. Y., Jassal, R. S., Novick, K. A., Schäfer, K. V. R., & Verbeeck, H. (2014). Characterizing the diurnal patterns of errors in the prediction of evapotranspiration by several land-surface models: An NACP analysis. *Journal of Geophysical Research: Biogeosciences*, *119*(7), 1458–1473. https://doi.org/10.1002/2014JG002623

Matheny, A. M., Bohrer, G., Vogel, C. S., Morin, T. H., He, L., Frasson, R. P. D. M., Mirfenderesgi, G., Schäfer, K. V. R., Gough, C. M., Ivanov, V. Y., & Curtis, P. S. (2014). Species-specific transpiration responses to intermediate disturbance in a northern hardwood forest. *Journal of Geophysical Research: Biogeosciences*, *119*, 2292–2311. https://doi.org/10.1002/2014JG002804

Matheny, A. M., Fiorella, R. P., Bohrer, G., Poulsen, C. J., Morin, T. H., Wunderlich, A., Vogel, C. S., & Curtis, P. S. (2017). Contrasting strategies of hydraulic control in two codominant temperate tree species. *Ecohydrology*, *10*(3), 1–16. https://doi.org/10.1002/eco.1815

Maxwell, R. M., & Condon, L. E. (2016). Connections between groundwater flow and transpiration partitioning. *Science*, *353*(6297), 377–380.

https://doi.org/10.1126/science.aaf7891

McDonnell, J. J. (2014). The two water worlds hypothesis: ecohydrological separation of water between streams and trees? *Wiley Interdisciplinary Reviews: Water*, *1*(4), 323–329. https://doi.org/10.1002/wat2.1027

Moreira, M., Sternberg, L., Martinelli, L., Victoria, R., Barbosa, E., Bonates, L., & Nepstad, D. (1997). Contribution of transpiration to forest ambient vapour based on isotopic measurements. *Global Change Biology*, *3*(5), 439–450. https://doi.org/10.1046/j.1365-2486.1997.00082.x

Mueller, B., Hirschi, M., Jimenez, C., Ciais, P., Dirmeyer, P. A., Dolman, A. J., Fisher, J. B., Jung, M., Ludwig, F., & Seneviratne, S. I. (2013). Benchmark products for land evapotranspiration: LandFlux-EVAL multi-data set synthesis. *Hydrology and Earth System Sciences*, *17*, 3707–3720. https://doi.org/10.5194/hess-17-3707-2013

Nave, L. E., Gough, C. M., Maurer, K. D., Bohrer, G., Hardiman, B. S., Le Moine, J., Munoz, A. B., Nadelhoffer, K. J., Sparks, J. P., Strahm, B. D., Vogel, C. S., & Curtis, P. S. (2011). Disturbance and the resilience of coupled carbon and nitrogen cycling in a north temperate forest. *Journal of Geophysical Research: Biogeosciences*, *116*(4), 1–14. https://doi.org/10.1029/2011JG001758

Ohmura, A., & Wild, M. (2002). Is the Hydrological Cycle Accelerating? *Science*, *298*, 1345–1347. https://doi.org/10.1126/science.1078972

Penman, H. L. (1948). Natural evaporation from open water, bare soil and grass. *PROCEEDINGS OF THE ROYAL SOCIETY OF LONDON SERIES A-MATHEMATICAL AND PHYSICAL SCIENCES*, *193*(1032), 120–145. https://doi.org/10.1098/rspa.1948.0037

Phillps, N., & Oren, R. (1998). A comparison of daily representations of canopy conductance based on two conditional time-averaging methods and the dependence of daily conductance on environmental factors. *Annals of Forest Science*, *55*, 217–235. https://doi.org/10.1051/forest:19980113

Putman, A. L., Fiorella, R. P., Bowen, G. J., & Cai, Z. (2019). A Global Perspective on Local Meteoric Water Lines: Meta-analytic Insight Into Fundamental Controls and Practical Constraints. *Water Resources Research*, *55*, 6896–6910. https://doi.org/10.1029/2019WR025181

Quade, M., Brüggemann, N., Graf, A., Vereecken, H., & Rothfuss, Y. (2018). *Investigation of Kinetic Isotopic Fractionation of Water During Bare Soil Evaporation*. *1978*, 6909–6928. https://doi.org/10.1029/2018WR023159

Schaeffer, S. M., Williams, D. G., & Goodrich, D. C. (2000). Transpiration of cottonwood/willow forest estimated from sap flux. *Agricultural and Forest Meteorology*, *105*, 257–270.

Schlesinger, W. H., & Jasechko, S. (2014). Transpiration in the global water cycle. *Agricultural and Forest Meteorology*, *189–190*, 115–117. https://doi.org/10.1016/j.agrformet.2014.01.011

Scholl, M. A., Ingebritsen, S. E., Janik, C. J., & Kauahikaua, J. P. (1996). Use of precipitation and groundwater isotopes to interpret regional hydrology on a tropical volcanic island: Kilauea volcano area, Hawaii. *Water Resources Research*, *32*(12), 3525–3537.

Scott, R. L., & Biederman, J. A. (2017). Partitioning evapotranspiration using long-term carbon dioxide and water vapor fluxes. *Geophysical Research Letters*, *44*, 6833–6840. https://doi.org/10.1002/2017GL074324

Shan, N., Ju, W., Migliavacca, M., Martini, D., Guanter, L., Chen, J., Goulas, Y., & Zhang, Y. (2019). Modeling canopy conductance and transpiration from solar-induced chlorophyll fluorescence. *Agricultural and Forest Meteorology*, *268*(February 2018), 189–201. https://doi.org/10.1016/j.agrformet.2019.01.031

Simonin, K. A., Roddy, A. B., Link, P., Apodaca, R., Tu, K. P., Hu, J., Dawson, T. E., & Barbour, M. M. (2013). Isotopic composition of transpiration and rates of change in leaf water isotopologue storage in response to environmental variables. *Plant, Cell and Environment*, *36*(12), 2190–2206. https://doi.org/10.1111/pce.12129

Spangenberg, J. E. (2012). Caution on the storage of waters and aqueous solutions in plastic containers for hydrogen and oxygen stable isotope analysis. *Rapid Communications in Mass Spectrometry*, *26*, 2627–2636. https://doi.org/10.1002/rcm.6386

Sperry, J. S., Hacke, U. G., Oren, R., & Comstock, J. P. (2002). Water deficits and hydraulic limits to leaf water supply. *Plant Cell and Environment*, *25*, 251–263.

Starkenburg, D., Metzger, S., Fochesatto, G. J., Alfieri, J. G., Gens, R., Prakash, A., & Crisobal, J. (2016). Assessment of Despiking Methods for Turbulence Data in Micrometeorology. *Journal of Atmospheric and Oceanic Technology*, *33*, 2001–2013. https://doi.org/10.1175/JTECH-D-15-0154.1

Stoy, P. C., El-madany, T. S., Fisher, J. B., Gentine, P., Gerken, T., & Good, S. P. (2019). Reviews and syntheses: Turning the challenges of partitioning ecosystem evaporation and transpiration into opportunities. *Biogeosciences*, *16*, 3747–3775. https://doi.org/10.5194/bg-16-3747-2019

Sulman, B. N., Roman, D. T., Scanlon, T. M., Wang, L., & Novick, K. A. (2016). Comparing methods for partitioning a decade of carbon dioxide and water vapor fluxes in a temperate forest. *Agricultural and Forest Meteorology*, *226–227*, 229–245. https://doi.org/10.1016/j.agrformet.2016.06.002

Sun, S., Meng, P., Zhang, J., Wan, X., Zheng, N., & He, C. (2014). Partitioning oak woodland evapotranspiration in the rocky mountainous area of North China was disturbed by foreign vapor, as estimated based on non-steady-state ^{18}O isotopic composition. *Agricultural and*

Forest Meteorology, *184*, 36–47. https://doi.org/10.1016/j.agrformet.2013.08.006

Sutanto, S. J., Van Den Hurk, B., Dirmeyer, P. A., Seneviratne, S. I., Röckmann, T., Trenberth, K. E., Blyth, E. M., Wenninger, J., & Hoffmann, G. (2014). HESS Opinions "a perspective on isotope versus non-isotope approaches to determine the contribution of transpiration to total evaporation." *Hydrology and Earth System Sciences*, *18*(8), 2815–2827. https://doi.org/10.5194/hess-18-2815-2014

Swann, A. L. S., Fung, I. Y., & Chiang, J. C. H. (2012). Mid-latitude afforestation shifts general circulation and tropical precipitation. *Proceedings of the National Academy of Sciences*, *109*(3), 712–716. https://doi.org/10.1073/pnas.1116706108

Talsma, C. J., Good, S. P., Jimenez, C., Martens, B., Fisher, J. B., Miralles, D. G., Mccabe, M. F., & Purdy, A. J. (2018). Partitioning of evapotranspiration in remote sensing-based models. *Agricultural and Forest Meteorology*, *260–261*, 131–143. https://doi.org/10.1016/j.agrformet.2018.05.010

Tsujimura, M., Sasaki, L., Yamanaka, T., Sugimoto, A., Li, S., Matsushima, D., Kotani, A., & Saandar, M. (2007). Vertical distribution of stable isotopic composition in atmospheric water vapor and subsurface water in grassland and forest sites, eastern Mongolia. *Journal of Hydrology*, *333*, 35–46. https://doi.org/10.1016/j.jhydrol.2006.07.025

Tyree, M. T., & Zimmerman, M. H. (2002). *Xylem Structure and the Ascent of Sap* (S.-V. N. Y. Inc. (ed.)). Springer.

Vinukollu, R. K., Meynadier, R., Shef, J., & Wood, E. F. (2011). Multi-model, multi-sensor estimates of global evapotranspiration: climatology, uncertainties and trends. *Hydrological Processes*, *25*, 3993–4010. https://doi.org/10.1002/hyp.8393

Wang, L., Caylor, K. K., Villegas, J. C., Barron-Gafford, G. A., Breshears, D. D., & Huxman, T. E. (2010). Partitioning evapotranspiration across gradients of woody plant cover: Assessment of a stable isotope technique. *Geophysical Research Letters*, *37*(9), 1–7. https://doi.org/10.1029/2010GL043228

Wang, L., Good, S. P., & Caylor, K. K. (2014). Global synthesis of vegetation control on evapotranspiration partitioning. *Geophysical Research Letters*, *41*, 6753–6757. https://doi.org/10.1002/2014GL061439

Wang, L., Good, S. P., Caylor, K. K., & Cernusak, L. A. (2012). Direct quantification of leaf transpiration isotopic composition. *Agricultural and Forest Meteorology*, *154–155*, 127–135. https://doi.org/10.1016/j.agrformet.2011.10.018

Wang, L., Niu, S., Good, S. P., Soderberg, K., Mccabe, M. F., Sherry, R. A., Luo, Y., Zhou, X., Xia, J., & Caylor, K. K. (2013). The effect of warming on grassland evapotranspiration partitioning using laser-based isotope monitoring techniques. *Geochimica et Cosmochimica Acta*, *111*, 28–38. https://doi.org/10.1016/j.gca.2012.12.047

Wang, P., Yamanaka, T., Li, X., & Wei, Z. (2015). Partitioning evapotranspiration in a temperate grassland ecosystem: Numerical modeling with isotopic tracers. *Agricultural and Forest Meteorology*, *208*, 16–31. https://doi.org/10.1016/j.agrformet.2015.04.006

Wang, X. F., & Yakir, D. (2000). Using stable isotopes of water in evapotranspiration studies. *Hydrological Processes*, *14*(8), 1407–1421. https://doi.org/10.1002/1099-1085(20000615)14:8<1407::AID-HYP992>3.0.CO;2-K

Wang, X., & Yakir, D. (1995). Temporal and spatial variations in the oxygen-18 content of leaf water in different plant species. *Plant, Cell and Environment*, *18*, 1377–1385.

Webb, E. K., Pearman, G. ., & Leuning, R. (1980). Correction of flux measurements for density effects due to heat and water vapour transfer. *Quarterly Journal of the Royal Meteorological Society*, *106*, 85–100. https://doi.org/10.1002/qj.49710644707

Wei, Z., Yoshimura, K., Okazaki, A., Kim, W., Liu, Z., & Yokoi, M. (2015). Partitioning of evapotranspiration using high-frequency water vapor isotopic measurement over a rice paddy field. *Water Resources Research*, *51*, 3716–3729. https://doi.org/10.1002/ 2014WR016737

Wei, Z., Yoshimura, K., Wang, L., Miralles, D. G., Jasechko, S., & Lee, X. (2017). Revisiting the contribution of transpiration to global terrestrial evapotranspiration. *Geophysical Research Letters*, *44*, 2792–2801. https://doi.org/10.1002/2016GL072235

Welp, L. R., Lee, X., Griffis, T. J., Wen, X. F., Xiao, W., Li, S., Sun, X., Hu, Z., Val Martin, M., & Huang, J. (2012). A meta-analysis of water vapor deuterium-excess in the midlatitude atmospheric surface layer. *Global Biogeochemical Cycles*, *26*(3), 1–12. https://doi.org/10.1029/2011GB004246

Wen, X., Yang, B., Sun, X., & Lee, X. (2016). Evapotranspiration partitioning through in-situ oxygen isotope measurements in an oasis cropland. *Agricultural and Forest Meteorology*, *230–231*, 89–96. https://doi.org/10.1016/j.agrformet.2015.12.003

West, A. G., Goldsmith, G. R., Brooks, P. D., & Dawson, T. E. (2010). Discrepancies between isotope ratio infrared spectroscopy and isotope ratio mass spectrometry for the stable isotope analysis of plant and soil waters. *Rapid Communications in Mass Spectrometry*, *24*, 1948–1954. https://doi.org/10.1002/rcm.4597

West, A. G., Patrickson, S. J., & Ehleringer, J. R. (2006). Water extraction times for plant and soil materials used in stable isotope analysis. *Rapid Communications in Mass Spectrometry*, *20*, 1317–1321. https://doi.org/10.1002/rcm.2456

Williams, D. G., Cable, W., Hultine, K., Hoedjes, J. C. B., Yepez, E. A., Simonneaux, V., Er-raki, S., Boulet, G., Bruin, H. A. R. De, & Chehbouni, A. (2004). Evapotranspiration components determined by stable isotope, sap flow and eddy covariance techniques. *Agricultural and Forest Meteorology*, *125*, 241–258. https://doi.org/10.1016/j.agrformet.2004.04.008

Wong, T. E., Nusbaumer, J., & Noone, D. C. (2017). Evaluation of modeled land-atmosphere exchanges with a comprehensive water isotope fractionation scheme in version 4 of the Community Land Model. *Journal of Advances in Modeling Earth Systems*, *9*(2), 978–1001. https://doi.org/10.1002/2016MS000842

Worden, J., Noone, D., & Bowman, K. (2007). Importance of rain evaporation and continental convection in the tropical water cycle. *Nature*, *445*(February). https://doi.org/10.1038/nature05508

Wu, Y., Du, T., Ding, R., Tong, L., & Li, S. (2017). Multiple Methods to Partition Evapotranspiration in a Maize Field. *Journal of Hydrometeorology*, *18*, 139–149. https://doi.org/10.1175/JHM-D-16-0138.1

Xiao, W., Lee, X., Hu, Y., Lui, S., Wang, W., Wen, X., Werner, M., & Xie, C. (2017). An Experimental Investigation of Kinetic Fractionation of Open-Water Evaporation Over a Large Lake. *Journal Geophysical Research Atmospheres*, *122*(11), 651–663. https://doi.org/10.1002/2017JD026774

Xiao, W., Wei, Z., & Wen, X. (2018). Evapotranspiration partitioning at the ecosystem scale using the stable isotope method—A review. *Agricultural and Forest Meteorology*, *263*(November 2017), 346–361. https://doi.org/10.1016/j.agrformet.2018.09.005

Yakir, D, Berry, J. A., Giles, L., & Osmond, C. B. (1994). Isotopic heterogeneity of water in transpiring ieaves: identification of the component that controls the $\delta^{18}O$ of atmospheric O_2 and CO_2. *Plant Cell and Environment*, *17*, 73–80.

Yakir, Dan, & Sternberg, S. L. (2000). The use of stable isotopes to study ecosystem gas exchange. *Oecologia*, *123*, 297–311.

Yakir, Dan, & Wang, X.-F. (1996). Fluxes of CO_2 and H_2O between terrestrial vegetation and the atmosphere. *Nature*, *380*, 515–517.

Yepez, E. A., Huxman, T. E., Ignace, D. D., English, N. B., Weltzin, J. F., Castellanos, A. E., & Williams, D. G. (2005). *Dynamics of transpiration and evaporation following a moisture pulse in semiarid grassland: A chamber-based isotope method for partitioning flux components*. *132*, 359–376. https://doi.org/10.1016/j.agrformet.2005.09.006

Yepez, E. A., Williams, D. G., Scott, R. L., & Lin, G. (2003). Partitioning overstory and understory evapotranspiration in a semiarid savanna woodland from the isotopic composition of water vapor. *Agricultural and Forest Meteorology*, *119*(1–2), 53–68. https://doi.org/10.1016/S0168-1923(03)00116-3

Zeng, Z., Piao, S., Li, L. Z. X., Wang, T., Ciais, P., Lian, X., Yang, Y., Mao, J., Shi, X., & Myneni, R. B. (2018). Impact of Earth Greening on the Terrestrial Water Cycle. *Journal of Climate*, *31*, 2633–2650. https://doi.org/10.1175/JCLI-D-17-0236.1

Zhang, Yongqiang, Peña-Arancibia, J. L., McVicar, T. R., Chiew, F. H. S., Vaze, J., Liu, C., Lu, X., Zheng, H., Wang, Y., Liu, Y. Y., Miralles, D. G., & Pan, M. (2016). Multi-decadal trends in global terrestrial evapotranspiration and its components. *Scientific Reports*, *6*(19124), 1–12. https://doi.org/10.1038/srep19124

Zhang, Yucui, Shen, Y., Sun, H., & Gates, J. B. (2011). Evapotranspiration and its partitioning in an irrigated winter wheat field: A combined isotopic and micrometeorologic approach. *Journal of Hydrology*, *408*(3–4), 203–211. https://doi.org/10.1016/j.jhydrol.2011.07.036

Zhou, S., Yu, B., Zhang, Y., Huang, Y., & Wang, G. (2016). Partitioning evapotranspiration based on the concept of underlying water use efficiency. *Water Resources Research*, *52*, 1160–1175. https://doi.org/10.1002/2015WR017766.Received

Zhou, S., Yu, B., Zhang, Y., Huang, Y., & Wang, G. (2018). Water use efficiency and evapotranspiration partitioning for three typical ecosystems in the Heihe River Basin, northwestern China. *Agricultural and Forest Meteorology*, *253–254*(February), 261–273. https://doi.org/10.1016/j.agrformet.2018.02.002

3.9 Supplementary information

Humidity correction

The isotopic composition ($\delta^{18}O$ and $\delta^{2}H$) of water vapor varies with CRDS cavity humidity (Aemisegger et al., 2012; Fiorella et al., 2018). To correct for this bias, we used version 1.2 of the University of Utah vapor processing scripts to derive cavity-humidity correction equations and instrument precision (Fiorella et al., 2018). A full description of cavity-humidity correction is available in Aron et al. (2019). Briefly, we used the Picarro Standard Delivery Module (SDM) to deliver liquid standards over a humidity range from 2,000 to 30,000 ppm. From this, we used a Deming regression to develop humidity-correction equations. Here we present the best fit and 95% confidence interval offset equations below:

Picarro L2130-i

$\Delta^{18}O_{offset} = 0.185 - 4270.00/[H_2O]$ (best fit)

$\Delta^{18}O_{offset} = 0.311 - 2908.93/[H_2O]$ (upper 95% CI)

$\Delta^{18}O_{offset} = 0.059 - 5631.07/[H_2O]$ (lower 95% CI)

$\Delta D_{offset} = 0.090 - 1121.81/[H_2O]$ (best fit)

$\Delta D_{offset} = 0.462 - 3849.46/[H_2O]$ (upper 95% CI)

$\Delta D_{offset} = -0.283 - 6093.08/[H_2O]$ (lower 95% CI)

Picarro L2120-i

$\Delta^{18}O_{offset} = 0.503 - 7513.12/[H_2O]$ (best fit)

$\Delta^{18}O_{offset} = 0.782 - 4640.83/[H_2O]$ (upper 95% CI)

$\Delta^{18}O_{offset} = 0.022 - 10385.42/[H_2O]$ (lower 95% CI)

$\Delta D_{offset} = 2.733 - 51785.75/[H_2O]$ (best fit)

$\Delta D_{offset} = 3.443 - 40247.47/[H_2O]$ (upper 95% CI)

$\Delta D_{offset} = 2.026 - 63324.02/[H_2O]$ (lower 95% CI).

We corrected for the humidity bias by subtracting the humidity-dependent offset from the measured isotopic composition:

$\delta X_{humidity\_corrected} = \delta X_{measured} - \Delta X_{offset}$*(humidity).

Sap flux and eddy covariance ET scaling

ET partitioning from sap flux and eddy covariance follows the approach described by Williams et al. (2004). This technique assumes that transpiration accounts for all of the ET flux on days when soil moisture is low. From the 'dry day' relationship between sap flux and latent heat, we developed a scaling equation to estimate the ratio of T to ET on days when soil moisture was higher and evaporation contributed to the ET flux.

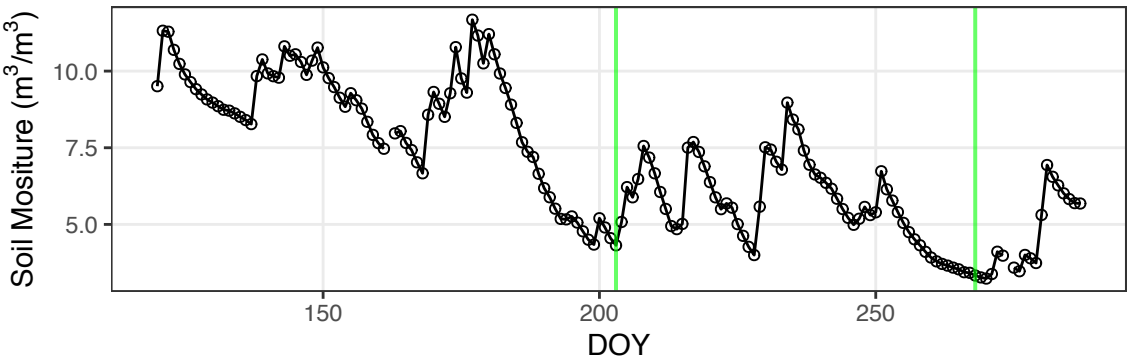

Figure S3.1 DOY 203 and 268 (noted with green vertical bars) were among the driest days during the growing season. We developed our scaling equation based on the sap flux and latent heat on these days.

The scaling equation is:

Scaled transpiration = 0.47*(latent heat) + 21.76.

Using this approach, F_T is defined as the ratio between scaled transpiration and latent heat.

References

Aemisegger, F., Sturm, P., Graf, P., Sodemann, H., Pfahl, S., Knohl, A., Wernli, H., 2012. Measuring variations of δ18O and δ2H in atmospheric water vapour using two commercial laser-based spectrometers: an instrument characterisation study. Atmos. Meas. Tech. 5, 1491–1511. https://doi.org/10.5194/amt-5-1491-2012

Aron, P.G., Poulsen, C.J., Fiorella, R.P., Matheny, A.M., 2019. Stable Water Isotopes Reveal Effects of Intermediate Disturbance and Canopy Structure on Forest Water Cycling. J. Geophys. Res. Biogeosciences 124, 1–18. https://doi.org/10.1029/2019JG005118

Fiorella, R.P., Bares, R., Lin, J.C., Ehleringer, J.R., Bowen, G.J., 2018. Detection and variability of combustion-derived vapor in an urban basin. Atmos. Chem. Phys. 18, 8529–8547. https://doi.org/10.5194/acp-18-8529-2018

Williams, D.G., Cable, W., Hultine, K., Hoedjes, J.C.B., Yepez, E.A., Simonneaux, V., Er-raki, S., Boulet, G., Bruin, H.A.R. De, Chehbouni, A., 2004. Evapotranspiration components determined by stable isotope, sap flow and eddy covariance techniques. Agric. For. Meteorol. 125, 241–258. https://doi.org/10.1016/j.agrformet.2004.04.008

Chapter 4 Spatiotemporal Variability of Stable Water Isotopes in Central Andean Precipitation

Co-authors: Christopher J. Poulsen, Richard P. Fiorella, Naomi E. Levin, R. Paul Acosta, Brian J. Yanites, Elizabeth J. Cassel

4.1 Abstract

The isotopic composition of precipitation (δ_p) and sedimentary materials are valuable tracers of water cycling and have been widely used to understand climate change in the Andes. However, understanding the spatiotemporal variability of δ_p in the central Andes (southern Peru and Bolivia) is hindered by a lack of multi-year observations and poor spatial distribution of precipitation isotope records, particularly across the Peruvian Altiplano and Western Cordillera. In this study we present a three-year record of bimonthly (twice per month) $\delta^{18}O_p$ and $\delta^{2}H_p$ from 19 stations in southern Peru that span a transect from the western Peruvian Amazon to near the Pacific coast. We observe a strong negative relationship between $\delta^{18}O_p$ and elevation. Seasonal $\delta^{18}O_p$ variation along the Eastern Cordillera and Altiplano is related to upstream rainout and local convection. Atmospheric back trajectories and $\delta^{18}O_p$ from the flank of the Western Cordillera show that precipitation is sourced from the Pacific Ocean. This finding has important implications for regional freshwater management and reconstructions of central Andean paleoaltimetry. To complement $\delta^{18}O_p$ and further explore regional isotopic variability, we report bimonthly d-excess$_p$ values and triple oxygen isotope data, expressed as $\Delta'^{17}O_p$, from a subset of the precipitation samples. We show that d-excess$_p$ and $\Delta'^{17}O_p$ complement $\delta^{18}O_p$ and add hydrologic information about airmass mixing and relative humidity at remote moisture sources. This chapter highlights the hydrologic insights that are gained from a combination of $\delta^{18}O_p$, d-excess$_p$, and $\Delta'^{17}O_p$ data and helps identify the processes that drive water cycling in the central Andes.

4.2 Introduction

Stable water isotopes and geologic materials that preserve the isotopic composition of paleowater (e.g., ice cores, sedimentary carbonates, and volcanic glass) are valuable tracers of water cycling and climate change. In the central Andes, the isotopic composition of precipitation ($\delta^{18}O_p$, $\delta^{17}O_p$, $\delta^{2}H_p$) can be a useful tracer of modern hydrology (Masiokas et al., 2020; Pabón-Caicedo et al., 2020) and past climate conditions (e.g., Hardy et al., 2003). However, there are relatively few observations of modern $\delta^{18}O_p$ and $\delta^{2}H_p$ and no observations of $\delta^{17}O_p$ from the central Andes (Valdivielso et al., 2020). Additional observations of central Andean precipitation isotopes will improve our understanding of regional water budgets and help manage water-intensive demands (e.g., agriculture, the generation of hydroelectric power, dense population centers in dry western regions) in a region that is vulnerable to shifts in the intensity, duration, and frequency of precipitation (Sarmiento and Kooperman, 2019).

The large-scale variability of central Andean $\delta^{18}O_p$ and $\delta^{2}H_p$ is primarily attributed to Rayleigh distillation, and precipitation isotopes are inversely related to the fraction of water vapor removed from a parcel via condensation (Dansgaard, 1964; Fiorella et al., 2015b; Gat, 1996; Gonfiantini et al., 2001; Jeffery et al., 2012; Rozanski et al., 1993; Sturm et al., 2007; Vimeux et al., 2005). However, central Andean $\delta^{18}O_p$ and $\delta^{2}H_p$ values are also quite variable across space and time (e.g., Fiorella et al., 2015b), and cannot be explained by Rayleigh distillation alone. In addition to Rayleigh distillation, the isotopic composition of precipitation in the central Andes may be related to moisture recycling (Ampuero et al., 2020; Salati et al., 1979) and the intensity of convective precipitation above the Amazon Basin (Fiorella et al., 2015b; Guy et al., 2019; Valdivielso et al., 2020; Vimeux et al., 2005, 2011; Vuille et al., 2012; Vuille and Werner, 2005), local topography that funnels moisture up valleys (Giovannettone and Barros, 2009), and interactions between Atlantic and Pacific moisture sources on the Altiplano (Aravena et al., 1999). Still, previous observations of $\delta^{18}O_p$ and $\delta^{2}H_p$ are not broadly distributed across the central Andes and there are aspects of precipitation isotope variability that remain uncertain (Valdivielso et al., 2020).

Most previous studies have considered either $\delta^{18}O_p$ or $\delta^{2}H_p$ and focused primarily on hydrologic processes associated with equilibrium fractionation (e.g., Gonfiantini et al., 2001). While informative, this approach ignores isotopic variability from kinetic fractionation and does

not consider moisture source conditions (e.g., Pfahl and Sodemann, 2014), evapotranspiration (Aemisegger et al., 2014; Salati et al., 1979), or tropospheric moisture transport (Samuels-Crow et al., 2014b) that affect central Andean water cycling. In this study, we look beyond a single isotope system ($\delta^{18}O_p$ or $\delta^{2}H_p$) to gain new understanding of central Andean precipitation isotope variability.

Traditionally, kinetic isotope effects in waters are quantified with deuterium excess (d-excess), which separates fractionation from equilibrium and kinetic processes (Dansgaard, 1964). However, d-excess is sensitive to temperature and is impractical in paleoclimate applications because very few geologic materials have both oxygen- and hydrogen-bearing minerals. Recently, triple oxygen isotopes ($\delta^{17}O$ and $\delta^{18}O$) have emerged as another metric to quantify kinetic fractionation in waters (e.g., Landais et al., 2010; Li et al., 2017; Schoenemann et al., 2014) and geologic materials (e.g., Levin et al., 2014; Pack and Herwartz, 2014; Passey et al., 2014; Rumble et al., 2007). The triple oxygen isotope system is largely insensitive to temperature (Barkan and Luz, 2005), but is understudied in the central Andes with only a few available observations from surface water (Aron et al., 2020; Surma et al., 2018) or structurally bonded gypsum water (Herwartz et al., 2017). Additional observations of precipitation d-excess and triple oxygen isotopes can help answer questions about evaporation, transpiration, and atmospheric moisture transport that affect water cycling in the central Andes.

Here, we combine a new three-year record of precipitation isotopes from southern Peru with other recent and contemporaneous central Andean $\delta^{18}O_p$ and $\delta^{2}H_p$ records to explain the spatiotemporal variability of precipitation isotopes in this region. We combine the new precipitation isotope dataset with atmospheric back trajectories to identify moisture sources in the central Andes. We describe new ways that precipitation isotopes can monitor terrestrial water cycling and show that triple oxygen isotopes and d-excess add complementary information to $\delta^{18}O_p$. Together, this chapter demonstrates that a suite of isotope data ($\delta^{18}O$, d-excess, and $\Delta'^{17}O$) helps constrain atmospheric moisture transport, surface evaporation, plant transpiration, and precipitation processes in the central Andes.

4.3 Background

4.3.1 Central Andes topography, precipitation, and atmospheric circulation

The Andes are a vast, topographically complex area with strong gradients in elevation, temperature, and precipitation. In southern Peru and Bolivia, the Andes are split into the Eastern and Western Cordilleras, both of which reach over 6 km in height. The Altiplano lies between the Cordilleras and has lower elevation (~ 4 km) and lower relief. Due to this high elevation and immense size, the Andes block low- and mid-troposphere zonal flow and exert first-order control on local to continental circulation, climate, and weather (Garreaud et al., 2003, 2009; Insel et al., 2010).

Dramatic precipitation gradients in the central Andes extend from the Amazon Rainforest, one of the wettest places on Earth, to the Atacama Desert, one of the driest (Figure 4.1). Moisture transport from the Amazon Basin and orographic uplift along the flank of the Eastern Cordillera generate tremendous amounts of precipitation (up to 6,000 mm/yr, mean annual precipitation (MAP)) (Chavez and Takahashi, 2017; Garreaud, 2009). In contrast, regions along the flank of the Western Cordillera are exceptionally dry (< 20 mm/yr) due to upwelling of cold waters from the coastal Humboldt current, large-scale subsidence, and orographic blocking (Garreaud et al., 2010, 2002; Rodwell and Hoskins, 2001; Takahashi and Battisti, 2007; Vuille et al., 2000). On the Altiplano, MAP is generally higher in southern Peru (greater than ~400 mm/yr) and lower in Bolivia (less than ~400 mm/yr) (Garreaud et al., 2003).

Seasonal rainfall patterns in the central Andes are closely tied to northward (austral winter) and southward (austral summer) shifts in the Intertropical Convergence Zone (ITCZ) that produce wet summers and dry winters (Figure 4.1). In the austral winter (June to September), upper-level (~200 hPa) circulation is dominated by a dry subtropical westerly jet that suppresses low-level (~850 hPa) moisture from reaching the Altiplano (Garreaud et al., 2003) (Figures 4.1b and 4.1d). In the austral summer (December to March), the subtropical westerly jet weakens and shifts southward. Intense summertime condensational heating over the Amazon Basin generates an upper-level (~200 hPa) high pressure circulation feature known as the Bolivian High (Figure 4.1c; Lenters and Cook, 1997), and easterly winds transport moisture across the Amazon Basin toward the central Andes. Orographic blocking deflects near-surface moisture flow and forms the South American Low Level Jet (SALLJ, Figure 4.1a), a low-level (~850 hPa) northerly/northwesterly

barrier jet that transports large amounts of moisture from the tropics to the subtropics and plays a critical role in South American hydrology (Campetella and Vera, 2002; Gandu and Geisler, 1991; Vera et al., 2006; Virji, 1981). Together, these circulation patterns trigger the development of a summer rainy season along the eastern central Andean flank and Altiplano (Falvey and Garreaud, 2005; Garreaud, 2009; Garreaud et al., 2003; Vuille, 1999).

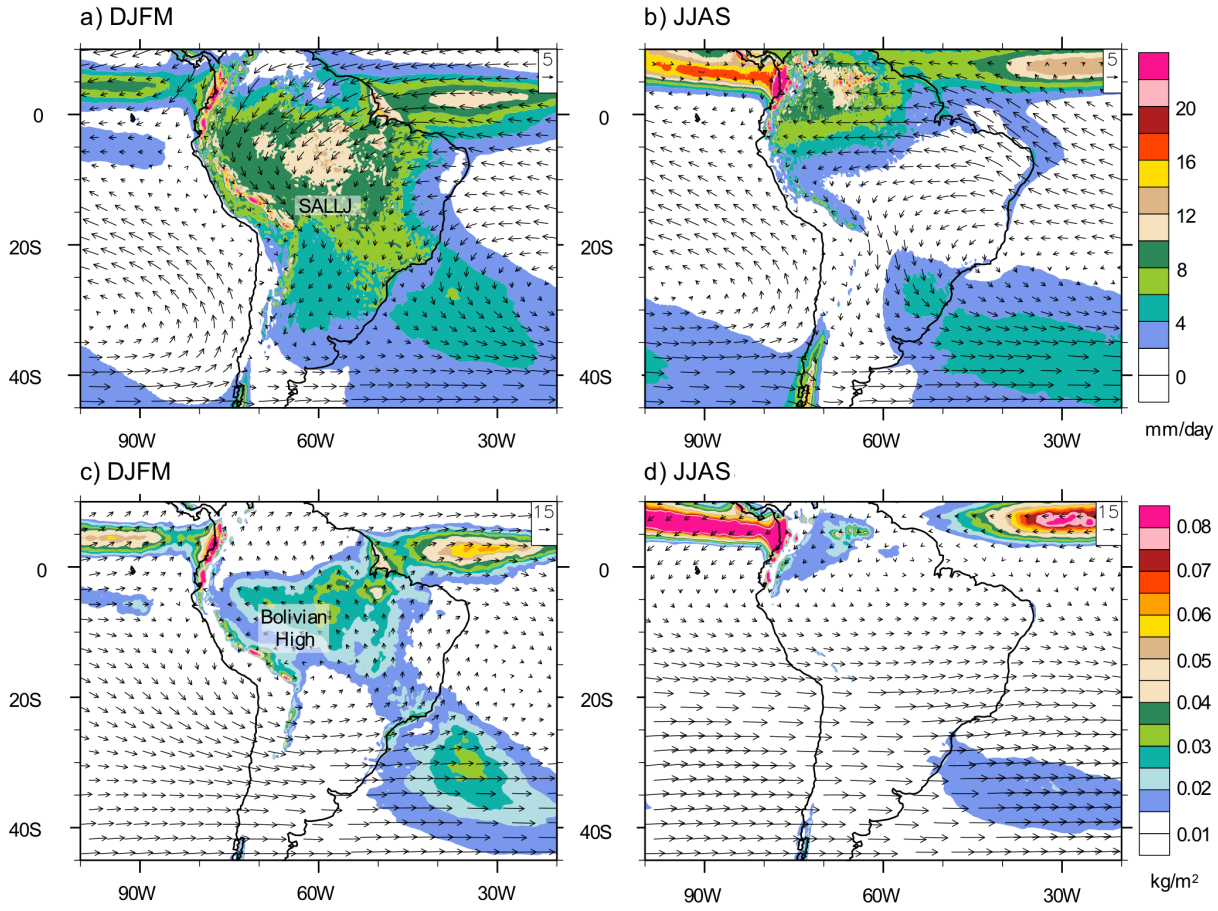

Figure 4.1 Mean 1989-2019 seasonal climatologies of the central Andes generated from ERA5 reanalysis data (Hersbach et al., 2020). Panels a) and b) show 850 hPa winds (vectors, m/s) and total daily precipitation (mm/day); c) and d) show 200 hPa winds (vectors, m/s) and total column rainwater (kg/m^2). Wind and moisture patterns are separated into summer (December, January, February, March (DJFM), panels a) and c)) and winter (June, July, August, September (JJAS), panels b) and d)) conditions to highlight seasonal climate variation in the central Andes.

Western Cordillera precipitation also occurs in the austral summer but is not directly tied to circulation features over the Amazon or Altiplano. Infrequent, small (generally < 10 mm) storms develop on the Western Cordillera in January and February when the southeast Pacific anticyclone

weakens and the ITCZ shifts southward (Aceituno, 1988). These dynamics are most commonly associated with El Niño Southern Oscillation (ENSO) (Bjerknes, 1969) and co-occur with extreme precipitation events along the subtropical coastal western Andes (Quinn and Neal, 1987; Takahashi and Martínez, 2019), but also generate a brief annual rainy season along the Western Cordillera. Generally, Western Cordillera precipitation only occurs above ~1000 meters above sea level (masl) (Garreaud et al., 2002; Rutllant et al., 2003; Vuille et al., 2000). Below 1000 masl, an inversion layer restricts inland moisture transport and precipitation is very rare (Garreaud et al., 2002; Lavado Casimiro et al., 2012).

4.3.2 Stable water isotope systematics

Stable water isotopes fractionate due to mass differences between ^{17}O and ^{18}O versus ^{16}O and ^{2}H versus ^{1}H. The different proportions of these isotopes in water record information about hydrologic processes because phase changes of water preferentially partition heavier isotopologues into more condensed phases and lighter isotopologues into less condensed phases. At equilibrium, this fractionation is temperature dependent (Horita and Wesolowski, 1994; Majoube, 1971). When two phases cannot reach equilibrium, an additional kinetic fractionation occurs due to differences in diffusivities between isotopologues (Cappa, 2003; Luz et al., 2009; Merlivat, 1978).

Mass dependent isotope fractionation follows a power law relationship that relates the fractionation factors (α) of coexisting phases (A and B) by a defined fractionation exponent (θ) (Matsuhisa et al., 1978; Young et al., 2002):

$$^{*}\alpha_{A\text{-}B} = (^{*}\alpha_{A\text{-}B})^{\theta} \qquad \text{Eq. 4.1}$$

where * denotes a heavy mass number. The value of the fractionation exponent (θ) is derived from mass law theory (Criss, 1999; Matsuhisa et al., 1978; Young et al., 2002) and defines the relationship between isotope ratios during equilibrium (θ_{eq}) and kinetic (θ_{diff}) processes. For example, the equilibrium power law relationship that relates $^{2}H/^{1}H$ and $^{18}O/^{16}O$ is $^{2H}\alpha_{eq} = (^{18O}\alpha_{eq})^{\theta}$; for triple oxygen isotopes, this relationship is $^{17O}\alpha_{eq} = (^{18O}\alpha_{eq})^{\theta}$. The kinetic θ value is abbreviated as θ_{diff} because kinetic fractionation results from the diffusion of water vapor through the air.

In nature, however, isotopic compositions rarely result from a single fractionating process. Following convention from the water isotope literature, we use λ notation to differentiate empirical isotope relationships from defined θ values. The most familiar λ value in isotope hydrology is the slope of the oxygen-hydrogen Global Meteoric Water Line (GMWL) (Craig, 1961). This value (8‰‰$^{-1}$) integrates equilibrium ($\theta_{eq} \approx 8$) and kinetic ($\sim 2.5 < \theta_{diff} < 8$; Gonfiantini et al., 2018) fractionation processes and defines a reference slope between meteoric water $\delta^{18}O$ and $\delta^{2}H$ values. Here, and throughout this chapter, δ is defined as $(R_{sample}/R_{standard} - 1)*1000$, where R is the ratio of heavy-to-light isotopes and the international standard is Vienna Standard Mean Ocean Water (VSMOW) (Coplen, 1996). Similarly, $\delta^{18}O$ and $\delta^{17}O$ are related by an established reference meteoric water line. Although recent work suggests a value of ~0.526 for the triple oxygen reference slope in tropical and temperate regions (Aron et al., 2020; Sharp et al., 2018), we continue to use the canonical value of 0.528 (Luz and Barkan, 2010; Meijer and Li, 1998) for the triple oxygen reference slope to maintain consistency with previous work and to distinguish fractionation from non-Rayleigh processes. This λ value integrates triple oxygen isotope fractionation associated with equilibrium ($\theta_{eq} = 0.529$; Barkan and Luz, 2005) and kinetic ($\theta_{diff} = 0.518$; Barkan and Luz, 2007) processes.

Because reference λ values in the $\delta^{18}O$–$\delta^{2}H$ and $\delta^{18}O$–$\delta^{17}O$ systems are very similar to their respective θ_{eq} values, deviations from meteoric water lines are typically attributed to kinetic fractionation (Cappa, 2003; Craig, 1961; Gat, 1996; Young et al., 2002). Deviations from the $\delta^{18}O$–$\delta^{2}H$ reference relationship are quantified with d-excess (Dansgaard, 1964):

$$\text{d-excess} = \delta^{2}H - 8*\delta^{18}O. \qquad \text{Eq. 4.2}$$

Deviations from the triple oxygen isotope reference relationship are quantified with $\Delta'^{17}O$ (Barkan and Luz, 2007):

$$\Delta'^{17}O = \delta'^{17}O - 0.528*\delta'^{18}O. \qquad \text{Eq. 4.3}$$

Mass dependent triple oxygen isotope deviations are typically quite small and are expressed in units of per meg (1 per meg = 0.001‰). The triple oxygen isotope reference relationship requires

δ' notation ($\delta' = \ln(\delta + 1)$; Hulston and Thode, 1965; Martin, 2002) to linearize the power law relationship (Eq. 4.1) between $\delta^{17}O$ and $\delta^{18}O$. Most hydrologic studies do not linearize δ scales when calculating d-excess, although an alternate logarithmic definition of d-excess does exist and may be useful at high latitudes or when isotope variation is large (Dütsch et al., 2017; Schoenemann et al., 2014; Uemura et al., 2012).

Both d-excess and $\Delta'^{17}O$ are primarily sensitive to kinetic fractionation and relative humidity during evaporation (Barkan and Luz, 2007; Pfahl and Sodemann, 2014; Uemura et al., 2008). As such, d-excess and $\Delta'^{17}O$ covary during kinetic fractionations (e.g., Aron et al., 2020; Li et al., 2017) and are relatively insensitive to Rayleigh distillation (Gat, 1996; Luz and Barkan, 2010). However, d-excess and $\Delta'^{17}O$ respond differently to temperature effects and processes that involve hydrologic mixing. First, d-excess is more sensitive to temperature than $\Delta'^{17}O$ (Barkan and Luz, 2005; Cao and Liu, 2011) because the $\delta^{18}O$–$\delta^{2}H$ θ_{eq} value varies with temperature (Majoube, 1971), whereas the $\delta^{18}O$–$\delta^{17}O$ θ_{eq} value is relatively insensitive to temperature (Barkan and Luz, 2005). This difference in temperature sensitivity can help distinguish isotopic variability driven by changes in temperature or relative humidity above moisture sources (e.g., Landais et al., 2012b, 2012a; Uechi and Uemura, 2019; Winkler et al., 2012). Second, hydrologic mixing causes a non-linear response in $\Delta'^{17}O$ because $\Delta'^{17}O$ is defined from logarithmic δ' values (Aron et al., 2020; Luz and Barkan, 2010; Matsuhisa et al., 1978). For example, mixing two airmasses with different initial $\delta^{18}O$ values decreases the $\Delta'^{17}O$ of the mixed airmass, whereas d-excess responds linearly to mixing because it is defined from δ values. Different d-excess and $\Delta'^{17}O$ mixing responses have been observed in tropical and mid-latitude meteoric waters (Landais et al., 2010; Li et al., 2015; Risi et al., 2013).

In the central Andes, the dominant hydrologic processes that affect the isotopic composition of precipitation are Rayleigh distillation, convection, and atmospheric mixing (e.g., Fiorella et al., 2015b; Insel et al., 2013; Vuille and Werner, 2005). However, identifying these processes with $\delta^{18}O_p$ or $\delta^{2}H_p$ alone is not always straightforward. Here we combine $\delta^{18}O_p$, d-excess$_p$, and $\Delta'^{17}O_p$ from southern Peru to explore the spatiotemporal variability of precipitation isotopes and the isotope effects of non-Rayleigh fractionation in the central Andes.

4.4 Methods

4.4.1 Precipitation network and sample collection

We present data from a network of 19 stations in southern Peru that extends from the western Peruvian Amazon (~13˚S) to near the Pacific coast (~17˚S) (Figure 4.2). Each station is managed by a local Peruvian observer and collocated alongside existing SENAMHI (Servicio Nacional de Meteorología e Hidrología del Perú, the National Meteorology and Hydrology Service of Peru) meteorological stations. SENAMHI stations record daily precipitation amount; some also record mid-day relative humidity and maximum and minimum or morning and afternoon temperature. We installed temperature and relative humidity sensors (Onset HOBO, U23 Pro v2) at stations that only record precipitation. We use the University of Delaware 0.5˚ monthly gridded climate data (1960-1990 average) to get the mean annual temperature (MAT) and MAP from each site (Legates and Willmott, 1990a, 1990b). Ten stations (San Gaban, Ollachea, Macusani, Ayaviri, Ichuña, Carumas, Majes, Ayo, Orcopampa, and Santo Tomas) were installed in May and June 2016 and 8 stations (Pampahuta, Ubinas, Quinistaquillas, Moquegua, Arequipa, Cotahuasi, and Puyca) were added in November 2017. The final station (Calca) was installed in July 2018. This chapter includes samples collected through May 2019. Samples collected since May 2019 are not included due to COVID-19 travel and laboratory restrictions. We expect that sample collection will continue until it is feasible to visit the stations.

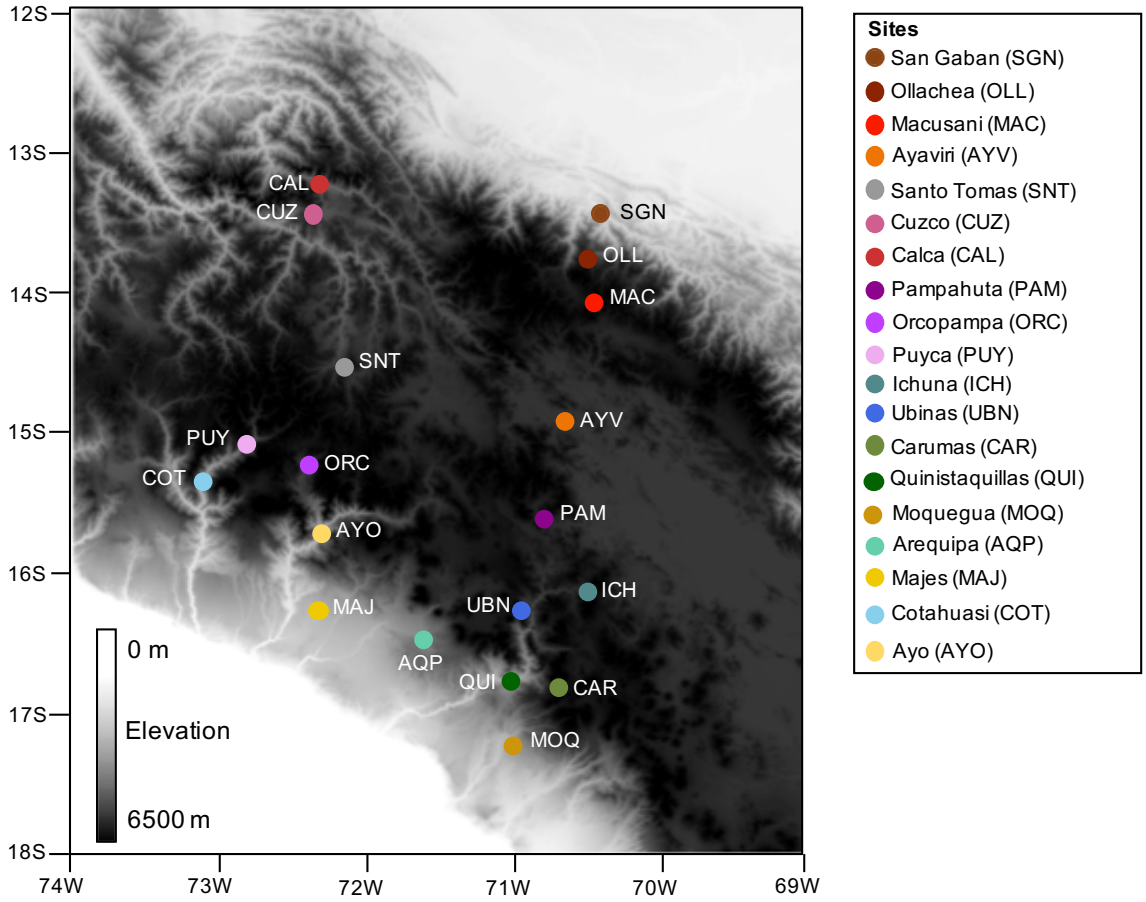

Figure 4.2 Topography and spatial distribution of precipitation collection stations in southern Peru.

Traditionally, precipitation is collected for isotopic analysis using mineral oil, which floats above collected water and prevents evaporation (e.g., Friedman et al., 1992; Scholl et al., 1996). However, it can be challenging to separate sample water from the oil, especially when sample volume is very low, and careful laboratory protocols are necessary to avoid contaminating isotopic analyzers with mineral oil. Recently, Gröning et al. (2012) proposed an alternative oil-free precipitation collection method that prevents evaporation and simplifies sample collection.

Initially, we built and deployed oil-free collectors following the description in Gröning et al. (2012). We used 3-9″ funnels to increase the volume of collected precipitation and collected samples in 1.5 L HDPE bottles (McMaster Carr, 4280T37). Each collection bottle was connected to a long (> 5 m) open-ended Bev-a-line vent tube (1/8″ ID) to minimize pressure fluctuations on the sample. On the 1st and 15th of every month, local station observers poured the collected sample

water into 20 ml HDPE storage vials (Wheaton, 986716), capped the storage vials with PolyCone caps, and cleaned and dried the collection bottle. Following collection, samples were stored in a cool, dark environment. We used plastic collection and storage vials because they do not break as easily as glass vials. We collected bimonthly samples because the high (> 20 mm/day) precipitation rates along the eastern flank occasionally exceeded the volume of water we were able to collect in a month.

After the first year of collection, we introduced mineral oil to the collection bottles as another measure to prevent evaporation. With the addition of oil, observers used a syringe to extract water from the bottom of the collection bottles and transferred sample water to 20 ml storage vials. Between samples, the collection bottles were cleaned, dried, and given a new layer of oil. All other collection procedures (frequency of collection, volume of water collected, etc.) remained constant through the study period. We switched from oil-free to oil-based collections because our stations are in very remote locations, we have no communication with the local observers during the year, and windy conditions at the sites can knock the collector equipment out of alignment, potentially exposing sample water to the atmosphere. Although the oil-based collection involves additional steps to transfer water and prepare the samples for isotopic analysis, we concluded that this technique was more reliable in remote locations and with non-expert observers.

We visited every site annually to gather the precipitation samples, clean and repair the collection equipment, download temperature and relative humidity data, and interview observers about local weather conditions. In the lab, we transferred sample water into 16 ml glass vials (The Lab Depot, 316018-2170) for secure long-term storage. At most, water samples included in this chapter were stored in HDPE vials for one year, so we do not expect any fractionation with the plastic collection or storage containers (Spangenberg, 2012).

4.4.2 Isotopic analysis

We measured the $\delta^{18}O$ and $\delta^{2}H$ values of every precipitation sample using a Picarro L2130-i with a high-precision vaporizer (A0211) and attached autosampler. We used the Picarro ChemCorrect software to monitor samples for organic contamination and normalized measured $\delta^{18}O$ and $\delta^{2}H$ values to the VSMOW-SLAP scale with four in-house liquid standards that were calibrated with USGS reference waters (USGS45, 46, 49, and 50). Reproducibility of $\delta^{18}O$ and

δ^2H values was determined from repeat analyses of deionized water and calculated using the Picarro L2130-i Drift and Precision Test worksheet. Analytical precision was determined to be better than 0.1‰ and 0.3‰ for $\delta^{18}O$ and δ^2H, respectively.

We measured the $\delta^{18}O$ and $\delta^{17}O$ values of 32 precipitation samples with a dual inlet Nu Perspective isotope ratio mass spectrometer (IRMS) at the University of Michigan using the cobalt(III) fluoride (CoF_3) method developed by Baker et al. (2002) and refined by Luz and Barkan (2005). Our methods have been described previously (Aron et al. 2020; Li et al., 2017, 2015; Passey et al., 2014), although triple oxygen isotope data from Li et al. (2015, 2017) and Passey et al. (2014) were acquired on a different mass spectrometer (Thermo 253) and fluorination line previously at Johns Hopkins University.

For $\delta^{18}O$ and $\delta^{17}O$ analysis, we inject ~2 μL of water through a septum port into a 360-370 ˚C CoF_3 nickel reactor to convert liquid water to O_2 gas and gaseous hydrofluoric acid (HF):

$$2H_2O_{(l)} + 4CoF_{3(s)} \rightarrow O_{2(g)} + 4HF_{(g)} + 4CoF_{2(s)}. \quad \text{Eq. 4.4}$$

Following this reaction, HF and O_2 are carried downstream of the reactor in helium gas. HF is trapped and removed in a nickel trap immersed in liquid nitrogen (−196 ˚C). The O_2 gas is further purified by passing through a custom-built stainless-steel column (~1 m, 1/8″ OD) packed with a 5 Å molecular sieve (Strem Chemicals, CAS#69912-79-4) and immersed in a methanol and dry ice slush (−80 ˚C). After purification, the O_2 gas collects in a liquid nitrogen trap that is packed with a 5 Å molecular sieve. This O_2 collection process takes approximately 15 minutes. After the O_2 is collected, helium gas is pumped away (14 minutes), liquid nitrogen is replaced by a methanol and dry ice slush, and the O_2 is transferred to a −180 ˚C cold finger packed with a 5 Å molecular sieve (12 minutes) that is part of the dual inlet system of the Nu mass spectrometer. After the O_2 transfer is complete, the cold finger is heated (9 minutes) to 90 ˚C to release O_2 from the molecular sieve, and the sample is introduced to the mass spectrometer.

The O_2 gas is analyzed in dual inlet mode for *m/z* 32, 33, and 34. To minimize analytical error, each analysis consists of 40 cycles during which the ratio of sample to reference gas (99.999% compressed oxygen, with approximate values of $\delta^{17}O_{VSMOW}$ = 10.3‰, $\delta^{18}O_{VSMOW}$ = 20.3‰) is determined. Each cycle consists of 50 seconds of integration time on the sample gas or reference gas and 20 seconds of idle time between integrations. Resistances on the *m/z* 32, 33, and

34 Faraday cups are 2×10^8, 3×10^{11}, and 1×10^{11} Ω, respectively. In total, sample preparation takes just over an hour and analysis in the mass spectrometer takes approximately two hours. Typically, samples are analyzed twice.

Raw $\delta^{18}O$ and $\delta^{17}O$ values are normalized to the VSMOW-SLAP scale following the approach established by Schoenemann et al. (2013) using values of 0.0000‰ for $\delta^{18}O_{VSMOW}$ and $\delta^{17}O_{VSMOW}$ (Gonfiantini, 1978), −55.5000‰ for $\delta^{18}O_{SLAP}$, and −29.6986‰ for $\delta^{17}O_{SLAP}$. This normalization approach corrects for pressure-baseline offsets (Yeung et al., 2018) and results in excellent inter-lab $\Delta'^{17}O$ reproducibility (Aron et al., 2020; Berman et al., 2013; Kaiser, 2009; Schoenemann et al., 2013).

In our lab, triple oxygen isotope data are generated in analytical sessions that last approximately 3-4 weeks. An analytical session ends when all the CoF_3 in the reactor is consumed. We analyze VSMOW2 and SLAP2 at the beginning, middle, and end of each session because isotopic measurements and instrument nonlinearities can evolve through time and this approach enables us to apply normalizations over a full session. The $\delta^{18}O$ and $\delta^{17}O$ values of VSMOW2 and SLAP2 are indistinguishable from the $\delta^{18}O$ and $\delta^{17}O$ values of VSMOW and SLAP (Lin et al., 2010). In addition, we regularly analyze USGS reference waters (USGS45, 46, 47, 48, 49, 50) to determine external precision of our system, to monitor isotopic drift, and to ensure analytical accuracy. In this study, the pooled standard deviation of replicate USGS analyses is 0.1‰ for $\delta^{17}O$, 0.2‰ for $\delta^{18}O$, and 7 per meg for $\Delta'^{17}O$. The precision of $\Delta'^{17}O$ is better than that of $\delta^{17}O$ and $\delta^{18}O$ because any isotopic fractionation that occurs during sample preparation is related by a $\delta'^{18}O$–$\delta'^{17}O$ slope that is nearly equivalent to the slope of the reference line (0.528) and has little effect on $\Delta'^{17}O$ (Barkan and Luz, 2007; Landais et al., 2006; Schoenemann et al., 2013).

4.4.3 Data caveats

Based on individual sample and station $\delta^{18}O$ and $\delta^{2}H$ values, we identified 119 precipitation samples that fail our quality control checks. This includes 12 samples with negative d-excess that are likely affected by evaporation and 107 samples that were likely collected from tap or surface water sources. The probable tap or surface water samples were identified from site-specific timeseries with less than 1‰ of seasonal $\delta^{18}O_p$ variation (seasonal $\delta^{18}O_p$ variation is at least 5‰ at most sites). This screening identified samples from Ollachea (27 samples, all collected

after 2017), Carumas (14 samples, all collected after 2017), Orcopampa (20 samples, all collected samples), Ichuña (24 samples, all collected samples), and Puyca (22 samples, all collected samples). We include these data in Table S4.1, but excluded them from our analysis.

Data are also missing or incomplete from four other sites. First, it did not rain enough to collect samples from Ayo so we do not report isotope data from this site. Second, in 2018-2019, the observer at Macusani collected samples correctly, but did not record collection dates so we exclude these data. Third, sample collection lasted only one year (2017-2018) in Cusco. Fourth, the observer in Majes was not available during our 2019 site visit, so we do not report 2018-2019 isotope data from this site.

4.4.4 Atmospheric back trajectories

We calculated atmospheric back trajectories to constrain moisture source regions across southern Peru using the Hybrid coordinate Single Parcel Lagrangian Integrated Trajectory model (HYSPLIT; Draxler and Hess, 1998) and 0.5˚ meteorological data from the Global Data Assimilation System (GDAS). Sets of 10-day back trajectories were calculated from 7 sites: San Gaban, the lowest elevation eastern flank site; Ayaviri and Santo Tomas, central Altiplano sites; Cotahuasi and Ubinas, high elevation western flank sites; and Majes and Moquegua, low elevation western flank sites. We chose these sites to compare the dominant eastern (Atlantic) and western (Pacific) moisture sources across the study region. Trajectories were initiated 4 times each day (0, 6, 12, 18 UTC) from 1000 m above ground level.

We identified four source regions that contribute moisture to the central Andes: 1) Atlantic, 2) eastern South America, which includes the South American continent east of the Western Cordillera, 3) western South America, which includes the South American continent west of the Western Cordillera, and 4) Pacific (Figure S4.1). We then used the Lagrangian tracer developed by Sodemann et al. (2008) to determine moisture footprints for each site. This tracer links precipitation to remote evaporation sources by tracking changes in air parcel specific humidity and identifies moisture source regions through increases in planetary boundary layer specific humidity along the trajectory. HYSPLIT-extracted boundary layer heights were doubled, as prior work with this tracer has suggested that using unscaled boundary layer heights may underestimate moisture contributions from shallow convection (Aemisegger et al., 2014; Fiorella et al., 2018; Sodemann et al., 2008). Mass contributions from each region were summed for each month and divided by

the total moisture footprint mass from all four regions to calculate the fraction of total moisture advected to the site originating in these four regions.

4.5 Results

4.5.1 Climate variability

Precipitation, temperature, and relative humidity variations are most pronounced between the wet (December, January, February, March; DJFM) and dry (June, July, August, September; JJAS) seasons, and are smaller on bimonthly and interannual timescales (Figure 4.3). Bimonthly precipitation ranged from 0 mm (many sites) to 857 mm (San Gaban, January 1, 2019) (Figure 4.3a). Bimonthly precipitation was always highest at San Gaban, the lowest elevation site along the eastern flank, decreased up the eastern flank, was relatively consistent across the Altiplano, and decreased at lower elevations down the western flank. A few low elevation sites on the western flank received almost no rainfall. For example, Majes (1498 masl) received a total of 10 mm of rain during the three years of sample collection; Ayo (1956 masl) received no precipitation during the study period.

More than half the total annual rainfall occurred from December to March at every site (Figure 4.3a). Seasonal variations in precipitation amount are most pronounced along the western flank where DJFM precipitation accounted for 92% of the annual total. On the Altiplano, precipitation fell primarily during DJFM (72%) and only occasionally occurred during JJAS (6%). Eastern flank precipitation was highest in DJFM (52%), but not uncommon in JJAS (18%).

Temperature and relative humidity were higher in the wet season and lower in the dry season (Figures 4.3b and 4.3c). Average temperature ranged from 1.0˚C (Macusani, 4345 masl, June 15, 2016) to 24.4˚C (San Gaban, 657 masl, December 15, 2017) and was strongly negatively correlated with elevation (Pearson's r = –0.97). Average relative humidity (RH) ranged from 16.8% (Carumas, 2976 masl, August 15, 2017) to 95.6% (San Gaban, January 15, 2019) (Figure 4.3c). Relative humidity decreased from the eastern flank towards the Pacific coast and was uncorrelated with elevation (r = –0.12). In general, seasonal temperature variations were larger at stations on the eastern flank and Altiplano (~5-8˚C) and smaller at stations on the western flank (~ 3-4˚C). In contrast, seasonal variations in relative humidity were generally larger on the western flank (~20-80%) than on the eastern flank (~10-40%).

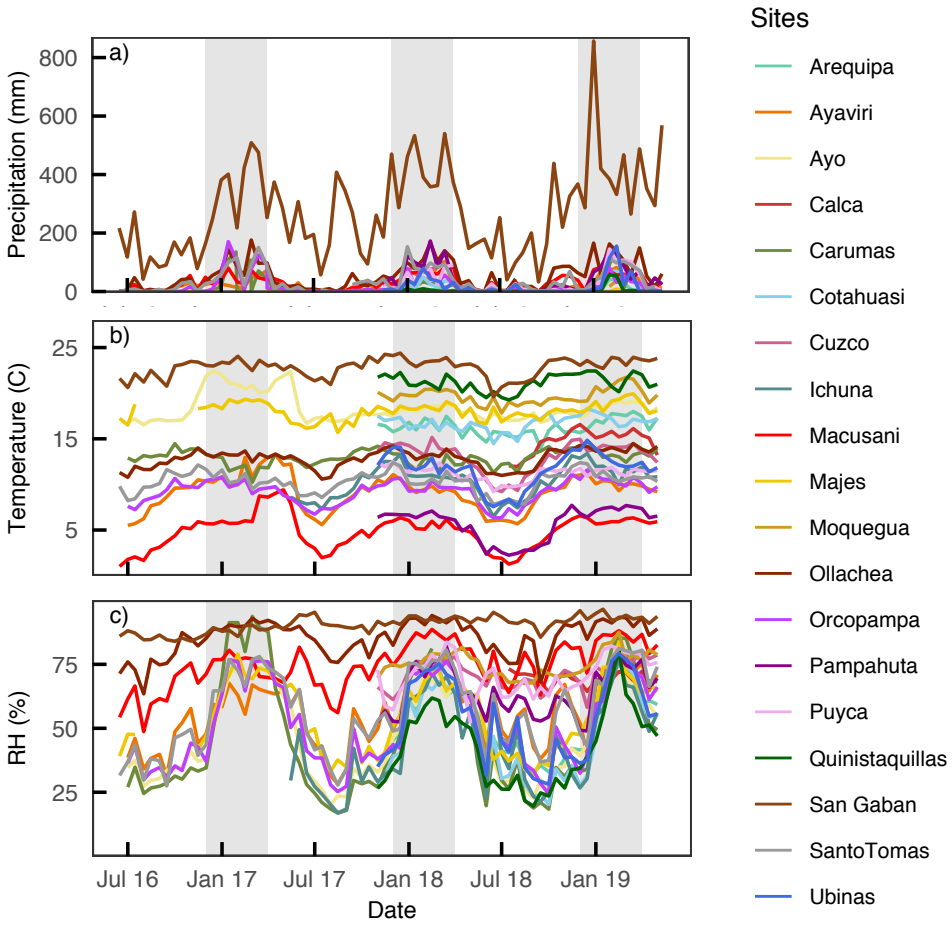

Figure 4.3 Timeseries of bimonthly a) precipitation, b) temperature, and c) relative humidity (RH) across in southern Peru from June 2016 through May 2019. The gray vertical bars indicate the austral summer rainy season (DJFM). The timeseries are colored according to site location.

4.5.2 Isotopic variation

Precipitation isotope data fall on or near the oxygen-hydrogen (Figure 4.4a, Table S4.1) and triple oxygen (Figure 4.4b, Table S4.2) global meteoric water lines. To expand this dataset beyond precipitation, we include $\delta^{18}O$, $\delta^{17}O$, and $\delta^{2}H$ data from 10 surface water samples collected from the same region in southern Peru as the precipitation samples (Aron et al., 2020). River water (n = 8) $\delta^{18}O$ and $\delta^{2}H$ values generally plot along the GMWL (Figure 4.4a), although the range of river $\delta^{18}O$ (–19.0 to –8.1‰) and $\delta^{2}H$ (–141.6 to –44.3‰) was smaller than the range of $\delta^{18}O_p$ (–29.3 to 2.0‰) and $\delta^{2}H_p$ (–216.1 to 35.2‰). Lake water (n = 2) $\delta^{18}O$ (–10.4 and –5.2) and $\delta^{2}H$ (–95.7 and –73.1) compositions fall below the GMWL, indicative of evaporation.

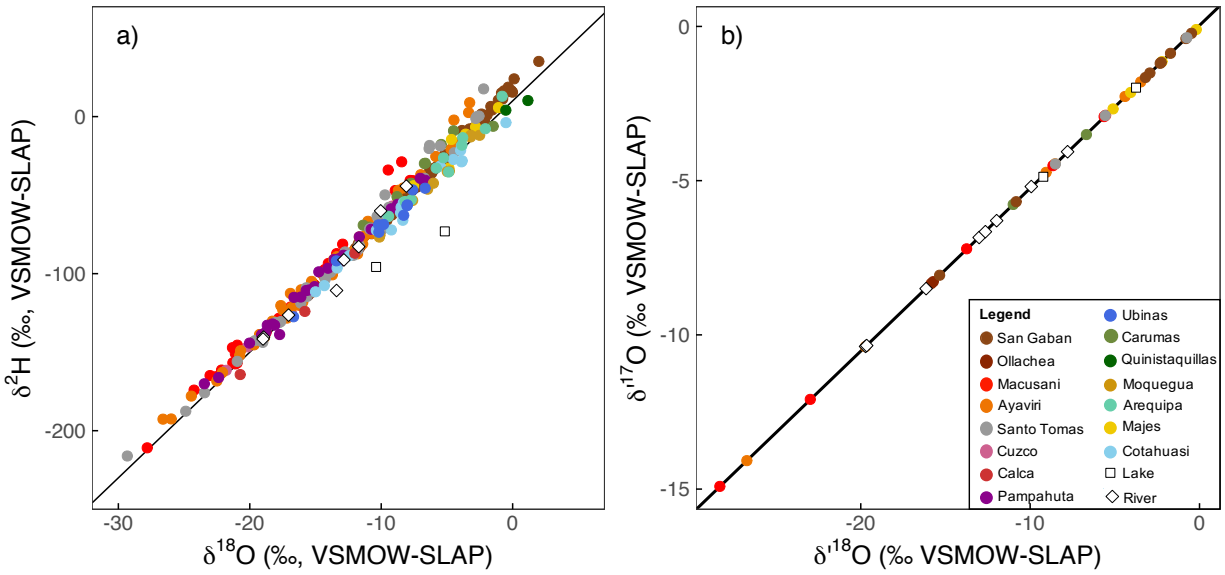

Figure 4.4 Bimonthly precipitation (filled circles), river (open diamonds), and lake (open squares) a) $\delta^{18}O$ versus $\delta^{2}H$ and b) $\delta'^{18}O$ versus $\delta'^{17}O$. Isotope data overlie the $\delta^{18}O$-$\delta^{2}H$ (Craig, 1961) and $\delta'^{18}O$-$\delta'^{17}O$ (Luz and Barkan, 2010) global meteoric water lines, respectively. Panel 4.4b contains a subset of 32 precipitation samples from panel 4.4a. Precipitation samples are colored according to site location.

The slope connecting precipitation, river, and lake $\delta'^{18}O$ and $\delta'^{17}O$ values (0.5276 ± 0.0003) is similar to the triple oxygen isotope reference slope (0.528; Luz and Barkan, 2010), and $\delta'^{18}O$ and $\delta'^{17}O$ are very well correlated ($r > 0.9999$, Figure 4.4b). Correlations between $\delta'^{18}O$ and $\delta'^{17}O$ are stronger than correlations between $\delta^{18}O$ and $\delta^{2}H$ because $^{17}O/^{16}O$ and $^{18}O/^{16}O$ fractionations are governed by the same mass law equation (Young et al., 2002) whereas $^{2}H/^{1}H$ and $^{18}O/^{16}O$ fractionations are subject to different governing equations (e.g., Horita & Wesolowski, 1994; Majoube, 1971). Because triple oxygen isotope values of precipitation, river, and lake water are indistinguishable from the reference $\delta'^{18}O$–$\delta'^{17}O$ relationship (Figure 4.4b), these mass-dependent fractionations are better viewed as $\delta'^{18}O$ versus $\Delta'^{17}O$ (Figure 4.5a). This isotope space is a more amenable way to visualize isotopic compositions that vary on different orders of magnitude (1‰ is equal to 1000 per meg).

Values of $\Delta'^{17}O$ ranged from −7 to 55 per meg (Figure 4.5a). Average $\Delta'^{17}O_p$ was 34 ± 13 per meg and varied from 1 to 55 per meg. River water $\Delta'^{17}O$ ranged from 20 to 54 per meg. Lake $\Delta'^{17}O$ values were lower (−7 and −5 per meg) than any other water type. For the full triple oxygen isotope dataset, $\Delta'^{17}O$ is positively correlated with d-excess ($r = 0.68$, Figure 4.5b) and weakly

correlated with $\delta'^{18}O$ (r = –0.18, Figure 4.5a). The slope of the linear regression between $\Delta'^{17}O$ and d-excess, 0.8 (± 0.1) per meg ‰$^{-1}$, is consistent with theoretical steady state predictions (Barkan and Luz, 2007; Li et al., 2015), but slightly lower than observations from Landais et al. (2010) who reported slopes between 1.6 and 2.0 per meg ‰$^{-1}$ in tropical monsoon precipitation in north central Africa.

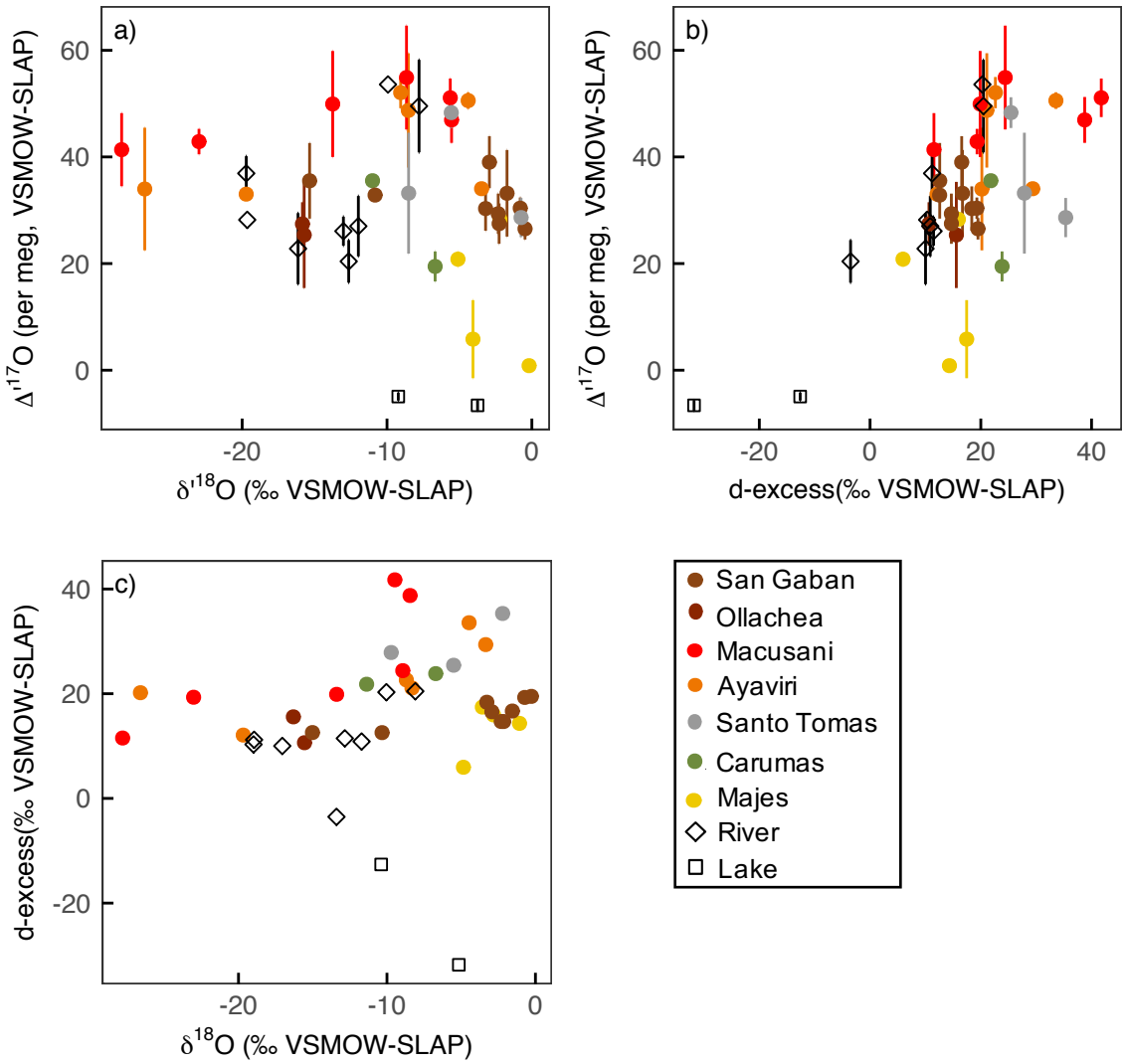

Figure 4.5 Scatterplots of a) $\delta'^{18}O$ vs. $\Delta'^{17}O$, b) d-excess vs. $\Delta'^{17}O$, and c) $\delta^{18}O$ vs. d-excess of precipitation (filled circles), river (open diamond), and lake (open square) water. Precipitation samples were selected from 7 sites and are colored by site location. Error bars on $\Delta'^{17}O$ are the standard deviation of multiple replicate analyses.

4.5.3 Temporal isotopic variation

Precipitation $\delta^{18}O_p$ and d-excess$_p$ values varied on bimonthly to interannual timescales (Figure 4.6). At every site, $\delta^{18}O_p$ values were lower during the wet season and higher during the dry season (Figures 4.6a and 4.6b). On the eastern flank and the Altiplano, the lowest $\delta^{18}O_p$ values typically occurred near the end of the rainy season in February and March (Figure 4.6a). On the western flank, the lowest $\delta^{18}O_p$ values occurred slightly earlier, typically in January and February (Figure 4.6b). d-excess$_p$ ranged from 0.2 to 41.8‰ and was generally lower (average 13.4‰) in DJFM and higher (average 18.0‰) in JJAS (Figures 4.6c and 4.6d). Seasonal $\delta^{18}O_p$ and d-excess$_p$ variations cannot be assessed on the western flank because precipitation at these sites only fell during the wet season (Figure 4.3a). Interannual precipitation isotope variability is typically associated with ENSO (e.g., Cai et al., 2020; Vuille and Werner, 2005), but our study period overlapped with weak ENSO events (National Weather Service, Climate Prediction Center) and we do not observe consistent interannual precipitation isotope variation.

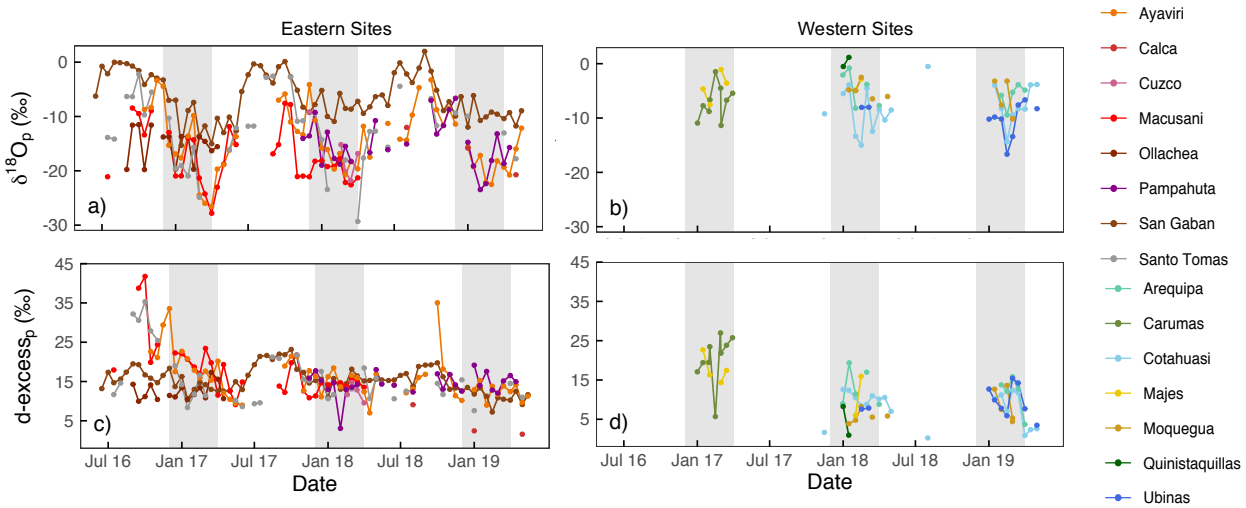

Figure 4.6 Timeseries of a) and b) bimonthly $\delta^{18}O_p$ (‰) and c) and d) d-excess$_p$ (‰) from June 2016 through May 2019. The gray vertical bars indicate the austral summer rainy season (DJFM). For clarity and to explain seasonal isotope variations, the data are separated into eastern and western sites and colored by site location. Eastern sites receive dry season precipitation; western sites typically do not. Missing data indicate rain did not fall during the collection period or the observer did not collect a sample.

In addition to the seasonal and interannual isotope variability, $\delta^{18}O_p$ and d-excess$_p$ values also varied on shorter bimonthly to monthly timescales (Figure 4.6). Sequential bimonthly $\delta^{18}O_p$ values generally varied only a few per mil, but occasionally differed by more than 10‰ (for example, Macusani in October 2017). Sequential d-excess$_p$ values were less variable, although a few samples from Altiplano sites had exceptionally high (> 25‰) d-excess$_p$. Such high d-excess$_p$ values are uncommon in most meteoric waters (Bowen et al., 2019; Gat, 1996), but are occasionally observed in central Andean dry season precipitation (Fiorella et al., 2015b; Guy et al., 2019; Vimeux et al., 2011).

We focus on temporal $\Delta'^{17}O_p$ variation from San Gaban, Macusani, and Ayaviri because the triple oxygen isotope data from these sites span the wet and dry seasons. On the Altiplano (Macusani and Ayaviri), $\Delta'^{17}O_p$, d-excess$_p$, and $\delta^{18}O_p$ values were higher in the dry season and lower in the wet season (Figure 4.7). At San Gaban, however, $\Delta'^{17}O_p$ exhibited no seasonal variation (Figure 4.7a), as 31 ± 4 per meg (average dry season $\Delta'^{17}O_p$ ± standard deviation) and 34 ± 2 per meg (average wet season $\Delta'^{17}O_p$ ± standard deviation) are indistinguishable given analytical $\Delta'^{17}O$ precision.

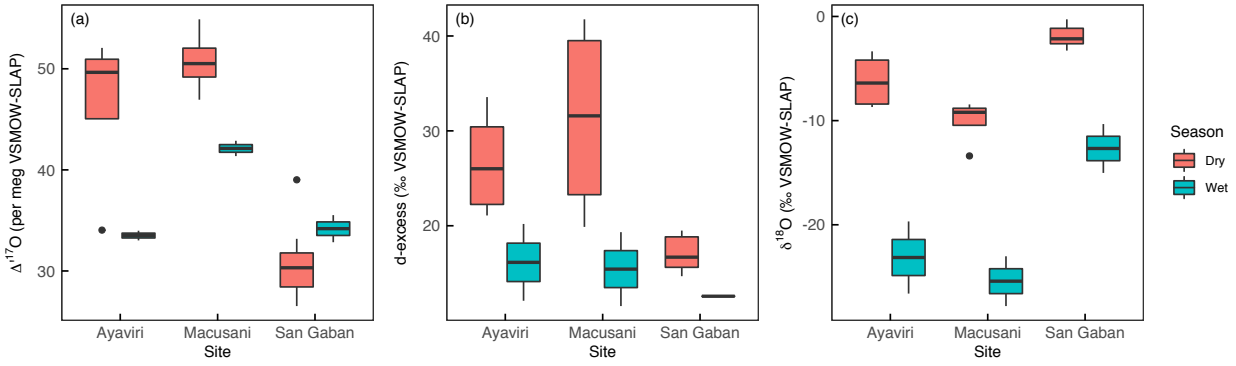

Figure 4.7 Box and whisker plots of a) $\Delta'^{17}O$ (per meg), b) d-excess (‰), and c) $\delta^{18}O$ (‰) from Ayaviri, Macusani, and San Gaban. Isotope values are separated to highlight seasonal differences between the wet (blue) and dry (red) seasons. For each population, the bolded line is the median $\Delta'^{17}O$ value, the upper and lower hinge correspond to the 1st and 3rd quartiles, respectively, and the whiskers correspond to no more than 1.5 times the interquartile range (IQR, the variation between the 1st and 3rd quartiles). The individually plotted points fall outside the IQR.

4.5.4 Spatial isotopic variation

Across all sites, the average annual amount-weighted $\delta^{18}O_p$ was strongly negatively correlated with elevation (r = –0.84, Figure 4.8a) and latitude (r = –0.70, Figure 4.8c) and nearly uncorrelated with MAP (r = –0.20, Figure 4.8b). The average annual amount-weighted $\delta^{18}O_p$ value was high at San Gaban (–7.7‰, 657 masl, 13.45˚S), decreased up the eastern flank to a minimum at Macusani (–18.8‰, 4345 masl, 14.07˚S), and was relatively consistent across the Altiplano, ranging from –18.8‰ (Macusani) to –15.9‰ (Santo Tomas, 3658 masl, 14.45˚S) (Figure 4.9b). On the western flank, average annual amount-weighted $\delta^{18}O_p$ values increased from Ubinas (–11.7‰, 3380 masl, 16.38˚S) to Quinistaquillas (–0.1‰, 1590 masl, 16.75˚S) (Figure 4.9b). The $\delta^{18}O_p$ lapse rate on the eastern flank was –3.0 ± 0.2‰/km for the full study period, but ranged from –2.8 ± 0.1‰/km in 2017 to –3.0‰/km in 2018. On the western flank, the $\delta^{18}O_p$ lapse rate was –4.4 ± 1.1‰/km and ranged from –5.3 ± 1.4‰/km in 2019 to –4.1 ± 1.4‰/km in 2018. Site-to-site correlations of bimonthly $\delta^{18}O_p$ vary across the network and were generally stronger (r values greater than 0.5) between sites on the eastern flank and eastern Altiplano than between sites on the western flank or western Altiplano (Table 4.1).

Average annual amount-weighted d-excess$_p$ values ranged from 22.1‰ (Carumas, 2976 masl) to 5.0‰ (Quinistaquillas, 1590 masl) (Figure 4.9c) and were poorly correlated with elevation (r = 0.37), latitude (r = 0.21), or MAP (r = 0.13). It is unlikely that the very high d-excess$_p$ value from Carumas (22.1‰) is representative of an average d-excess$_p$ value. This value was calculated from 9 precipitation samples collected during the 2017 rainy season when relative humidity was uncharacteristically high (~90%). Unfortunately, the observer at Carumas did not collect samples properly in 2018 and 2019, so we cannot compare interannual precipitation isotope variability at this site. Excluding this value, average annual amount-weighted d-excess$_p$ was highest at Macusani (17.3‰) and decreased from north to south across the Altiplano (Figure 4.9c). Amount-weighted mean d-excess$_p$ values were lower at sites on the western flank (5.0 to 13.3‰) than at sites on the Altiplano or eastern flank (12.4 to 17.3‰) (Figure 4.9c).

The 32 precipitation samples selected for triple oxygen isotope analysis are from 7 sites (San Gaban, Ollachea, Macusani, Ayaviri, Santo Tomas, Carumas, and Majes). We observe relatively little $\Delta'^{17}O_p$ temporal variation at each site, but consistent spatial patterns across southern Peru. In general, $\Delta'^{17}O_p$ was higher on the Altiplano (29 to 55 per meg) and lower on the dry

western flank (1 to 35 per meg). Excluding the precipitation samples with very high (> 25‰) d-excess, $\Delta'^{17}O_p$ was weakly correlated with elevation (r = 0.43, Figure 4.8d) and latitude (r = 0.47, Figure 4.8f) and uncorrelated with MAP (r = 0.19, Figure 4.8e). Surface water $\Delta'^{17}O$ was highest in rivers along the eastern flank (50 to 54 per meg) and lowest (–7 and –5 per meg) in lake samples (Figure 4.8d). On the Altiplano, surface water $\Delta'^{17}O$ values were uncorrelated with elevation (r = 0.04) and moderately positively correlated with latitude (r = 0.56).

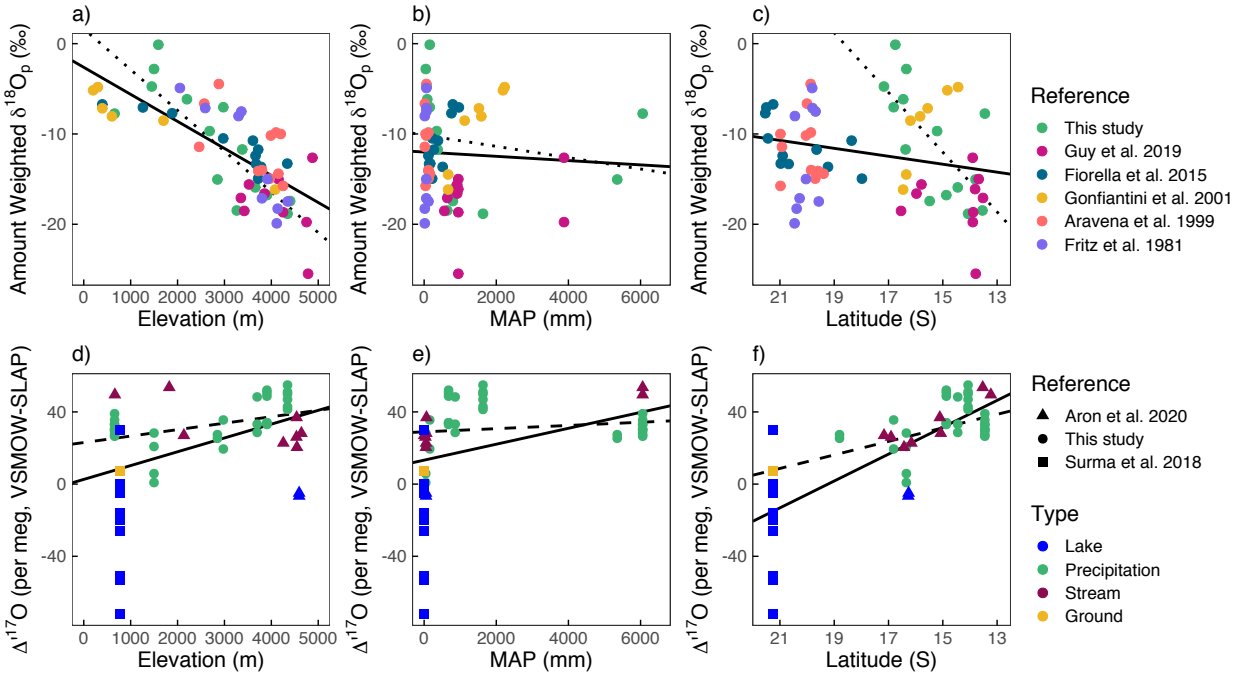

Figure 4.8 Scatterplots of central Andean amount weighted mean $\delta^{18}O_p$ and $\Delta'^{17}O$ variation with elevation (a and d), MAP (mean annual precipitation, b and e), and latitude (c and f). In panels a), b), and c), color differentiates $\delta^{18}O_p$ from the six available studies. In panels d), e), and f), shape differentiates the available studies and color differentiates water type. In every panel, the solid black line is the best fit linear regression through from all water types and studies. The dotted line (panels a), b), and c)) is the best fit linear regression through $\delta^{18}O_p$ data from this study. The dashed line (panels d), e), and f)) is the best fit linear regression through $\Delta'^{17}O_p$ data from samples in this study with d-excess$_p$ within one standard deviation of the site-specific amount weighted mean d-excess$_p$. We exclude samples with d-excess$_p$ beyond one standard deviation of the amount weighted mean from the dashed linear regression because these samples are likely not representative of average isotopic compositions.

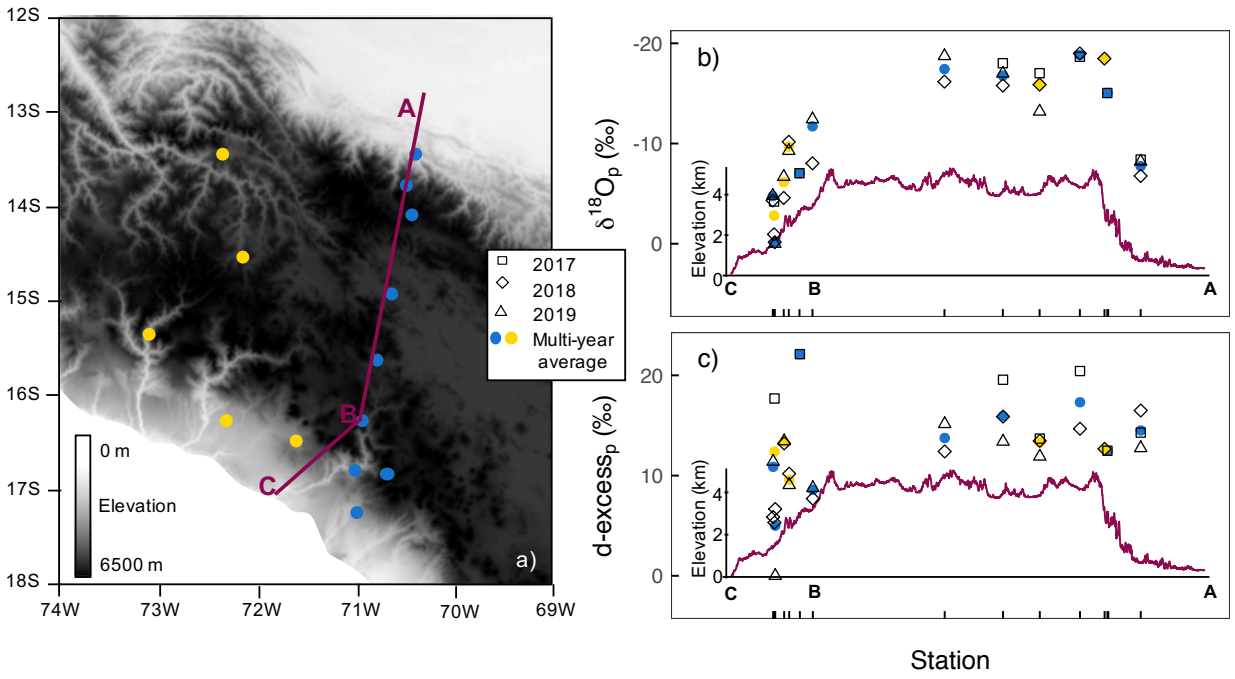

Figure 4.9 Elevation profile along the A-B-C transect a) and spatiotemporal variability of average annual amount-weighted b) $\delta^{18}O_p$ and c) d-excess$_p$ in southern Peru. In b) and c), the filled yellow and blue circles represent the multiyear average. Blue sites fall on or near the elevation profile; an elevation profile through the yellow sites is not shown, but the dominant topographical features through this region are the same as those along the A-B-C transect. The open symbols show amount-weighted $\delta^{18}O_p$ and d-excess$_p$ values in 2017 (square), 2018 (diamond), and 2019 (triangle). Throughout the region, d-excess$_p$ is relatively invariant and $\delta^{18}O_p$ is inversely related to elevation, indicating Rayleigh distillation along both flanks and distinct moisture sources from the Atlantic and Pacific.

Table 4.1 Correlation coefficient (Pearson r) matrix between bimonthly $\delta^{18}O_p$ timeseries. Missing (NA) correlations occur when samples were not collected concurrently. Bolded values indicate a statistically significant ($p < 0.05$) relationship.

	OLL	MAC	AYV	CUZ	SNT	PAM	COT	UBN	CAR	MOQ	AQP	QUI	MAJ
SGN	0.02	**0.65**	**0.67**	-0.04	**0.60**	0.29	0.22	0.09	0.18	0.48	0.44	-0.22	0.15
OLL		0.36	-0.07	*NA*	0.20	*NA*	*NA*	*NA*	-0.30	*NA*	*NA*	*NA*	-0.22
MAC			**0.68**	0.47	**0.63**	-0.08	0.09	*NA*	0.30	0.91	0.32	*NA*	-0.47
AYV				0.88	**0.62**	**0.61**	**0.49**	0.26	0.40	0.18	**0.60**	0.71	-0.43
CUZ					*NA*	0.36	0.38	*NA*	*NA*	*NA*	*NA*	*NA*	*NA*
SNT						0.24	0.37	0.17	0.80	-0.70	0.40	*NA*	0.10
PAM							**0.54**	0.51	*NA*	-0.23	0.25	0.19	-0.95
COT								0.27	*NA*	-0.29	**0.91**	0.96	0.73
UBN									*NA*	-0.25	0.73	*NA*	*NA*
CAR										*NA*	*NA*	*NA*	-0.80
MOQ											-0.07	*NA*	*NA*
AQP												0.97	*NA*
QUI													*NA*

4.5.5 Atmospheric back trajectories

Moisture trajectories varied across the region and switched from an eastern-dominated moisture source on the eastern flank to a western-dominated moisture source on the western flank (Figure 4.10). At San Gaban, the low elevation eastern flank site, moisture was sourced entirely from the east (Atlantic Ocean and Amazon Basin) and varied little throughout the study period (Figure 4.10a). Eastern-sourced moisture dominated (> 70%) at Santo Tomas and Ayaviri (central Altiplano, Figures 4.10b and 4.10c), but these sites also received some western sourced moisture. The contribution of western moisture to Santo Tomas and Ayaviri was typically higher in the spring and summer (~20%) and lower in the winter and fall (~5-10%). High on the western flank, Cotahuasi and Ubinas received moisture from a combination of eastern and western sources (Figures 4.10d and 4.10e). Western sourced moisture accounted for more than 50% of the moisture flux during the spring and summer and ~20-30% in the winter and fall at these sites (Figures 4.10d and 4.10e). Western sourced moisture dominated (> 90%) at low elevation on the western flank (Majes and Moquegua, Figures 4.10f and 4.10g). Moisture fluxes from oceanic sources (open symbols in Figure 4.10) were generally smaller than those from terrestrial regions on the eastern flank, Altiplano, and high western flank (closed symbols in Figure 4.10). The direct Atlantic moisture flux was very small (< 10%) because the moisture tracer identified increases in specific humidity from evapotranspiration over the Amazon Basin as a moisture source region.

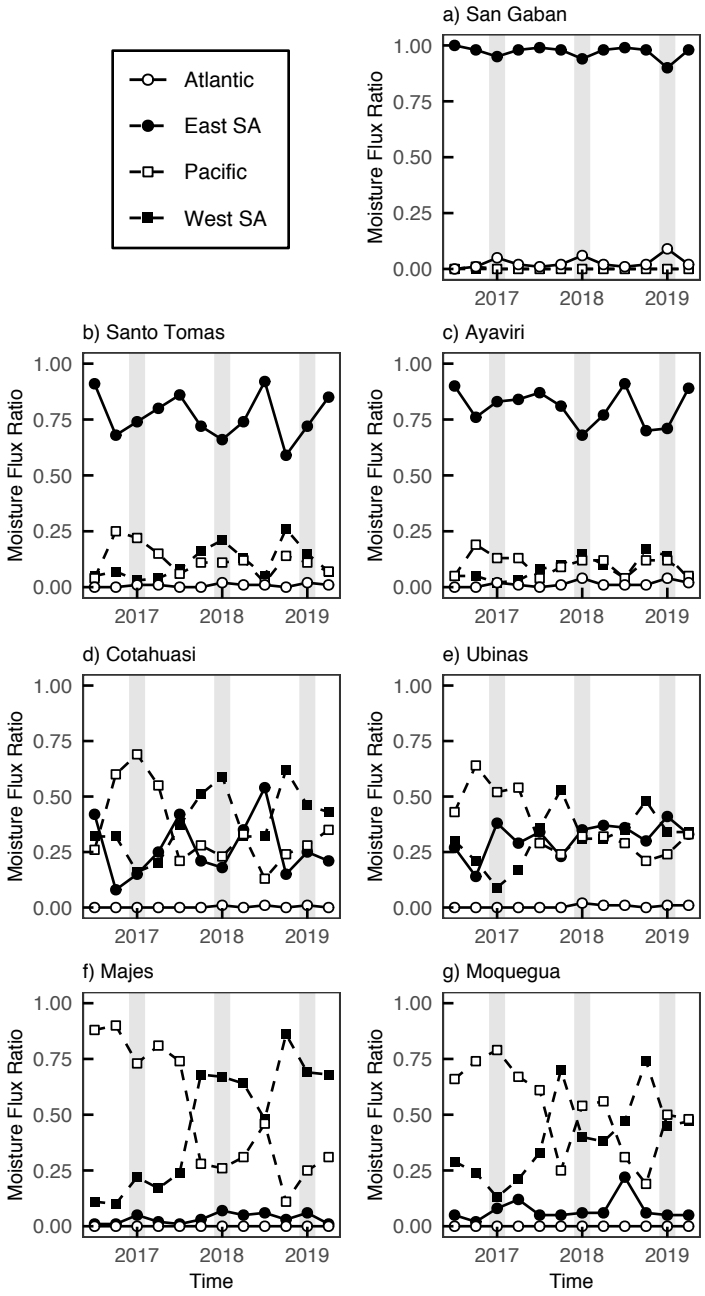

Figure 4.10 Timeseries of moisture fluxes from four regions at a) San Gaban, b) Santo Tomas, c) Ayaviri, d) Cotahuasi, e) Ubinas, f) Majes, and g) Moquegua. The points represent the ratio of moisture advected from each source region relative to the total moisture flux. Filled symbols indicate land-based source regions; open symbols indicate oceanic source regions. Eastern (Atlantic (open) and eastern South America (filled)) source regions are plotted as circles; western (Pacific (open) and western South America (filled)) source regions are plotted as squares. The gray vertical bars indicate the DJF rainy season in 2017, 2018, and 2019.

4.6 Discussion

4.6.1 Controls on central Andean $\delta^{18}O_p$

The most pronounced temporal $\delta^{18}O_p$ variation is a seasonal pattern with higher $\delta^{18}O_p$ values in the dry season and lower $\delta^{18}O_p$ values in the wet season (Figures 4.6a and 4.6b). This seasonal pattern is observed throughout the central Andes (Aravena et al., 1999; Fiorella et al., 2015b; Fritz et al., 1981; Gonfiantini et al., 2001; Guy et al., 2019) and results from a number of fractionating processes. First, a strengthening of the SALLJ increases upstream precipitation, which preferentially removes heavy isotopes and results in lighter isotopic compositions in vapor advected to the central Andes during the wet season (Fiorella et al., 2015b; Guy et al., 2019; Vimeux et al., 2005, 2011). Second, deep convection can entrain isotopically light vapor from the upper and middle troposphere and decrease $\delta^{18}O_p$ values collected at the surface (Blossey et al., 2010; Galewsky et al., 2016; Lee and Fung, 2010; Moore et al., 2014; Risi et al., 2008; Samuels-Crow et al., 2014a; Worden et al., 2007). Although small, localized convective cells can entrain near-surface vapor with relatively high isotopic compositions and increase $\delta^{18}O_p$ values (Aggarwal et al., 2016; Kurita, 2013; Tharammal et al., 2017), the high elevation Altiplano and intense daytime heating across the Amazon Basin destabilize the atmosphere and lead to the development of deep convective cells (Garreaud et al., 2003, 2009; Vuille et al., 1998) that can decrease $\delta^{18}O_p$ values in this region. Convective precipitation is more common on the Altiplano during the rainy season when the moisture flux onto the Altiplano is greater (Garreaud, 2009). Third, water droplets likely undergo very little sub-cloud evaporation during the wet season when the air column is nearly saturated and relative humidity is high (Figure 4.3c). With little sub-cloud evaporation, the $\delta^{18}O$ value of rain droplets does not increase during descent. Generally, these processes are consistent on interannual timescales and across the central Andes (Figure 4.11a).

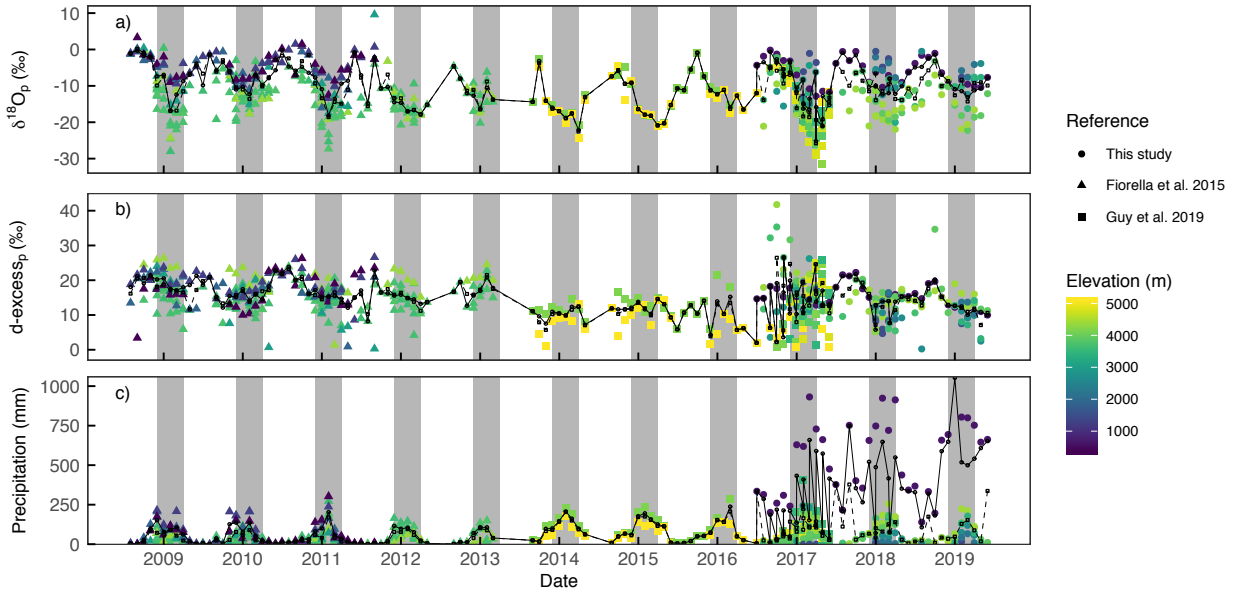

Figure 4.11 Timeseries of monthly a) $\delta^{18}O_p$, b) d-excess$_p$, and c) precipitation from this study (circles), Fiorella et al., 2015 (triangles), and Guy et al., 2019 (squares). The vertical gray bars mark the DJFM rainy season. Because elevation is the dominant control on $\delta^{18}O_p$, data are colored by site-specific elevation. The thin black line connects the timeseries of amount weighted (small open black circles) and median (small open black squares) values. The difference between amount weighted and median values is small, except for precipitation data at San Gaban, the low elevation site on the eastern flank in southern Peru. Although this site receives almost an order of magnitude more rain than any other site in these records, $\delta^{18}O_p$ and d-excess$_p$ values are similar and follow a consistent seasonal pattern with higher $\delta^{18}O_p$ and d-excess$_p$ values in the dry season and lower values in the wet season.

Spatial variability of bimonthly $\delta^{18}O_p$ values is likely driven by a combination of synoptic and local scale controls. Site-to-site correlations of bimonthly $\delta^{18}O_p$ values are stronger on the eastern flank and eastern Altiplano (Table 4.1) because so much moisture is transported up the eastern flank by synoptic-scale air flow. Site-to-site correlations are weaker on the western Altiplano and western flank (Table 4.1) because precipitation is more sporadic and variable. Occasionally, concurrent bimonthly $\delta^{18}O_p$ values from neighboring sites on the Altiplano differed by up to 15‰ (Figures 4.6a and 4.6b), so we also cannot rule out effects of local-scale controls from small-scale convergence and convection (Kumar et al., 2019; Romatschke and Houze, 2010), local topography such as ridges and valleys that funnel moisture (Giovannettone and Barros, 2009), or the addition of water vapor from evaporation of local lakes or other surface water (Delclaux et al., 2007; Pillco Zolá et al., 2019) on $\delta^{18}O_p$ across the study region.

To identify the environmental controls on amount-weighted central Andean $\delta^{18}O_p$ values, we performed a stepwise multiple linear regression with elevation, latitude, longitude, and MAP as possible predictor variables (Bowen and Wilkinson, 2002; Lechler and Niemi, 2011). We excluded temperature because it is very strongly correlated with elevation ($r = –0.97$) across our study region. The stepwise multiple linear regression iteratively tests and removes predictor variables to determine the best fit regression model with the fewest input parameters. Each model iteration was assessed with the Akaike information criterion (AIC), and the iterative process stopped when the lowest AIC score was reached. Low AIC scores balance goodness of model fit with model parsimony.

The regression model of southern Peru $\delta^{18}O_p$ data with the lowest AIC score includes elevation and latitude as predictor variables (Table S4.3). A similar stepwise multiple linear regression analysis of $\delta^{18}O_p$ data from central (Gonfiantini et al., 2001) and southern (Fiorella et al., 2015b) Bolivia retains models with elevation and MAP (Gonfiantini et al., 2001) and elevation (Fiorella et al., 2015b) as predictor variables. We compare our results from southern Peru against these two datasets because $\delta^{18}O_p$ and elevation are strongly correlated in the central Andes (Figure 4.8a) and $\delta^{18}O_p$ observations from these studies span over 4000 m in elevation ($\delta^{18}O_p$ and $\delta^{2}H_p$ in Aravena et al. (1999), Fritz et al. (1981), and Guy et al. (2019) only span approximately 2000 m each). Together, these results reveal that elevation is a dominant control on $\delta^{18}O_p$ throughout the central Andes, but that there is less consistency among other predictor variables. Here we focus on latitude because it is retained in the best fit model of the southern Peru $\delta^{18}O_p$ data and because focusing on this latitude–$\delta^{18}O_p$ relationship leads to new insights about hydrology in the central Andes.

Latitude is not directly associated with a water isotope fractionation, but is well correlated with average annual amount-weighted $\delta^{18}O_p$ values from southern Peru (Figure 4.8c) and is a statistically significant predictor variable of $\delta^{18}O_p$ in our dataset (Table S4.3). A similar relationship between $\delta^{18}O_p$ and latitude is not observed in other central Andean precipitation isotope studies (Figure 4.8c), and there is no clear mechanism that predicts a relationship between precipitation isotopes and latitude in this region. Instead, the relationship between $\delta^{18}O_p$ and latitude in southern Peru results from rainout of distinct eastern- and western-derived moisture on the flanks of the Eastern and Western Cordilleras, respectively (Figure 4.10). As these airmasses

ascend, they cool adiabatically and preferentially lose heavy isotopologues during condensation (Figure 4.8a). The inverse elevation–$\delta^{18}O_p$ relationship on the eastern flank is well established (Fiorella et al., 2015b; Gonfiantini et al., 2001) and is related to Rayleigh distillation of Atlantic and Amazonian sourced moisture during orographic precipitation. The inverse relationship between elevation and $\delta^{18}O_p$ observed on the western flank (Figures 4.6b and 4.8a) suggests that Western Cordillera precipitation isotopes reflect Rayleigh distillation of Pacific sourced moisture. Atmospheric back trajectories affirm this interpretation (Figure 4.10). Independently, neither precipitation isotopes nor moisture trajectories could verify the influence of western-sourced moisture. Here, the combination of these techniques shows that not only is western-sourced vapor transported towards the central Andes (inferred from moisture trajectories), but also that this water makes it to the ground as precipitation (inferred from high $\delta^{18}O_p$ values). High western flank $\delta^{18}O_p$ values could alternatively be explained by post-condensation evaporation, either as raindrops fell or before precipitation samples were transferred from the collection buckets, but annual average amount-weighted d-excess$_p$ values at western flank sites are ~10‰ (Figures 4.6d and 4.9c) and indicate very little evaporative effect on $\delta^{18}O_p$ values.

Finally, MAP is uncorrelated ($r = –0.06$) with average annual amount-weighted $\delta^{18}O_p$ (Figure 4.8b) throughout the central Andes. These correlations do not improve substantially between bimonthly ($r = 0.13$**,** our data) or monthly ($r = –0.08$, all available monthly data) data. Although the "amount effect", an observed inverse relationship between local monthly precipitation amount and monthly $\delta^{18}O_p$ values is used to explain variations in the isotopic composition of tropical precipitation (Dansgaard, 1964), we do not observe a relationship between $\delta^{18}O_p$ values and local precipitation amount in the central Andes (Figure 4.8b). The amount effect has been used to explain $\delta^{18}O$ variation in the Amazon Basin (e.g., Brienen et al., 2012; van Breukelen et al., 2008; Wang et al., 2017) and some central Andean ice cores (e.g., Hurley et al., 2015), but local precipitation rates are frequently poor predictors of tropical precipitation isotopes (e.g., Vimeux et al., 2005) because factors such as upstream rainout, evapotranspiration, moisture convergence, and cloud type affect isotopic composition of precipitation but are not necessarily correlated with local precipitation amount (Konecky et al., 2019).

4.6.2 ENSO and central Andean $\delta^{18}O_p$

The climate in the central Andes is modulated by global circulation phenomena and regional atmospheric teleconnections, including the Madden-Julian Oscillation (MJO, Madden and Julian, 1994), El Niño Southern Oscillation (ENSO, Cai et al., 2020), Pacific Decadal Oscillation (PDO, Mantua et al., 1997), Arctic (AO) and Antarctic (AAO) Modes (Thompson and Wallace, 2000), and North Atlantic Oscillation (NAO, Garreaud et al., 2009; Paegle et al., 2000). Of these, ENSO is the dominant control on interannual climate variability in South America and accounts for approximately two thirds of the interannual precipitation and temperature fluctuations (Garreaud et al. 2009).

In the central Andes, negative phase ENSO (El Niño) conditions generally lead to above average rainfall along the west coast and below average rainfall in the Amazon and Altiplano (Cai et al., 2020; Diaz et al., 1998; Garreaud et al., 2009; Montini et al., 2019; Silva and Ambrizzi, 2006; Viale et al., 2018). ENSO driven $\delta^{18}O$ variability has been observed in central Andean precipitation (Fiorella et al., 2015b; Guy et al., 2019; Vuille and Werner, 2005), climate model simulations (Insel et al., 2013; Vuille, 2003; Vuille et al., 2003), and ice cores (Bradley et al., 2003; Hardy et al., 2003; Hoffmann, 2003; Hoffmann et al., 2003; Thompson et al., 2017, 1984). In general, ENSO causes higher $\delta^{18}O_p$ values in regions with lower rainfall and lower $\delta^{18}O_p$ values in regions with more rainfall, although the relationship between ENSO and $\delta^{18}O_p$ is complex and variable (Thompson et al., 2017; Vimeux et al., 2009).

Our study period followed a very strong El Niño in 2015-2016 and occurred during weak La Niña (2016-2017 and 2017-2018) and weak El Niño (2018-2019) conditions (National Weather Service, Climate Prediction Center). In this study, we observe no clear relationship between $\delta^{18}O_p$ and ENSO (Figures 4.6a and 4.6b). Average annual amount-weighted $\delta^{18}O_p$ varied up to 4‰ at each site (Figure 4.9b), but was not consistently lower in 2016-2017 and 2017-2018 nor higher in 2018-2019. The longer precipitation isotope record (Figure 4.11) includes strong La Niña (2010-2011) and El Niño (2015-2016) events that do have lower and higher $\delta^{18}O_p$ values, respectively (Figure 4.11a). However, the interannual variability of $\delta^{18}O_p$ is inconsistent with weaker ENSO events from 2008-2019, indicating that the relationship between ENSO and central Andean $\delta^{18}O_p$ is complex and does not follow a simple high precipitation/more negative $\delta^{18}O_p$ (La Niña) or low precipitation/less negative $\delta^{18}O_p$ (El Niño) pattern. Broadly, the absence of a clear relationship

between ENSO and $\delta^{18}O_p$ is further evidence that the amount effect does not fully account for $\delta^{18}O_p$ variability in the central Andes.

4.6.3 Additional hydrologic information from d-excess and $\Delta'^{17}O$

To this point, interpretations of precipitation isotopes have mainly focused on $\delta^{18}O_p$ and isotopic variability that results from large-scale circulations patterns, rainout, and convection. However, processes such as evaporation, moisture recycling, and airmass mixing also affect central Andean water cycling and isotope variability. In this section, we focus on d-excess and $\Delta'^{17}O$, which are sensitive to relative humidity and hydrologic mixing, and show how these data complement $\delta^{18}O$.

High (> 10‰) d-excess$_p$ values are common in the central Andes due to moisture recycling and evapotranspiration (ET) from the Amazon Basin (Ampuero et al., 2020; Lettau et al., 1979; Salati et al., 1979). In this study, we observe high d-excess$_p$ values and two primary types of d-excess$_p$ variation: 1) a consistent 5-10‰ seasonal cycle with higher d-excess$_p$ values in the dry season and lower d-excess$_p$ values in the wet season and 2) infrequent high (> 25‰) dry season d-excess$_p$ values at Altiplano stations (Figures 4.6c, 4.6d, and 4.11c).

Seasonal variations in d-excess$_p$ are most prominent at San Gaban (Figure 4.6c), the lowest elevation site on the eastern flank, where the precipitation isotope record is continuous and moisture is sourced entirely from the tropical Atlantic and Amazon Basin (Figure 4.10a). Though muted, a similar seasonal d-excess$_p$ cycle is also observed in central Bolivia (Figure 4.11b). The seasonal d-excess$_p$ cycle may be related to changes in near-surface relative humidity above the tropical Atlantic (Dai, 2006; Pfahl and Sodemann, 2014) and land-atmosphere water fluxes as moisture is transported across the Amazon Basin (Ampuero et al., 2020; Gallaire et al., 2000; Gonfiantini et al., 2001; Roche et al., 1999; Salati et al., 1979). When relative humidity above the tropical Atlantic is lower (e.g., during JJAS), the kinetic fractionation associated with evaporation and the diffusion of water vapor through the air is larger and the d-excess of evaporated vapor is higher. When relative humidity above the tropical Atlantic is higher (e.g., during DJFM), water vapor undergoes a smaller kinetic fractionation and the d-excess of evaporated vapor is lower. Assuming isotopic equilibrium during condensation, downstream precipitation of these airmasses will retain vapor d-excess signals and have higher d-excess$_p$ in the winter and lower d-excess$_p$ in the summer. Similar logic could also explain seasonal $\Delta'^{17}O_p$ variation.

In addition to seasonal variations in remote relative humidity, ET fluxes from the Amazon Basin may amplify the observed d-excess$_p$ and $\Delta'^{17}O_p$ cycles. Although complex heterogeneity of vegetation and soil moisture (Marengo, 2005) makes separating evaporation and transpiration fluxes in the Amazon a challenge (Eltahir and Bras, 1994; Lawrence et al., 2007; Xu et al., 2019), an increase in the bare ground evaporation flux from the Amazon during the dry season would theoretically increase the d-excess and $\Delta'^{17}O$ of local vapor and downstream precipitation. However, additional work is needed on Amazon and Andean vapor and precipitation isotope variability to understand the magnitude of this effect (Pattnayak et al., 2019) and to decouple the kinetic isotope effects of ET and moisture source conditions. Higher western South America spring and summer moisture flux ratios (Figures 4.10b-g) may point to seasonal ET fluxes on the Western Cordillera as well, although additional work is needed in this region to observe and understand the role of plants in terrestrial water cycling in the very dry western central Andes.

Generally, the $\Delta'^{17}O$ values reported here are similar to the range of meteoric water $\Delta'^{17}O$ values from previous studies in the central Andes (Aron et al., 2020; Herwartz et al., 2017; Surma et al., 2018) and other tropical precipitation (Landais et al., 2010). Central Andean surface water d-excess and $\Delta'^{17}O$ covary ($r = 0.92$, Figure 4.5b) and are sensitive to well-established kinetic fractionations. For example, low d-excess (–12.6 and –31.8‰) and $\Delta'^{17}O$ (–5 and –7 per meg) from lake water on the Altiplano are indicative of evaporation; high d-excess (20.3 and 20.5‰) and $\Delta'^{17}O$ (54 and 50 per meg) from eastern flank streams are associated with upstream moisture recycling (Salati et al., 1979).

Temporal variations of $\Delta'^{17}O_p$, and the relationship with d-excess$_p$, are more complicated. On the Altiplano (Macusani and Ayaviri), $\Delta'^{17}O_p$ is generally well correlated with d-excess$_p$, with higher $\Delta'^{17}O_p$ values in the dry season and lower $\Delta'^{17}O_p$ values in the wet season (Figures 4.7a and 4.7b). However, at San Gaban, where the seasonal d-excess$_p$ variation is very pronounced (Figure 4.6c), $\Delta'^{17}O_p$ values are nearly invariant (Figure 4.7a). In this case, the difference between wet and dry season d-excess$_p$ at San Gaban is ~4.6‰ (Figure 4.7c). Using the observed slope between d-excess$_p$ and $\Delta'^{17}O_p$ in this study (0.8 per meg ‰$^{-1}$) or the maximum possible steady-state d-excess–$\Delta'^{17}O$ slope (2 per meg ‰$^{-1}$) (Barkan and Luz, 2007), this 4.6‰ d-excess variation translates to an expected ~4 to 10 per meg $\Delta'^{17}O$ variation. This range is similar to or smaller than the analytical $\Delta'^{17}O$ precision in this study (7 per meg) and the long-term $\Delta'^{17}O$ precision (~10 per meg) reported

by our lab (Aron et al., 2020; Li et al., 2017, 2015; Passey and Ji, 2019) and other triple oxygen isotope labs (e.g., Berman et al., 2013; Schauer et al., 2016). This suggests that seasonal $\Delta'^{17}O_p$ variation may exist, but is too small to be observed in this dataset. The relationship between $\Delta'^{17}O_p$ and d-excess$_p$ may also be affected by moisture transport. For example, airmass mixing at Majes (a low elevation, western flank site) may explain why $\Delta'^{17}O_p$ is low (~3 per meg) but d-excess$_p$ high (~16‰) in March 2017 (Figure 4.5b).

Finally, we focus on the samples with very high d-excess$_p$ (> 25‰) and $\Delta'^{17}O_p$ (> 40 per meg) (Figures 4.5a and 4.5b). Such high d-excess$_p$ values are uncommon in tropical precipitation, but are occasionally observed elsewhere in the central Andes (Fiorella et al., 2015b; Guy et al., 2019; Vimeux et al., 2011) and other high elevation regions (Liotta et al., 2006). These high d-excess$_p$ values are thought to reflect kinetic fractionation during ice crystal formation (Jouzel and Merlivat, 1984) and precipitation at very low temperatures (Samuels-Crow et al., 2014b) or deep convection (Bony et al., 2008; Galewsky et al., 2016) that is common on the Altiplano (Garreaud et al., 2003). Similarly high $\Delta'^{17}O_p$ values are observed in winter or cold season dominated precipitation in the western and central US (Li et al., 2015; Tian et al., 2018). Such high $\Delta'^{17}O_p$ values may result from condensation at cold (< 0 ˚C) temperatures (Aron et al., 2020; Luz and Barkan, 2010), which likely occurs during deep convection. However, the vertical profile of $\Delta'^{17}O$ through the atmosphere is largely unknown (Risi et al., 2013), and more work is needed to explain seasonal $\Delta'^{17}O_p$ variation. High winter $\Delta'^{17}O_p$ values are likely related to small temperature dependent variations between $\delta^{18}O$ and $\delta^{17}O$, but this is an ongoing area of research.

Despite the analytical limitations and spatiotemporal uncertainties of $\Delta'^{17}O_p$ variation, most of the triple oxygen isotope data from the central Andes agree with theoretical expectations and observations of global hydrologic triple oxygen isotope variability (Aron et al., 2020; Luz and Barkan, 2010). Clearly, additional work is still needed to observe and understand the hydrologic processes and environmental conditions that cause $\Delta'^{17}O$ to vary, but these results show that the triple oxygen isotope system is a useful tracer of modern hydrologic processes and is an appealing metric of paleohydrologic conditions.

4.6.4 Implications for paleoaltimetry and paleoclimate

Observations of modern precipitation isotopes help evaluate isotope-enabled climate models (e.g., Brady et al., 2019; Insel et al., 2013; Vuille et al., 2003) and inform interpretations

of proxy-based isotope records (e.g., Apaéstegui et al., 2018; Canavan et al., 2014; Cassel et al., 2014; Polissar et al., 2009; Quade et al., 2015; Thompson et al., 2000). In the central Andes, these models and proxies are used to answer an array of questions about paleoclimate (e.g., Baker et al., 2001; Bershaw et al., 2010; Mulch et al., 2010; Vimeux et al., 2009), paleoaltimetry (e.g., Garzione et al., 2008; Kar et al., 2016; Leier et al., 2013), paleohydrology (e.g., Jordan et al., 2019; Poulsen et al., 2010; Rech et al., 2019), and paleocirculation (e.g., Carrapa et al., 2019; Feng and Poulsen, 2014; Insel et al., 2010; Rohrmann et al., 2016). In particular, the timing and geodynamical processes of Andean uplift remain a topic of ongoing work (e.g., Barnes and Ehlers, 2009; Ehlers and Poulsen, 2009; Garzione et al., 2008; Saylor and Horton, 2014; Sundell et al., 2019), and many attempts to reconstruct Andean elevations have relied on the stable isotope ratios from geologic materials (Garzione et al., 2017; Rowley and Garzione, 2007).

Isotopic lapse rates are a critical, but challenging, component of paleoaltimetry studies. Generally, the eastern flank $\delta^{18}O_p$ lapse rates observed in the central Andes are similar to the empirically derived global average windward $\delta^{18}O$ lapse rate (–2.8‰/km, Poage and Chamberlain, 2001; Quade et al., 2007a) and thermodynamic models of the isotope-elevation relationship (Rowley, 2007; Rowley et al., 2001). The eastern flank $\delta^{18}O_p$ lapse rate in southern Peru (–3.0 ± 0.2‰/km, Figure 4.8a, this study) is slightly steeper than $\delta^{18}O_p$ lapse rates in northern (–2.0 ± 0.3‰/km, Gonfiantini et al., 2001) and southern (–1.9 ± 0.3‰/km, Fiorella et al., 2015) Bolivia, although all three are within one per mil of the global average. The differences among these $\delta^{18}O_p$ lapse rates may be related to relationships between local topography and moisture transport or vertical atmospheric temperature profiles. Western flank $\delta^{18}O_p$ lapse rates are less consistent with the global average and range from –4.4 ± 1.1‰/km in southern Peru (Figure 4.9b) to ~–10‰/km in northern Chile (Aravena et al., 1999; Fritz et al., 1981). Stream water from the flank of the Western Cordillera in southern Peru also record a $\delta^{18}O$ lapse rate ~–10‰/km (Bershaw et al., 2016). Such steep isotopic lapse rates are inconsistent with Rayleigh distillation (Rowley, 2007), and likely result from the mixing of low elevation Pacific sourced moisture (high $\delta^{18}O$) with high elevation Atlantic sourced moisture (low $\delta^{18}O$) (Aravena et al., 1999). In southern Peru, the western flank $\delta^{18}O$ lapse rate is steeper from stream water than from precipitation because high elevation streams drain melted snow and ice (low $\delta^{18}O$ (typically < –15‰), Bershaw et al., 2016) whereas precipitation originates from western moisture sources and $\delta^{18}O$ values tend to be higher

(Figure 4.6b). These results highlight the substantial variability in $\delta^{18}O$ lapse rates throughout the central Andes and the importance of precipitation isotope data in paleoaltimetry studies. Moving forward, paleoaltimetry estimates should carefully consider isotopic lapse rates on a case-by-case basis (e.g., Sundell et al., 2019) because these elevation-isotope relationships are not constant across the region.

Another challenge in interpreting central Andean isotope data is the potential for evaporative enrichment. Low d-excess values make evaporative effects relatively easy to detect in waters (e.g., Fiorella et al., 2015a). Traditionally there has not been an equivalent metric to identify evaporative effects in the geologic record because very few geologic materials have both oxygen- and hydrogen-containing minerals. Triple oxygen isotopes can fill this gap because oxygen-bearing materials contain all three stable oxygen isotopes and $\Delta'^{17}O$ is sensitive to kinetic fractionation (Barkan and Luz, 2007). Like d-excess, $\Delta'^{17}O$ is lower in evaporated materials (Figure 4.5b) and is relatively insensitive to changes in elevation (Figure 4.8d). Here we show that $\Delta'^{17}O$ in waters faithfully records information about regional climate and hydrology in the central Andes. This suggest that triple oxygen isotope data from oxygen-bearing geologic minerals can help determine paleoaridity or paleohumidity (Gázquez et al., 2018; Surma et al., 2018), reconstruct the isotopic composition of paleo-precipitation (Passey and Ji, 2019), and differentiate evaporative isotope effects from those that reflect uplift or mountain building (Rech et al., 2019).

Finally, we note the potential influence of Pacific-sourced water vapor on central Andean paleoaltimetry. A Pacific moisture source has been inferred from precipitation isotope records in some regions of northern Chile and the Atacama Desert (Aravena et al., 1999; Herrera et al., 2018; Valdivielso et al., 2020), but is generally disregarded in Western Cordilleran water budgets (Garreaud, 1999; Garreaud et al., 2010) and in reconstructions of central Andean paleoaltimetry (e.g., Garzione et al., 2006). Results from this study suggest that Pacific-sourced moisture plays an important role in the dry western central Andes and may affect the isotopic composition of geologic materials in that region.

4.7 Conclusion

Precipitation isotopes in the central Andes record atmospheric circulation (e.g., airmass mixing and convection), land-atmosphere water fluxes, and information about moisture sources. In this study, we combined a new three-year record of bimonthly $\delta^{18}O_p$ and $\delta^{2}H_p$ from southern

Peru with recent and contemporaneous $\delta^{18}O_p$ and d-excess$_p$ from the central Andes (Fiorella et al., 2015b; Guy et al., 2019) to improve our understanding of spatiotemporal precipitation isotope variability in this region. First, we find consistent seasonal $\delta^{18}O_p$ and d-excess$_p$ cycles with higher values in the dry season and lower values in the wet season. Seasonal $\delta^{18}O_p$ is related to upstream precipitation (e.g., Fiorella et al., 2015b; Guy et al., 2019; Vimeux et al., 2005) and deep convection (e.g., Galewsky et al., 2016; Moore et al., 2014); seasonal d-excess$_p$ likely reflects variations in relative humidity at remote moisture sources (Dai, 2006; Pfahl and Sodemann, 2014) and possibly a seasonal shift in the partitioning of Amazonian evapotranspiration fluxes (Ampuero et al., 2020; Pattnayak et al., 2019). Second, using atmospheric back trajectories and $\delta^{18}O_p$ we identify a clear Pacific moisture source in the dry western central Andes. Monitoring and quantifying Pacific-sourced vapor may play an important role in managing freshwater resources in coastal Peru because this region receives very little precipitation but is home to major metropolitan centers (e.g., Lima and Arequipa). Third, we show that d-excess and $\Delta'^{17}O$ covary and record information about moisture recycling, evaporation, local convection, and cold-temperature condensation in the central Andes. This suggests that triple oxygen isotopes may help disentangle isotope records from evaporative enrichment (Quade et al., 2007b; Rech et al., 2019) from those that reflect uplift and mountain building processes. Together, these results highlight the utility of precipitation isotopes to trace and quantify water cycling and hydrologic change in the central Andes.

Acknowledgements and funding

We thank the many, many individuals in Peru who supported this project and collected precipitation samples. This includes: Edgar Garcia Peña, Jose Antonio Luna Zapata, Sixto Flores Sancho, Jose Dionicio Cardenas Roque, Franco Rufino Bedoya Prado, Elsa Elizabeth Monesimos Aliaga, Lenor Abila de Morocc, Rosalio Washington Coaquira, Monica Quispe Ramos, Fanny Cahouana, Julia Socorro Villca, Yisenia Lopez Vilco, Fernando Apaza Vilca, Sonia Pari Zapana, Alberto Arana Mamani, Juana Lidra Apaza Cari, Francisco Ligue, Susana Gonzalez Yañez, Erick Diego Ramos Gonzalez, Rolando Palamo Ticona, Pascual Merma Ortiz, Julio Manzano Sanchez, Rosa, Lucio, Pascula and Roque Zanabria Alvarado. This work was supported by NSF Tectonics Program award 1550101. In addition, PGA received support from a Rackham Predoctoral

Fellowship, two Rackham Graduate Student Research Awards, a Rackham International Research Award, and the Scott Turner Award from the Department of Earth and Environmental Sciences.

4.8 References

Aceituno, P., 1988. On the Functioning of the Southern Oscillation in the South American Sector. Part 1: Surface Climate. Mon. Weather Rev. 116, 505–524.

Aemisegger, F., Pfahl, S., Sodemann, H., Lehner, I., Seneviratne, S.I., Wernli, H., 2014. Deuterium excess as a proxy for continental moisture recycling and plant transpiration. Atmos. Chem. Phys. 14, 4029–4054. https://doi.org/10.5194/acp-14-4029-2014

Aggarwal, P.K., Romatschke, U., Araguas-Araguas, L., Belachew, D., Longstaffe, F.J., Berg, P., Schumacher, C., Funk, A., 2016. Proportions of convective and stratiform precipitation revealed in water isotope ratios. Nat. Geosci. 9, 624–629. https://doi.org/10.1038/ngeo2739

Ampuero, A., Stríkis, N.M., Apaéstegui, J., Vuille, M., Novello, V.F., Espinoza, J.C., Cruz, F.W., Vonhof, H., Mayta, V.C., Martins, V.T.S., Cordeiro, R.C., Azevedo, V., Sifeddine, A., 2020. The Forest Effects on the Isotopic Composition of Rainfall in the Northwestern Amazon Basin. J. Geophys. Res. Atmos. 125, 1–16. https://doi.org/10.1029/2019jd031445

Apaéstegui, J., Cruz, F.W., Vuille, M., Fohlmeister, J., Espinoza, J.C., Sifeddine, A., Strikis, N., Guyot, J.L., Ventura, R., Cheng, H., Edwards, R.L., 2018. Precipitation changes over the eastern Bolivian Andes inferred from speleothem ($\delta^{18}O$) records for the last 1400 years. Earth Planet. Sci. Lett. 494, 124–134. https://doi.org/10.1016/j.epsl.2018.04.048

Aravena, R., Suzuki, O., Pena, H., Pollastri, A., Fuenzalida, H., Grilli, A., 1999. Isotopic composition and origin of the precipitation in Northern Chile. Appl. Geochemistry 14, 411–422. https://doi.org/10.1016/S0883-2927(98)00067-5

Aron, P.G., Levin, N.E., Beverly, E.J., Huth, T.E., Passey, B.H., Pelletier, E.M., Poulsen, C.J., Winkelstern, I.Z., Yarian, D.A., 2020. Global variations of triple oxygen isotopes in meteoric waters. Chem. Geol., in review

Baker, L., Franchi, I.A., Maynard, J., Wright, I.P., Pillinger, C.T., 2002. A Technique for the Determination of $^{18}O/^{16}O$ and $^{17}O/^{16}O$ Isotopic Ratios in Water from Small Liquid and Solid Samples. Anal. Chem. 74, 1665–1673. https://doi.org/10.1021/ac010509s

Baker, P.A., Rigsby, C.A., Seltzer, G.O., Fritz, S.C., Lowenstein, T.K., Bacher, N.P., Veliz, C., 2001. Tropical climate changes at millennial and orbital timescales on the bolivian Altiplano. Nature 409, 698–701. https://doi.org/10.1038/35055524

Bao, H., Cao, X., Hayles, J.A., 2016. Triple Oxygen Isotopes: Fundamental Relationships and Applications. Annu. Rev. Earth Planet. Sci. 44, 463–492. https://doi.org/10.1146/annurev-earth-060115-012340

Barkan, E., Luz, B., 2007. Diffusivity fractionations of $H_2{}^{16}O/H_2{}^{17}O$ and $H_2{}^{16}O/H_2{}^{18}O$ in air and their implications for isotope hydrology. Rapid Commun. Mass Spectrom. 21, 2999–3005. https://doi.org/10.1002/rcm.3180

Barkan, E., Luz, B., 2005. High precision measurements of $^{17}O/^{16}O$ and $^{18}O/^{16}O$ ratios in H_2O. Rapid Commun. Mass Spectrom. 19, 3737–3742. https://doi.org/10.1002/rcm.2250

Barnes, J.B., Ehlers, T.A., 2009. End member models for Andean Plateau uplift. Earth-Science Rev. 97, 105–132. https://doi.org/10.1016/j.earscirev.2009.08.003

Berman, E.S.F., Levin, N.E., Landais, A., Li, S., Owano, T., 2013. Measurement of $\delta^{18}O$, $\delta^{17}O$, and ^{17}O-excess in Water by Off-Axis Integrated Cavity Output Spectroscopy and Isotope Ratio Mass Spectrometry. Anal. Chem. 85, 10392–10398. https://doi.org/10.1021/ac402366t

Bershaw, J., Garzione, C.N., Higgins, P., MacFadden, B.J., Anaya, F., Alvarenga, H., 2010. Spatial-temporal changes in Andean plateau climate and elevation from stable isotopes of mammal teeth. Earth Planet. Sci. Lett. 289, 530–538. https://doi.org/10.1016/j.epsl.2009.11.047

Bershaw, J., Saylor, J.E., Garzione, C.N., Leier, A., Sundell, K.E., 2016. Stable isotope variations ($\delta^{18}O$ and δD) in modern waters across the Andean Plateau. Geochim. Cosmochim. Acta 194, 310–324. https://doi.org/10.1016/j.gca.2016.08.011

Bjerknes, J., 1969. Atmospheric Teleconnections from the Equatorial Pacific. Mon. Weather Rev. 97, 163–172.

Blossey, P.N., Kuang, Z., Romps, D.M., 2010. Isotopic composition of water in the tropical tropopause layer in cloud-resolving simulations of an idealized tropical circulation. J. Geophys. Res. Atmos. 115, 1–23. https://doi.org/10.1029/2010JD014554

Bony, S., Risi, C., Vimeux, F., 2008. Influence of convective processes on the isotopic composition ($\delta^{18}O$ and δD) of precipitation and water vapor in the tropics: 1. Radiative-convective equilibrium and Tropical Ocean-Global Atmosphere-Coupled Ocean-Atmosphere Response Experiment (TOGA-COARE). J. Geophys. Res. Atmos. 113, 1–21. https://doi.org/10.1029/2008JD009942

Bowen, G.J., Cai, Z., Fiorella, R.P., Putman, A.L., 2019. Isotopes in the Water Cycle: Regional- to Global-Scale Patterns and Applications. Annu. Rev. 47, 453–479. https://doi.org/10.1146/annurev-earth-053018- 060220

Bowen, G.J., Wilkinson, B.H., 2002. Spatial distribution of $\delta^{18}O$ in meteoric precipitation. Geology 30, 315–318.

Bradley, R.S., Vuille, M., Hardy, D., Thompson, L.G., 2003. Low latitude ice cores record Pacific sea surface temperatures. Geophys. Res. Lett. 30, 2–5. https://doi.org/10.1029/2002GL016546

Brienen, R.J.W., Helle, G., Pons, T.L., Guyot, J.L., Gloor, M., 2012. Oxygen isotopes in tree rings are a good proxy for Amazon precipitation and El Niño-Southern Oscillation variability. Proc. Natl. Acad. Sci. U. S. A. 109, 16957–16962. https://doi.org/10.1073/pnas.1205977109

Cai, W., Mcphaden, M.J., Grimm, A.M., Rodrigues, R.R., Taschetto, A.S., Garreaud, R.D., Dewitte, B., Poveda, G., Ham, Y., Santoso, A., Ng, B., Anderson, W., Wang, G., Geng, T., Jo, H., Marengo, J.A., Alves, L.M., Osman, M., Li, S., Wu, L., Karamperidou, C., Takahashi, K., Vera, C., 2020. Climate impacts of the El Niño–Southern Oscillation on South America. Nat. Rev. Earth Environ. 1, 215–231. https://doi.org/10.1038/s43017-020-0040-3

Campetella, C.M., Vera, C.S., 2002. The influence of the Andes mountains on the South American low-level flow. Geophys. Res. Lett. 29, 6–9. https://doi.org/10.1029/2002GL015451

Canavan, R.R., Carrapa, B., Clementz, M.T., Quade, J., DeCelles, P.G., Schoenbohm, L.M., 2014. Early cenozoic uplift of the Puna plateau, central andes, based on stable isotope paleoaltimetry of hydrated volcanic glass. Geology 42, 447–450. https://doi.org/10.1130/G35239.1

Cao, X., Liu, Y., 2011. Equilibrium mass-dependent fractionation relationships for triple oxygen isotopes. Geochim. Cosmochim. Acta 75, 7435–7445. https://doi.org/10.1016/j.gca.2011.09.048

Cappa, C.D., 2003. Isotopic fractionation of water during evaporation. J. Geophys. Res. 108, 1–10. https://doi.org/10.1029/2003JD003597

Carrapa, B., Clementz, M., Feng, R., 2019. Ecological and hydroclimate responses to strengthening of the Hadley circulation in South America during the Late Miocene cooling 116, 9747–9752. https://doi.org/10.1073/pnas.1810721116

Chavez, S.P., Takahashi, K., 2017. Orographic rainfall hot spots in the Andes-Amazon transition according to the TRMM precipitation radar and in situ data. J. Geophys. Res. 122, 5870–5882. https://doi.org/10.1002/2016JD026282

Coplen, T.B., 1996. New guidelines for reporting stable hydrogen, carbon, and oxygen isotope-ratio data. Geochim. Cosmochim. Acta 60, 3359–3360.

Craig, H., 1961. Isotopic Variations in Meteoric Waters. Science (80-.). 133, 1702–1703. https://doi.org/10.1126/science.133.3465.1702

Criss, R.E., 1999. Principles of Stable Isotope Distribution. Oxford University Press, New York.

Dai, A., 2006. Recent climatology, variability, and trends in global surface humidity. J. Clim. 19, 3589–3606. https://doi.org/10.1175/JCLI3816.1

Dansgaard, W., 1964. Stable isotopes in precipitation. Tellus 16, 436–468.

https://doi.org/10.3402/tellusa.v16i4.8993

Delclaux, F., Coudrain, A., Condom, T., 2007. Evaporation estimation on Lake Titicaca: a synthesis review and modelling. Hydrol. Process. 21, 1664–1677. https://doi.org/10.1002/hyp.6360

Diaz, A.F., Studzinski, C.D., Mechoso, C.R., 1998. Relationships between precipitation anomalies in Uruguay and southern Brazil and sea surface temperature in the Pacific and Atlantic oceans. J. Clim. 11, 251–271. https://doi.org/10.1175/1520-0442(1998)011<0251:RBPAIU>2.0.CO;2

Draxler, R.R., Hess, G.D., 1998. An overview of the HYSPLIT_4 modelling system for trajectories, dispersion and deposition. Aust. Meteorol. Mag. 47, 295–308.

Dütsch, M., Pfahl, S., Sodemann, H., 2017. The impact of nonequilibrium and equilibrium fractionation on two different deuterium excess definitions. J. Geophys. Res. Atmos. 122, 12,732-12,746. https://doi.org/10.1002/2017JD027085

Ehlers, T.A., Poulsen, C.J., 2009. Influence of Andean uplift on climate and paleoaltimetry estimates. Earth Planet. Sci. Lett. 281, 238–248. https://doi.org/10.1016/j.epsl.2009.02.026

Eltahir, E.A.B., Bras, R.L., 1994. Precipitation recycling in the Amazon basin. Q. J. R. Meteorol. Soc. 120, 861–880. https://doi.org/10.1002/qj.49712051806

Falvey, M., Garreaud, R.D., 2005. Moisture variability over the South American Altiplano during the South American low level jet experiment (SALLJEX) observing season. J. Geophys. Res. Atmos. 110, 1–12. https://doi.org/10.1029/2005JD006152

Feng, R., Poulsen, C.J., 2014. Andean elevation control on tropical Pacific climate and ENSO. Paleoceanography 29, 795–809. https://doi.org/10.1002/2014PA002640.Received

Fiorella, R.P., Poulsen, C.J., Matheny, A.M., 2018. Seasonal Patterns of Water Cycling in a Deep, Continental Mountain Valley Inferred From Stable Water Vapor Isotopes. J. Geophys. Res. Atmos. 123, 7271–7291. https://doi.org/10.1029/2017JD028093

Fiorella, R.P., Poulsen, C.J., Pillco, R.S., Jeffery, M.L., Ehlers, T.A., 2015a. Modern and long-term evaporation of central Andes surface waters suggests paleo archives underestimate Neogene elevations. Earth Planet. Sci. Lett. 432, 59–72. https://doi.org/10.1016/j.epsl.2015.09.045

Fiorella, R.P., Poulsen, C.J., Zolá, R.S.P., Barnes, J.B., Tabor, C.R., Ehlers, T.A., 2015b. Spatiotemporal variability of modern precipitation $\delta^{18}O$ in the central Andes and implications for paleoclimate and paleoaltimetry estimates. J. Geophys. Res. Atmos. 120, 1–27. https://doi.org/10.1002/2014JD022893.Received

Friedman, I., Smith, G.I., Gleason, J.D., Warden, A., Harris, J.M., 1992. Stable Isotope

Composition of Waters in Southeastern California 1. Modern Precipitation. J. Geophys. Res. 97, 5795–5812.

Fritz, P., Suzuki, O., Silva, C., Salati, E., 1981. Isotope hydrology of groundwaters in the Pampa del Tamarugal, Chile. J. Hydrol. 53, 161–184. https://doi.org/10.1016/0022-1694(81)90043-3

Galewsky, J., Steen-Larsen, H.C., Field, R.D., Worden, J., Risi, C., Schneider, M., 2016. Stable isotopes in atmospheric water vapor and applications to the hydrologic cycle. Rev. Geophys. 54, 809–865. https://doi.org/10.1002/2015RG000512

Gallaire, R., Gourcy, L., Dtaupin, J., Coundrain-Ribstein, A., Poudyaud, B., Ríos, J., 2000. Isotopos del agua marcadores de la variabilidad climatica: isotopos de las lluvias de Laika Cota, La Paz Bolivia, in: Simposio Nacional de Cambios Globales. pp. 78–84.

Gandu, A.W., Geisler, J.E., 1991. A primitive equations model study of the effect of topography on the summer circulation over tropical South America. J. Atmos. Sci. 48, 1822–1836. https://doi.org/10.1175/1520-0469(1991)048<1822:APEMSO>2.0.CO;2

Garreaud, R., 2009. The Andes climate and weather. Adv. Geosci. 7, 1–9. https://doi.org/10.5194/adgeo-22-3-2009

Garreaud, R., 1999. Multiscale Analysis of the Summertime Precipitation over the Central Andes. Mon. Weather Rev. 127, 901–921. https://doi.org/10.1175/1520-0493(1999)127<0901:MAOTSP>2.0.CO;2

Garreaud, R., Vuille, M., Clement, A.C., 2003. The climate of the Altiplano: observed current conditions and mechanisms of past changes. Paleoceanogr. Paleoclimatology, Paleoecol. 194, 5–22. https://doi.org/10.1016/S0031-0182(03)00269-4

Garreaud, R.D., Molina, A., Farias, M., 2010. Andean uplift, ocean cooling and Atacama hyperaridity: A climate modeling perspective. Earth Planet. Sci. Lett. 292, 39–50. https://doi.org/10.1016/j.epsl.2010.01.017

Garreaud, R.D., Rutllant, J.A., Fuenzalida, H., 2002. Coastal lows along the subtropical west coast of South America: Mean structure and evolution. Mon. Weather Rev. 130, 75–88. https://doi.org/10.1175/1520-0493(2002)130<0075:CLATSW>2.0.CO;2

Garreaud, R.D., Vuille, M., Compagnucci, R., Marengo, J., 2009. Present-day South American climate. Palaeogeogr. Palaeoclimatol. Palaeoecol. 281, 180–195. https://doi.org/10.1016/j.palaeo.2007.10.032

Garzione, C.N., Hoke, G.D., Libarkin, J.C., Withers, S., MacFadden, B., Eiler, J., Ghosh, P., Mulch, A., 2008. Rise of the Andes. Science (80-.). 320, 1304–1307. https://doi.org/10.1126/science.1148615

Garzione, C.N., Molnar, P., Libarkin, J.C., MacFadden, B.J., 2006. Rapid late Miocene rise of the Bolivian Altiplano: Evidence for removal of mantle lithosphere. Earth Planet. Sci. Lett. 241, 543–556. https://doi.org/10.1016/j.epsl.2005.11.026

Gat, J., 1996. Oxygen and hydrogen isotopes in the hydrologic cycle. Annu. Rev. Earth Planet. Sci. 24, 225–262. https://doi.org/10.1146/annurev.earth.24.1.225

Gázquez, F., Morellón, M., Bauska, T., Herwartz, D., Surma, J., Moreno, A., Staubwasser, M., Valero-garcés, B., Delgado-huertas, A., Hodell, D.A., 2018. Triple oxygen and hydrogen isotopes of gypsum hydration water for quantitative paleo-humidity reconstruction. Earth Planet. Sci. Lett. 481, 177–188. https://doi.org/10.1016/j.epsl.2017.10.020

Giovannettone, J.P., Barros, A.P., 2009. Probing Regional Orographic Controls of Precipitation and Cloudiness in the Central Andes Using Satellite Data. J. Hydrol. 10, 167–182. https://doi.org/10.1175/2008JHM973.1

Gonfiantini, R., 1978. Standards for stable isotope measurements in natural compounds. Nature 271, 534–536. https://doi.org/10.1038/271534a0

Gonfiantini, R., Roche, M.A., Olivry, J.C., Fontes, J.C., Zuppi, G.M., 2001. The altitude effect on the isotopic composition of tropical rains. Chem. Geol. 181, 147–167. https://doi.org/10.1016/S0009-2541(01)00279-0

Gonfiantini, R., Wassenaar, L.I., Araguas-Araguas, L., Aggarwal, P.K., 2018. A unified Craig-Gordon isotope model of stable hydrogen and oxygen isotope fractionation during fresh or saltwater evaporation. Geochim. Cosmochim. Acta 235, 224–236. https://doi.org/10.1016/j.gca.2018.05.020

Gröning, M., Lutz, H.O., Roller-lutz, Z., Kralik, M., Gourcy, L., Pöltenstein, L., 2012. A simple rain collector preventing water re-evaporation dedicated for $\delta^{18}O$ and $\delta^{2}H$ analysis of cumulative precipitation samples. J. Hydrol. 449, 195–200. https://doi.org/10.1016/j.jhydrol.2012.04.041

Guy, H., Seimon, A., Perry, L.B., Konecky, B.L., Rado, M., Andrade, M., Potocki, M., Mayewski, P.A., 2019. Subseasonal Variations of Stable Isotopes in Tropical Andean Precipitation. J. Hydrometeorol. 20, 915–933. https://doi.org/10.1175/JHM-D-18-0163.1

Hardy, D.R., Vuille, M., Bradley, R.S., 2003. Variability of snow accumulation and isotopic composition on Nevado Sajama, Bolivia. J. Geophys. Res. D Atmos. 108, 1–10. https://doi.org/10.1029/2003jd003623

Hersbach, H., Bell, B., Berrisford, P., Hirahara, S., Andras, H., Joaquın, M.-S., Nicolas, J., Peubey, C., Radu, R., Schepers, D., Simmons, A., Soci, C., Abdalla, S., Abellan, X., Balsamo, G., Bechtold, P., Biavati, G., Bidlot, J., Bonavita, M., De Chiara, G., Dahlgren, P., Dee, D., Diamantakis, M., Dragani, R., Flemming, J., Forbes, R., Fuentes, M., Geer, A., Haimberger, L., Healy, S., Hogan, R.J., Holm, E., Janiskova, M., Keeley, S., Patrick, L.,

Lopez, P., Lupu, C., Radnoti, G., Rosnay, P. de, Rozum, I., Vamborg, F., Villaume, S., Thepaut, J.-N., 2020. The ERA5 Global Reanalysis. Q. J. R. Meteorol. Soc. 1–90.

Herrera, C., Gamboa, C., Custodio, E., Jordan, T., Godfrey, L., Jódar, J., Luque, J.A., Vargas, J., Sáez, A., 2018. Groundwater origin and recharge in the hyperarid Cordillera de la Costa, Atacama Desert, northern Chile. Sci. Total Environ. 624, 114–132. https://doi.org/10.1016/j.scitotenv.2017.12.134

Herwartz, D., Surma, J., Voigt, C., Assonov, S., Staubwasser, M., 2017. Triple oxygen isotope systematics of structurally bonded water in gypsum. Geochim. Cosmochim. Acta 209, 254–266. https://doi.org/10.1016/j.gca.2017.04.026

Hoffmann, G., 2003. Tropical Water Cycle. Am. 5201, 776–777.

Hoffmann, G., Ramirez, E., Taupin, J.D., Francou, B., Ribstein, P., Delmas, R., Dürr, H., Gallaire, R., Simoes, J., Schotterer, U., Stievenard, M., Werner, M., 2003. Coherent isotope history of Andean ice cores over the last century. Geophys. Res. Lett. 30, 1–4. https://doi.org/10.1029/2002GL014870

Horita, J., Wesolowski, D.J., 1994. Liquid-vapor fractionation of oxygen and hydrogen isotopes of water from the freezing to the critical temperature. Geochim. Cosmochim. Acta 58, 3425–3437.

Hulston, J.R., Thode, H.G., 1965. Variations in the S S and S Contents of Meteorites and Their Relation to Chemical and Nuclear Effects. J. Geophys. Res. 70, 3475–3484.

Hurley, J. V., Vuille, M., Hardy, D.R., 2019. On the Interpretation of the ENSO Signal Embedded in the Stable Isotopic Composition of Quelccaya Ice Cap, Peru. J. Geophys. Res. Atmos. 124, 131–145. https://doi.org/10.1029/2018JD029064

Insel, N., Poulsen, C.J., Ehlers, T. a., Sturm, C., 2012. Response of meteoric $\delta^{18}O$ to surface uplift - Implications for Cenozoic Andean Plateau growth. Earth Planet. Sci. Lett. 317–318, 262–272. https://doi.org/10.1016/j.epsl.2011.11.039

Insel, N., Poulsen, C.J., Ehlers, T.A., 2010. Influence of the Andes Mountains on South American moisture transport, convection, and precipitation. Clim. Dyn. 35, 1477–1492. https://doi.org/10.1007/s00382-009-0637-1

Insel, N., Poulsen, C.J., Sturm, C., Ehlers, T.A., 2013. Climate controls on Andean precipitation $\delta^{18}O$ interannual variability. J. Geophys. Res. Atmos. 118, 9721–9742. https://doi.org/10.1002/jgrd.50619

Jeffery, M.L., Poulsen, C.J., Ehlers, T. a., 2012. Impacts of Cenozoic global cooling, surface uplift, and an inland seaway on South American paleoclimate and precipitation $\delta^{18}O$. Bull. Geol. Soc. Am. 124, 335–351. https://doi.org/10.1130/B30480.1

Jordan, T.E., Herrera L., C., Godfrey, L. V., Colucci, S.J., Gamboa P., C., Urrutia M., J., González L., G., Paul, J.F., 2019. Isotopic characteristics and paleoclimate implications of the extreme precipitation event of march 2015 in Northern Chile. Andean Geol. 46, 1–31. https://doi.org/10.5027/andgeov46n1-3087

Jouzel, J., Merlivat, L., 1984. Deuterium and Oxygen 18 in Precipitation: Modeling of the Isotopic Effects During Snow Formation. J. Geophys. Res. 89, 11,749–11,757. https://doi.org/10.1029/JD089iD07p11749

Kaiser, J., 2009. Reformulated ^{17}O correction of mass spectrometric stable isotope measurements in carbon dioxide and a critical appraisal of historic 'absolute' carbon and oxygen isotope ratios. Geochim. Cosmochim. Acta 72, 1312–1334. https://doi.org/10.1016/j.gca.2007.12.011

Kar, N., Garzione, C.N., Jaramillo, C., Shanahan, T., Carlotto, V., Pullen, A., Moreno, F., Anderson, V., Moreno, E., Eiler, J., 2016. Rapid regional surface uplift of the northern Altiplano plateau revealed by multiproxy paleoclimate reconstruction. Earth Planet. Sci. Lett. 447, 33–47. https://doi.org/10.1016/j.epsl.2016.04.025

Konecky, B.L., Noone, D.C., Cobb, K.M., 2019. The Influence of Competing Hydroclimate Processes on Stable Isotope Ratios in Tropical Rainfall. Geophys. Res. Lett. 46, 1622–1633. https://doi.org/10.1029/2018GL080188

Kumar, S., Vidal, Y., Moya-álvarez, A.S., Martínez-castro, D., 2019. Effect of the surface wind flow and topography on precipitating cloud systems over the Andes and associated Amazon basin : GPM observations. Atmos. Res. 225, 193–208. https://doi.org/10.1016/j.atmosres.2019.03.027

Kurita, N., 2013. Water isotopic variability in response to mesoscale convective system over the tropical ocean. J. Geophys. Res. Atmos. 118, 10,376-10,390. https://doi.org/10.1002/jgrd.50754

Landais, A., Barkan, E., Yakir, D., Luz, B., 2006. The triple isotopic composition of oxygen in leaf water. Geochim. Cosmochim. Acta 70, 4,105–4,115. https://doi.org/10.1016/j.gca.2006.06.1545

Landais, A., Ekaykin, A., Barkan, E., Winkler, R., Luz, B., 2012a. Seasonal variations of ^{17}O-excess and d-excess in snow precipitation at Vostok station, East Antarctica. J. Glaciol. 58, 725–733. https://doi.org/10.3189/2012JoG11J237

Landais, A., Risi, C., Bony, S., Vimeux, F., Descroix, L., Falourd, S., Bouygues, A., 2010. Combined measurements of $^{17}O_{excess}$ and d-excess in African monsoon precipitation: Implications for evaluating convective parameterizations. Earth Planet. Sci. Lett. 298, 104–112. https://doi.org/10.1016/j.epsl.2010.07.033

Landais, A., Steen-Larsen, H.C., Guillevic, M., Masson-Delmotte, V., Vinther, B., Winkler, R.,

2012b. Triple isotopic composition of oxygen in surface snow and water vapor at NEEM (Greenland). Geochim. Cosmochim. Acta 77, 304–316. https://doi.org/10.1016/j.gca.2011.11.022

Lavado Casimiro, W.S., Ronchail, J., Labat, D., Espinoza, J.C., Guyot, J.L., 2012. Basin-scale analysis of rainfall and runoff in Peru (1969–2004): Pacific, Titicaca and Amazonas drainages. Hydrol. Sci. J. 57, 625–642. https://doi.org/10.1080/02626667.2012.672985

Lawrence, D.M., Thornton, P.E., Oleson, K.W., Bonan, G.B., 2007. The Partitioning of Evapotranspiration into Transpiration, Soil Evaporation, and Canopy Evaporation in a GCM: Impacts on Land – Atmosphere Interaction. J. Hydrometeorol. 8, 862–880. https://doi.org/10.1175/JHM596.1

Lechler, A.R., Niemi, N.A., 2011. Controls on the spatial variability of modern meteoric $\delta^{18}O$: Empirical constraints from the western U.S. and east Asia and implications for stable isotope studies. Am. J. Sci. 311, 664–700. https://doi.org/10.2475/08.2011.02

Lee, J.-E., Fung, I., 2010. "Amount effect" of water isotopes and quantitative analysis of post-condensation processes. Hydrol. Process. 22, 1–8. https://doi.org/10.1002/hyp.6637

Legates, D.R., Willmott, C.J., 1990a. Mean Seasonal and Spatial Variability in Gauge-Corrected, Global Precipitation. Int. J. Climatol. 10, 111–127.

Legates, D.R., Willmott, C.J., 1990b. Mean seasonal and spatial variability in global surface air temperature. Theor. Appl. Climatol. 41, 11–21. https://doi.org/10.1007/BF00866198

Leier, A., McQuarrie, N., Garzione, C., Eiler, J., 2013. Stable isotope evidence for multiple pulses of rapid surface uplift in the Central Andes, Bolivia. Earth Planet. Sci. Lett. 371–372, 49–58. https://doi.org/10.1016/j.epsl.2013.04.025

Lenters, J.D., Cook, K.H., 1997. On the Origin of the Bolivian High and Related Circulation Features of the South American Climate. J. Atmos. Sci. 54, 656–678. https://doi.org/10.1175/1520-0469(1997)054<0656:OTOOTB>2.0.CO;2

Lettau, H., Lettau, K., Molion, L.C., 1979. Amozonia's hydrological cycle and the role of atmospheric recycling in assessing deforestation effects. Montly Weather Rev. 107, 227–238. https://doi.org/10.1175/1520-0493(1979)107<0227:AHCATR>2.0.CO;2

Levin, N.E., Raub, T.D., Dauphas, N., Eiler, J.M., 2014. Triple oxygen isotope variations in sedimentary rocks. Geochim. Cosmochim. Acta 139, 173–189. https://doi.org/10.1016/j.gca.2014.04.034

Li, S., Levin, N.E., Chesson, L.A., 2015. Continental scale variation in ^{17}O-excess of meteoric waters in the United States. Geochim. Cosmochim. Acta 164, 110–126. https://doi.org/10.1016/j.gca.2015.04.047

Li, S., Levin, N.E., Soderberg, K., Dennis, K.J., Caylor, K.K., 2017. Triple oxygen isotope composition of leaf waters in Mpala, central Kenya. Earth Planet. Sci. Lett. 468, 38–50. https://doi.org/10.1016/j.epsl.2017.02.015

Lin, Y., Clayton, R.N., Groning, M., 2010. Calibration of $\delta^{17}O$ and $\delta^{18}O$ of international measurement standards – VSMOW, VSMOW2, SLAP, and SLAP2. Rapid Commun. Mass Spectrom. 24, 773–776. https://doi.org/10.1002/rcm.4449

Liotta, M., Favara, R., Valenza, M., 2006. Isotopic composition of the precipitations in the central mediterranean: Origin marks and orographic precipitation effects. J. Geophys. Res. Atmos. 111, 1–12. https://doi.org/10.1029/2005JD006818

Luz, B., Barkan, E., 2010. Variations of $^{17}O/^{16}O$ and $^{18}O/^{16}O$ in meteoric waters. Geochim. Cosmochim. Acta 74, 6276–6286. https://doi.org/10.1016/j.gca.2010.08.016

Luz, B., Barkan, E., Yam, R., Shemesh, A., 2009. Fractionation of oxygen and hydrogen isotopes in evaporating water. Geochim. Cosmochim. Acta 73, 6697–6703. https://doi.org/10.1016/j.gca.2009.08.008

Madden, R., Julian, P., 1994. A review of the intraseasonal oscillation in the Tropics. Mon. Weather Rev. 122, 814–837.

Majoube, M., 1971. Oxygen-18 and deuterium fractionation between water and steam. J. Chem. Phys. 68, 1432–1436.

Mantua, N.J., Hare, S.R., Zhang, Y., Wallace, J.M., Francis, R.C., 1997. A Pacific Interdecadal Climate Oscillation with Impacts on Salmon Production. Bull. Am. Meteorol. Soc. 78, 1069–1079. https://doi.org/10.1175/1520-0477(1997)078<1069:APICOW>2.0.CO;2

Marengo, J.A., 2005. Characteristics and spatio-temporal variability of the Amazon river basin water budget. Clim. Dyn. 24, 11–22. https://doi.org/10.1007/s00382-004-0461-6

Martin, F.M., 2002. Isotopic fractionation and the quantification of ^{17}O anomalies in the oxygen three-isotope system: an appraisal and geochemical significance. Geochim. Cosmochim. Acta 66, 1881–1889.

Masiokas, M., Rabatel, A., Rivera, A., Ruiz, L., Pitte, P., Ceballos, J.L., Barcaza, G., Soruco, A., Bown, F., 2020. A review of the current state and recent changes of the Andean cryosphere. Front. Earth Sci. 8, 1–27. https://doi.org/10.3389/FEART.2020.00099

Matsuhisa, Y., Goldsmith, J.R., Clayton, R.N., 1978. Mechanisms of hydrothermal crystallization of quartz at 250°C and 15 kbar. Geochim. Cosmochim. Acta 42, 173–182. https://doi.org/10.1016/0016-7037(78)90130-8

Meijer, H.A.J., Li, W.J., 1998. The Use of Electrolysis for Accurate $\delta^{17}O$ and $\delta^{18}O$ Isotope Measurements in Water. Isot. Evironmental Heal. Stud. 34, 349–369.

https://doi.org/10.1080/10256019808234072

Merlivat, L., 1978. Molecular diffusivities of $H_2{}^{16}O$, $HD^{16}O$, and $H_2{}^{18}O$ in gases. J. Chem. Phys. 69, 2864–2871. https://doi.org/10.1063/1.436884

Montini, T.L., Jones, C., Carvalho, L.M. V., 2019. The South American Low-Level Jet: A New Climatology, Variability, and Changes. J. Geophys. Res. Atmos. 24, 1–19. https://doi.org/10.1029/2018JD029634

Moore, M., Kuang, Z., Blossey, P.N., 2014. A moisture budget perspective of the amount effect. Geophys. Res. Lett. 41, 1329–1335. https://doi.org/10.1002/2013GL058302

Mulch, A., Uba, C.E., Strecker, M.R., Schoenberg, R., Chamberlain, C.P., 2010. Late Miocene climate variability and surface elevation in the central Andes. Earth Planet. Sci. Lett. 290, 173–182. https://doi.org/10.1016/j.epsl.2009.12.019

National Weather Service, Climate Prediction Center: https://origin.cpc.ncep.noaa.gov/products/analysis_monitoring/ensostuff/ONI_v5.php, Accessed June 1, 2020

Pabón-Caicedo, J.D., Arias, P.A., Carril, A.F., Espinoza, J.C., Borrel, L.F., Goubanova, K., Lavado-Casimiro, W., Masiokas, M., Solman, S., Villalba, R., 2020. Observed and Projected Hydroclimate Changes in the Andes. Front. Earth Sci. 8, 1–29. https://doi.org/10.3389/feart.2020.00061

Pack, A., Herwartz, D., 2014. The triple oxygen isotope composition of the Earth mantle and understanding $\Delta^{17}O$ variations in terrestrial rocks and minerals. Earth Planet. Sci. Lett. 390, 138–145. https://doi.org/10.1016/j.epsl.2014.01.017

Paegle, J.N., Byerle, L.A., Mo, K.C., 2000. Intraseasonal modulation of South American summer precipitation. Mon. Weather Rev. 128, 837–850. https://doi.org/10.1175/1520-0493(2000)128<0837:IMOSAS>2.0.CO;2

Passey, B.H., Hu, H., Ji, H., Montanari, S., Li, S., Henkes, G.A., Levin, N.E., 2014. Triple oxygen isotopes in biogenic and sedimentary carbonates. Geochim. Cosmochim. Acta 141, 1–25. https://doi.org/10.1016/j.gca.2014.06.006

Passey, B.H., Ji, H., 2019. Triple oxygen isotope signatures of evaporation in lake waters and carbonates: A case study from the western United States. Earth Planet. Sci. Lett. 518, 1–12. https://doi.org/10.1016/j.epsl.2019.04.026

Pattnayak, K.C., Tindall, J.C., Brienen, R.J.W., Barichivich, J., Gloor, E., 2019. Can We Detect Changes in Amazon Forest Structure Using Measurements of the Isotopic Composition of Precipitation? Geophys. Res. Lett. 46, 14807–14816. https://doi.org/10.1029/2019GL084749

Pfahl, S., Sodemann, H., 2014. What controls deuterium excess in global precipitation? Clim. Past

10, 771–781. https://doi.org/10.5194/cp-10-771-2014

Pillco Zolá, R., Bengtsson, L., Berndtsson, R., Martí-Cardona, B., Satgé, F., Timouk, F., Bonnet, M.P., Mollericon, L., Gamarra, C., Pasapera, J., 2019. Modelling Lake Titicaca's daily and monthly evaporation. Hydrol. Earth Syst. Sci. 23, 657–668. https://doi.org/10.5194/hess-23-657-2019

Poage, M.A., Chamberlain, C.P., 2001. Stable Isotope Composition of Precipitation and Surface Waters: Considerations for Studies of Paleoelevation Change. Am. J. Sci. 301, 1–15.

Polissar, P.J., Freeman, K.H., Rowley, D.B., McInerney, F.A., Currie, B.S., 2009. Paleoaltimetry of the Tibetan Plateau from D/H ratios of lipid biomarkers. Earth Planet. Sci. Lett. 287, 64–76. https://doi.org/10.1016/j.epsl.2009.07.037

Poulsen, C.J., Ehlers, T.A., Insel, N., 2010. Onset of convective rainfall during gradual late miocene rise of the central andes. Science (80-.). 328, 490–493. https://doi.org/10.1126/science.1185078

Quade, J., Dettinger, M.P., Carrapa, B., DeCelles, P.G., Murray, K.E., Huntington, K.W., Cartwright, A., Canavan, R.R., Gehrels, G.E., Clementz, M., 2015. The growth of the central Andes, 22°S-26°S. Geol. Soc. Am. 212, 277–308. https://doi.org/10.1130/2015.1212(15).

Quade, J., Garzione, C., Eiler, J., 2007a. Paleoelevation Reconstruction using Pedogenic Carbonates. Rev. Mineral. Geochemistry 66, 53–87.

Quade, J., Rech, J.A., Latorre, C., Betancourt, J.L., Gleeson, E., Kalin, M.T.K., 2007b. Soils at the hyperarid margin: The isotopic composition of soil carbonate from the Atacama Desert, Northern Chile. Geochim. Cosmochim. Acta 71, 3772–3795. https://doi.org/10.1016/j.gca.2007.02.016

Quinn, W.H., Neal, V.T., 1987. El Nino Occurrences Over the Past Four and a Half Centuries. J. Geophys. Res. 92, 14,449–14,461.

Rech, J.A., Currie, B.S., Jordan, T.E., Riquelme, R., Lehmann, S.B., Kirk-Lawlor, N.E., Li, S., Gooley, J.T., 2019. Massive middle Miocene gypsic paleosols in the Atacama Desert and the formation of the Central Andean rain-shadow. Earth Planet. Sci. Lett. 506, 184–194. https://doi.org/10.1016/j.epsl.2018.10.040

Risi, C., Bony, S., Vimeux, F., 2008. Influence of convective processes on the isotopic composition ($\delta^{18}O$ and δD) of precipitation and water vapor in the tropics: 2. Physical interpretation of the amount effect. J. Geophys. Res. Atmos. 113, 1–12. https://doi.org/10.1029/2008JD009943

Risi, C., Landais, A., Winkler, R., Vimeux, F., 2013. Can we determine what controls the spatio-temporal distribution of d-excess and ^{17}O-excess in precipitation using the LMDZ general circulation model? Clim. Past 9, 2173–2193. https://doi.org/10.5194/cp-9-2173-2013

Roche, M., Gonfiantini, R., Fontes, J., Lara, N., Noriega, L., 1999. The isotopic composition of precipitation on the Andes and Amazon of Bolivia, in: Isotope Techniques in Water Resources Development and Management. Vienna, Austria, pp. 249–261.

Rodwell, M.J., Hoskins, B.J., 2001. Subtropical anticyclones and summer monsoons. J. Clim. 14, 3192–3211. https://doi.org/10.1175/1520-0442(2001)014<3192:SAASM>2.0.CO;2

Rohrmann, A., Sachse, D., Mulch, A., Pingel, H., Tofelde, S., Alonso, R.N., Strecker, M.R., 2016. Miocene orographic uplift forces rapid hydrological change in the southern central Andes. Sci. Rep. 6, 1–7. https://doi.org/10.1038/srep35678

Romatschke, U., Houze, R.A., 2010. Extreme summer convection in South America. J. Clim. 23, 3761–3791. https://doi.org/10.1175/2010JCLI3465.1

Rowley, D.B., 2007. Stable Isotope-Based Paleoaltimetry: Theory and Validation. Rev. Mineral. Geochemistry 66, 23–52. https://doi.org/10.2138/rmg.2007.66.2

Rowley, D.B., Garzione, C.N., 2007. Stable Isotope-Based Paleoaltimetry. Annu. Rev. Earth Planet. Sci. 35, 463–508. https://doi.org/10.1146/annurev.earth.35.031306.140155

Rowley, D.B., Pierrehumbert, R.T., Currie, B.S., 2001. A new approach to stable isotope-based paleoaltimetry: Implications for paleoaltimetry and paleohypsometry of the High Himalaya since the late Miocene. Earth Planet. Sci. Lett. 188, 253–268. https://doi.org/10.1016/S0012-821X(01)00324-7

Rozanski, K., Araguás-Araguás, L., Gonfiantini, R., 1993. Isotopic Patterns in Modern Global Precipitation, in: Swart, P.K., Lohmann, K.C., Mckenzie, J., Savin, S. (Eds.), Climate Change in Continental Isotopic Records Geophysical Monograph Series, (Vol. 78). American Geophysical Union, Washington, DC, pp. 1–36. https://doi.org/10.1029/GM078p0001

Rumble, D., Miller, M.F., Franchi, I.A., Greenwood, R.C., 2007. Oxygen three-isotope fractionation lines in terrestrial silicate minerals: An inter-laboratory comparison of hydrothermal quartz and eclogitic garnet. Geochim. Cosmochim. Acta 71, 3592–3600. https://doi.org/10.1016/j.gca.2007.05.011

Rutllant, J.A., Fuenzalida, H., Aceituno, P., 2003. Climate dynamics along the arid northern coast of Chile: The 1997–1998 Dinámica del Clima de la Región de Antofagasta (DICLIMA) experiment. J. Geophys. Res. 108, 1–13. https://doi.org/10.1029/2002JD003357

Salati, E., Dall'Olio, A., Matsui, E., Gat, J.R., 1979. Recycling of water in the Amazon Basin: An isotopic study. Water Resour. Res. 15, 1250–1258. https://doi.org/10.1029/WR015i005p01250

Samuels-Crow, K.E., Galewsky, J., Hardy, D.R., Sharp, Z.D., Worden, J., Braun, C., 2014a. Upwind convective influences on the isotopic composition of atmospheric water vapor over

the tropical Andes. J. Geophys. Res. Atmos. 119, 7051–7063. https://doi.org/10.1002/2014JD021487.Received

Samuels-Crow, K.E., Galewsky, J., Sharp, Z.D., Dennis, K.J., 2014b. Deuterium excess in subtropical free troposphere water vapor: Continuous measurements from the Chajnantor Plateau, northern Chile. Geophys. Res. Lett. 41, 8652–8659. https://doi.org/10.1002/2014GL062302

Sarmiento, F.O., Kooperman, G.J., 2019. A Socio-Hydrological Perspective on Recent and Future Precipitation Changes Over Tropical Montane Cloud Forests in the Andes. Front. Earth Sci. 7, 1–6. https://doi.org/10.3389/feart.2019.00324

Saylor, J.E., Horton, B.K., 2014. Nonuniform surface uplift of the Andean plateau revealed by deuterium isotopes in Miocene volcanic glass from southern Peru. Earth Planet. Sci. Lett. 387, 120–131. https://doi.org/10.1016/j.epsl.2013.11.015

Schauer, A.J., Schoenemann, S.W., Steig, E.J., 2016. Routine high-precision analysis of triple water-isotope ratios using cavity ring-down spectroscopy. Rapid Commun. Mass Spectrom. 30, 2059–2069. https://doi.org/10.1002/rcm.7682

Schoenemann, S.W., Schauer, A.J., Steig, E.J., 2013. Measurement of SLAP2 and GISP $\delta^{17}O$ and proposed VSMOW-SLAP normalization for $\delta^{17}O$ and $^{17}O_{excess}$. Rapid Commun. Mass Spectrom. 27, 582–590. https://doi.org/10.1002/rcm.6486

Schoenemann, S.W., Steig, E.J., Ding, Q., Markle, B.R., Schauer, A.J., 2014. Triple water-isotopologue record from WAIS Divide, Antarctica: Controls on glacial-interglacial changes in $^{17}O_{excess}$ of precipitation. J. Geophys. Res. Atmos. 119, 8741–8763. https://doi.org/10.1002/2014JD021770.Received

Scholl, M.A., Ingebritsen, S.E., Janik, C.J., Kauahikaua, J.P., 1996. Use of precipitation and groundwater isotopes to interpret regional hydrology on a tropical volcanic island: Kilauea volcano area, Hawaii. Water Resour. Res. 32, 3525–3537.

Sharp, Z.D., Wostbrock, J.A.G., Pack, A., 2018. Mass-dependent triple oxygen isotope variations in terrestrial materials. Geochemical Perspect. Lett. 7, 27–31. https://doi.org/10.7185/geochemlet.1815

Silva, G.A.M., Ambrizzi, T., 2006. Inter-El Niño variability and its impact on the South American low-level jet east of the Andes during austral summer − two case studies. Adv. Geosci. 6, 283–287. https://doi.org/10.5194/adgeo-6-283-2006

Sodemann, H., Schwierz, C., Wernli, H., 2008. Interannual variability of Greenland winter precipitation sources: Lagrangian moisture diagnostic and North Atlantic Oscillation influence. J. Geophys. Res. Atmos. 113, 1–17. https://doi.org/10.1029/2007JD008503

Spangenberg, J.E., 2012. Caution on the storage of waters and aqueous solutions in plastic containers for hydrogen and oxygen stable isotope analysis. Rapid Commun. Mass Spectrom.

26, 2627–2636. https://doi.org/10.1002/rcm.6386

Sturm, C., Hoffmann, G., Langmann, B., 2007. Simulation of the Stable Water Isotopes in Precipitation over South America: Comparing Regional to Global Circulation Models. J. Clim. 20, 3730–3750. https://doi.org/10.1175/JCLI4194.1

Sundell, K.E., Saylor, J.E., Lapen, T.J., Horton, B.K., 2019. Implications of variable late Cenozoic surface uplift across the Peruvian central Andes. Sci. Rep. 9, 1–12. https://doi.org/10.1038/s41598-019-41257-3

Surma, J., Assonov, S., Herwartz, D., Voigt, C., Staubwasser, M., 2018. The evolution of ^{17}O-excess in surface water of the arid environment during recharge and evaporation. Sci. Rep. 8, 1–10. https://doi.org/10.1038/s41598-018-23151-6

Takahashi, K., Battisti, D.S., 2007. Processes controlling the mean tropical Pacific precipitation pattern. Part II: The SPCZ and the Southeast Pacific dry zone. J. Clim. 20, 5696–5706. https://doi.org/10.1175/2007JCLI1656.1

Takahashi, K., Martínez, A.G., 2019. The very strong coastal El Niño in 1925 in the far-eastern Pacific. Clim. Dyn. 52, 7389–7415. https://doi.org/10.1007/s00382-017-3702-1

Tharammal, T., Bala, G., Noone, D., 2017. Impact of deep convection on the isotopic amount effect in tropical precipitation. J. Geophys. Res. 122, 1505–1523. https://doi.org/10.1002/2016JD025555

Thompson, D.W.J., Wallace, J.M., 2000. Annular modes in the extratropical circulation. Part I: Month-to-month variability. J. Clim. 13, 1000–1016. https://doi.org/10.1175/1520-0442(2000)013<1000:AMITEC>2.0.CO;2

Thompson, L.G., Davis, M.E., Mosley-Thompson, E., Beaudon, E., Porter, S.E., Kutuzov, S., Lin, P.-N., Mikhalenko, V.N., Mountain, K.R., 2017. Impacts of Recent Warming and the 2015/2016 El Niño on Tropical Peruvian Ice Fields. J. Geophys. Res. Atmos. 122, 688–701. https://doi.org/10.1002/2017JD026592

Thompson, L.G., Mosley-Thompson, E., Arnao, B.M., 1984. El Niño-Southern Oscillation Events Recorded in the Stratigraphy of the Tropical Quelccaya Ice Cap, Peru. Science (80-.). 226, 50–53.

Thompson, L.G., Mosley-Thompson, E., Henderson, K.A., 2000. Ice-core palaeoclimate records in tropical South America since the last glacial maximum. J. Quat. Sci. 15, 377–394. https://doi.org/10.1002/1099-1417(200005)15:4<377::AID-JQS542>3.0.CO;2-L

Tian, C., Wang, L., Kaseke, K.F., Bird, B.W., 2018. Stable isotope compositions (δ^2H, $\delta^{18}O$ and $\delta^{17}O$) of rainfall and snowfall in the central United States. Sci. Rep. 8, 1–15. https://doi.org/10.1038/s41598-018-25102-7

Uechi, Y., Uemura, R., 2019. Dominant influence of the humidity in the moisture source region on the ^{17}O-excess in precipitation on a subtropical island. Earth Planet. Sci. Lett. 513, 20–28. https://doi.org/10.1016/j.epsl.2019.02.012

Uemura, R., Masson-Delmotte, V., Jouzel, J., Landais, A., Motoyama, H., Stenni, B., 2012. Ranges of moisture-source temperature estimated from Antarctic ice cores stable isotope records over glacial-interglacial cycles. Clim. Past 8, 1109–1125. https://doi.org/10.5194/cp-8-1109-2012

Uemura, R., Matsui, Y., Yoshimura, K., Motoyama, H., Yoshida, N., 2008. Evidence of deuterium excess in water vapor as an indicator of ocean surface conditions. J. Geophys. Res. Atmos. 113, 1–10. https://doi.org/10.1029/2008JD010209

Valdivielso, S., Vázquez-Suñé, E., Custodio, E., 2020. Origin and Variability of Oxygen and Hydrogen Isotopic Composition of Precipitation in the Central Andes: a Review. J. Hydrol. 587, 124899. https://doi.org/10.1016/j.jhydrol.2020.124899

van Breukelen, M.R., Vonhof, H.B., Hellstrom, J.C., Wester, W.C.G., Kroon, D., 2008. Fossil dripwater in stalagmites reveals Holocene temperature and rainfall variation in Amazonia. Earth Planet. Sci. Lett. 275, 54–60. https://doi.org/10.1016/j.epsl.2008.07.060

Vera, C., Baez, J., Douglas, M., Emmanuel, C.B., Marengo, J., Meitin, J., Nicolini, M., Nogues-Paegle, J., Paegle, J., Penalba, O., Salio, P., Saulo, C., Silva Dias, M.A., Silva Dias, P., Zipser, E., 2006. The South American Low-Level Jet Experiment. Bull. Am. Meteorol. Soc. 87, 63–77. https://doi.org/10.1175/BAMS-87-1-63

Viale, M., Valenzuela, R., Garreaud, R.D., Ralph, F.M., 2018. Impacts of atmospheric rivers on precipitation in Southern South America. J. Hydrometeorol. 19, 1671–1687. https://doi.org/10.1175/JHM-D-18-0006.1

Vimeux, F., Gallaire, R., Bony, S., Hoffmann, G., Chiang, J.C.H., 2005. What are the climate controls on δD in precipitation in the Zongo Valley (Bolivia)? Implications for the Illimani ice core interpretation. Earth Planet. Sci. Lett. 240, 205–220. https://doi.org/10.1016/j.epsl.2005.09.031

Vimeux, F., Ginot, P., Schwikowski, M., Vuille, M., Hoffmann, G., Thompson, L.G., Schotterer, U., 2009. Climate variability during the last 1000 years inferred from Andean ice cores: A review of methodology and recent results. Palaeogeogr. Palaeoclimatol. Palaeoecol. 281, 229–241. https://doi.org/10.1016/j.palaeo.2008.03.054

Vimeux, F., Tremoy, G., Risi, C., Gallaire, R., 2011. A strong control of the South American SeeSaw on the intra-seasonal variability of the isotopic composition of precipitation in the Bolivian Andes. Earth Planet. Sci. Lett. 307, 47–58. https://doi.org/10.1016/j.epsl.2011.04.031

Virji, H., 1981. A preliminary study of summertime tropospheric circulation patterns over South

America estimated from cloud winds. Mon. Weather Rev. 109, 599–610. https://doi.org/10.1175/1520-0493(1981)109<0599:APSOST>2.0.CO;2

Vuille, M., 2003. Modeling $\delta^{18}O$ in precipitation over the tropical Americas: 2. Simulation of the stable isotope signal in Andean ice cores. J. Geophys. Res. 108, 1–17. https://doi.org/10.1029/2001JD002039

Vuille, M., 1999. ATMOSPHERIC CIRCULATION OVER THE BOLIVIAN ALTIPLANO DURING DRY AND WET PERIODS AND EXTREME PHASES OF THE SOUTHERN OSCILLATION. Int. J. Climatol. 1600, 1579–1600.

Vuille, M., Bradley, R.S., Keimig, F., 2000. Climate variability in the Andes of Ecuador and its relation to tropical Pacific and Atlantic Sea Surface temperature anomalies. J. Clim. 13, 2520–2535. https://doi.org/10.1175/1520-0442(2000)013<2520:CVITAO>2.0.CO;2

Vuille, M., Bradley, R.S., Werner, M., Healy, R., Keimig, F., 2003. Modeling $\delta^{18}O$ in precipitation over the tropical Americas: 1. Interannual variability and climatic controls. J. Geophys. Res. D Atmos. 108, 1–24. https://doi.org/10.1029/2001jd002038

Vuille, M., Burns, S.J., Taylor, B.L., Cruz, F.W., Bird, B.W., Abbott, M.B., Kanner, L.C., Cheng, H., Novello, V.F., 2012. A review of the South American monsoon history as recorded in stable isotopic proxies over the past two millennia. Clim. Past 8, 1309–1321. https://doi.org/10.5194/cp-8-1309-2012

Vuille, M., Hardy, D.R., Braun, C., Keimig, F., Bradley, R.S., 1998. Atmospheric circulation anomalies associated with 1996/1997 summer precipitation events on Sajama Ice Cap, Bolivia. J. Geophys. Res. Atmos. 103, 11191–11204. https://doi.org/10.1029/98JD00681

Vuille, M., Werner, M., 2005. Stable isotopes in precipitation recording South American summer monsoon and ENSO variability: Observations and model results. Clim. Dyn. 25, 401–413. https://doi.org/10.1007/s00382-005-0049-9

Wang, X., Edwards, R.L., Auler, A.S., Cheng, H., Kong, X., Wang, Y., Cruz, F.W., Dorale, J.A., Chiang, H., 2017. Hydroclimate changes across the Amazon lowlands over the past 45,000 years. Nature 541, 204–207. https://doi.org/10.1038/nature20787

Winkler, R., Landais, A., Sodemann, H., Dümbgen, L., Prié, F., Masson-Delmotte, V., Stenni, B., Jouzel, J., 2012. Deglaciation records of ^{17}O-excess in East Antarctica: Reliable reconstruction of oceanic normalized relative humidity from coastal sites. Clim. Past 8, 1–16. https://doi.org/10.5194/cp-8-1-2012

Worden, J., Noone, D., Bowman, K., Beer, R., Eldering, A., Fisher, B., Gunson, M., Goldman, A., Herman, R., Kulawik, S.S., Lampel, M., Osterman, G., Rinsland, C., Rodgers, C., Sander, S., Shephard, M., Webster, C.R., Worden, H., 2007. Importance of rain evaporation and continental convection in the tropical water cycle. Nature 445, 528–532.

https://doi.org/10.1038/nature05508

Xu, D., Agee, E., Wang, J., Ivanov, V.Y., 2019. Estimation of Evapotranspiration of Amazon Rainforest Using the Maximum Entropy Production Method. Geophys. Res. Lett. 46, 1402–1412. https://doi.org/10.1029/2018GL080907

Yeung, L.Y., Hayles, J.A., Hu, H., Ash, J.L., Sun, T., 2018. Scale distortion from pressure baselines as a source of inaccuracy in triple-isotope measurements. Rapid Commun. Mass Spectrom. 32, 1811–1821. https://doi.org/10.1002/rcm.8247

Young, E.D., Galy, A., Nagahara, H., 2002. Kinetic and equilibrium mass-dependent isotope fractionation laws in nature and their geochemical and cosmochemical significance. Geochim. Cosmochim. Acta 66, 1095–1104. https://doi.org/10.1016/S0016-7037(01)00832-8

4.9 Supplementary information

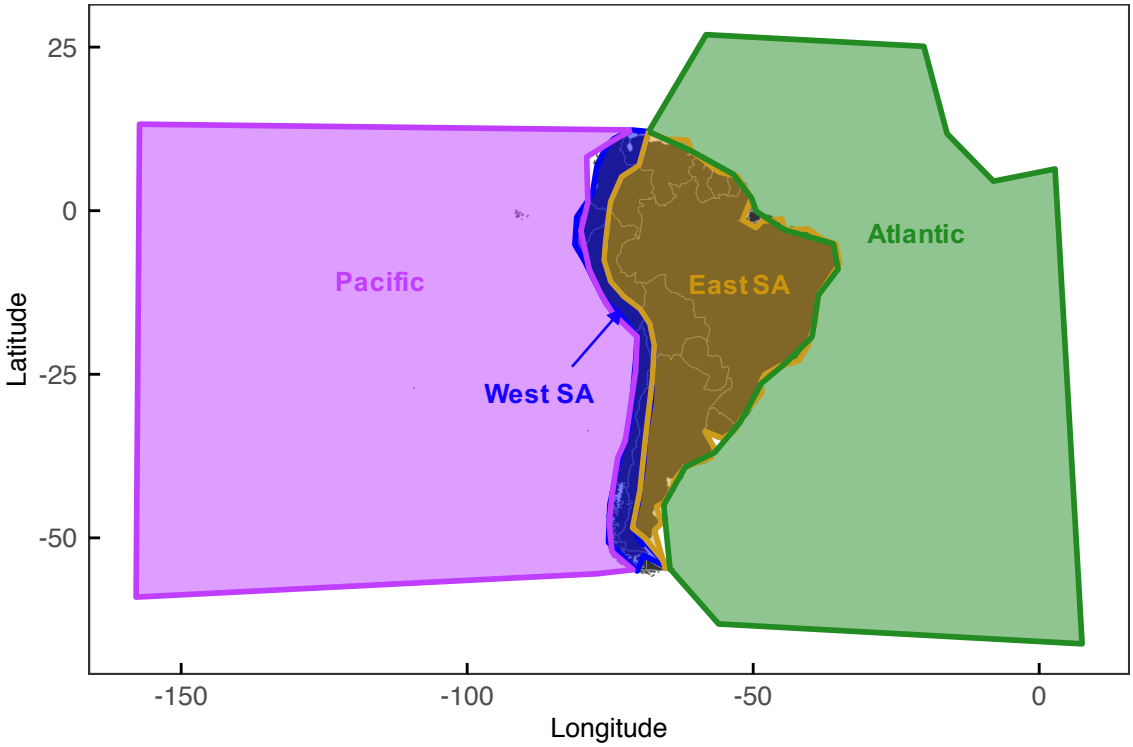

Figure S4.1 Moisture source regions in the central Andes.

Table S4.1 Bimonthly meteorologic data (temperature, relative humidity, and precipitation) and precipitation isotopes ($\delta^{18}O_p$ and $\delta^{2}H_p$) from 19 stations in southern Peru. $\delta^{18}O_p$ and $\delta^{2}H_p$ in orange are likely tap or surface water. $\delta^{18}O_p$ and $\delta^{2}H_p$ in blue have negative d-excess$_p$ values. Meteorologic data are missing when no data was recorded by a SENAMHI observer or the meteorologic sensors were broken. Isotopic data are missing when rain did not fall during a collection period or the observer did not collect a sample.

San Gaban (13.451806°S, 70.409139°W, 657 masl)							
Year	**Month**	**Day**	**Temperature (°C)**	**Relative Humidity (%)**	**Total Precipitation (mm)**	**$\delta^{18}O$ (‰, VSMOW)**	**$\delta^{2}H$ (‰, VSMOW)**
2016	6	15	21.6	86.0	217.0	–6.3	–36.9
2016	7	1	20.6	88.1	117.8	–0.8	11.3
2016	7	15	22.1	87.2	272.3	–2.1	–2.5
2016	8	1	21.2	84.6	41.9	0.0	15.6
2016	8	15	22.5	84.7	118.2	–0.1	16.5
2016	9	1	21.6	86.5	83.2	–0.3	17.3
2016	9	15	20.8	84.6	90.3	–0.7	13.5
2016	10	1	23.0	84.0	169.4	–1.6	4.3
2016	10	15	23.1	85.3	125.7	–4.1	–17.1
2016	11	1	23.5	84.1	183.7	–2.3	–3.8
2016	11	15	23.4	85.3	78.4	–2.9	–6.9
2016	12	1	23.0	86.8	162.7	–3.3	–7.8
2016	12	15	23.0	89.4	247.6	–7.0	–42.5
2017	1	1	23.4	87.9	381.5	–7.0	–39.6
2017	1	15	23.3	88.3	401.3	–15.3	–111.9
2017	2	1	24.1	85.8	217.4	–8.9	–58.2
2017	2	15	23.2	90.1	422.6	–7.4	–44.5
2017	3	1	22.5	90.3	509.0	–13.6	–94.9
2017	3	15	23.6	88.5	476.1	–11.7	–80.9
2017	4	1	23.0	88.8	252.7	–15.0	–107.6
2017	4	15	23.2	90.0	374.5	–10.3	–70.1
2017	5	1	22.6	88.9	287.0	–13.0	–91.1
2017	5	15	23.0	90.9	168.1	–10.1	–65.9
2017	6	1	22.4	94.4	307.5	–12.7	–88.3
2017	6	15	21.8	94.0	181.8	–5.4	–26.7
2017	7	1	21.4	95.4	195.4	–2.3	0.7
2017	7	15	21.7	90.9	57.0	–0.3	18.8
2017	8	1	21.0	90.2	158.9	–0.7	16.4
2017	8	15	22.8	90.1	408.1	–2.4	1.6
2017	9	1	23.2	89.4	344.0	–3.9	–8.8
2017	9	15	23.3	89.1	271.4	–0.9	15.0

2017	10	1	22.7	90.2	130.0	0.1	24.0
2017	10	15	24.0	86.9	94.0	–2.7	–3.3
2017	11	1	23.4	91.8	261.1	–5.2	–24.0
2017	11	15	24.3	90.3	186.2	–8.3	–51.6
2017	12	1	24.1	91.7	470.1	–9.3	–58.8
2017	12	15	24.4	90.6	286.5	–7.8	–46.9
2018	1	1	23.4	93.9	461.1	–5.2	–30.6
2018	1	15	22.9	93.9	533.2	–10.0	–64.3
2018	2	1	23.4	92.1	390.6	–10.9	–74.2
2018	2	15	23.5	92.6	358.1	–5.8	–31.6
2018	3	1	23.6	91.4	362.2	–8.5	–50.0
2018	3	15	23.9	92.3	540.4	–8.7	–52.8
2018	4	1	22.9	93.9	372.7	–7.2	–42.5
2018	4	15	23.1	93.1	290.1	–9.4	–60.2
2018	5	1	23.2	91.2	147.7	–8.2	–50.2
2018	5	15	22.9	93.1	163.4	–6.4	–35.5
2018	6	1	21.8	92.0	179.4	–6.0	–33.1
2018	6	15	19.6	95.4	114.9	–8.0	–48.4
2018	7	1	20.7	93.5	252.6	–2.0	1.0
2018	7	15	21.1	91.5	39.6	–0.1	16.0
2018	8	1	21.1	91.0	100.0	–2.2	–3.6
2018	8	15	21.2	92.3	132.5	–3.8	–11.2
2018	9	1	21.6	90.7	200.3	–1.1	10.5
2018	9	15	22.6	85.6	32.8	2.0	35.2
2018	10	1	23.6	89.6	163.2	–1.7	6.5
2018	10	15	23.7	91.9	438.5	–5.2	–25.1
2018	11	1	23.9	91.4	219.7	–8.9	–58.3
2018	11	15	23.6	92.8	325.7	–7.3	–44.8
2018	12	1	23.1	96.0	367.9	–9.9	–66.9
2018	12	15	23.6	92.6	286.1	–6.4	–37.3
2019	1	1	23.0	94.9	856.7	–12.0	–83.9
2019	1	15	22.7	96.6	419.9	–6.2	–35.8
2019	2	1	23.9	92.1	384.4	–10.7	–74.6
2019	2	15	23.8	93.0	331.9	–10.1	–73.5
2019	3	1	23.0	94.2	467.5	–9.2	–62.7
2019	3	15	23.9	92.7	264.7	–9.6	–66.1
2019	4	1	23.7	93.4	487.9	–10.4	–72.9
2019	4	15	23.5	91.0	352.0	–9.3	–61.8
2019	5	1	23.8	93.7	293.5	–11.8	–84.9
2019	5	15	22.7	93.9	568.5	–9.0	–60.0

Ollachea (13.794306°S, 70.469927°W, 2850 masl)							
Year	**Month**	**Day**	**Temperature (°C)**	**Relative Humidity (%)**	**Total Precipitation (mm)**	**$\delta^{18}O$ (‰, VSMOW)**	**$\delta^{2}H$ (‰, VSMOW)**
2016	6	15	11.3	71.4	0.0		
2016	7	1	10.8	76.0	4.4		
2016	7	15	12.0	72.9	47.6		
2016	8	1	11.6	63.5	2.7		
2016	8	15	11.6	77.0	7.5		
2016	9	1	12.3	74.8	2.5	–19.8	–143.8
2016	9	15	12.3	75.4	4.5	–11.6	–82.8
2016	10	1	13.0	79.3	20.2	–11.5	–80.9
2016	10	15	12.8	87.4	41.0	–19.8	–144.1
2016	11	1	13.2	85.1	43.5	–11.6	–82.2
2016	11	15	14.0	82.2	3.2		
2016	12	1	13.3	85.2	33.0	–13.8	–98.7
2016	12	15	13.0	88.8	55.2	–13.7	–98.8
2017	1	1	13.4	88.4	71.7	–19.7	–144.0
2017	1	15	13.2	90.4	143.7	–13.7	–99.2
2017	2	1	13.2	89.7	86.0	–13.7	–97.8
2017	2	15	13.7	90.0	54.8	–19.7	–144.3
2017	3	1	12.5	93.0	176.3	–13.8	–99.2
2017	3	15	13.4	91.2	96.5	–14.6	–99.3
2017	4	1	12.9	92.2	97.7	–16.3	–114.9
2017	4	15	13.3	91.0	32.0	–15.6	–113.8
2017	5	1	12.9	88.6	19.7		
2017	5	15	13.1	88.5	18.0		
2017	6	1	12.6	90.0	21.0		
2017	6	15	12.2	86.5	7.7		
2017	7	1	11.5	84.5	8.2		
2017	7	15	10.6	80.9	4.8	–15.5	–112.5
2017	8	1	10.8	76.1	9.6	–15.4	–112.5
2017	8	15	12.1	75.7	0.0		
2017	9	1	12.6	79.6	17.2		
2017	9	15	12.9	82.6	61.5	–15.5	–112.9
2017	10	1	12.5	84.6	24.1		
2017	10	15	13.3	77.6	20.2		
2017	11	1	13.5	85.8	33.1	–15.5	–113.0
2017	11	15	14.0	87.6	52.9	–15.6	–113.0
2017	12	1	14.2	82.4	42.9	–15.5	–112.6
2017	12	15	13.8	88.6	69.1	–15.5	–112.5
2018	1	1	13.4	93.0	98.6	–15.5	–112.5

2018	1	15	12.7	93.1	78.4	–15.6	–112.7
2018	2	1	13.2	90.5	109.2	–15.6	–112.8
2018	2	15	13.3	94.1	167.3		
2018	3	1	13.1	92.8	103.7		
2018	3	15	13.9	91.2	139.7	–15.6	–112.7
2018	4	1	13.1	93.7	108.6		
2018	4	15	12.9	88.3	27.2	–15.7	–112.9
2018	5	1	12.5	90.1	37.3		
2018	5	15	12.4	86.8	2.3		
2018	6	1	11.2	79.6	0.0		
2018	6	15	11.2	82.8	64.7		
2018	7	1	11.0	78.5	4.2		
2018	7	15	11.1	75.3	3.2	–11.6	–82.7
2018	8	1	11.3	75.4	43.2		
2018	8	10	NA	NA	NA	–11.7	–83.4
2018	8	15	11.2	86.2	17.2		
2018	9	1	11.5	84.2	17.4	–11.7	–83.4
2018	9	15	12.6	68.1	1.6	–11.7	–83.2
2018	10	1	13.8	77.2	16.4		
2018	10	15	13.8	86.0	80.2	–11.7	–83.5
2018	11	1	13.5	90.7	86.0		
2018	11	15	13.8	89.9	86.3	–11.7	–83.5
2018	12	1	14.3	91.5	63.6	–9.4	–64.4
2018	12	15	14.2	84.8	50.8	–9.4	–64.0
2019	1	1	13.6	91.7	165.8	–9.4	–63.8
2019	1	15	13.7	92.8	59.7	–9.3	–64.5
2019	2	1	14.1	91.2	162.8	–9.3	–64.3
2019	2	15	13.8	93.4	136.0	–9.4	–63.7
2019	3	1	13.5	93.2	106.6	–9.3	–64.0
2019	3	15	14.5	89.7	57.9	–9.4	–63.7
2019	4	1	13.9	93.2	149.3	–15.4	–112.4
2019	4	15	13.6	86.3	52.8		
2019	5	1	14.2	88.9	15.9		
2019	5	15	13.4	88.6	60.4		
2019	5	21	NA	NA	NA	–9.8	–63.8

Macusani (14.07°S, 70.43908°W, 4345 masl)							
Year	**Month**	**Day**	**Temperature (°C)**	**Relative Humidity (%)**	**Total Precipitation (mm)**	**$\delta^{18}O$ (‰, VSMOW)**	**$\delta^{2}H$ (‰, VSMOW)**
2016	6	15	1.0	54.3	0.0		
2016	7	1	1.8	61.5	0.0		

2016	7	15	2.1	66.6	24.0	–21.1	–150.9
2016	8	1	1.7	48.7	0.0		
2016	8	15	2.8	59.5	0.0		
2016	9	1	3.1	61.6	1.0		
2016	9	15	3.7	60.6	0.0	–8.4	–28.8
2016	10	1	4.4	70.4	22.0	–9.5	–34.0
2016	10	15	5.3	72.7	22.5	–13.4	–87.2
2016	11	1	5.2	75.6	55.0	–8.9	–47.1
2016	11	15	5.9	67.7	3.5		
2016	12	1	5.7	71.3	49.0		
2016	12	15	5.7	76.8	26.0	–12.9	–81.2
2017	1	1	6.0	76.9	39.5	–21.0	–145.5
2017	1	15	5.7	80.5	80.0	–20.9	–146.9
2017	2	1	5.8	76.9	33.5	–14.0	–93.5
2017	2	15	6.0	77.5	25.5	–14.3	–97.4
2017	3	1	5.9	77.2	73.0	–21.3	–147.1
2017	3	15	8.7	70.2	47.0	–24.2	–174.1
2017	4	1	8.6	69.8	39.5	–27.8	–210.9
2017	4	15	9.0	69.4	44.0	–23.0	–164.9
2017	5	1	9.4	67.9	33.5	–18.8	–137.5
2017	5	15	7.9	71.9	11.0	–11.9	–85.9
2017	6	1	4.4	81.7	11.0	–15.2	–106.5
2017	6	15	3.5	76.3	0.0		
2017	7	1	3.0	66.9	2.5		
2017	7	15	2.0	67.2	0.5		
2017	8	1	2.2	57.9	0.5		
2017	8	15	3.3	56.1	0.0		
2017	9	1	3.7	69.1	3.0	–16.9	–121.2
2017	9	15	4.3	74.1	12.6	–15.2	–109.3
2017	10	1	5.0	74.4	16.5	–7.6	–40.8
2017	10	15	4.2	68.9	38.2	–7.8	–40.6
2017	11	1	5.3	76.2	14.0	–21.1	–156.0
2017	11	15	5.8	79.3	36.5	–21.0	–156.9
2017	12	1	6.0	74.6	25.0	–21.1	–157.5
2017	12	15	6.4	78.3	37.5	–18.2	–131.2
2018	1	1	6.1	83.6	63.8	–18.2	–131.1
2018	1	15	5.2	87.3	64.0	–19.2	–139.0
2018	2	1	5.1	85.4	69.5	–19.2	–138.8
2018	2	15	6.0	88.7	61.1	–17.8	–128.4
2018	3	1	5.2	86.4	60.0	–22.2	–161.4
2018	3	15	6.2	84.4	83.5	–22.6	–165.6
2018	4	1	5.2	86.9	84.0	–21.3	–156.8

2018	4	15	5.1	80.9	3.5		
2018	5	1	4.8	81.0	5.2		
2018	5	15	4.0	75.5	7.5		
2018	6	1	2.5	68.6	0.0		
2018	6	15	2.0	80.2	31.0		
2018	7	1	1.9	69.0	0.0		
2018	7	15	1.3	64.0	4.0		
2018	8	1	1.6	71.8	33.0		
2018	8	15	2.6	79.7	8.0		
2018	9	1	3.1	74.0	9.5		
2018	9	15	3.5	63.1	0.0		
2018	10	1	4.4	72.5	27.0		
2018	10	15	5.1	80.4	36.0		
2018	11	1	5.7	83.8	55.5		
2018	11	15	6.2	81.2	52.3		
2018	12	1	6.6	81.7	38.5		
2018	12	15	6.3	71.4	2.5		
2019	1	1	5.7	84.3	74.5		
2019	1	15	5.7	86.6	82.9		
2019	2	1	5.9	86.3	69.5		
2019	2	15	5.9	88.1	56.0		
2019	3	1	6.3	86.4	59.5		
2019	3	15	6.3	83.7	41.5		
2019	4	1	6.0	86.7	70.0		
2019	4	15	5.8	79.2	26.0		
2019	5	1	5.9	82.6	14.5		
2019	5	15			31.0		

Ayaviri (14.87172°S, 70.59325°W, 3906 masl)							
Year	**Month**	**Day**	**Temperature (°C)**	**Relative Humidity (%)**	**Total Precipitation (mm)**	**$\delta^{18}O$ (‰, VSMOW)**	**$\delta^{2}H$ (‰, VSMOW)**
2016	6	15			0.0		
2016	7	1	5.5	38.5	0.3		
2016	7	15	5.7	46.1	9.1		
2016	8	1	6.2	34.1	0.0		
2016	8	15	7.7	38.3	0.1		
2016	9	1	7.9	39.8	6.5		
2016	9	15	8.6	31.3	0.0		
2016	10	1	9.6	48.7	13.2		
2016	10	15	9.6	52.2	19.1	–8.7	–46.9
2016	11	1	9.7	57.8	30.8	–8.3	–45.4
2016	11	15	10.5	44.2	20.3	–3.4	2.6

2016	12	1	10.3	47.8	23.5	–4.5	–2.2
2016	12	15	10.3	59.3	30.7	–15.3	–104.9
2017	1	1	10.9	58.4	25.2	–16.9	–112.6
2017	1	15	9.9	67.6	20.5	–17.6	–120.3
2017	2	1	10.0	62.9	13.8	–13.6	–91.1
2017	2	15	13.0	55.5	15.1	–9.8	–62.7
2017	3	1	10.8	67.0	49.0	–24.5	–178.0
2017	3	15	12.2	65.2	52.4	–26.0	–192.5
2017	4	1	13.0	64.2	72.3	–26.6	–192.7
2017	4	15	13.3	63.4	15.4	–19.7	–145.3
2017	5	1	12.1	64.7	21.7	–18.9	–140.6
2017	5	15	12.2	59.2	1.4	–16.2	–120.3
2017	6	1	7.8	65.1	30.0	–13.7	–100.8
2017	6	15	6.7	48.0	0.0		
2017	7	1	6.2	43.4	9.2		
2017	7	15	5.6	43.0	0.2		
2017	8	1	6.7	31.6	0.0		
2017	8	15	7.5	28.3	0.0		
2017	9	1	8.3	34.1	0.0		
2017	9	15	8.8	57.7	14.8	–7.0	–37.0
2017	10	1	9.8	51.2	14.0	–5.9	–25.4
2017	10	15	9.3	44.9	31.5	–11.0	–66.7
2017	11	1	10.5	49.7	4.8	–12.8	–89.3
2017	11	15	10.2	60.3	35.5	–13.4	–89.2
2017	12	1	11.1	49.8	28.3	–4.1	–16.8
2017	12	15	10.6	55.2	28.2	–10.7	–74.4
2018	1	1	9.7	71.6	68.1	–15.8	–110.3
2018	1	15	9.1	73.8	62.9	–16.1	–110.3
2018	2	1	9.5	71.7	42.9	–19.7	–143.9
2018	2	15	9.8	77.0	42.7	–16.8	–121.5
2018	3	1	9.1	75.2	88.5	–20.7	–149.0
2018	3	15	9.5	78.6	102.2	–18.3	–130.3
2018	4	1	9.2	71.8	23.0	–19.7	–144.8
2018	4	15	8.3	60.3	0.4	–11.8	–87.4
2018	5	1	8.1	62.6	28.3	–17.5	–123.1
2018	5	15	7.7	54.2	0.9		
2018	6	1	6.0	40.2	0.0		
2018	6	15	6.0	64.0	22.0	–11.3	–76.1
2018	7	1	6.1	49.1	0.0		
2018	7	15	6.0	45.4	1.0	–14.2	–101.3
2018	8	1	5.7	54.8	20.7	–14.4	–101.7
2018	8	15	6.3	57.6	14.0	–9.7	–61.8

2018	9	1	7.9	42.5	1.2	–4.7	–20.7
2018	9	15	9.0	38.1	0.1		
2018	10	1	9.3	42.0	9.1	–3.3	8.9
2018	10	15	9.5	63.0	22.9	–8.8	–51.8
2018	11	1	9.7	67.2	19.1	–11.7	–76.6
2018	11	15	10.9	58.9	14.0	–8.5	–56.6
2018	12	1	11.0	52.0	20.4	–11.4	–81.1
2018	12	15	11.2	39.8	0.5		
2019	1	1	10.1	67.5	28.4	–15.6	–111.8
2019	1	15	10.4	67.0	66.5	–19.3	–138.8
2019	2	1	10.3	70.0	70.2	–17.2	–128.3
2019	2	15	9.3	79.5	82.2	–22.1	–162.9
2019	3	1	10.1	72.6	45.6	–22.5	–168.4
2019	3	15	10.1	72.0	63.6	–18.2	–131.4
2019	4	1	9.8	75.4	40.7	–19.3	–142.3
2019	4	15	9.5	64.7	14.2	–20.8	–152.0
2019	5	1	9.2	70.9	16.7	–16.0	–118.1
2019	5	15	8.5	66.9	11.0	–12.1	–85.9

Ichuña (16.14075°S, 70.53725°W, 3792 masl)							
Year	**Month**	**Day**	**Temperature (°C)**	**Relative Humidity (%)**	**Total Precipitation (mm)**	**$\delta^{18}O$ (‰, VSMOW)**	**$\delta^{2}H$ (‰, VSMOW)**
2016	6	15					
2016	7	1				–5.7	–27.0
2016	7	15				–5.6	–24.8
2016	8	1					
2016	8	15					
2016	9	1				–5.6	–24.8
2016	9	15					
2016	10	1				–5.3	–23.1
2016	10	15				–5.2	–22.2
2016	11	1				–5.2	–22.0
2016	11	15				–5.2	–21.6
2016	12	1				–5.1	–22.7
2016	12	15				–5.2	–22.2
2017	1	1				–2.4	0.4
2017	1	15				–2.8	–1.1
2017	2	1				–19.9	–143.5
2017	2	15				–20.0	–145.4
2017	3	1				–20.1	–145.9

2017	3	15				−20.0	−145.8
2017	4	1				−20.1	−145.7
2017	4	15				−20.0	−145.9
2017	5	1					
2017	5	15	8.6	29.6			
2017	6	1	8.1	49.5			
2017	6	15	7.9	32.6			
2017	7	1	8.0	27.2			
2017	7	15	7.3	24.3			
2017	8	1	8.6	20.2			
2017	8	15	8.5	17.0			
2017	9	1	8.9	18.5			
2017	9	15	9.6	42.2			
2017	10	1	11.1	29.1			
2017	10	15	10.7	34.9			
2017	11	1	11.8	29.1			
2017	11	15	12.5	32.1			
2017	12	1	12.5	34.1		−15.7	−111.0
2017	12	15	13.3	32.3		−15.7	−111.4
2018	1	1	11.0	61.3		−15.7	−111.4
2018	1	15	10.9	62.5		−15.7	−111.3
2018	2	1	10.9	65.0		−15.7	−111.2
2018	2	15	11.0	71.6		−15.8	−111.6
2018	3	1	10.8	66.8		−15.7	−111.4
2018	3	15	10.8	70.2		−15.7	−111.3
2018	4	1	10.6	63.5		−12.7	−89.1
2018	4	15	11.0	46.2		−12.7	−89.0
2018	4	23	10.5	56.4		−12.6	−88.9
2018	5	1	9.5	41.3		−15.5	−111.3
2018	5	15	7.8	23.1			
2018	6	1	6.5	62.5		−15.7	−112.9
2018	6	15	7.6	40.3			
2018	7	1	8.2	34.2			
2018	7	15	7.4	49.8		−15.1	−111.9
2018	8	1	8.2	30.1			
2018	8	15	8.8	23.4			
2018	9	1	10.4	21.4			
2018	9	15	9.8	25.1			
2018	10	1	10.8	47.1			
2018	10	15	11.9	40.5			
2018	11	1	13.1	32.0			
2018	11	15	12.9	26.7		−14.1	−105.6
2018	12	1	13.4	30.3		−14.4	−106.3

2018	12	15	12.0	54.6		–14.5	–105.9
2019	1	1	12.0	57.7		–14.8	–110.2
2019	1	15	11.4	68.0		–15.0	–110.0
2019	2	1	10.0	77.2		–21.7	–166.7
2019	2	15	11.7	66.8		–12.8	–95.8
2019	3	1	11.4	66.1		–13.2	–95.8
2019	3	15	11.9	56.5		–13.5	–94.8
2019	4	1	10.8	48.8			
2019	4	15	10.8	56.0		–18.2	–147.9
2019	5	1	10.9	56.4			
2019	5	15	10.1	45.8			

Carumas (16.81117°S, 70.695063°W, 2976 masl)							
Year	**Month**	**Day**	**Temperature (°C)**	**Relative Humidity (%)**	**Total Precipitation (mm)**	**$\delta^{18}O$ (‰, VSMOW)**	**$\delta^{2}H$ (‰, VSMOW)**
2016	6	15			0.0		
2016	7	1	12.9	27.0	2.2		
2016	7	15	12.5	34.8	2.9		
2016	8	1	13.2	24.5	0.0		
2016	8	15	13.0	26.7	0.0		
2016	9	1	13.2	27.4	0.0		
2016	9	15	13.1	28.5	0.0		
2016	10	1	14.5	31.3	0.0		
2016	10	15	13.5	30.1	0.0		
2016	11	1	13.9	34.5	0.0		
2016	11	15	13.9	33.3	0.0		
2016	12	1	13.3	34.5	0.0		
2016	12	15	13.1	50.0	0.0		
2017	1	1	13.0	69.9	19.5	–10.9	–70.4
2017	1	15	11.5	91.3	109.4	–7.7	–42.4
2017	1	30			135.3	–8.8	–50.9
2017	2	1	11.8	91.3	2.9	–6.6	–29.7
2017	2	15	12.1	80.0	4.0	–1.5	–6.2
2017	2	28			107.6	–4.5	–9.0
2017	3	1	10.2	93.7	1.0	–11.4	–69.2
2017	3	15	11.9	89.4	70.5	–6.7	–29.9
2017	3	30			46.2	–5.4	–17.7
2017	4	1	11.8	87.7	46.4		
2017	4	15	13.3	65.9	0.2		
2017	5	1	12.9	55.3	0.0		
2017	5	15	12.9	43.7	0.0		

2017	6	1	12.5	36.4	1.2		
2017	6	15	11.9	28.1	0.0	–10.0	–62.7
2017	7	1	12.2	24.6	0.0		
2017	7	15	12.6	21.0	0.0		
2017	8	1	12.8	18.5	0.0		
2017	8	15	12.8	16.8	0.0		
2017	9	1	12.8	17.9	0.0		
2017	9	15	13.6	29.6	0.0		
2017	10	1	14.0	28.3	0.0		
2017	10	15	13.8	29.3	0.0		
2017	11	1	14.2	27.0	0.0		
2017	11	15	13.7	34.3	0.0		
2017	12	1	13.4	39.5	0.0		
2017	12	15	13.3	47.5	0.0		
2018	1	1	12.2	68.2	28.8	–9.0	–54.5
2018	1	15	11.6	75.2	15.6	–9.0	–54.4
2018	2	1	12.9	75.7	33.8	–9.0	–54.3
2018	2	15	12.7	81.2	26.2	4.1	–9.0
2018	3	1	11.3		27.9	–8.8	–53.4
2018	3	15	13.3		12.0	4.1	–8.9
2018	4	1	12.1		25.3	4.1	–8.6
2018	4	15	12.2		0.0		
2018	5	1	13.2	59.6	2.4		
2018	5	15	12.9	36.6	0.0		
2018	6	1	12.4	19.7	0.0		
2018	6	15	11.3	42.2	0.7		
2018	7	1	12.2	29.8	0.0		
2018	7	15	12.3	26.3	1.3		
2018	8	1	11.4	37.9	6.0		
2018	8	15	12.7	21.8	0.0		
2018	9	1	13.4	18.9	0.0		
2018	9	15	13.7	21.0	0.0		
2018	10	1	14.1	18.4	0.0		
2018	10	15	13.5	34.7	0.0		
2018	11	1	13.8	31.1	0.0		
2018	11	15	14.0	35.2	0.0		
2018	12	1	13.9	33.1	0.0		
2018	12	15	14.8	34.0	0.0		
2019	1	1	13.9	52.6	9.4		
2019	1	15	13.0	67.7	7.6	–13.2	–96.5
2019	2	1	13.2	81.1	92.6	–13.2	–97.8
2019	2	15	13.0	85.4	154.8	–13.3	–98.1
2019	3	1	12.4	85.1	10.5	–13.3	–98.2
2019	3	15	13.2	76.8	71.3	–13.3	–98.3

2019	4	1	13.5	63.6	6.0	–13.3	–98.3
2019	4	15	13.1	51.6	0.0	–13.3	–98.3
2019	5	1	14.0	49.5	0.0		
2019	5	15	18.8	36.3	0.0		

Orcopampa (15.265889°S, 72.342778°W, 3779 masl)							
Year	**Month**	**Day**	**Temperature (°C)**	**Relative Humidity (%)**	**Total Precipitation (mm)**	**$\delta^{18}O$ (‰, VSMOW)**	**$\delta^{2}H$ (‰, VSMOW)**
2016	6	15			0.0		
2016	7	1	7.6	36.4	0.0		
2016	7	15	7.2	43.0	3.3		
2016	8	1	8.2	29.9	0.0		
2016	8	15	8.5	33.0	0.0		
2016	9	1	8.8	34.7	1.0		
2016	9	15	9.4	30.7	0.0		
2016	10	1	10.7	35.3	0.0		
2016	10	15	9.8	33.5	0.6		
2016	11	1	9.8	44.2	17.0		
2016	11	15	9.7	42.7	0.5		
2016	12	1	10.4	37.1	0.9		
2016	12	15	10.6	51.4	8.0	–23.1	–171.7
2017	1	1	10.8	63.3	58.6	–23.1	–171.3
2017	1	15	9.7	76.9	170.6	–23.5	–172.9
2017	2	1	10.0	76.0	102.2		
2017	2	15	10.6	64.6	6.9		
2017	3	1	9.0	76.0	78.1		
2017	3	15	9.5	76.4	124.9		
2017	4	1	9.6	76.0	91.9	–23.6	–172.5
2017	4	1	9.8	67.5	11.3		
2017	5	1	8.8	66.1	9.6		
2017	5	15	8.5	50.3	0.7		
2017	6	1	7.8	55.4	9.1		
2017	6	15	7.2	41.2	0.0		
2017	7	1	6.7	38.4	2.9		
2017	7	15	7.4	38.4	0.0		
2017	8	1	7.3	27.9	0.0		
2017	8	15	7.6	25.2	0.0		
2017	9	1	8.1	27.3	0.0		
2017	9	15	8.6	49.8	4.1	–19.6	–147.4
2017	10	1	9.9	37.1	3.0		
2017	10	15	9.4	40.3	9.4	–19.5	–147.9
2017	11	1	9.8	38.0	2.1		

2017	11	15	10.0	39.9	7.6		
2017	12	1	10.6	43.6	1.1	−19.6	−148.3
2017	12	15	10.7	42.2	4.3	−19.5	−147.9
2018	1	1	9.3	72.7	79.3	−19.7	−148.6
2018	1	15	9.3	71.2	23.3	−19.7	−148.7
2018	2	1	9.3	74.1	94.8	−19.7	−148.6
2018	2	15	10.4	70.6	67.9	−19.6	−148.5
2018	3	1	9.7	73.1	29.4	−23.2	−171.2
2018	3	15	9.6	76.1	56.6	−23.2	−171.5
2018	4	1	9.6	71.7	24.3	−23.2	−171.4
2018	4	15	9.5	64.5	15.1		
2018	5	1	9.6	61.6	11.6		
2018	5	15	8.1	52.2	4.3		
2018	6	1	6.9	32.4	0.0		
2018	6	15	6.4	60.6	10.4		
2018	7	1	6.3	45.9	0.0		
2018	7	15	7.3	42.6	2.0		
2018	8	1	6.6	51.7	9.7		
2018	8	15	7.7	36.1	3.7		
2018	9	1	8.3	33.5	0.0		
2018	9	15	9.2	28.4	0.0		
2018	10	1	9.7	24.3	0.0		
2018	10	15	9.4	50.5	14.0	−7.1	−49.0
2018	11	1	10.2	43.2	5.1	−7.1	−49.7
2018	11	15	11.1	38.7	3.3		
2018	12	1	10.6	32.4	0.0		
2018	12	15	11.6	39.6	0.9	−7.0	−49.3
2019	1	1	11.0	59.5	22.1	−7.1	−49.6
2019	1	15	10.6	60.5	21.2	−7.2	−50.0
2019	2	1	10.5	75.3	82.0	−7.2	−49.9
2019	2	15	10.1	76.4	31.1	−7.2	−50.0
2019	3	1	9.8	77.3	55.7	−7.2	−49.9
2019	3	15	10.8	73.1	34.0	−7.2	−49.9
2019	4	1	10.1	69.9	30.7		
2019	4	15	9.1	61.3	0.9		
2019	5	1	9.7	66.2	2.9		
2019	5	15	9.2	57.0	0.8		

Majes (16.343056˚S, 72.1525˚W, 1498 masl)							
Year	**Month**	**Day**	**Temperature (°C)**	**Relative Humidity (%)**	**Total Precipitation (mm)**	**$\delta^{18}O$ (‰, VSMOW)**	**$\delta^{2}H$ (‰, VSMOW)**
2016	6	15	16.9	40.3	0.0		
2016	7	1	16.2	49.9	0.0		
2016	7	15	17.9	48.9	0.0		
2016	8	1			0.0		
2016	8	15			0.0		
2016	9	1			0.0		
2016	9	15			0.0		
2016	10	1			0.0		
2016	10	15			0.0		
2016	11	1	17.9	50.0	0.0		
2016	11	15	18.0	45.9	0.0		
2016	12	1	17.7	52.2	0.0		
2016	12	15	18.3	58.1	0.0		
2017	1	1	18.1	63.1	0.0		
2017	1	15	18.9	72.4		–4.7	–14.6
2017	2	1	18.6	77.2	0.1	–7.5	–44.0
2017	2	15	19.0	71.9	0.0		
2017	3	1	18.8	65.7		–1.1	5.7
2017	3	15	18.9	70.8		–3.6	–11.2
2017	4	1	18.5	73.2	0.0		
2017	4	15	17.7	68.9	0.0		
2017	5	1	17.6	66.7	0.0		
2017	5	15	16.4	65.7	0.0		
2017	6	1	16.3	64.4	0.0		
2017	6	15	15.8	50.2	0.0		
2017	7	1	15.9	52.7	0.0		
2017	7	15	16.6	40.6	0.0		
2017	8	1	16.8	38.9	0.0		
2017	8	15	15.4	40.3	0.0		
2017	9	1	16.5	37.4	0.0		
2017	9	15	16.3	49.4	0.0		
2017	10	1	18.0	37.9	0.0		
2017	10	15	17.3	45.3	0.0		
2017	11	1	18.0	39.8	0.0		
2017	11	15	17.9	43.2	0.0		
2017	12	1	16.3	52.1	0.0		
2017	12	15	18.3	53.0	0.0		
2018	1	1	17.9	66.4	0.2	–1.2	–20.3
2018	1	15	18.0	62.0	0.0		

2018	2	1	18.2	67.8		–4.9	–32.9
2018	2	15	18.0	73.2	0.1	–2.8	–6.6
2018	3	1	17.8	73.5	0.0		
2018	3	15	19.1	62.4	0.0		
2018	4	1	18.6	67.6	0.0		
2018	4	15	17.4	66.5	0.0		
2018	5	1	15.7	59.9	0.4		
2018	5	15	16.9	59.2	0.0		
2018	6	1	16.7	46.3	0.0		
2018	6	15	18.5	37.8	0.0		
2018	7	1	16.9	41.2	0.0		
2018	7	15	17.4	37.2	0.0		
2018	8	1	17.9	40.5	0.0		
2018	8	15	17.4	34.2	0.0		
2018	9	1	17.4	32.8	0.0		
2018	9	15	17.1	35.9	0.0		
2018	10	1	17.9	35.2	0.0		
2018	10	15	18.1	44.3	0.0		
2018	11	1	18.0	43.3	0.0		
2018	11	15	18.1	48.7	0.0		
2018	12	1	17.9	45.3	0.0		
2018	12	15	18.3	54.1	0.0		
2019	1	1	19.0	59.8	0.1		
2019	1	15	18.0	73.9	0.0		
2019	2	1	19.3	73.3	0.0		
2019	2	15	19.3	83.9	8.7		
2019	3	1	19.8	68.8	0.0		
2019	3	15	20.0	69.3	0.0		
2019	4	1	18.8	61.7	0.1		
2019	4	15	17.7	63.6	0.0		
2019	5	1	18.1	64.4	0.0		
2019	5	15	18.2	52.4	0.6		

Santo Tomas (14.450333°S, 72.095917°W, 3658 masl)							
Year	**Month**	**Day**	**Temperature (°C)**	**Relative Humidity (%)**	**Total Precipitation (mm)**	**$\delta^{18}O$ (‰, VSMOW)**	**$\delta^{2}H$ (‰, VSMOW)**
2016	6	15	9.9	31.7	0.0		
2016	7	1	8.5	36.8	5.8		
2016	7	15	8.7	43.1	8.8	–13.9	–99.2
2016	8	1	9.9	29.8	0.0	–14.2	–98.7
2016	8	15	9.9	37.9	0.0		
2016	9	1	10.3	37.2	7.6	–6.3	–18.4

2016	9	15	11.7	27.5	0.0	–6.4	–20.3
2016	10	1	11.3	46.0	7.2	–2.2	17.6
2016	10	15	11.0	47.1	28.0	–9.7	–49.9
2016	11	2	11.2	49.3	34.0	–5.5	–18.6
2016	11	15	12.2	39.5	2.0		
2016	12	1	11.7	43.6	27.0		
2016	12	15	10.8	63.8	33.0	–10.3	–63.5
2017	1	1	11.7	63.9	59.2	–19.6	–142.7
2017	1	15	10.4	75.3	99.6	–19.0	–143.8
2017	2	1	10.6	71.3	115.2	–21.0	–155.8
2017	2	15	11.3	65.2	21.0	–15.7	–109.0
2017	3	1	9.9	75.2	91.6	–24.9	–187.6
2017	3	15	10.4	76.4	150.8		
2017	4	1	10.5	71.9	86.2		
2017	4	15	10.8	70.8	7.2		
2017	5	1	10.1	68.3	26.6		
2017	5	15	10.4	57.5	4.6	–16.1	–118.8
2017	6	1	9.0	64.1	16.0	–12.1	–88.4
2017	6	15	9.0	48.3	0.0		
2017	7	1	9.3	41.3	n.d.	–11.8	–85.0
2017	7	15	8.8	42.6	7.0	–11.8	–84.6
2017	8	1	9.6	33.6	0.0		
2017	8	15	10.2	27.9	n.d.	–2.8	–1.2
2017	9	1	10.6	33.8	n.d.	–2.6	0.4
2017	9	15	10.8	53.2	23.6		
2017	10	1	11.4	49.2	32.0		
2017	10	15	11.0	45.6	37.0	–2.7	–0.1
2017	11	1	10.9	52.4	24.2	–10.9	–71.6
2017	11	15	11.2	55.3	43.6	–10.8	–71.0
2017	12	1	12.4	48.6	6.6		
2017	12	15	12.1	49.6	10.4	–9.4	–57.8
2018	1	1	10.3	73.9	153.4	–14.3	–103.4
2018	1	15	10.2	73.8	81.6	–23.4	–175.9
2018	2	1	10.3	71.1	69.8		
2018	2	15	10.8	74.9	98.0		
2018	3	1	10.3	75.0	83.6	–18.0	–131.1
2018	3	15	11.6	78.8	93.4		
2018	4	1	10.6	71.6	39.0	–29.3	–216.1
2018	4	15	10.6	62.7	8.2	–17.7	–130.5
2018	5	1	10.4	64.4	26.8	–12.8	–86.1
2018	5	15	8.2	54.2	5.4	–12.7	–87.0
2018	6	1	9.0	36.9	0.0		

2018	6	15	7.8	63.4	11.8	–15.6	–114.5
2018	7	1	8.1	46.1	0.0		
2018	7	15	8.4	44.6	2.8	–4.4	–23.0
2018	8	1	8.1	53.4	21.2		
2018	8	15	7.9	56.1	28.2		
2018	9	1	9.4	44.6	7.9		
2018	9	15	11.2	36.8	2.2		
2018	10	1	10.8	37.4	2.4	–6.7	–39.2
2018	10	15	11.0	56.3	32.6	–11.7	–81.7
2018	11	1	10.9	65.0	16.8		
2018	11	15	12.0	58.1	68.8		
2018	12	1	12.4	48.1	5.6	–9.4	–59.5
2018	12	15	12.3	43.0	6.0		
2019	1	1	10.9	68.8	35.6	–9.9	–71.9
2019	1	15	11.5	66.9	48.0		
2019	2	1	10.7	77.5	111.0		
2019	2	15	10.3	81.2	97.8		
2019	3	1	10.6	80.3	104.0		
2019	3	15	10.8	79.5	91.0		
2019	4	1	10.7	80.5	72.4	–13.0	–89.7
2019	4	15	10.9	66.4	10.2		
2019	5	1	10.3	74.0	17.6		
2019	5	12				–17.8	–131.2
2019	5	15	10.3	66.3	8.4		

Ayo (15.679167°S, 72.270278°W, 1956 masl)							
Year	**Month**	**Day**	**Temperature (°C)**	**Relative Humidity (%)**	**Total Precipitation (mm)**	**$\delta^{18}O$ (‰, VSMOW)**	**$\delta^{2}H$ (‰, VSMOW)**
2016	6	15			0.0		
2016	7	1	16.9	34.7	0.0		
2016	7	15	17.2	37.6	0.0		
2016	8	1	16.5	27.4	0.0		
2016	8	15	17.0	29.6	0.0		
2016	9	1	17.1	30.4	0.0		
2016	9	15	17.0	33.6	0.0		
2016	10	1	17.0	34.7	0.0		
2016	10	15	17.1	34.8	0.0		
2016	11	1	18.0	40.9	0.0		
2016	11	15	19.9	37.1	0.0		
2016	12	1	21.9	37.9	0.0		
2016	12	15	22.4	49.8	0.0		
2017	1	1	22.0	60.5	0.0		

2017	1	15	21.1	71.6	0.0		
2017	2	1	21.0	73.0	0.0		
2017	2	15	20.5	67.1	0.0		
2017	3	1	20.8	73.5	0.0		
2017	3	15	20.1	76.4	0.0		
2017	4	1	20.2	74.1	0.0		
2017	4	15	21.4	70.0	0.0		
2017	5	1	21.9	62.4	0.0		
2017	5	15	22.4	59.6	0.0		
2017	6	1	18.0	42.9	0.0		
2017	6	15	16.7	33.1	0.0		
2017	7	1	17.2	29.4	0.0		
2017	7	15	17.4	26.0	0.0		
2017	8	1	16.9	20.1	0.0		
2017	8	15	16.9	23.5	0.0		
2017	9	1	17.1	23.3	0.0		
2017	9	15	17.7	34.1	0.0		
2017	10	1	17.6	31.0	0.0		
2017	10	15	17.7	35.7	0.0		
2017	11	1	17.6	32.9	0.0		
2017	11	15	17.8	36.2	0.0		
2017	12	1	17.5	46.4	0.0		
2017	12	15	18.2	49.7	0.0		
2018	1	1	18.2	63.3	0.0		
2018	1	15	18.1	59.2	0.0		
2018	2	1	18.4	71.5	0.0		
2018	2	15	18.6	68.6	0.0		
2018	3	1	18.6	67.4	0.0		
2018	3	15	18.8	62.2	0.0		
2018	4	1	18.5	67.3	0.0		
2018	4	15	17.8	64.7	0.0		
2018	5	1	18.2	60.4	0.0		
2018	5	15	17.5	49.3	0.0		
2018	6	1	16.9	28.1	0.0		
2018	6	15	17.8	37.8	0.0		
2018	7	1	17.4	28.6	0.0		
2018	7	15	17.0	29.7	0.0		
2018	8	1	17.0	37.3	0.0		
2018	8	15	17.2	26.2	0.0		
2018	9	1	17.8	22.6	0.0		
2018	9	15	16.8	30.0	0.0		
2018	10	1	17.1	25.9	0.0		
2018	10	15	17.9	34.7	0.0		
2018	11	1	17.9	35.0	0.0		
2018	11	15	17.8	42.2	0.0		

2018	12	1	17.3	39.3	0.0		
2018	12	15	17.7	44.1	0.0		
2019	1	1	18.7	55.4	0.0		
2019	1	15	18.5	63.0	0.0		
2019	2	1	18.9	74.3	0.0		
2019	2	15	19.1	79.6	0.0		
2019	3	1	18.9	70.3	0.0		
2019	3	15	19.1	65.5	0.0		
2019	4	1	18.9	56.4	0.0		
2019	4	15	17.8	59.1	0.0		
2019	5	1	18.4	54.6	0.0		
2019	5	15	17.3	65.2	0.0		

Puyca (15.0605°S, 72.692306°W, 3661 masl)							
Year	**Month**	**Day**	**Temperature (°C)**	**Relative Humidity (%)**	**Total Precipitation (mm)**	**$\delta^{18}O$ (‰, VSMOW)**	**$\delta^{2}H$ (‰, VSMOW)**
2017	11	15	11.9	58.7	22.2		
2017	12	1	12.5	57.2	13.1		
2017	12	15	11.8	64.7	10.6	–11.0	–76.7
2018	1	1	11.3	69.8	65.4	–10.9	–75.5
2018	1	15	11.8	73.8	29.8	–11.0	–75.8
2018	2	1	11.5	74.0	72.2	–13.1	–103.5
2018	2	15	11.7	78.9	76.3	–13.0	–103.7
2018	3	1	12.4	75.9	24.2	–13.0	–103.9
2018	3	15	11.6	83.7	85.2	–13.1	–104.0
2018	4	1	11.3	81.5	89.9		
2018	4	15	10.3	69.1	n.d.		
2018	5	1	11.1	52.4		–7.7	–50.2
2018	5	15	10.5	63.6	3.2	–12.4	–84.3
2018	6	1	10.7	71.2	0.0	–12.4	–84.8
2018	6	15	9.2	73.5	26.2		
2018	7	1	9.9	62.1	0.0		
2018	7	15	9.7	62.3	0.0		
2018	8	1	9.8	65.6	26.8		
2018	8	15	9.9	69.3	8.8		
2018	9	1	10.3	61.4	5.4		
2018	9	15	11.7	66.0	0.0		
2018	10	1	11.6	62.5	0.0	–14.2	–103.6
2018	10	15	11.4	70.4	7.0	–14.2	–103.8
2018	11	1	11.7	64.5	0.0	–14.2	–103.7
2018	11	15	11.4	66.0	8.2		
2018	12	1	11.8	67.5	0.0		

2018	12	15	10.9	70.0	6.2		
2019	1	1	11.6	73.7	27.6	–14.2	–103.9
2019	1	15	11.6	80.7	28.6	–14.1	–103.8
2019	2	1	11.9	82.1	145.5	–14.3	–104.2
2019	2	15	11.2	81.0	103.4	–14.3	–104.2
2019	3	1	10.9	79.6	107.5	–14.3	–104.8
2019	3	15	11.7	79.6	102.3	–14.3	–104.5
2019	4	1	11.5	78.7	60.8	–14.3	–100.4
2019	4	15	11.4	74.8	10.2	–14.2	–99.9
2019	5	1	11.5	75.7	15.6		
2019	5	15	11.5	70.3	0.6	–9.8	–69.7

Cotahuasi (15.211336°S, 72.893308°W, 2683 masl)							
Year	**Month**	**Day**	**Temperature (°C)**	**Relative Humidity (%)**	**Total Precipitation (mm)**	**$\delta^{18}O$ (‰, VSMOW)**	**$\delta^{2}H$ (‰, VSMOW)**
2017	11	15	17.0	31.3	1.7	–9.2	–72.2
2017	12	1	17.2	39.1	1.4	–3.6	–35.2
2017	12	15	17.4	40.2	0.1	2.6	20.6
2018	1	1	16.0	61.9	30.9	–5.5	–31.5
2018	1	15	16.4	54.4	5.2	–3.9	–18.8
2018	2	1	16.3	67.5	49.7	–13.4	–96.4
2018	2	15	17.2	65.1	24.8	–15.0	–111.6
2018	3	1	16.0	68.3	16.2	–4.5	–27.3
2018	3	15	16.8	66.2	35.9	–12.5	–88.7
2018	4	1	16.2	65.2	36.0	–8.5	–57.8
2018	4	15	15.8	64.6	17.5	–10.4	–72.4
2018	5	1	16.8	55.6	11.0	–8.5	–61.3
2018	5	15	16.5	42.0	0.0		
2018	6	1	16.2	25.7	0.0		
2018	6	15	14.5	46.8	3.8	–5.7	–48.0
2018	7	1	15.7	30.4	0.0		
2018	7	15	15.7	31.5	0.0		
2018	8	1	14.7	38.3	6.1	–0.5	–3.8
2018	8	15	16.2	28.1	0.0		
2018	9	1	17.1	23.4	0.0		
2018	9	15	17.1	24.1	0.0		
2018	10	1	17.9	20.2	0.0		
2018	10	15	16.6	34.2	6.2	0.7	–23.2
2018	11	1	17.3	29.5	0.0		
2018	11	15	17.4	35.6	0.0		
2018	12	1	17.6	27.7	0.0		

2018	12	15	18.3	31.4	0.0		
2019	1	1	18.0	46.3	2.0	–0.4	–10.6
2019	1	15	17.7	56.2	6.4	–4.0	–21.5
2019	2	1	17.2	71.4	67.8	–8.3	–54.9
2019	2	15	16.3	74.6	70.3	–14.3	–107.6
2019	3	1	16.4	74.1	48.8	–9.5	–63.7
2019	3	15	17.2	71.5	46.7	–8.3	–54.8
2019	4	1	16.9	60.6	9.7	–8.4	–66.0
2019	4	15	16.9	54.3	2.2	–3.9	–28.8
2019	5	1	17.2	55.6	3.1	–3.8	–28.1
2019	5	15	16.2	42.7	1.9	–4.0	–34.6

Arequipa (16.458194°S, 71.575806°W, 2200 masl)							
Year	**Month**	**Day**	**Temperature (°C)**	**Relative Humidity (%)**	**Total Precipitation (mm)**	**$\delta^{18}O$ (‰, VSMOW)**	**$\delta^{2}H$ (‰, VSMOW)**
2017	11	15	16.4	38.7	0.0		
2017	12	1	15.8	45.5	0.0		
2017	12	15	16.1	48.1	0.0		
2017	12	31	16.8	60.5	8.9	–2.1	–7.7
2018	1	16	16.0	56.6	4.9	–0.8	13.0
2018	2	1	17.3	66.9	10.1	–8.2	–54.1
2018	2	15	16.8	72.4	0.4		
2018	3	1	15.9	73.6	11.7	–3.8	–13.4
2018	3	15	17.5	63.0	0.0		
2018	4	1	16.4	64.9	4.2	–7.7	–53.0
2018	4	15	15.1	65.0	0.0		
2018	5	1	16.3	61.7	0.0		
2018	5	15	15.4	55.6	0.0		
2018	6	1	14.7	41.5	0.0		
2018	6	15	15.8	45.9	0.3		
2018	7	1	15.6	41.2	0.0		
2018	7	15	15.3	40.4	0.0		
2018	8	1	15.2	44.1	0.9		
2018	8	15	15.8	36.1	0.0		
2018	9	1	15.9	32.7	0.0		
2018	9	15	14.0	35.5	0.0		
2018	10	1	15.9	33.0	0.0		
2018	10	15	16.6	33.0	0.0		
2018	11	1	15.7	38.0	0.0		
2018	11	15	15.9	42.2	0.0		
2018	12	1	15.7	41.5	0.0		

2018	12	15	16.0	41.6	0.0		
2019	1	1	17.0	52.5	0.0		
2019	1	15	16.7	64.5	0.1	–1.8	–17.8
2019	2	1	17.8	73.9	42.8	–5.8	–32.8
2019	2	15	17.7	81.7	37.7	–9.4	–63.4
2019	3	1	17.5	72.4	28.8	–5.3	–26.3
2019	3	15	18.0	69.5	7.2	–3.9	–18.2
2019	4	1	17.5	59.2	2.5	–4.9	–35.3
2019	4	15	16.0	60.9	0.0		
2019	5	1	17.3	59.3	0.0		
2019	5	15	17.1	50.6	0.0		

Quinistaquillas (16.749293°S, 70.878766°W, 1590 masl)							
Year	**Month**	**Day**	**Temperature (°C)**	**Relative Humidity (%)**	**Total Precipitation (mm)**	**$\delta^{18}O$ (‰, VSMOW)**	**$\delta^{2}H$ (‰, VSMOW)**
2017	11	15	22.1	29.5	0.0		
2017	12	1	21.6	35.4	0.0		
2017	12	15	22.3	39.0	0.0		
2018	1	1	20.9	52.8	9.0	–0.5	4.1
2018	1	15	20.8	52.1	2.5	1.2	10.2
2018	2	1	21.3	58.7	9.2		
2018	2	15	20.9	61.8	5.2		
2018	3	1	20.4	60.8	1.8		
2018	3	15	22.1	50.7	0.0		
2018	4	1	21.3	54.6	1.8		
2018	4	15	20.1	52.0	0.0		
2018	5	1	21.1	50.0	1.2		
2018	5	15	20.1	42.0	0.0		
2018	6	1	19.5	27.2	0.0		
2018	6	15	20.2	29.7	0.0		
2018	7	1	19.5	26.2	0.0		
2018	7	15	19.3	26.1	0.0		
2018	8	1	19.6	31.7	0.3		
2018	8	15	20.8	21.8	0.0		
2018	9	1	21.4	19.5	0.0		
2018	9	15	20.8	24.8	0.0		
2018	10	1	22.1	23.5	0.0		
2018	10	15	22.0	30.4	0.0		
2018	11	1	22.1	26.6	0.0		
2018	11	15	22.1	33.8	0.0		
2018	12	1	22.1	34.4	0.0		
2018	12	15	22.4	38.7	0.0		

2019	1	1	22.4	45.0	2.5		
2019	1	15	21.8	55.1	1.5		
2019	2	1	20.7	70.0	57.6		
2019	2	15	20.2	80.5	53.1		
2019	3	1	21.5	63.2	1.2		
2019	3	15	22.4	59.7	3.8	–1.5	–23.5
2019	4	1	22.0	50.6	1.8		
2019	4	15	20.7	51.3	0.0		
2019	5	1	21.0	47.0	0.0		
2019	5	15	21.0	35.4	0.0		

Ubinas (16.372056°S, 70.853944°W, 3380 masl)							
Year	**Month**	**Day**	**Temperature (°C)**	**Relative Humidity (%)**	**Total Precipitation (mm)**	**$\delta^{18}O$ (‰, VSMOW)**	**$\delta^{2}H$ (‰, VSMOW)**
2017	11	15	13.2	39.6	5.2		
2017	12	1	14.1	41.6	8.0		
2017	12	15	14.1	44.9	0.0		
2018	1	1	11.9	67.5	38.5		
2018	1	15	11.6	68.9	25.6		
2018	2	1	12.0	72.3	79.2		
2018	2	16	12.9	73.1	41.6	–8.0	–56.7
2018	3	6	11.1	75.2	33.7	–8.0	–56.2
2018	3	15	12.1	71.1	7.7		
2018	4	1	11.4	68.9	31.5		
2018	4	15	11.8	56.4	0.0		
2018	5	1	12.0	58.1	12.0		
2018	5	15	9.9	47.7	0.0		
2018	6	1	8.0	31.7	0.0		
2018	6	15	7.6	59.8	7.4		
2018	7	1	8.0	44.9	0.0		
2018	7	15	8.4	40.8	0.8		
2018	8	1	7.6	54.2	23.8		
2018	8	15	9.2	34.7	0.0		
2018	9	1	10.1	30.3	0.0		
2018	9	15	11.2	29.3	0.0		
2018	10	1	11.7	28.1	0.0		
2018	10	15	12.0	45.4	0.0		
2018	11	1	13.0	38.5	0.0		
2018	11	15	13.8	38.8	0.0		
2018	12	1	13.8	36.3	0.0		
2018	12	15	14.8	37.6	0.0		
2019	1	1	13.9	54.6	7.4	–10.2	–68.9

2019	1	15	13.2	63.1	13.2	–9.8	–68.6
2019	2	1	12.5	76.3	115.1	–10.2	–73.6
2019	2	15	12.1	79.2	154.8	–16.7	–127.5
2019	3	1	11.9	76.8	23.6	–13.4	–91.9
2019	3	15	12.0	74.3	70.1	–7.6	–46.6
2019	4	1	12.4	64.0	0.9	–6.7	–45.6
2019	4	15	11.4	54.8	0.4		
2019	5	1	11.8	55.6	4.8	–8.3	–62.8
2019	5	15	11.2	59.8	0.6	–12.3	–108.9

Pampahuta (15.485278°S, 70.675778°W, 4400 masl)							
Year	**Month**	**Day**	**Temperature (°C)**	**Relative Humidity (%)**	**Total Precipitation (mm)**	**$\delta^{18}O$ (‰, VSMOW)**	**$\delta^{2}H$ (‰, VSMOW)**
2017	11	15	6.7	56.9	21.4	–14.1	–96.6
2017	12	1	6.7	52.7	47.9	–13.6	–90.9
2017	12	15	6.7	52.5	8.2	–9.2	–58.7
2018	1	1	6.7	72.2	121.3	–19.0	–138.8
2018	1	15	6.4	76.0	100.5	–12.9	–88.3
2018	2	1	6.8	70.1	83.4	–17.7	–138.8
2018	2	15	7.1	75.8	172.9	–18.8	–137.3
2018	3	1	6.5	76.8	82.5	–15.5	–110.4
2018	3	15	6.2	82.1	137.5	–18.3	–132.0
2018	4	1	5.9	71.3	36.6	–11.1	–88.8
2018	4	15	4.9	63.6	0.9		
2018	5	1	5.1	63.8	24.2	–16.6	–115.1
2018	5	15	3.8	60.8	2.2	–10.8	–71.7
2018	6	1	2.3	52.8	0.0		
2018	6	15	3.0	66.0	11.8	–16.1	–114.9
2018	7	1	2.4	59.2	0.0		
2018	7	15	2.7	56.6	0.0		
2018	8	1	2.5	62.7	25.6	–15.1	–108.2
2018	8	15	2.8	61.6	2.0		
2018	9	1	3.1	53.5	2.0		
2018	9	15	3.6	52.8	0.0		
2018	10	1	3.6	54.5	7.2	–7.0	–39.3
2018	10	15	5.2	62.7	19.8	–13.2	–92.9
2018	11	1	6.1	60.9	22.0	–11.7	–76.6
2018	11	15	6.7	57.8	11.8	–8.8	–55.9
2018	12	1	6.3	49.2	5.0	–6.6	–40.6

2018	12	15	6.6	49.0	0.6		
2019	1	1	5.9	72.0	66.2	–14.8	–98.8
2019	1	15	6.3	68.4	83.0	–19.1	–138.9
2019	2	1	6.4	74.6	140.6	–23.5	–170.1
2019	2	15	5.9	78.9	123.6	–22.4	–166.1
2019	3	1	6.4	74.7	88.2	–18.1	–132.8
2019	3	15	6.6	73.3	42.6	–13.2	–90.4
2019	4	1	6.3	76.8	69.4	–18.7	–132.8
2019	4	15	5.8	66.0	10.8	–15.7	–110.7
2019	5	1	6.1	69.5	46.6		
2019	5	15	4.9	32.0	24.6		
2019	5	21				–20.0	–144.2

Moquegua (17.169167°S, 70.931667°W, 1450 masl)							
Year	**Month**	**Day**	**Temperature (°C)**	**Relative Humidity (%)**	**Total Precipitation (mm)**	**$\delta^{18}O$ (‰, VSMOW)**	**$\delta^{2}H$ (‰, VSMOW)**
2017	11	15	19.7	73.8	0.0		
2017	12	1	19.1	75.0	0.0		
2017	12	15	19.9	74.1	0.0		
2018	1	1	19.7	75.6	0.0		
2018	1	15	19.7	73.5	0.3	–4.8	–34.7
2018	2	1	20.4	77.4	2.6	–5.0	–35.0
2018	2	15	20.4	79.1	1.5	–2.5	–11.9
2018	3	1	20.2	79.0	0.0		
2018	3	15	20.4	77.5	0.0	–6.5	–46.2
2018	4	1	20.1	80.0	0.3		
2018	4	15	19.0	81.7	0.0		
2018	4	22			0.5	–6.0	–42.4
2018	5	1	19.6	77.5	0.5		
2018	5	15	18.5	76.7	0.0		
2018	6	1	18.2	69.6	0.0		
2018	6	15	19.5	71.0	0.4		
2018	7	1	17.8	71.3	0.0		
2018	7	15	19.0	67.9	0.0		
2018	8	1	18.6	68.3	0.0		
2018	8	15	19.0	67.5	0.0		
2018	9	1	19.1	67.8	0.0		
2018	9	15	18.7	72.8	0.0		
2018	10	1	19.4	71.4	0.0		
2018	10	15	19.5	70.3	0.0		
2018	11	1	19.3	70.4	0.0		

2018	11	15	19.3	71.0	0.0		
2018	12	1	19.1	72.0	0.0		
2018	12	15	19.2	73.9	0.0		
2019	1	1	20.7	77.0	0.0		
2019	1	15	20.1	82.8	0.2		
2019	1	19				–3.2	–13.0
2019	2	1	20.8	83.6	17.1	–7.6	–53.4
2019	2	15	21.4	87.6	36.9		
2019	2	17				–3.2	–11.9
2019	3	1	21.7	76.7	0.0	–10.1	–75.5
2019	3	10				–10.1	–76.7
2019	3	15	21.5	78.6	0.0		
2019	4	1	20.2	76.5	0.0	–9.1	–73.9
2019	4	15	18.9	80.7	0.0		
2019	5	1	19.8	78.8	0.0		
2019	5	15	19.4	77.0	0.0		

Cuzco (13.54003˚S, 71.89643˚W, 3263 masl)							
Year	**Month**	**Day**	**Temperature (°C)**	**Relative Humidity (%)**	**Total Precipitation (mm)**	**$\delta^{18}O$ (‰, VSMOW)**	**$\delta^{2}H$ (‰, VSMOW)**
2017	11	15	14.6	63.8	47.5		
2017	12	1	14.3	61.2	12.5	–9.2	–57.0
2017	12	15	14.5	64.7	31.2		
2018	1	1	14.3	72.7	90.6		
2018	1	15	13.8	76.2	68.0		
2018	2	1	13.2	75.8	68.1		
2018	2	18	15.2	73.7	47.2	–15.2	–109.8
2018	3	1	14.0	76.1	113.6	–20.2	–146.6
2018	3	14	13.7	76.4	103.8	–21.8	–161.5
2018	4	1	13.9	77.9	41.9	–16.8	–125.1
2018	4	15	12.9	73.3	6.0		
2018	5	1	12.3	71.5	14.3		
2018	5	15	11.8	70.1	0.2		
2018	6	1	10.5	66.5	0.0		
2018	6	15	9.5	72.6	16.2		
2018	7	1	9.2	66.0	0.0		
2018	7	15	9.9	65.4	2.2		
2018	8	1	9.3	66.6	13.6		
2018	8	15	10.8	69.4	3.8		
2018	9	1	11.4	68.3	3.3		
2018	9	15	12.0	61.8	0.5		
2018	10	1	13.3	64.3	6.5		

2018	10	15	12.8	69.0	37.1		
2018	11	1	13.9	72.7	44.0		
2018	11	15	14.8	71.3	24.9		
2018	12	1	15.0	67.8	55.5		
2018	12	15	13.7	58.2	4.6		
2019	1	1	13.8	74.0	95.8		
2019	1	15	14.3	72.3	72.1		
2019	2	1	14.1	75.5	55.1		
2019	2	15	14.1	77.5	27.7		
2019	3	1	14.1	78.5	87.5		
2019	3	15	14.5	76.3	79.0		
2019	4	1	13.6	80.5	92.2		
2019	4	15	13.3	77.2	25.4		
2019	5	1	12.4	78.7	13.5		

Calca (13.32401˚S, 71.95628˚W, 2929 masl)							
Year	**Month**	**Day**	**Temperature (°C)**	**Relative Humidity (%)**	**Total Precipitation (mm)**	**$\delta^{18}O$ (‰, VSMOW)**	**$\delta^{2}H$ (‰, VSMOW)**
2018	7	15	12.0	73.3	0.0		
2018	8	1	12.0	71.1	13.6	–12.0	–87.0
2018	8	15	12.6	71.3	11.4		
2018	9	1	13.1	70.7	3.6		
2018	9	15	14.7	68.2	0.2		
2018	10	1	15.0	64.1	11.6		
2018	10	15	14.8	68.4	23.7		
2018	11	1	15.1	71.9	57.2		
2018	11	15	16.1	69.4	44.9		
2018	12	1	16.6	68.2	47.7		
2018	12	15	15.9	64.4	5.5		
2019	1	1	15.1	68.7	64.5	–15.8	–124.0
2019	1	15	15.3	69.6	52.9		
2019	2	1	15.8	69.2	48.3		
2019	2	15	15.2	72.2	25.9		
2019	3	1	15.5	71.6	50.6		
2019	3	15	16.1	68.7	59.5		
2019	4	1	15.4	72.3	73.9		
2019	4	15	15.1	68.2	5.3		
2019	5	1	13.2	68.3	6.3	–20.7	–164.3
2019	5	15	13.8	69.1	17.3		

Table S4.2 Precipitation $\delta^{17}O$ and $\delta^{18}O$. The VSMOW2, SLAP2, and USGS data required to normalize the raw $\delta^{17}O$ and $\delta^{18}O$ are included in the supplement to Chapter 5.

San Gaban (13.451806˚S, 70.409139˚W, 657 masl)					
		Raw data (vs. reference O_2)		**Normalized Data (VSMOW-SLAP)**	
Collection Date	**n (number of analyses)**	**$\delta^{17}O$**	**$\delta^{18}O$**	**$\delta^{17}O$**	**$\delta^{18}O$**
7/15/16	2	–0.783	–1.536	–1.217	–2.355
7/15/16		–0.750	–1.472	–1.175	–2.285
9/1/16	3	0.131	0.200	–0.245	–0.511
9/1/16		–0.014	–0.075	–0.188	–0.411
9/1/16		–0.059	–0.157	–0.235	–0.495
9/15/16	2	–0.237	–0.502	–0.422	–0.859
9/15/16		–0.184	–0.398	–0.365	–0.746
10/1/16	3	–0.585	–1.152	–0.780	–1.526
10/1/16		–0.677	–1.343	–0.869	–1.725
10/1/16		–0.820	–1.605	-0.966	–1.888
11/2/16	2	–0.961	–1.871	–1.176	–2.283
11/2/16		–0.937	–1.827	–1.155	–2.234
11/15/16	2	–1.286	–2.507	–1.508	–2.934
11/15/16		–1.286	–2.497	–1.507	–2.920
12/1/16	2	–1.450	–2.792	–1.680	–3.231
12/1/16		–1.405	–2.717	–1.630	–3.148
4/1/17	3	–8.328	–15.782	–8.219	–15.570
4/1/17		–7.992	–15.159	–7.858	–14.912
4/1/17	2	–8.154	–15.451	–8.024	–15.199
4/15/17		–5.948	–11.300	–5.739	–10.904
4/15/17		–5.815	–11.047	–5.593	–10.628

Ollachea (13.794306˚S, 70.469927˚W, 2850 masl)					
		Raw data (vs. reference O_2)		**Normalized Data (VSMOW-SLAP)**	
Collection Date	**n (number of analyses)**	**$\delta^{17}O$**	**$\delta^{18}O$**	**$\delta^{17}O$**	**$\delta^{18}O$**
4/1/17	2	–8.337	–15.772	–8.187	–15.484
4/1/17		–8.447	–16.004	–8.293	–15.708
4/15/17	2	–8.353	–15.813	–8.188	–15.496
4/15/17		–8.580	–16.250	–8.413	–15.931

Macusani (14.07˚S, 70.43908˚W, 4345 masl)					
		Raw data (vs. reference O_2)		**Normalized Data (VSMOW-SLAP)**	
Collection Date	**n (number of analyses)**	**$\delta^{17}O$**	**$\delta^{18}O$**	**$\delta^{17}O$**	**$\delta^{18}O$**
9/15/16	3	–2.548	–4.912	–2.840	–5.470
9/15/16		–2.616	–5.027	–2.912	–5.590
9/15/16		–2.595	–4.989	–2.876	–5.525
10/1/16	2	–2.579	–4.973	–2.871	–5.531
10/1/16		–2.671	–5.139	–2.968	–5.704
10/15/16	2	–6.656	–12.672	–7.148	–13.601
10/15/16		–6.726	–12.779	–7.221	–13.711
11/1/16	4	–4.157	–7.938	–4.535	–8.655
11/1/16		–4.182	–7.996	–4.560	–8.714
11/1/16		–4.084	–7.825	–4.427	–8.477
11/1/16		–4.121	–7.910	–4.495	–8.621
4/1/17	2	–14.777	–27.904	–14.801	–27.932
4/1/17		–14.786	–27.902	–14.802	–27.916
4/15/17	2	–12.148	–22.970	–12.071	–22.814
4/15/17		–12.054	–22.799	–11.966	–22.623

Ayaviri (14.87172˚S, 70.59325˚W, 3906 masl)					
		Raw data (vs. reference O_2)		**Normalized Data (VSMOW-SLAP)**	
Collection Date	**n (number of analyses)**	**$\delta^{17}O$**	**$\delta^{18}O$**	**$\delta^{17}O$**	**$\delta^{18}O$**
10/15/16	2	–4.272	–8.173	–4.624	–8.841
10/15/16		–4.453	–8.507	–4.814	–9.192
11/1/16	4	–3.961	–7.604	–4.321	–8.289
11/1/16		–4.080	–7.795	–4.446	–8.489
11/1/16		–4.176	–7.970	–4.535	–8.652
11/1/16		–4.120	–7.864	–4.475	–8.536
11/15/16	2	–1.562	–3.014	–1.770	–3.413
11/15/16		–1.614	–3.114	–1.824	–3.517
12/1/16	2	–2.061	–3.987	–2.297	–4.438
12/1/16		–2.009	–3.892	–2.240	–4.336
4/1/17	2	–14.026	–26.480	–13.987	–26.403
4/1/17		–14.012	–26.435	–13.971	–26.342
4/15/17	2	–10.618	–20.084	–10.460	–19.778
4/15/17		–10.368	–19.615	–10.193	–19.279

Santo Tomas (14.450333°S, 72.095917°W, 3658 masl)					
		Raw data (vs. reference O_2)		**Normalized Data (VSMOW-SLAP)**	
Collection Date	**n (number of analyses)**	**$\delta^{17}O$**	**$\delta^{18}O$**	**$\delta^{17}O$**	**$\delta^{18}O$**
10/1/16	2	–0.292	–0.604	–0.394	–0.804
10/1/16		–0.234	–0.495	–0.337	–0.687
10/15/16	2	–4.132	–7.885	–4.461	–8.509
10/15/16		–4.113	–7.820	–4.439	–8.437
11/1/16	2	–2.613	–5.030	–2.848	–5.481
11/1/16		–2.686	–5.161	–2.924	–5.618

Majes (16.343056°S, 72.1525°W, 1498 masl)					
		Raw data (vs. reference O_2)		**Normalized Data (VSMOW-SLAP)**	
Collection Date	**n (number of analyses)**	**$\delta^{17}O$**	**$\delta^{18}O$**	**$\delta^{17}O$**	**$\delta^{18}O$**
3/1/17	1	–0.305	–0.541	–0.100	–0.191
3/15/17	4	–2.219	–4.156	–2.097	–3.961
3/15/17		–2.387	–4.488	–2.272	–4.306
3/15/17		–2.322	–4.382	–2.204	–4.194
3/15/17		–2.108	–3.974	–1.981	–3.769
2/1/18	2	–2.763	–5.233	–2.664	–5.081
2/1/18		–2.775	–5.253	–2.677	–5.101
2/15/18	1	–1.302	–2.480	–1.140	–2.212

Carumas (16.81117°S, 70.695063°W, 2976 masl)					
		Raw data (vs. reference O_2)		**Normalized Data (VSMOW-SLAP)**	
Collection Date	**n (number of analyses)**	**$\delta^{17}O$**	**$\delta^{18}O$**	**$\delta^{17}O$**	**$\delta^{18}O$**
3/1/17	1	–5.726	–10.852	–5.756	–10.940
3/15/17	2	–3.622	–6.854	–3.561	–6.773
3/15/17		–3.506	–6.629	–3.440	–6.539

Table S4.3 Stepwise multiple linear regression model parameters and AIC scores. The model with the lowest AIC score from this study, Fiorella et al., 2015, and Gonfiantini et al., 2001 are noted in italics. AIC scores were calculated with the stats package in R.

Regression model parameters	AIC score
This study	
elevation + latitude + longitude + MAP	19.09
elevation + latitude + longitude	17.18
elevation + latitude	*15.47*
elevation	37.57
latitude	44.96
Fiorella et al., 2015	
elevation + latitude + MAP + longitude	8.68
elevation + latitude + MAP	7.36
elevation + latitude	6.85
elevation	*6.29*
latitude	20.96
Gonfiantini et al., 2001	
elevation + latitude + MAP + longitude	10.61
elevation + latitude + MAP	8.61
elevation + MAP	*6.66*
elevation	8.33
latitude	14.79

References

Fiorella, R.P., Poulsen, C.J., Zolá, R.S.P., Barnes, J.B., Tabor, C.R., Ehlers, T.A., 2015. Spatiotemporal variability of modern precipitation $\delta^{18}O$ in the central Andes and implications for paleoclimate and paleoaltimetry estimates. J. Geophys. Res. Atmos. 120, 1–27. https://doi.org/10.1002/2014JD022893.Received

Gonfiantini, R., Roche, M.A., Olivry, J.C., Fontes, J.C., Zuppi, G.M., 2001. The altitude effect on the isotopic composition of tropical rains. Chem. Geol. 181, 147–167. https://doi.org/10.1016/S0009-2541(01)00279-0

Chapter 5 Global Variations of Meteoric Water Triple Oxygen Isotopes[4]

Co-authors: Naomi E. Levin, Emily J. Beverly, Tyler E. Huth, Benjamin H. Passey, Elise M. Pelletier, Christopher J. Poulsen, Ian Z. Winkelstern, Drake A. Yarian

5.1 Abstract

The past decade has seen a remarkable expansion of studies that use mass-dependent variations of triple oxygen isotopes (^{16}O, ^{17}O, ^{18}O) in isotope hydrology and isotope geochemistry. Recent technological and analytical advances demonstrate that small deviations of $\delta'^{18}O$ and $\delta'^{17}O$ from a mass-dependent reference relationship are systematic and are explained by well-known equilibrium and kinetic fractionation processes. These measurements complement traditional metrics like deuterium-excess, help reconstruct past environmental conditions from geologic records, and constrain isotope effects of evaporation that are impossible to discern with $\delta^{18}O$ alone. In this review, we synthesize published meteoric (derived from precipitation) water triple oxygen isotope data with a new, near-global surface water dataset of $\delta'^{18}O$, $\delta'^{17}O$, $\delta^{2}H$, $\Delta'^{17}O$, and deuterium-excess. Here, $\Delta'^{17}O$ is defined as $\delta'^{17}O - \lambda_{ref}\,\delta'^{18}O$, where δ' notation is a logarithmic definition of the common δ value ($\delta'=1000\ln(\delta/1000 + 1)$ and λ_{ref} is equal to 0.528. Building upon more than a decade of work, we present an updated triple oxygen isotope meteoric water line,

$$\delta'^{17}O = 0.5265*\delta'^{18}O\ (\pm\ 0.0002) + 0.0118\ (\pm\ 0.0027‰),$$

that captures $\delta'^{18}O$ and $\delta'^{17}O$ variability in tropical and temperate regions, and should be used as a new point of reference in future triple oxygen isotope studies. We explain the observed relationships between $\delta'^{18}O$, $\Delta'^{17}O$, and deuterium-excess and provide a practical guide to interpret

[4] In review as: Aron, P.G., Levin, N.E., Beverly, E.J., Huth, T.E., Passey, B.H., Pelletier, E.M., Poulsen, C.J., Winkelstern, I.Z., Yarian, D.A., (2020) Global variations of meteoric water triple oxygen isotopes, Chemical Geology. Raw data and supplementary code are accessible at https://github.com/phoebearon/17O

these data in hydrologic and paleoclimate applications. We end with important considerations for modern hydrologic and paleoclimate $\Delta'^{17}O$ studies and directions of future triple oxygen isotope work.

5.2 Introduction

Ratios of ^{18}O to ^{16}O are among the most common isotopic measurements in Earth science and play a critical role tracing biogeochemical cycles and reconstructing past climate conditions (Dansgaard, 1964; Joussaume et al., 1984; Zachos, 2001). Studies of ^{17}O, the rarest stable oxygen isotope (Table 5.1), have lagged because $^{17}O/^{16}O$ ratios were long considered invariant, too difficult to measure, or redundant to $^{18}O/^{16}O$ ratios (Gat, 1996). However, recent technological and analytical advances show that small, mass dependent deviations between $^{17}O/^{16}O$ and $^{18}O/^{16}O$ contain new information about water cycling and past environmental conditions (Barkan and Luz, 2005). This review captures the emerging field of triple oxygen isotope (^{16}O, ^{17}O, ^{18}O) hydrology at an important moment: many laboratories are now able to make ^{17}O measurements and large datasets are rapidly emerging, but triple oxygen isotope variability is not yet fully understood and there are important inconsistencies between studies. Therefore, this review synthesizes new and published meteoric (derived from precipitation) water isotope data and explains the hydrologic processes that drive triple oxygen isotope variations. This review is intended as an introduction to triple oxygen isotope hydrology and as a primer to how this emerging field may contribute to hydrologic and paleoclimate research.

Table 5.1 The three stable oxygen isotopes.

Isotope	Symbol	Protons	Neutrons	Mass (u)	Natural Terrestrial Abundance (%)
Oxygen-16	^{16}O	8	8	15.995	99.757
Oxygen-17	^{17}O	8	9	16.999	0.038
Oxygen-18	^{18}O	8	10	17.999	0.205

Oxygen isotopes fractionate due to non-mass-dependent and mass-dependent effects (Bao et al., 2016; Thiemens et al., 2012). Non-mass-dependent fractionation arises from chemical effects, including nuclear spin, transition state chemistry, molecular symmetry, and photochemical reactions (Criss and Farquhar, 2008; Thiemens and Heidenreich, 1983). These effects can result in large variations between $^{17}O/^{16}O$ and $^{18}O/^{16}O$ and have a range of applications in atmospheric

chemistry, planetary science, and biological productivity that are already well reviewed (Bao et al., 2009; Bhattacharya et al., 2000; Blunier et al., 2012, 2002; Luz et al., 2009; Thiemens, 2006; Thiemens et al., 1995). In contrast, mass-dependent effects arise from differences in bond energy, reaction rate, and diffusivity (Matsuhisa et al., 1978; Young et al., 2002) that result in very small variations between $^{17}O/^{16}O$ and $^{18}O/^{16}O$. These mass-dependent variations, which are sensitive to fractionation during equilibrium isotope exchange and the diffusion of water vapor through air, have recently gained attention as a new way to study modern hydrology and reconstruct past environmental conditions (e.g., Bao et al., 2016; Barkan and Luz, 2005; Luz and Barkan, 2010; Pack and Herwartz, 2014; Rumble et al., 2007).

Decoupling fractionation effects from equilibrium and kinetic processes is critical to interpreting isotope data and identifying processes such as Rayleigh distillation and evaporation. In modern waters, the degree of kinetic fractionation is often quantified using deuterium-excess (d-excess = $\delta^2H - 8*\delta^{18}O$, Dansgaard, 1964; see Section 5.3.1 for the definition of δ notation). However, d-excess varies with both temperature and relative humidity, so interpretations of d-excess data are not always straightforward (Gat, 1996). Mass-dependent variations between $^{17}O/^{16}O$ and $^{18}O/^{16}O$ are also sensitive to kinetic fractionation as water vapor diffuses through unsaturated air (Barkan and Luz, 2007), but are relatively insensitive to temperature (Barkan and Luz, 2005). Therefore, triple oxygen isotopes and d-excess provide complementary information to trace evapotranspiration, moisture transport, or precipitation processes (e.g., Galewsky et al., 2016) and identify temperature and relative humidity condition at moisture sources (Landais et al., 2008, 2012a, 2012b; Uemura et al., 2010; Winkler et al., 2012).

Translating these principles to the past and differentiating equilibrium and kinetic fractionation effects in paleoclimate records is challenging because most geologic archives (e.g., carbonates, sulfates, phosphates, etc.) do not have both oxygen- and hydrogen-containing minerals. Much like d-excess (Figure 5.1), triple oxygen isotopes therefore add a degree of freedom ($^{17}O/^{16}O$) to paleoclimate records and can clarify some processes and fractionations that cannot be unresolved with traditional oxygen isotope ratios ($^{18}O/^{16}O$) alone (e.g., Rech et al., 2019). Functionally, triple oxygen isotope ratios preserved in minerals add new information about aridity and paleo-humidity (Alexandre et al., 2019; Gázquez et al., 2018; Passey and Ji, 2019; Surma et al., 2018), enable reconstructions of the isotopic composition of ancient waters (e.g., Gehler et al., 2011; Herwartz et al., 2015; Liljestrand et al., 2020; Passey and Ji, 2019) and

constrain effects of diagenesis and formation conditions of sedimentary records (Levin et al., 2014).

However, in order to use triple oxygen isotopes to study hydrology and paleoclimate, it is important to fully understand their variations in modern systems. Modern global variations of triple oxygen isotopes were first described in 2010 from a near-global set of meteoric waters (Luz and Barkan, 2010). Subsequent observations (Figure 5.2, Table 5.2) show that there is far more variability than initially realized (Figures 5.3a and 5.3b) and that triple oxygen isotope ratios do not neatly fit a global meteoric water line (Sharp et al., 2018). Therefore, this review re-evaluates global variations of meteoric water $\delta'^{18}O$, $\delta'^{17}O$, $\delta^{2}H$, $\Delta'^{17}O$, and d-excess. We synthesize published and new meteoric water data to explain hydrologic processes and fractionation that drive variation in $\Delta'^{17}O$ and d-excess (Section 5.5), evaluate the $\delta'^{18}O$–$\delta'^{17}O$ relationship (Section 5.6), review important analytical considerations for $\Delta'^{17}O$ measurements (Section 5.7), and present directions of future hydrologic triple oxygen isotope work (Section 5.9).

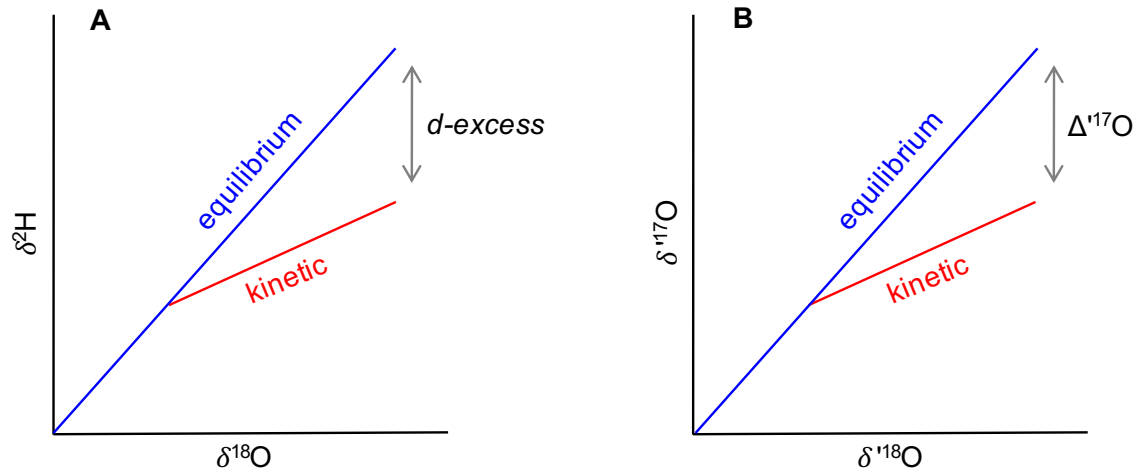

Figure 5.1 Schematic showing the similarities between (A) d-excess and (B) $\Delta'^{17}O$. Note that $\Delta'^{17}O$ is defined from $\delta'^{18}O$ and $\delta'^{17}O$. See Equation 5.4 for the definition of δ' notation.

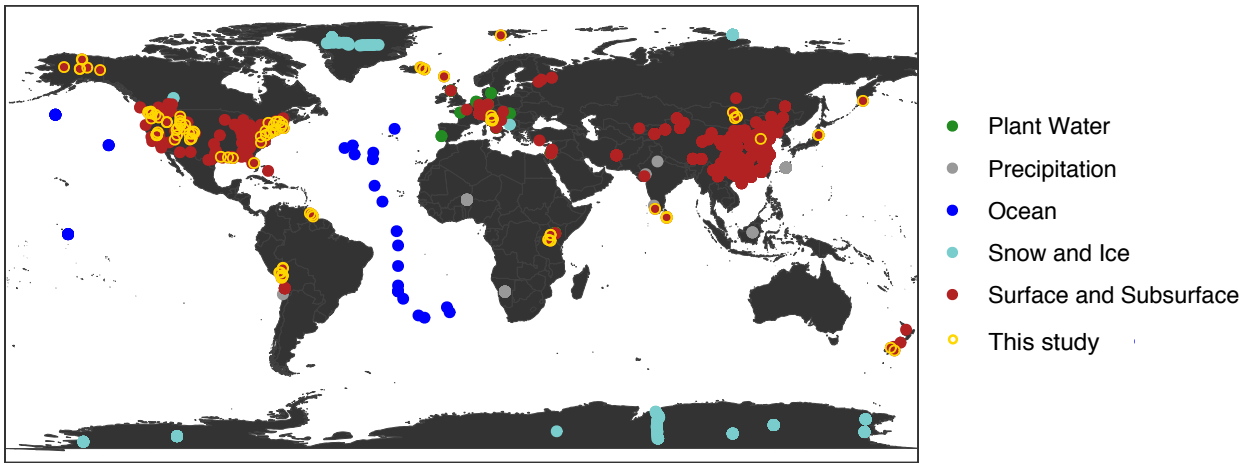

Figure 5.2 Geographical distribution of published meteoric water triple oxygen isotope data, colored by sample type. Plant water includes water extracted from stems and leaves. Surface and subsurface includes surface water, soil water, groundwater, cave water, and tap water. New surface water data reported in this review are outlined in gold; published studies are listed in Table 5.2.

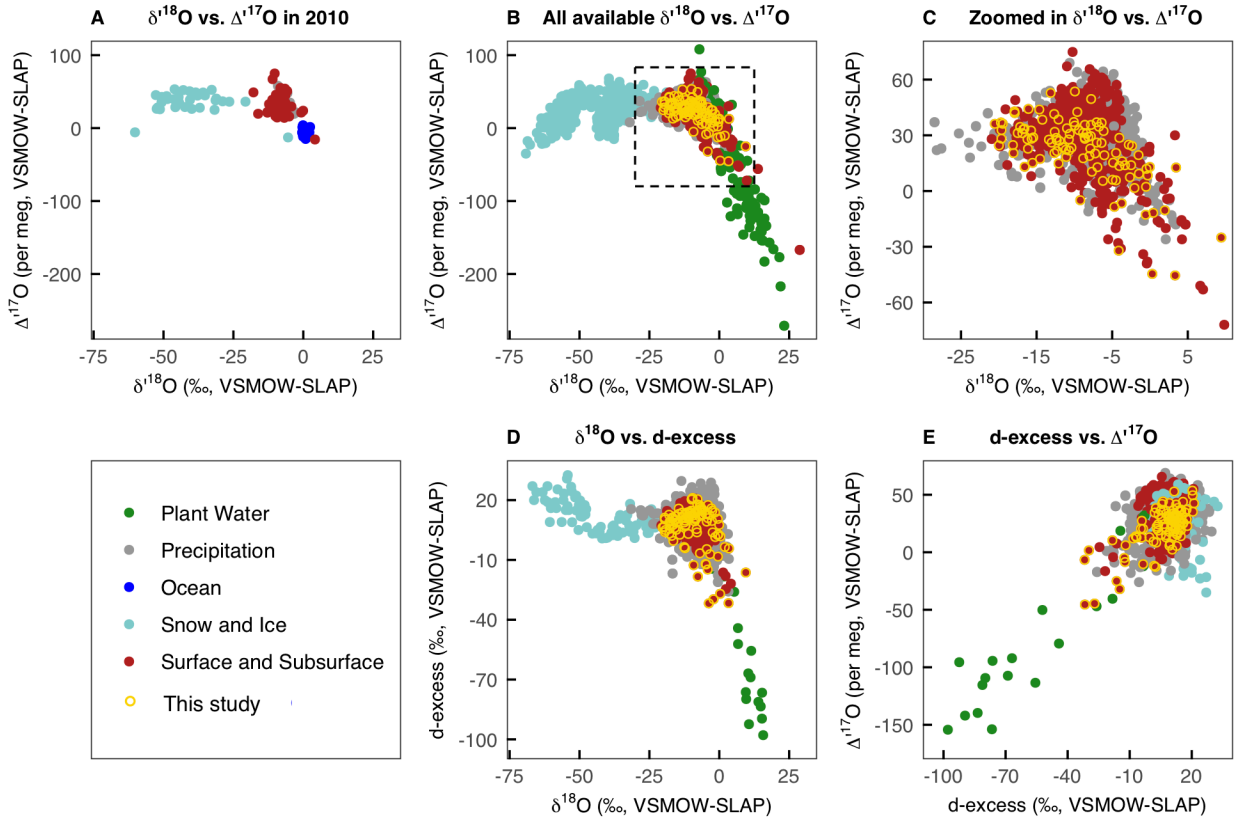

Figure 5.3 Scatterplots of meteoric water isotope data. Color indicates sample type. New surface water data reported in this study are outlined in gold. The top row includes plots of the data as $\delta'^{18}O$ versus $\Delta'^{17}O$ from (A) Luz and Barkan (2010), (B) all published sources (Table 5.2), and (C) precipitation, surface, and subsurface waters within a normal meteoric range (–30 to 10‰). The dashed box in (B) outlines the limits of the zoomed in data in (C). The bottom row shows plots with (D) $\delta^{18}O$ versus d-excess and (E) d-excess versus $\Delta'^{17}O$ from all the available published meteoric water triple oxygen isotope data (Table 5.2). There are more points in (B) than (D) or (E) because not all studies include δ^2H data.

Table 5.2 Summary of published hydrologic triple oxygen water isotope studies.

Water Type	Timeframe	Location	Analysis Method	Reference
Plant Water				
Leaf	April 2015	Europe and Israel	IRMS	Landais et al., 2006
Stem and leaf	Summer 2012	Central Kenya	IRMS	Li et al., 2017
Meteoric Water				
various	Various, 2002-2010	global	IRMS	Luz and Barkan, 2010
Precipitation	Seasonal, short convective cell	Niger	IRMS	Landais et al., 2010
Surface water	Spring 2011	Iran	IRMS	Surma et al., 2015
Tap	2008-2011	Continental United States	IRMS	Li et al., 2015
Precipitation, cave drip	March 2012-July 2014	Switzerland	Picarro	Affolter et al., 2015
Surface water	March 2014	Atacama Desert, Chile	IRMS	Surma et al., 2018
Precipitation	Event scale, 2014-2018	Central United States	LGR	Tian et al., 2018
Precipitation	Event scale, 2012-2016	Namibia	LGR	Kaseke et al., 2018
Tap	Monthly, December 2014 to November 2015	China	LGR	Tian et al., 2019
Precipitation	Weekly, January 2011to December 2012	Japan	Picarro	Uechi and Uemura, 2019
Surface water	June 2014	Western United States	IRMS	Passey and Ji, 2019
Surface water	Various, 2016-2019	global	IRMS	this study
Polar Precipitation				
Snow and ice	Last 150,000 years	Vostok, Antarctica	IRMS	Landais et al., 2008
Snow	2000	Vostok, Antarctica	IRMS	Landais et al., 2012a
Snow and water vapor	2003-2005	Greenland	IRMS	Landais et al., 2012b
Ice	Glacial-interglacial cycles	East Antarctica	IRMS	Winkler et al., 2012

Ice	LGM to Holocene	WAIS Divide, Antarctica	IRMS	Schoenemann et al., 2016
Snow	December 2009-January 2010	Coast to Dome A transect, East Antarctica	IRMS	Pang et al., 2015
Snow	January 2010	East Antarctica	IRMS	Pang et al., 2019
Modeling				
Vapor	Glacial-interglacial cycles	Vostok, Antarctica	Single column model	Risi et al., 2010
Precipitation	Modern and LGM	global	LMDZ (atmospheric transport GCM)	Risi et al., 2013
Precipitation	Modern seasonal cycle	Antarctica	Intermediate complexity model	Schoenemann et al., 2016

Analysis method abbreviations: isotope ratio mass spectrometer (IRMS), Los Gatos Research (LGR), Laboratory of Dynamic Meteorology (LMDZ), general circulation model (GCM).

5.3 Isotope terminology and fractionation

A summary of common symbols, explanations, and values in hydrologic triple oxygen isotope studies is provided in Table 5.3.

Table 5.3 Common symbols, explanations, and values for triple oxygen isotopes.

Symbol	Value	Explanation	Reference
θ_{eq}	0.529	Liquid-vapor equilibrium fractionation exponent	Barkan and Luz, 2005
θ_{diff}	0.518	water vapor diffusion fractionation exponent	Barkan and Luz, 2007
$^{18}\alpha_{eq}$	Variable (temperature dependent)	$^{18}O/^{16}O_{l\text{-}v}$ equilibrium fractionation factor	Majoube, 1971
$^{17}\alpha_{eq}$	$^{17}\alpha_{eq} = (^{18}\alpha_{eq})^{\theta eq}$	$^{17}O/^{16}O_{l\text{-}v}$ equilibrium fractionation factor	Equation 5.2
$^{18}\alpha_{diff}$	1 (pure turbulent transport) to 1.0285 (pure molecular diffusion transport)	$^{18}O/^{16}O_{l\text{-}v}$ diffusive transport fractionation factor	Merlivat, 1978
$^{17}\alpha_{diff}$	$^{17}\alpha_{diff} = (^{18}\alpha_{diff})^{\theta diff}$	$^{17}O/^{16}O_{l\text{-}v}$ diffusive transport fractionation factor	Equation 5.2
λ_{ref}	0.528	slope of the $\delta'^{18}O$–$\delta'^{17}O$ reference line commonly used in hydrologic studies	Luz and Barkan, 2010
δ	$\delta = 1000(R_{sample}/R_{standard} - 1)$	"delta"	McKinney et al., 1950
δ'	$\delta' = 1000\ln(\delta/1000 + 1)$	"delta prime"	Miller, 2002
$\Delta'^{17}O$	$\Delta'^{17}O = \delta'^{17}O - \lambda_{ref}\,\delta'^{18}O$	"cap ^{17}O"	Barkan and Luz, 2007

5.3.1 Isotope notation

Isotope partitioning between two substances (A and B) is expressed as an isotopic fractionation factor, α:

$$\alpha_{A\text{-}B} = R_A/R_B \qquad \text{Eq. 5.1}$$

where R is the ratio of the rare to common isotope (e.g., $^{2}H/^{1}H$, $^{18}O/^{16}O$, or $^{17}O/^{16}O$). During a single mass-dependent fractionating process, α values of coexisting phases (e.g., liquid and vapor), materials (e.g., water and mineral), or components related by simple processes (e.g., diffused gas

and residual gas) are related by a power law relationship and can be derived from mass law theory (Matsuhisa et al., 1978; Young et al., 2002):

$$^{*}\alpha_{A\text{-}B} = (^{*}\alpha_{A\text{-}B})^{\theta} \quad \text{Eq. 5.2}$$

where θ, the fractionation exponent, is a constant that defines the relationship between α values and * denotes a heavy mass number (e.g., 17 or 18 for oxygen, 2 for hydrogen).

Triple oxygen isotope fractionation exponents are well characterized for equilibrium (θ_{eq}) and kinetic (θ_{diff}) processes. Liquid-vapor θ_{eq} is predicted by mass law theory (Young et al., 2002, $\theta_{eq} = 0.529$) and has been verified empirically (Barkan and Luz, 2005, $\theta_{eq} = 0.529 \pm 0.001$); the kinetic fractionation exponent for diffusion of water vapor through air is derived from the kinetic theory of gases and the ideal gas law (Marrero and Mason, 1972, $\theta_{diff} = 0.5184$) and has also been confirmed experimentally (Barkan and Luz, 2007, $\theta_{diff} = 0.5185 \pm 0.0003$). The small, but statistically significant, difference between the values of θ_{eq} and θ_{diff} means that triple oxygen isotopes can differentiate equilibrium and kinetic fractionation.

In nature, isotopic compositions rarely reflect fractionation from a single process, but instead integrate multiple fractionating processes and several θ values. Here, we use λ notation to represent relationships that integrate multiple fractionating processes from those that result from a single fractionating process (θ). The most familiar λ value in isotope hydrology is the slope (~ 8) of the oxygen-hydrogen global meteoric water line, $\delta^2H = 8*\delta^{18}O + 10$ (Craig, 1961), where δ notation is defined as

$$\delta = 1000\left(\frac{R_{sample}}{R_{standard}} - 1\right). \quad \text{Eq. 5.3}$$

Linear meteoric water isotope relationships are ubiquitous in isotope hydrology because they provide a useful reference frame from which to assess isotopic variability and quantify non-equilibrium fractionation (Gat, 1996). However, these relationships are not truly linear because mass-dependent fractionation follows a power law function (Equation 5.2). This non-linearity is rarely observed in natural waters (e.g., Craig, 1961; Dansgaard, 1964; Rozanski et al., 1993) because the range of isotope values on Earth is relatively small and the scatter of data points around

an apparent linear relationship is too great to resolve the slight curvature (Figures 5.4a and 5.4c). However, over a sufficiently large isotopic range, curvature appears between δ values (Figures 5.4b and 5.4d). This curvature is concave when the slope between isotopic compositions is greater than 1 (Figure 5.4b) and convex when the slope between isotopic compositions is less than 1 (Figure 5.4d). Logarithmic δ′ ("delta prime") notation linearizes the exponential relationship between isotopic compositions (Figures 5.4b and 5.4d; Hulston and Thode, 1965; Martin, 2002):

$$\delta' = 1000\ ln\left(\frac{\delta}{1000} + 1\right). \qquad \text{Eq. 5.4}$$

This notation is used in all triple oxygen isotope studies and some studies of d-excess (e.g., Dütsch et al., 2017).

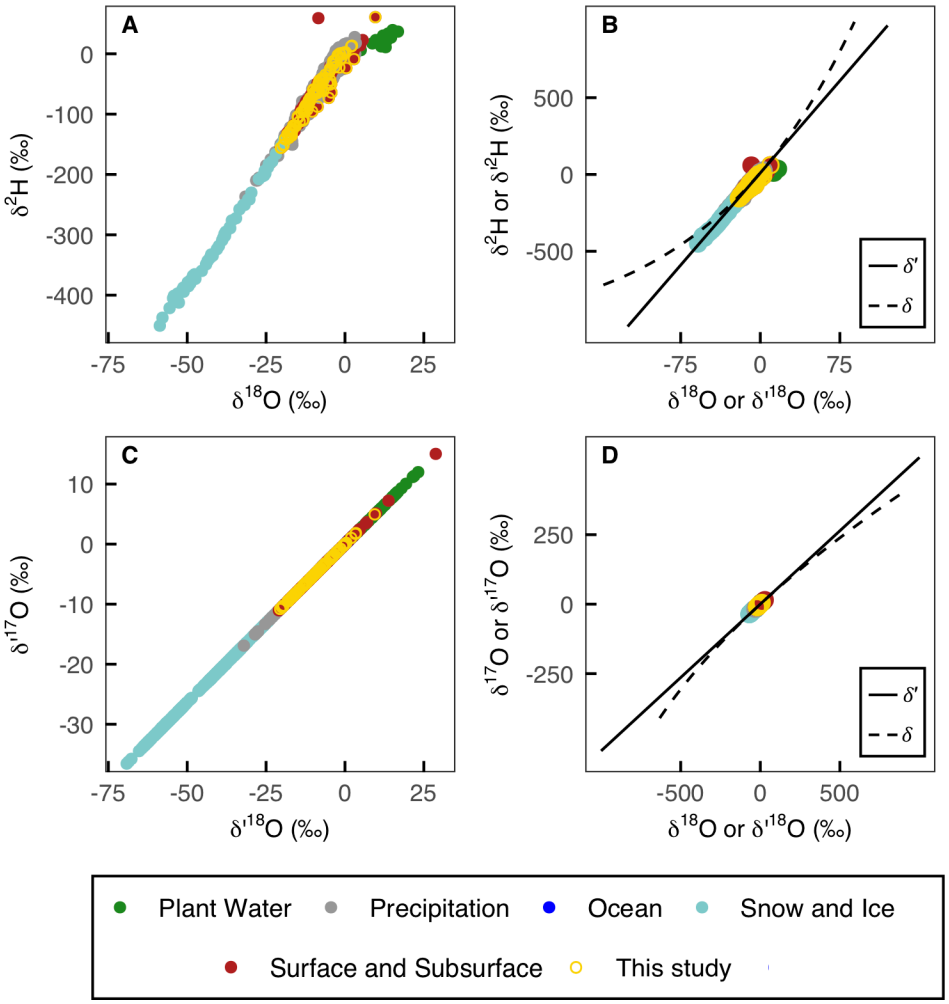

Figure 5.4 Scatterplots of meteoric water isotope values. Published data (Table 5.2) are colored by sample type; new data reported in this review are outlined in gold. Over the natural range of (A) $\delta^{18}O$ versus $\delta^{2}H$ and (C) $\delta'^{18}O$ versus $\delta'^{17}O$, meteoric water isotope relationships are nearly linear. The same data are shown in (B) and (D), respectively, but are overlaid with calculated $\delta^{18}O$, $\delta^{17}O$, or $\delta^{2}H$ (dashed black line) and calculated $\delta'^{18}O$, $\delta'^{17}O$, or $\delta'^{2}H$ (solid black line) over larger isotopic ranges. There are fewer points in (A) than (C) because some triple oxygen isotope studies do not include $\delta^{2}H$ data. The curvature between δ-δ relationships is concave when the slope between isotope values is greater than 1 (B, $\delta^{18}O$–$\delta^{2}H$) and convex when the slope between isotope values is less than 1 (D, $\delta^{18}O$–$\delta^{17}O$).

5.3.2 Definition of $\Delta'^{17}O$

Variations in the relationship between $\delta'^{18}O$ and $\delta'^{17}O$ are orders of magnitude smaller than variations of $\delta'^{18}O$ and $\delta'^{17}O$ values, so the most practical way to view and interpret triple oxygen isotope compositions is as a deviation from a reference line (Barkan and Luz, 2007):

$$\Delta'^{17}O = \delta'^{17}O - \lambda_{ref}\,\delta'^{18}O. \qquad \text{Eq. 5.5}$$

In this definition, λ_{ref} is the slope of a mass-dependent reference line and δ' notation ensures that isotopic deviations are calculated from a $\delta'^{18}O$–$\delta'^{17}O$ relationship that is exactly linear. Without δ' notation, $\Delta^{17}O$ varies non-linearly as a function of $\delta^{18}O$ (Figure 5.5). d-excess also varies non-linearly when it is defined with δ notation, but a logarithmic definition of d-excess is typically considered only at high latitudes or when $\delta^{18}O$ variation is large (Dütsch et al., 2017; Schoenemann et al., 2014; Uemura et al., 2012). For triple oxygen isotopes, δ' notation is important because the non-linear calculation artifact is the same order of magnitude as analytical precision and environmentally-induced variability (Figure 5.5). The slope of the $\delta'^{18}O$–$\delta'^{17}O$ reference line is discussed in Section 5.6, but hydrologic studies typically use a value of 0.528 for λ_{ref}. Unless otherwise noted, all $\Delta'^{17}O$ values in this review are calculated from a reference frame with λ_{ref} equal to 0.528. Values of $\Delta'^{17}O$ are typically very small and are expressed in units of per meg (1,000 per meg = 1‰).

We use the "capital delta" (Δ) notation to define $\Delta'^{17}O$ as the deviation from a reference line (Equation 5.5) and to maintain symbolic consistency among different isotope systems (e.g., $\Delta^{34}S$ and $\Delta^{25}Mg$; Criss and Farquhar, 2008; Young and Galy, 2004). Some triple oxygen isotope studies choose to use ^{17}O-excess rather than $\Delta'^{17}O$ (e.g., Barkan and Luz, 2007; Landais et al., 2008; Li et al., 2015; Luz and Barkan, 2010) to highlight the relative excess of ^{17}O in meteoric waters as compared to ocean water. This notation emphasizes similarities between the triple oxygen isotope system and d-excess (Figure 5.1), but we choose to use Δ' notation to clearly define $\Delta'^{17}O$ values as the deviation from a reference line. We specifically use Δ' (not Δ) to indicate that this parameter is calculated using δ' values (not δ values).

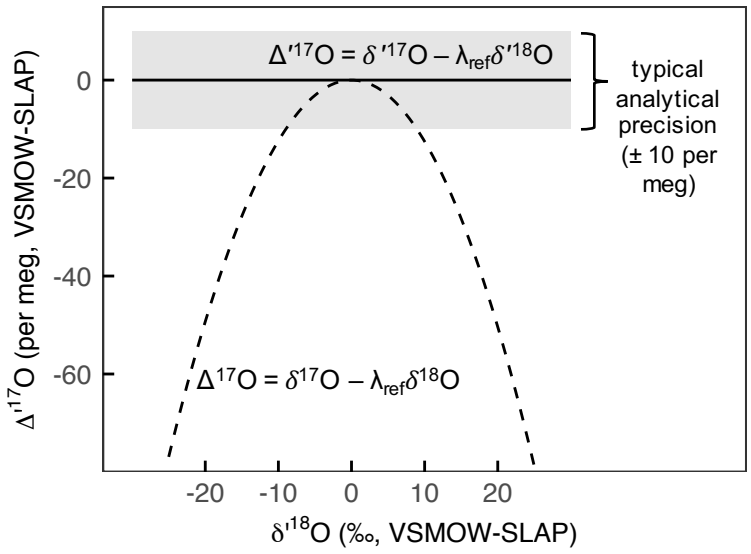

Figure 5.5 Comparison of $\Delta'^{17}O$ (solid black line) versus $\Delta^{17}O$ (dashed black line) across a common range of meteoric water $\delta'^{18}O$ compositions. The grey bar shows typical $\Delta'^{17}O$ analytical precision (± 10 per meg). Note that $\Delta'^{17}O$ is calculated with δ' values while $\Delta^{17}O$ is calculated with δ values. Without δ' notation, $\Delta^{17}O$ varies non-linearly as a function of $\delta'^{18}O$, and introduces a bias in $\Delta^{17}O$ that is greater than analytical precision and a similar magnitude to environmentally driven variability. δ' notation linearizes the definition of $\Delta'^{17}O$ and removes the non-linear calculation artifact.

5.4 Motivation from a decade of $\Delta'^{17}O$ observations

Meteoric water isotope patterns are best observed from amount-weighted precipitation (Dansgaard, 1964; Rozanski et al., 1993) or flowing surface waters (Kendall and Coplen, 2001) because these waters integrate fractionating processes in the hydrosphere, atmosphere, and biosphere. Efforts to understand patterns in $\delta^{18}O$ and $\delta^{2}H$ have culminated in the global meteoric water line (Craig, 1961), $\delta^{18}O$ and $\delta^{2}H$ isoscapes (e.g., Bowen, 2010), and well-tuned isotope-enabled general circulation models (Brady et al., 2019; Joussaume et al., 1984). These products are a point of reference for nearly every hydrologic and paleoclimate study of $\delta^{18}O$ and $\delta^{2}H$ (e.g., Jasechko, 2019; Noone et al., 2013; Poulsen et al., 2010; Rowley and Garzione, 2007).

Comprehensive global and continent scale water isotope studies such as those by Craig (1961), Dansgaard (1964), Rozanski et al. (1993), and Kendall and Coplen (2001) do not yet exist for triple oxygen isotopes. Global variability of meteoric water $\Delta'^{17}O$ and $\delta'^{18}O$ was first described in 2010 from a dataset comprised of two international standards, SLAP (Standard Light Antarctic Precipitation), GISP (Greenland Ice Sheet Precipitation) (Barkan and Luz, 2005), 29 Antarctic

snow samples (Landais et al., 2008), and 52 meteoric waters (Luz and Barkan, 2010). From this compilation, Luz and Barkan (2010) defined a global meteoric water line, established λ_{ref} as the slope of this line, and set the expectation that $\Delta'^{17}O$ values of meteoric water should be relatively invariant over a ~70‰ range in $\delta'^{18}O$ (Figure 5.3a). However, subsequent observations show that meteoric water $\Delta'^{17}O$ is far more variable than initially recognized (compare Figures 5.3a and 5.3b). These additional meteoric water $\delta'^{17}O$ and $\delta'^{18}O$ data fit multiple regression lines, suggesting that the defined global meteoric water line may not represent all meteoric waters (Miller, 2018; Sharp et al., 2018). Before we can use $\Delta'^{17}O$ to study hydrology and reconstruct past environmental conditions, it is critical that we understand the environmental processes that drive its variability.

We use this review paper to provide both a synopsis of what we know about $\Delta'^{17}O$ variation in meteoric water and as a guide for how practitioners might use triple oxygen isotope data in hydrologic and paleoclimate studies. As part of this review, we report a new, near-global surface water dataset that spans 6 continents and 17 Köppen climate classes and expands the available observations of meteoric water triple oxygen isotope variation. In the following sections we 1) explore the trends in meteoric water isotope data and the hydrologic processes that drive $\Delta'^{17}O$ variation, 2) evaluate the global $\delta'^{18}O$–$\delta'^{17}O$ relationship, and 3) present an updated triple oxygen isotope meteoric water relationship that better fits the available data. For the first objective, we use a comprehensive definition of meteoric water (plant water, precipitation, surface and subsurface, snow and ice, and ocean water) to explain triple oxygen isotope variation in as many parts of the hydrosphere as possible; for the second and third objectives, we use a much more limited definition of meteoric water (precipitation and surface water only).

5.5 Global variations of $\Delta'^{17}O$ in meteoric waters

Throughout this review we present triple oxygen isotope variability in $\delta'^{18}O$–$\Delta'^{17}O$ isotope space. This space highlight mass-dependent deviations from the reference relationship (Figure 5.3a-c; Farquhar and Thiemens, 2000; McKeegan and Leshin, 2001) and is a helpful way to simultaneously visualize isotopic compositions of $\delta'^{18}O$ (‰) and $\Delta'^{17}O$ (per meg, where 1 per meg = 0.001‰). The more familiar δ-δ isotope space is a poor way to visualize $\delta'^{18}O$–$\delta'^{17}O$ variation because values of θ_{eq} and θ_{diff} are orders of magnitude smaller than variations of $\delta'^{18}O$ and $\delta'^{17}O$

so $\delta'^{18}O$–$\delta'^{17}O$ compilations always appear linear (Figure 5.4c). The $\delta'^{18}O$ versus $\Delta'^{17}O$ isotope space is analogous to $\delta^{18}O$ versus d-excess (Figure 5.1) in the $\delta^{18}O$–$\delta^{2}H$ system.

5.5.1 Why do most meteoric waters have positive $\Delta'^{17}O$ values?

Mass-dependent triple oxygen isotope variations are explained by well-understood fractionation models (Criss, 1999). These models are commonly associated with $\delta^{18}O$, $\delta^{2}H$, and d-excess, but also apply to $\delta'^{18}O$, $\delta'^{17}O$, and $\Delta'^{17}O$. For example, positive meteoric water $\Delta'^{17}O$ and d-excess values are largely explained by the Craig and Gordon (1965) model of evaporation. This variation is shown schematically in Figure 5.6 and step-wise in Figures 5.7 and 5.8. Here, we focus primarily on $\delta'^{17}O$, $\delta'^{18}O$, and $\Delta'^{17}O$, and include $\delta^{18}O$, $\delta^{2}H$, and d-excess to highlight similarities between the triple oxygen ($\delta'^{18}O$–$\delta'^{17}O$) and oxygen-hydrogen ($\delta^{18}O$–$\delta^{2}H$) isotope systems.

First, beginning from the ocean (Figure 5.7, row 1), equilibrium isotope exchange occurs between water vapor and liquid water in a saturated layer near the evaporating surface (Figures 5.6 and 5.7, row 2). Because the value of θ_{eq} (0.529) is greater than that of λ_{ref} (0.528), $\delta'^{18}O$ and $\delta'^{17}O$ of the initial vapor fall below the reference line and equilibrium vapor $\Delta'^{17}O$ is slightly negative (–9 per meg and –11 per meg at 5˚C and 25˚C, respectively, Figures 5.6 and 5.7, panel 2b). Equilibrium vapor $\Delta'^{17}O$ values vary little within a typical temperature range (~0-30˚C) because the value of θ_{eq} is relatively insensitive to temperature (Barkan and Luz, 2005) and similar to the value of λ_{ref}.

Second, as vapor diffuses through to the unsaturated atmosphere, $\Delta'^{17}O$ values of atmospheric vapor increases because the value of θ_{diff} (0.518) is less than the value of λ_{ref} (Figures 5.6 and 5.7, panel 3b). The magnitude of this kinetic effect is negatively correlated with turbulence above the saturated layer and sensitive to the relative humidity above the site of evaporation (Barkan and Luz, 2007; Criss, 1999; Merlivat, 1978; Uemura et al., 2010b). Under high relative humidity conditions, vapor $\Delta'^{17}O$ remains close to zero. Under low relative humidity conditions, vapor $\Delta'^{17}O$ values are higher (Figures 5.6 and 5.7, panel 3b).

Third, equilibrium condensation proceeds along a slope (θ_{eq} = 0.529) that is greater than the value of λ_{ref}. This fractionation increases the $\Delta'^{17}O$ value of the more condensed phase (precipitation) and decreases the $\Delta'^{17}O$ value of the less condensed phase (remaining vapor) (Figures 5.6 and 5.7, panel 4b). Precipitation and vapor $\Delta'^{17}O$ values are slightly sensitive to

temperature during condensation because equilibrium fractionations are larger at lower temperatures than at higher temperatures (Figures 5.6; 5.7, panel 5.4b; and 5.8e) (Horita and Wesolowski, 1994; Majoube, 1971). The increase in precipitation $\Delta'^{17}O$ associated with equilibrium condensation is typically smaller than the effect from diffusion because the value of λ_{ref} is closer to the value of θ_{eq} than the value of θ_{diff}. We include code in Supplement 5.1 to further explore the isotopic effects of evaporation and condensation.

Following initial condensation, a number of hydrologic processes add additional variability to meteoric water $\Delta'^{17}O$ values. The next sections explore the trends in meteoric water $\Delta'^{17}O$ variability and the hydrologic processes that explain $\Delta'^{17}O$ observations.

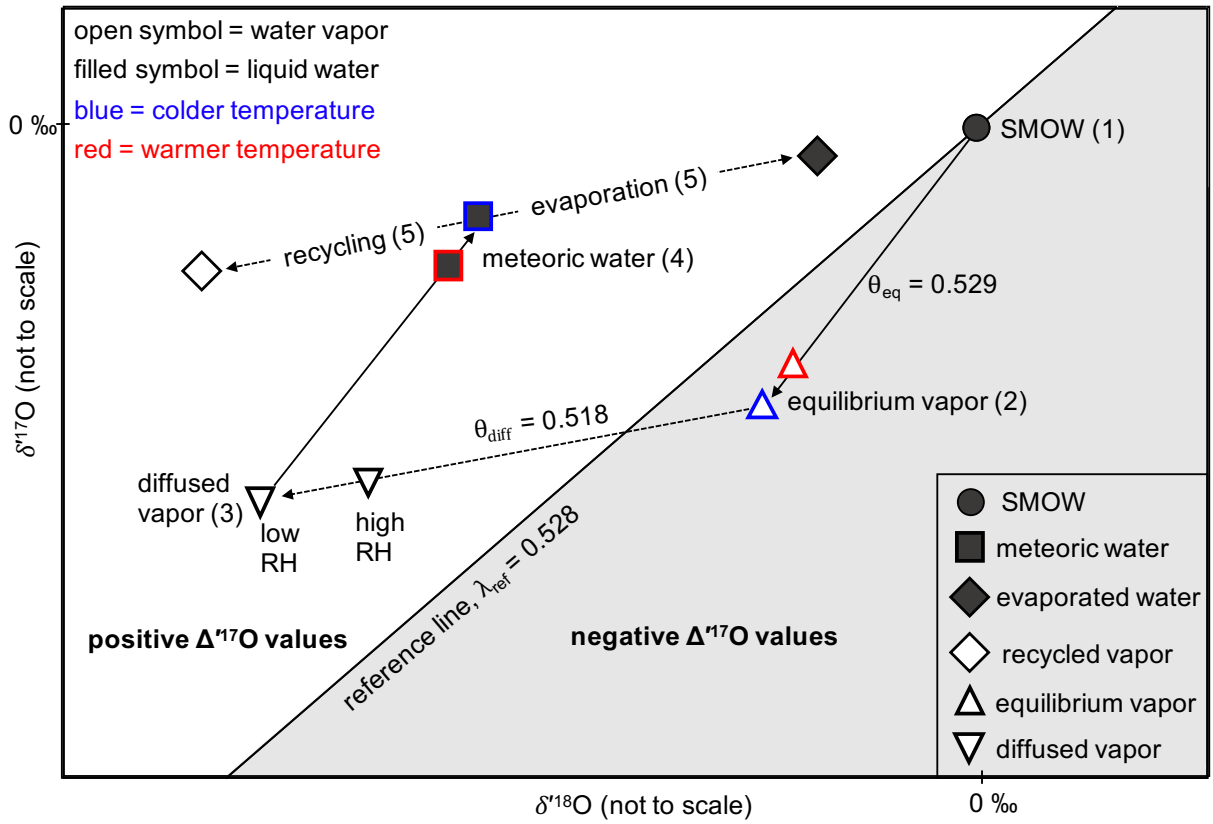

Figure 5.6 Generalized pathway of $\delta'^{18}O$ and $\delta'^{17}O$ fractionation in the water cycle. In this $\delta'^{18}O$ versus $\delta'^{17}O$ isotope space, $\Delta'^{17}O$ is defined as the deviation from the reference line. The white background indicates isotope space with positive $\Delta'^{17}O$ values; the gray background indicates isotope space with negative $\Delta'^{17}O$ values. Waters at different points in the hydrologic cycle are differentiated with symbols and numbered 1-5 to show stepwise variation associated with evaporation and condensation. Beginning from the ocean (SMOW, 1), water evaporates into a saturated equilibrium layer (2), diffuses through the unsaturated atmosphere (3), condenses (4), and evaporates (5). Vapor is noted with open symbols; liquid is noted in filled symbols. Red (warmer) and blue (colder) outlines indicate the effects of temperature dependent fractionations. For clarity, values of λ_{ref}, θ_{eq} (solid line), and θ_{diff} (dotted line) are included. Additional details and a step-by-step description of $\delta'^{18}O$ and $\delta'^{17}O$ fractionations are explained in Figure 5.7. The symbols do not indicate end points, but instead show points along a trajectory (marked with arrows) along which isotopic compositions can continue.

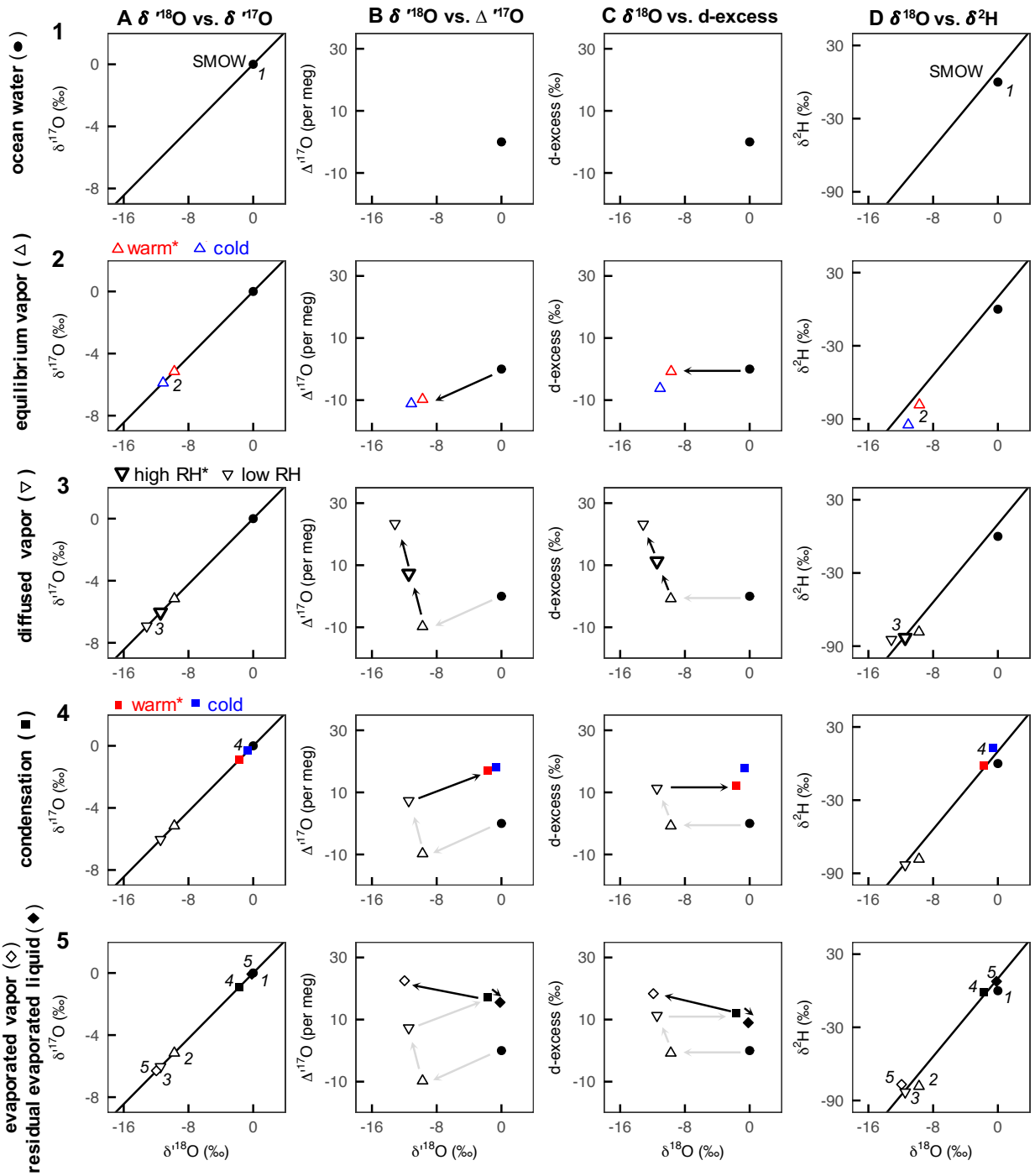

Figure 5.7 Step-wise variation of $\delta'^{17}O$, $\delta'^{18}O$, δ^2H, $\Delta'^{17}O$, and d-excess as water evaporates and condenses in a closed system. Isotopic variation is shown between $\delta'^{18}O$ and $\delta'^{17}O$ (column A), $\delta'^{18}O$ and $\Delta'^{17}O$ (column B), $\delta^{18}O$ and d-excess (column D), $\delta^{18}O$ and δ^2H (column D). The solid black lines in columns (A) and (D) show the triple oxygen and oxygen-hydrogen reference relationship, respectively. In each column, water begins in the ocean (row 1), evaporates into a saturated layer (row 2), diffuses through an unsaturated atmosphere (row 3), condenses to meteoric water (row 4), and evaporates (row 5). In row 4, we assume the isotopic composition of

precipitation is equal to that of surface water. The isotopic composition of evaporated vapor and residual liquid was calculated assuming pan evaporation at 16˚C and 10% evaporation. In all panels, vapor is shown with open symbols and liquid is shown with filled symbols. In columns B and C, black arrows show the isotopic variation associated with each row; gray arrows are included to show the 'trajectory' of isotope variability. For clarity, arrows are replaced by numbers in columns A and D. Fractionation associated with equilibrium evaporation (row 2), atmospheric vapor diffusion (row 3), and condensation (row 4) are shown under different temperature and humidity scenarios with color and bolded symbols. When multiple scenarios are included, the star (*) notes which scenario is used in subsequent calculations (rows). We focus primarily on variations of triple oxygen isotopes and d-excess, and include variations between $\delta^{18}O$ and $\delta^{2}H$ (column D) for reference.

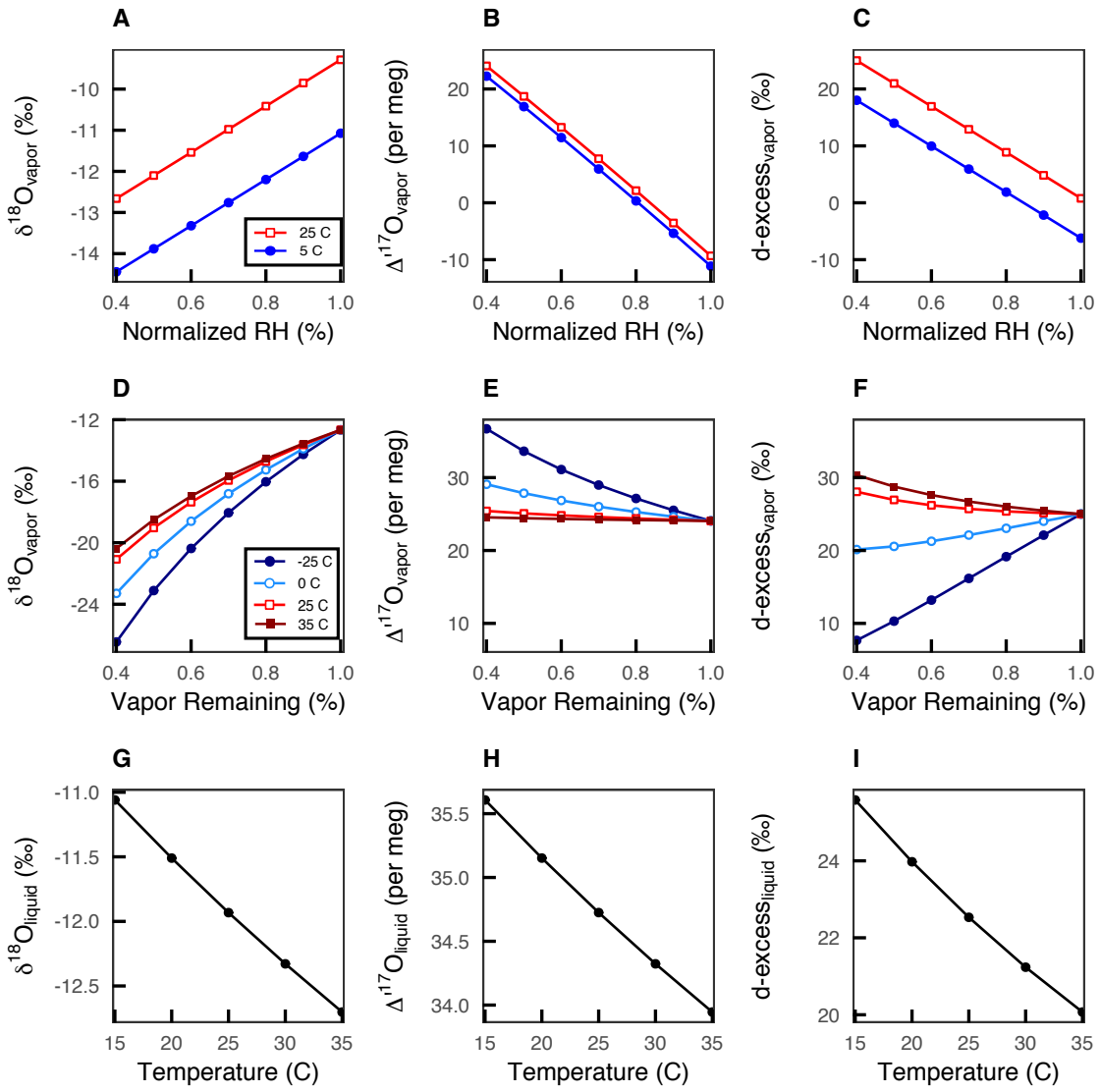

Figure 5.8 Isotope variations of $\delta^{18}O$ (A, D, G,), $\Delta'^{17}O$ (B, E, H), and d-excess (C, F, I) during evaporation from the ocean (A, B, C), Rayleigh distillation (D, E, F), and condensation (G, H, I) under different temperature scenarios. Fractionation under each temperature scenario is independent and does not represent a 'trajectory' from ocean water to precipitation. The final (RH = 0.4) 25˚C water vapor from the top row (A, B, C) is the starting vapor in the middle row (D, E, F). The final (f = 0.4) 0˚C vapor in the middle row is in isotopic equilibrium with the liquid in the bottom row.

5.5.2 Broad trends in meteoric water $\Delta'^{17}O$ variability

Average meteoric water $\Delta'^{17}O$ is 20 to 30 per meg, but $\Delta'^{17}O$ values range from less than –250 per meg to greater than 100 per meg (Figure 5.3b). Generally, more evaporated waters have lower $\Delta'^{17}O$ values and less evaporated waters have higher $\Delta'^{17}O$ values (Figure 5.9). Among the water types separated by color in Figure 5.9, seawater is quite under-studied with only 38 published

$\Delta'^{17}O$ values (Luz and Barkan, 2010). Most ocean samples have slightly higher $\delta^{18}O$ (–0.4 to 2.4‰, average of 0.4‰) and lower $\Delta'^{17}O$ (–15 to 4 per meg, average of –5 per meg) values than SMOW ($\delta^{18}O_{SMOW}$ = 0‰, $\delta^{17}O_{SMOW}$ = 0‰, $\Delta'^{17}O_{SMOW}$ = 0 per meg) (Luz and Barkan, 2010), but still very little is known about how $\Delta'^{17}O$ varies in the ocean.

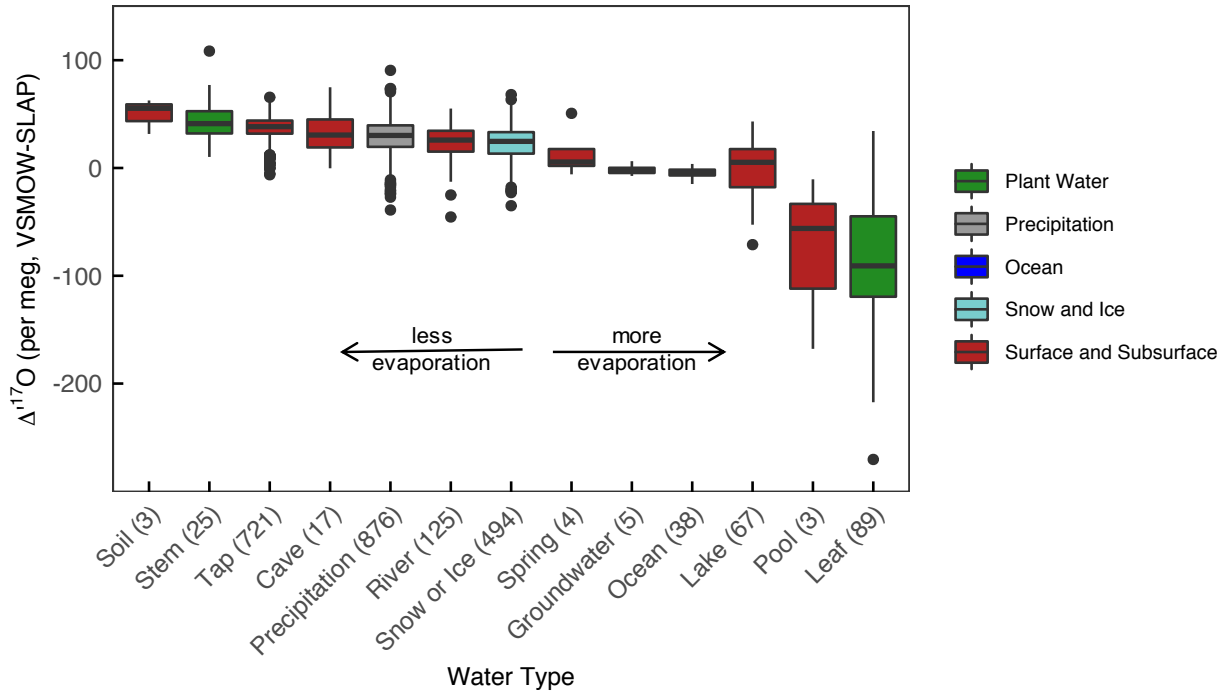

Figure 5.9 Box and whisker plot of water $\Delta'^{17}O$ distribution. Water types are listed individually, but are colored according to broader categories to give a sense of variation within groups. The numbers in parentheses indicate the total number of published observations for each water type. The new surface water data reported in this review are included. In each box, the bolded line is the median $\Delta'^{17}O$ value, the upper and lower hinge correspond to the 1st and 3rd quartiles, respectively, and the whisker correspond to no more than 1.5 times the interquartile range (IQR, the variation between the 1st and 3rd quartiles). The individually plotted points fall outside the IQR. In general, more evaporated waters have lower $\Delta'^{17}O$ values and less evaporated waters have higher $\Delta'^{17}O$ values.

For all the available meteoric water data, $\Delta'^{17}O$ is positively correlated with d-excess (Pearson's r = 0.58, Figure 5.3e) and uncorrelated with $\delta'^{18}O$ (r = –0.16, Figure 5.3b). However, these correlations vary substantially among water types (Table 5.4), and are always stronger for waters that have undergone substantial kinetic fractionation. For example, highly evaporated waters such as plant water and lakes have a strong positive correlation between $\Delta'^{17}O$ and d-excess (r = 0.95 and 0.58, respectively, Table 5.4) and a strong negative correlation between $\Delta'^{17}O$ and

$\delta'^{18}O$ (r = –0.93 and –0.78, respectively, Table 5.4). Less evaporated waters such as precipitation and rivers have weaker correlations between $\Delta'^{17}O$ and d-excess (r = 0.28 and 0.16, respectively, Table 5.4) or $\delta'^{18}O$ (r = –0.21 and –0.11, respectively, Table 5.4). Evaporated waters have such a strong correlation among $\delta'^{18}O$, $\Delta'^{17}O$, and d-excess because both d-excess and $\Delta'^{17}O$ are sensitive to relative humidity and vary as a function of kinetic fractionation. The slope between d-excess and $\Delta'^{17}O$ is ~ 0.7 to 2.0 per meg $‰^{-1}$ (e.g., Landais et al., 2010; Li et al., 2015), but the exact value varies as a function of relative humidity and fractionation factors (Barkan and Luz, 2007).

Table 5.4 Pearson correlation coefficient between $\Delta'^{17}O$ and d-excess or $\delta^{18}O$.

Water Type	$\Delta'^{17}O$–d-excess Correlation	$\Delta'^{17}O$–$\delta^{18}O$ Correlation
All Data	0.58	−0.16
Plant Water	0.95	−0.93
Lake	0.58	−0.78
Rain	0.28	−0.21
River	0.16	−0.11
Ocean	NA*	0.02
Snow or Ice	−0.35	0.37

*There is no reported correlation between $\Delta'^{17}O$ and d-excess for ocean water because no studies report $\delta^{18}O$, $\delta^{17}O$, and $\delta^{2}H$ of ocean water.

Most meteoric waters occupy a crowded region in $\delta'^{18}O$–$\Delta'^{17}O$ isotope space, and many of the broad patterns that differentiate plant water and snow or ice disappear among samples with $\delta^{18}O$ between –30 and 10‰ (Figure 5.3c). However, the observed $\Delta'^{17}O$ variability of these meteoric waters is more than 80 per meg, significantly greater than the precision of well-tuned triple oxygen isotope measurements, and systematic trends exist within this cloud of isotope data that are related to spatiotemporal variability and hydrologic processes. In the next sections, we explore $\Delta'^{17}O$ patterns and the hydrologic processes that drive $\Delta'^{17}O$ variation.

5.5.3 $\Delta'^{17}O$ spatial variability

Spatial patterns of meteoric water $\delta^{18}O$ are well established and vary with latitude, elevation, and proximity to moisture sources (Bowen, 2010; Brady et al., 2019; Dansgaard, 1964; Kendall and Coplen, 2001; Rozanski et al., 1993). Spatial patterns are not as clear for $\Delta'^{17}O$. Global (Luz and Barkan, 2010; this study) and continental (Li et al., 2015; Tian et al., 2019) scale datasets of meteoric water $\Delta'^{17}O$ variability provide initial insights, but most hydrologic $\Delta'^{17}O$ observations

tend to be clustered in small regions (Figure 5.2) and do not systematically span latitudinal or elevational gradients. Isotope-enabled climate models can fill some of these gaps (Risi et al., 2013), but there are still relatively few $\Delta'^{17}O$ observations to evaluate model performance.

In general, $\Delta'^{17}O$ is lower in meteoric waters in arid regions due to sub-cloud and surface evaporation and is higher in regions where annual precipitation is dominated by cold-season rain or regions that receive a high degree of recycled moisture. $\Delta'^{17}O$ appears invariant with changes in mean annual precipitation, mean annual temperature, and elevation (Li et al., 2015; Schoenemann et al., 2014; Tian et al., 2019; Uechi and Uemura, 2019). Latitudinal $\Delta'^{17}O$ gradients are observed in the United States (Li et al., 2015) but not in China (Tian et al., 2019), and additional work is needed to fully understand these patterns.

Spatial correlations between $\Delta'^{17}O$ and d-excess are complex and varied (Risi et al., 2013), but the existing data are limited. In a few regions, for example downwind of the Great Lakes in North America where moisture is highly recycled (Bowen et al., 2012), spatial patterns of $\Delta'^{17}O$ and d-excess covary (Li et al., 2015). However, the continental-scale spatial patterns of $\Delta'^{17}O$ and d-excess differ across the United States (Li et al., 2015) and China (Tian et al., 2019), suggesting that different processes may dominate the isotopic composition of $\Delta'^{17}O$ and d-excess across large spatial scales.

5.5.4 Temporal precipitation $\Delta'^{17}O$ variability

Temporal precipitation $\Delta'^{17}O$ variability is also uncertain because the frequency of precipitation sampling is inconsistent and relatively few studies have focused on temporal $\Delta'^{17}O$ variability (Table 5.2). Still, a temporal pattern of mid-latitude precipitation $\Delta'^{17}O$ is emerging, with lower values in the summer and higher values in the winter (Affolter et al., 2015; Li et al., 2015; Tian et al., 2018; Uechi and Uemura, 2019). A detailed explanation of this variability remains unclear, but is generally attributed to a seasonal switch between stronger kinetic fractionation effects in the summer and stronger equilibrium fractionation effects in the winter. Temperature during equilibrium condensation may explain some of the observed variability, but additional research is needed to clarify this. Future precipitation $\Delta'^{17}O$ observations should focus on amount-weighted monthly samples to better characterize average isotopic compositions and

minimize the influence of small-scale weather features (Dansgaard, 1964; Gat, 1996; Rozanski et al., 1993).

5.5.5 Triple oxygen isotope interpretation guide

From a mechanistic point of view, $\Delta'^{17}O$ variability arises from 1) changes in θ values (θ_{eq} versus θ_{diff}), 2) differences between the values of λ_{ref} and θ_{eq} or θ_{diff}, or 3) non-linear isotope responses that result from the logarithmic δ' notation (Table 5.5). Following evaporation from the ocean and initial condensation (Section 5.5.1; Craig and Gordon, 1965), multiple hydrologic processes affect $\Delta'^{17}O$ values (Table 5.5, Figures 5.6-5.8). Isotope responses to these processes can combine, compound, or negate each other, which can make interpreting $\Delta'^{17}O$ data a challenge. This section describes triple oxygen isotope variability associated with individual hydrologic processes and is intended to guide and aid interpretations of $\Delta'^{17}O$ data.

Table 5.5 Processes and explanations of $\Delta'^{17}O$ variation.

Process	$\Delta'^{17}O$ Response	Magnitude of $\Delta'^{17}O$ Response	Explanation
Evaporation from the ocean	increase	Typically ~ 20-30 per meg. Higher values with low humidity and/or low turbulence at the evaporating site.	θ_{eq} vs. θ_{diff} and θ_{diff} less than λ_{ref}
Condensation	increase	~ 10 per meg. Higher $\Delta'^{17}O$ expected in colder conditions.	θ_{eq} greater than λ_{ref}
Recycling	increase	Typically < 20 per meg	θ_{diff} less than λ_{ref}
Stratospheric intrusions	increase	? Depends on stratospheric and tropospheric $\Delta'^{17}O$ values	Addition of stratospheric water vapor
Post-condensation evaporation	decrease	Potentially > 200 per meg in plant water, typically no more than ~ 50-60 per meg in surface water	θ_{diff} less than λ_{ref}
Mixing	decrease	0 to >100 per meg. Depends on the mixing fraction and initial $\delta^{18}O$ and $\Delta'^{17}O$ of the mixing waters	Non-linear response
Supersaturation	decrease	~ 10 to 30 per meg	θ_{diff} less than λ_{ref}
Rayleigh distillation	temperature dependent	< 10 per meg. Larger effect at lower temperatures.	$\lambda_{Rayleigh} \approx \lambda_{ref}$
Convection	?	?	?

5.5.5.1 Processes that cause $\Delta'^{17}O$ to decrease

5.5.5.1.1 Evaporation

Evaporation leaves the residual water body with higher $\delta^{17}O$ and $\delta^{18}O$ compositions (Gat, 1996; Gonfiantini et al., 2018) and a lower $\Delta'^{17}O$ value because the value of θ_{diff} is less than the value of λ_{ref} (Figures 5.6 and 5.7). We observe these effects in plant and surface waters, which can have very high $\delta^{18}O$ and $\delta^{17}O$ values and very low $\Delta'^{17}O$ values (Figure 5.3b; Cernusak et al., 2016; Landais et al., 2006; Li et al., 2017). This response is independent of initial $\delta^{18}O$, such that low $\Delta'^{17}O$ values do not require high $\delta^{18}O$ and vice versa (Figure 5.10).

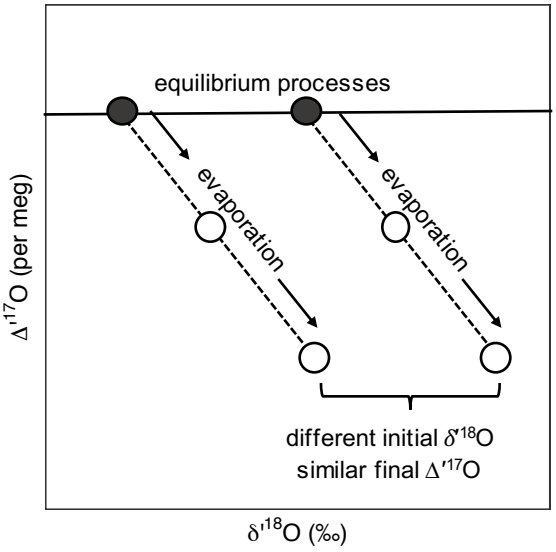

Figure 5.10 Schematic of $\delta'^{18}O$ versus $\Delta'^{17}O$ based on steady-state isotope mass balance models during evaporation. During evaporation, the $\Delta'^{17}O$ response is independent of initial $\delta'^{18}O$ composition.

Evaporation occurs in the hydrosphere under steady-state (constant water levels) or non-steady-state (progressive water loss) conditions. The isotopic composition of residual water in both of these scenarios is predicted by well-established models (Criss, 1999; Gázquez et al., 2018; Passey and Ji, 2019; Surma et al., 2018). First, steady-state evaporation occurs in simple flow-through or closed-basin systems where the volume of inflowing water is equal to the volume of

water loss via evaporation, outflow, and/or groundwater seepage. In this scenario, the isotopic composition of the residual evaporated liquid water is:

$$R_W = \frac{\alpha_{eq}\alpha_{diff}(1-h)R_I h X_E R_A}{X_E + \alpha_{eq}\alpha_{diff}(1-h)(1-X_E)} \quad \text{Eq. 5.6}$$

where α_{eq} is the temperature dependent equilibrium fractionation factor (Barkan and Luz, 2005; Horita and Wesolowski, 1994; Majoube, 1971), α_{diff} is the kinetic fractionation factor, h is the relative humidity normalized to the temperature of the evaporating surface, X_E is the volumetric ratio of water lost to evaporation relative to inflowing water, and R_I, R_A, and R_W are the isotope ratios of inflowing water, atmospheric water vapor, and residual evaporated water, respectively. Importantly, this model assumes that the isotopic composition of the evaporating body is well mixed and that inflowing water is isotopically uniform and unevaporated, which is not always the case (e.g., Surma et al., 2018, 2015). Second, non-steady-state evaporation occurs in isolated water bodies that evaporate to dryness. The isotopic composition of the water body during this 'pan' evaporation is (Criss, 1999; Passey and Ji, 2019; Surma et al., 2018):

$$R_W = f^u (R_{Wi} - R_{Wss}) + R_{Wss} \quad \text{Eq. 5.7}$$

where f is the fraction of water remaining, R_W is the isotope ratio of the evaporating body, R_{Wi} is the isotope ratio of the initial water, R_{Wss} is the predicted final steady-state isotope ratio, and the exponent u relates equilibrium and kinetic fractionation factors by the relative humidity (h), where u is:

$$u = \frac{1-\alpha_{eq}\alpha_{diff}(1-h)}{\alpha_{eq}\alpha_{diff}(1-h)} \quad \text{Eq. 5.8}$$

and R_{Wss} is:

$$R_{Wss} = \frac{\alpha_{eq} h R_A}{1-\alpha_{eq}\alpha_{diff}(1-h)}. \quad \text{Eq. 5.9}$$

These models predict isotope variation in both the triple oxygen and oxygen-hydrogen systems. In general, residual waters have lower $\Delta'^{17}O$ and d-excess values when the effects of kinetic fractionation are greatest, i.e., when relative humidity is low and/or when values of α_{diff} or X_E are high. Additional work is needed to clarify the role of turbulence at the evaporating site and to constrain the values of α_{diff} and X_E (Passey and Ji, 2019).

5.5.5.1.2 Mixing

Due to the logarithmic δ' notation used in the definition of $\Delta'^{17}O$, mixing liquid or vapor water bodies with different $\delta^{18}O$ compositions causes $\Delta'^{17}O$ to decrease (Figure 5.11c; Luz and Barkan, 2010; Matsuhisa et al., 1978). This phenomenon is most pronounced when $\Delta'^{17}O$ of the mixing water bodies are identical and $\delta^{18}O$ are very different. The $\delta^{18}O$ and d-excess responses to mixing are a linear function of the fraction of each mixed water (Figures 5.11a and 5.11b) because $\delta^{18}O$ and d-excess are defined with δ notation (not logarithmic δ' notation). Isotopic effects of mixing are not limited to natural hydrologic processes, but can also affect analytical systems as gases move through prep lines and isotope analyzers (see Section 5.7.2.5 for additional details). We provide code in Supplement 5.2 to explore the isotope effects of mixing in natural and analytical settings.

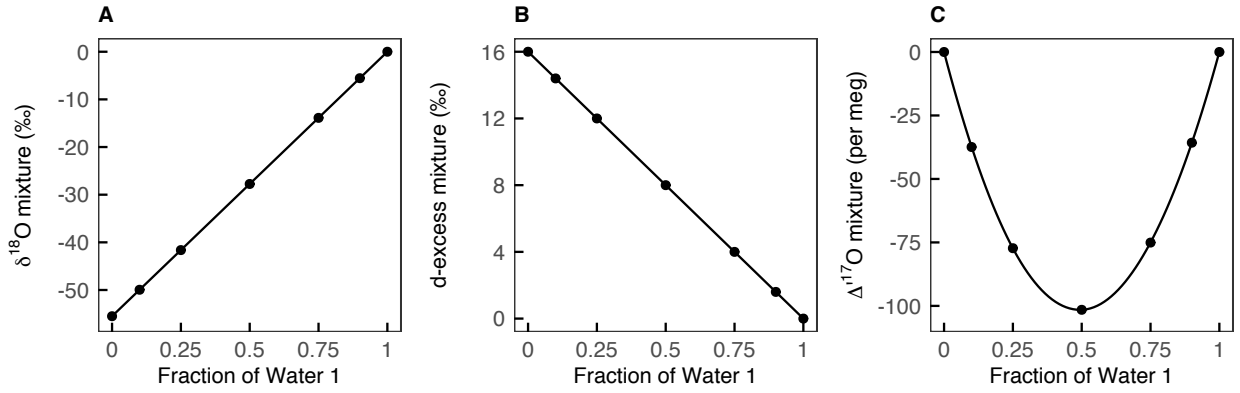

Figure 5.11 Variations of (A) $\delta^{18}O$, (B) d-excess, and (C) $\Delta'^{17}O$ compositions when mixing VSMOW (water 1) and SLAP (water 2). $\delta^{18}O$ and d-excess vary linearly with mixing. $\Delta'^{17}O$ responds non-linearly to mixing because it is defined with δ' notation.

5.5.5.1.3 Supersaturation

Kinetic effects during condensation under very cold (< ~ –20˚C) supersaturated conditions cause low $\Delta'^{17}O$ values in snow and ice (Angert et al., 2004; Jouzel and Merlivat, 1984; Landais et al., 2012a, 2012b, 2008; Pang et al., 2019, 2015; Risi et al., 2010; Schoenemann et al., 2014; Schoenemann and Steig, 2016; Winkler et al., 2012) and a pattern of downward tailing $\Delta'^{17}O$ at very low ($\delta^{18}O < –30‰$) isotopic compositions in compilations of meteoric water data (Figure 5.3b). Supersaturation is common in high latitude and polar regions and develops when the saturation vapor pressure of a condensing surface is less than the vapor pressure surrounding a water droplet or ice crystal (Schoenemann et al., 2014). Under these conditions, a strong vapor pressure gradient develops between water vapor and the condensing surface. Water vapor must diffuse across this gradient to condense, a process that causes kinetic fractionation and lowers $\Delta'^{17}O$ values of the condensate. Although equilibrium effects during condensation (Section 5.5.1) and moisture recycling in Antarctica (Pang et al., 2019) generally increase $\Delta'^{17}O$, low $\Delta'^{17}O$ values observed in polar regions (Figure 5.3b) suggest that strong kinetic effects dominate under very cold supersaturated conditions (Angert et al., 2004; Jouzel and Merlivat, 1984; Landais et al., 2012a).

Snow and ice $\Delta'^{17}O$ and d-excess exhibit opposite trends at very low $\delta^{18}O$ values (Figures 5.3b and 5.3d), reflecting the distinctions in how θ_{eq} changes with temperature in each system. With decreasing temperatures, θ_{eq} values increase in the $\delta^{18}O$–$\delta^{2}H$ system (Horita and Wesolowski, 1994; Majoube, 1971), but decrease for $\delta'^{18}O$–$\delta'^{17}O$ (Table 5.6, Figures 5.7 and 5.8). Such variations in θ_{eq} result in relatively small changes in $\Delta'^{17}O$ and d-excess relative to other hydrologic processes (Table 5.5), but can have a larger effect under cold supersaturated conditions.

Table 5.6 Temperature dependence of equilibrium fractionation factors and $\lambda_{Rayleigh}$.

Temperature (C)	$^{18}\alpha_{eq}$	$^{17}\alpha_{eq}$	$\lambda_{Rayleigh}$
Explanation	Majoube 1971	$(^{18}\alpha_{eq})^{0.529}$	$(^{17}\alpha_{eq} - 1)/ (^{18}\alpha_{eq} - 1)$
40	1.00823	1.00435	0.5280
25	1.00937	1.00495	0.5278
0	1.01172	1.00618	0.5275
-25	1.01483	1.00782	0.5272

5.5.5.2 Processes that cause $\Delta'^{17}O$ to increase

5.5.5.2.1 Moisture recycling

Moisture recycling increases $\Delta'^{17}O$ in evaporated vapor and subsequent precipitation because the value of θ_{diff} is less than the value of λ_{ref} (Figures 5.6 and 5.7). Maintaining isotopic and mass balance and following the logic that describes fractionation of residual water during evaporation (Section 5.5.5.1.1), evaporated vapor has lower $\delta'^{18}O$, lower $\delta'^{17}O$, and higher $\Delta'^{17}O$ than the initial water body from which it evaporated. Condensation of this recycled moisture further increases $\Delta'^{17}O$ (Figures 5.6 and 5.7).

As with evaporation, d-excess and $\Delta'^{17}O$ values of vapor and precipitation increase with the degree of moisture recycling (Aemisegger et al., 2014; Salati et al., 1979; Tian et al., 2019) and are positively correlated when moisture recycling causes isotope fractionation (Figures 5.3e and 5.7, panels 5b and 5c).

5.5.5.2.2 Stratospheric intrusions

Stratospheric water vapor undergoes non-mass-dependent fractionation and has extremely high (greater than 1,000 per meg) $\Delta'^{17}O$ values (Miller, 2018; Winkler et al., 2012). This vapor may contribute to near polar surface water fluxes during the Antarctic winter when the tropopause is low (Franz et al., 2005; Roscoe et al., 2004), but is generally considered negligible in most hydrologic triple oxygen isotope studies and is not evident in compilations of global meteoric water data (Figure 5.3) (e.g., Landais et al., 2008; Luz and Barkan, 2010).

5.5.5.3 Processes with little effect on $\Delta'^{17}O$

5.5.5.3.1 Rayleigh distillation

Rayleigh distillation explains many of the spatial patterns observed in $\delta^{18}O$, $\delta^{17}O$, and $\delta^{2}H$ of meteoric water (Gat, 1996; Risi et al., 2013), but has little effect on $\Delta'^{17}O$ (Figure 5.12). Generally, $\Delta'^{17}O$ is considered insensitive to Rayleigh distillation because the $\delta'^{18}O$–$\delta'^{17}O$ slope during Rayleigh distillation, here termed $\lambda_{Rayleigh}$, is nearly identical to the value of λ_{ref} (0.528) (Figure 5.12b, Luz and Barkan, 2010). In other words, $\delta'^{18}O$ and $\delta'^{17}O$ vary along a line that is nearly parallel to λ_{ref}, so $\Delta'^{17}O$ remains essentially invariant.

The value of $\lambda_{Rayleigh}$ is, however, slightly sensitive temperature (0.5278 at 25 ˚C, 0.5272 at –25 ˚C; Table 5.6) and can increase (decrease) the $\Delta'^{17}O$ value of vapor (condensate) by a few per meg when $\lambda_{Rayleigh}$ is less than λ_{ref} (Figure 5.8). The temperature sensitivity of $\lambda_{Rayleigh}$ arises from the equilibrium fractionation factors (α values) for ^{18}O and ^{17}O (Majoube, 1971):

$$\lambda_{\text{Rayleigh}} = \frac{(^{17}\alpha_{eq} - 1)}{(^{18}\alpha_{eq} - 1)} \qquad \text{Eq. 5.10}$$

(Barkan and Luz, 2005; Luz and Barkan, 2010). Values of $\lambda_{Rayleigh}$ are slightly higher at warmer temperatures and slightly lower at cooler temperatures, but never deviate far from 0.528 (Table 5.6). As a result, variability of $\Delta'^{17}O$ attributed to Rayleigh distillation is generally smaller than typical analytical precision (± 10 per meg), but can combine with other processes such as equilibrium condensation as a small factor in meteoric water $\Delta'^{17}O$ variability. At very warm temperatures (> 35˚C), $\lambda_{Rayleigh}$ is almost identical to λ_{ref}, and $\Delta'^{17}O$ is indeed invariant during Rayleigh distillation (Table 5.6, Figure 5.8).

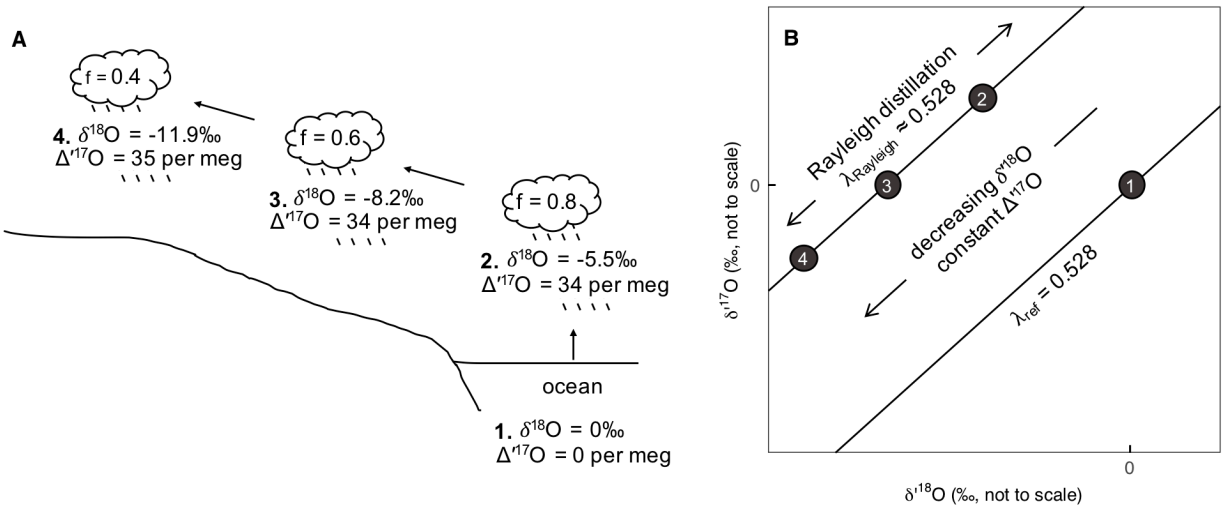

Figure 5.12 Variation of liquid $\delta'^{18}O$ and $\Delta'^{17}O$ during Rayleigh distillation in (A) a schematic and (B) $\delta'^{18}O$–$\delta'^{17}O$ isotope space. Water starts in the ocean (1), evaporates, and condenses, leaving airmasses with (2) 80%, (3) 60%, and (4) 40% of the initial airmass remaining. In the schematic (A), f is the percentage of the initial airmass that remains after rainout. The isotopic composition of precipitation (steps 2-4) was calculated at 25˚C and is assumed to be in isotopic equilibrium with the vapor (middle row) shown in Figure 5.8. Because $\lambda_{Rayleigh}$ is approximately equal to λ_{ref}, $\Delta'^{17}O$ is relatively insensitive to Rayleigh distillation.

5.5.5.4 Temperature effects on $\Delta'^{17}O$ and d-excess

The different temperature sensitivities of $\Delta'^{17}O$ and d-excess are most noticeable at low temperatures (low $\delta^{18}O$ values, compare Figures 5.3b and 5.3d) and pronounced because $\Delta'^{17}O$ is defined with δ' values while d-excess is defined with δ values. Theoretical calculations and laboratory experiments show that $\Delta'^{17}O$ is less sensitive to temperature than d-excess (Figures 5.7 and 5.8) because the triple oxygen liquid-vapor θ_{eq} value is independent of temperature (Figure 5.13b; Barkan and Luz, 2005; Cao and Liu, 2011), whereas the oxygen-hydrogen liquid-vapor θ_{eq} value varies slightly with temperature (Figure 5.13a; Horita and Wesolowski, 1994; Majoube, 1971). These θ_{eq} temperature sensitivities arise from differences in the temperature dependent equilibrium liquid-vapor fractionation factors ($\alpha_{l\text{-}v}$) for oxygen and hydrogen because

$$\theta_{l\text{-}v} = \frac{ln\ (^{A}\alpha_{l-v})}{ln\ (^{B}\alpha_{l-v})} \qquad \text{Eq. 5.11}$$

where A is the $^{2}H/^{1}H$ or $^{17}O/^{16}O$ fractionation factor and B is the $^{18}O/^{16}O$ fractionation factor. The triple oxygen $\theta_{l\text{-}v}$ value is nearly invariant (0.529, Figure 5.13b) because $^{17}O/^{16}O$ and $^{18}O/^{16}O$ are subject to the same temperature effects; the oxygen-hydrogen $\theta_{l\text{-}v}$ value (~ 8, Figure 5.13a) varies with temperature because $^{2}H/^{1}H$ fractionation is governed by a different temperature dependent relationship than $^{18}O/^{16}O$ fractionation (Horita and Wesolowski, 1994; Majoube, 1971).

The different temperature sensitivities of $\Delta'^{17}O$ and d-excess provide complementary information to decouple the isotope effects of temperature and relative humidity on meteoric waters. For example, a combination of $\Delta'^{17}O$ and d-excess data can provide complementary information about the relative humidity and temperature and moisture source conditions (Landais et al., 2012a, 2012b, 2008; Uemura et al., 2010; Winkler et al., 2012).

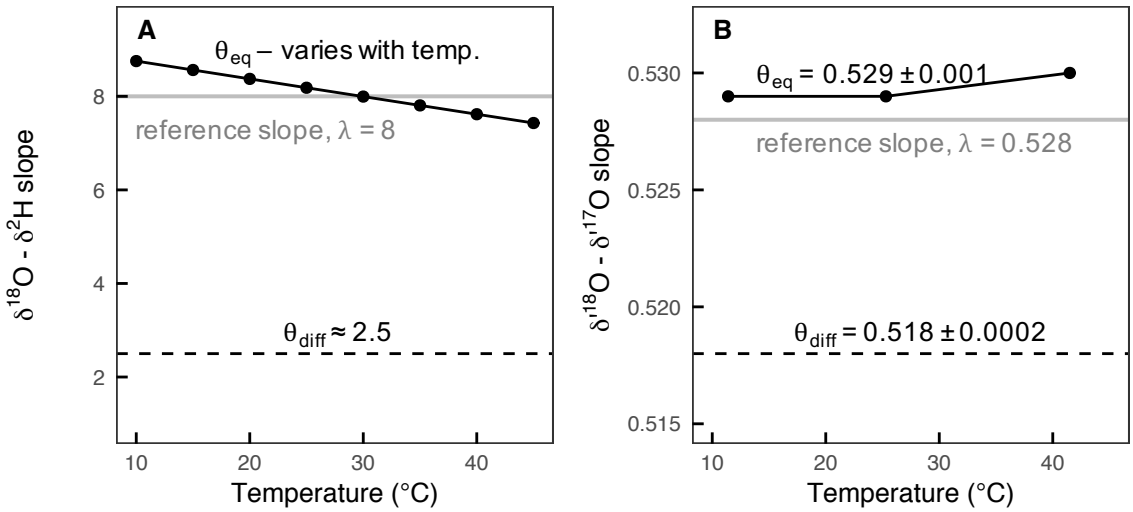

Figure 5.13 Temperature dependence of the slopes in A) $\delta^{18}O$–$\delta^{2}H$ and (B) $\delta'^{18}O$–$\delta'^{17}O$ isotope systems. Relevant isotope relationships are associated with equilibrium fractionation (θ_{eq}, solid black line), the diffusion of water vapor through the air (θ_{diff}, dashed black line), and the meteoric water reference relationship (solid gray line). The reference slopes are well-established (Craig, 1961 and Luz and Barkan, 2010, respectively) and do not vary with temperature. Similarly, θ_{diff} values are independent of temperature (Barkan and Luz, 2007). The θ_{diff} value associated with the $\delta^{18}O$–$\delta^{2}H$ relationship is still uncertain, but is generally between ~ 2.5 and 8 (Gonfiantini et al., 2018). Finally, the triple oxygen ($\delta'^{18}O$–$\delta'^{17}O$) θ_{eq} value is insensitive to temperature (Barkan and Luz, 2005) but the value of θ_{eq} varies slightly with temperature in the oxygen-hydrogen ($\delta^{18}O$–$\delta^{2}H$) system. These different θ_{eq} temperature sensitivities result in a slight temperature dependence in d-excess but little temperature-dependent variation in $\Delta'^{17}O$.

5.5.5.5 Convective activity

Convection is occasionally cited to explain low- and mid-latitude meteoric water $\Delta'^{17}O$ variability (e.g., Landais et al., 2010; Li et al., 2015; Risi et al., 2013), but the mechanisms connecting convective activity to $\Delta'^{17}O$ are unclear. During convection, water vapor is subject to complex atmospheric dynamics, including vertical mixing, transport and moisture convergence, equilibrium isotopic exchange, and diffusive fractionation from sub-cloud evaporation (Galewsky et al., 2016). These effects are relatively well understood for $\delta^{18}O$ and $\delta^{2}H$ (e.g., Risi et al., 2008; Vimeux et al., 2011), but have not yet been explored for $\Delta'^{17}O$.

5.6 Global variations of $\delta'^{17}O$ and $\delta'^{18}O$ in meteoric waters

5.6.1 Triple oxygen isotope reference slope

Up to this point in this discussion, $\Delta'^{17}O$ variability has been presented in a framework where λ_{ref} is equal to 0.528. This is the standard approach in hydrologic triple oxygen isotope studies because $\lambda_{Rayleigh}$ is also ~0.528 (Table 5.6) and Rayleigh processes dominate isotopic fractionation in the hydrosphere. However, a value of 0.528 as a reference slope is somewhat arbitrary. Here we explain the history of using 0.528 for λ_{ref} and explore how the assigned value of λ_{ref} affects $\Delta'^{17}O$.

Observed $\delta'^{18}O$–$\delta'^{17}O$ slopes for water integrate multiple equilibrium (θ_{eq}) and kinetic (θ_{diff}) fractionation processes. The value of λ_{ref} was initially defined from a set of meteoric water $\delta'^{17}O$ and $\delta'^{18}O$ measurements made with electrolysis and continuous flow IRMS that fit a line with an observed slope (λ_{obs}) of 0.528 (Meijer and Li, 1998, $\lambda_{obs} = 0.5281 \pm 0.0015$). The value of this slope was later confirmed with a different set of water samples and higher precision dual inlet IRMS measurements (Luz and Barkan, 2010 $\lambda_{obs} = 0.528 \pm 0.0001$) and defined as λ_{ref}. The observed slope is closer to 0.529 (θ_{eq}) than to 0.518 (θ_{diff}) and it is nearly identical to $\lambda_{Rayleigh}$, indicating that most meteoric waters in these initial studies were more strongly affected by equilibrium fractionation (e.g., Rayleigh distillation) than by kinetic fractionation. However, recent work indicates that many waters outside polar regions fit a regression line with a slightly shallower slope than 0.528 (Miller, 2018; Sharp et al., 2018), suggesting that the commonly used value for λ_{ref}, 0.528, may not fit the triple oxygen isotope global meteoric water line.

5.6.2 Meteoric water lines

Meteoric water lines establish the most fundamental relationships in isotope hydrology and provide a point of reference from which to interpret isotope data (e.g., Brooks et al., 2010; Craig, 1961; Jasechko, 2019). Here we use the well-established $\delta^{18}O$–$\delta^{2}H$ meteoric water relationship (Craig, 1961) as a model to re-evaluate and update the meteoric water triple oxygen isotope relationship.

The $\delta^{18}O$–$\delta^{2}H$ global meteoric water line was initially built from ~400 precipitation, river, and lakes samples (Craig, 1961). Later, the meteoric water $\delta^{18}O$–$\delta^{2}H$ relationship was re-evaluated

using amount-weighted and arithmetic mean monthly precipitation from a near-global distribution of IAEA/WMO sites (Dansgaard, 1964; Rozanski et al., 1993) and rivers from the United States (Kendall and Coplen, 2001). The re-evaluated global meteoric water lines have slightly higher slopes and intercepts, but are statistically indistinguishable from the original line defined by Craig (1961). Agreement among these lines indicates that the $\delta^{18}O$–$\delta^{2}H$ global meteoric water line is well characterized and represents global variation in $\delta^{18}O$ and $\delta^{2}H$ (Gat, 1996).

The triple oxygen global meteoric water line was first defined as (Luz and Barkan, 2010):

$$\delta'^{17}O = 0.528\ (\pm\ 0.0001) * \delta'^{18}O + 0.033\ (\pm\ 0.003) \qquad \text{Eq. 5.12}$$

from GISP and SLAP (Barkan and Luz, 2005), 29 Vostok snow samples (Landais et al., 2008), and a set of 52 meteoric waters (precipitation, surface water, cave water, and snow) (Luz and Barkan, 2010). The basic features of this line, an empirically determined slope and positive y-intercept, are similar to the oxygen-hydrogen global meteoric water line. However, the initial $\delta'^{18}O$–$\delta'^{17}O$ global meteoric water line was constructed with a large proportion of high latitude precipitation and samples (lakes, snow, and evaporated snow) with isotopic compositions that are not representative of average freshwater from temperate and tropical regions (Miller, 2018; Sharp et al., 2018). Here, we re-evaluate the triple oxygen isotope global meteoric water line by expanding the dataset to include more samples from temperate and tropical regions.

Following the approaches used to build $\delta^{18}O$–$\delta^{2}H$ meteoric water relationships, the triple oxygen global meteoric water line should be built from a regression line through $\delta'^{17}O$ and $\delta'^{18}O$ from integrated monthly precipitation (Dansgaard, 1964; Rozanski et al., 1993) and/or flowing surface waters (rivers) (Kendall and Coplen, 2001). Precipitation data are slightly preferable because they are generally unevaporated, but sample collection requires substantial effort and currently no monthly precipitation $\delta^{17}O$ data are available (Table 5.2). For now, river water is an adequate substitute because it often represents the isotopic composition of amount weighted seasonal precipitation (e.g., Kendall and Coplen, 2001). However, the isotopic composition of river water can be affected by post-precipitation processes such as evaporation or isotopic exchange with atmospheric vapor, so ultimately it will be important to re-evaluate the triple oxygen isotope meteoric water line with integrated monthly precipitation data. This evaluation is

especially important for $\delta'^{17}O$ and $\delta'^{18}O$ because one of the main applications of triple oxygen isotopes is to constrain evaporation.

The available triple oxygen isotope data (Table 5.2) from which to define an updated meteoric water line include 1 river from northwestern Switzerland (Affolter et al., 2015), 9 rivers from the western United States (Passey and Ji, 2019), 14 rivers from the Sistan Basin in eastern Iran (Surma et al., 2015), and 17 rivers from locations throughout Asia and Europe (Luz and Barkan, 2010). We do not include precipitation data that were collected on daily or event timescales (Affolter et al., 2015; Kaseke et al., 2018; Landais et al., 2010; Luz and Barkan, 2010; Surma et al., 2018; Tian et al., 2018; Uechi and Uemura, 2019), but expand the dataset to include new triple oxygen isotope data from 84 rivers (Section 5.8 and Supplement 5.6). With these new results, the available river data span a 30‰ range (–20 to +10‰) in $\delta'^{18}O$ and reflect common isotope variability in temperate and tropical regions (Bowen et al., 2019; Sharp et al., 2018). The best-fit line between $\delta'^{18}O$ and $\delta'^{17}O$ from the compiled river data is:

$$\delta'^{17}O = 0.5264*\delta'^{18}O\ (\pm\ 0.0002) + 0.0080\ (\pm\ 0.0025‰). \quad \text{Eq. 5.13}$$

Excluding rivers from very arid environments that may be affected by evaporation (Passey and Ji, 2019; Surma et al., 2015), the best-fit line is:

$$\delta'^{17}O = 0.5265*\delta'^{18}O\ (\pm\ 0.0002) + 0.0118\ (\pm\ 0.0027‰). \quad \text{Eq. 5.14}$$

Equation 5.14 is indistinguishable from the best-fit line from a recent compilation of meteoric waters with $\delta'^{18}O$ greater than –20‰ that reflect temperate and tropical conditions ($\delta'^{17}O = 0.52654*\delta'^{18}O\ (\pm\ 0.00036) + 0.014\ (\pm\ 0.003)$; Sharp et al. 2018). The similarity of these best-fit lines suggests that the triple oxygen meteoric water line from non-polar regions has a slope ~0.5265. Combining all the available water data collected poleward of 60˚N and 60˚S, the best-fit $\delta'^{18}O$–$\delta'^{17}O$ line is:

$$\delta'^{17}O = 0.5285*\delta'^{18}O\ (\pm\ 0.00005) + 0.0450\ (\pm\ 0.0024‰). \quad \text{Eq. 5.15}$$

We include all sample types in Equation 5.15 because most high latitude triple oxygen isotope data are from Antarctica where there are very few flowing surface waters and almost no liquid precipitation. Differences between Equations 5.14 and 5.15 and the clear curvature in $\delta'^{18}O$–$\Delta'^{17}O$ plots of the global compilation (Fig 3b) demonstrate that triple oxygen isotopes do not fit a single, global meteoric water line. Instead, we suggest that $\delta'^{17}O$ and $\delta'^{18}O$ data should be considered relative to meteoric water lines from temperate and tropical (Equation 5.14) and polar (Equation 5.15) regions separately.

However, complete and proper establishment of triple oxygen isotope meteoric water lines will require additional data. Equations 5.14 and 5.15 are built from only 102 and 506 samples respectively, far fewer than the tens of thousands of $\delta^{18}O$ and $\delta^{2}H$ observations that went into the oxygen-hydrogen global meteoric water line (Craig, 1961; Dansgaard, 1964; Kendall and Coplen, 2001; Rozanski et al., 1993). Future hydrologic triple oxygen isotope studies should focus on surface waters and monthly precipitation collections and should evaluate these meteoric water lines as more data become available.

5.6.3 How does changing the value of λ_{ref} affect $\Delta'^{17}O$?

Although $\delta'^{17}O$ and $\delta'^{18}O$ data from our compilation of global waters do not fit a single line, it is critical that all $\Delta'^{17}O$ values are reported from the same reference frame (using the same value of λ_{ref}). Different values of λ_{ref} can complicate data comparisons (e.g., Luz and Barkan, 2010; Pack and Herwartz, 2014), especially when comparing different materials (e.g., water and mineral). Therefore, we recommend the use of 0.528 for λ_{ref} in all triple oxygen isotope studies, as recommended by others (e.g., Sharp et al., 2018). This value maintains consistency with previous work (Table 5.2) and has mechanistic significance because it is similar to the value of $\lambda_{Rayleigh}$ (Table 5.6).

However, it is very important to consider the value of λ_{ref}, especially because the triple oxygen isotope regression slope in in temperate and tropical regions (Equation 5.14) differs from the slope in polar regions (Equation 5.15). When a single value of λ_{ref} is used (as is recommended), differences between empirical $\delta'^{18}O$–$\delta'^{17}O$ slopes can produce latitudinal $\Delta'^{17}O$ variation that results from a calculation artifact, not hydrologic processes. Here, we refer to observed $\delta'^{18}O$–$\delta'^{17}O$ slopes as λ_{obs} and explore the $\Delta'^{17}O$ variation artifacts that result when λ_{ref} and λ_{obs} differ.

When λ_{obs} is equal to λ_{ref} (e.g., Rayleigh distillation), $\delta'^{18}O$ and $\delta'^{17}O$ fractionate along a line parallel to λ_{ref} and $\Delta'^{17}O$ remains constant (Figures 5.3a, 5.12, and 5.14a). More commonly, however, λ_{obs} deviates from λ_{ref} (Table 5.7) and results in systematic $\Delta'^{17}O$ bias (Figure 5.14). Figure 5.14b shows the residual between $\Delta'^{17}O$ values calculated with λ_{ref} equal to 0.528 ($\Delta'^{17}O_{0.528}$) and $\Delta'^{17}O$ values calculated with λ_{obs}, where λ_{obs} is not equal to 0.528. Positive residuals indicate that $\Delta'^{17}O_{0.528}$ values are biased low and negative residuals indicate $\Delta'^{17}O_{0.528}$ values are biased high (Figures 5.14c and 5.14d). The $\Delta'^{17}O$ residual increases as $\delta'^{18}O$ (or $\delta'^{17}O$) deviate from 0‰. Datasets with λ_{obs} greater than λ_{ref} are only observed in polar regions so no isotope data are observed in the upper right-hand quadrant in Figure 5.14b. Similarly, no very low $\delta'^{18}O$ ($< \sim -30$‰) data are observed in the upper left-hand quadrant in Figure 5.14b because datasets with λ_{obs} less than λ_{ref} are generally from mid-latitude and tropical regions and tend not to have very low $\delta'^{18}O$ values. We recommend that authors report $\Delta'^{17}O$ values with λ_{ref} equal to 0.528 and also recalculate $\Delta'^{17}O$ values with other values of λ_{ref} to further explore explanations for observed isotope variability (e.g., Uechi and Uemura, 2019).

Differences between λ_{obs} and λ_{ref} need not always be a complication, however. In fact, values of λ_{obs} contain important information about water cycling and hydrologic processes. In general, λ_{obs} values are lower (closer to θ_{diff}) when kinetic processes dominate isotopic compositions and higher (closer to θ_{eq}) when equilibrium fractionation controls isotopic compositions (Table 5.7). Accordingly, low λ_{obs} values ($< \sim 0.525$) are typically associated with evaporated waters (e.g., λ_{plant}, Table 5.7). Very high λ_{obs} values (greater than 0.530) have been observed in ice among samples from the Vostok ice core (Landais et al., 2012a, 2008), and are likely related to a combination of humidity and wind speed conditions at the moisture source and other kinetic effects during condensation under very cold supersaturated conditions (Landais et al., 2008; Miller, 2018).

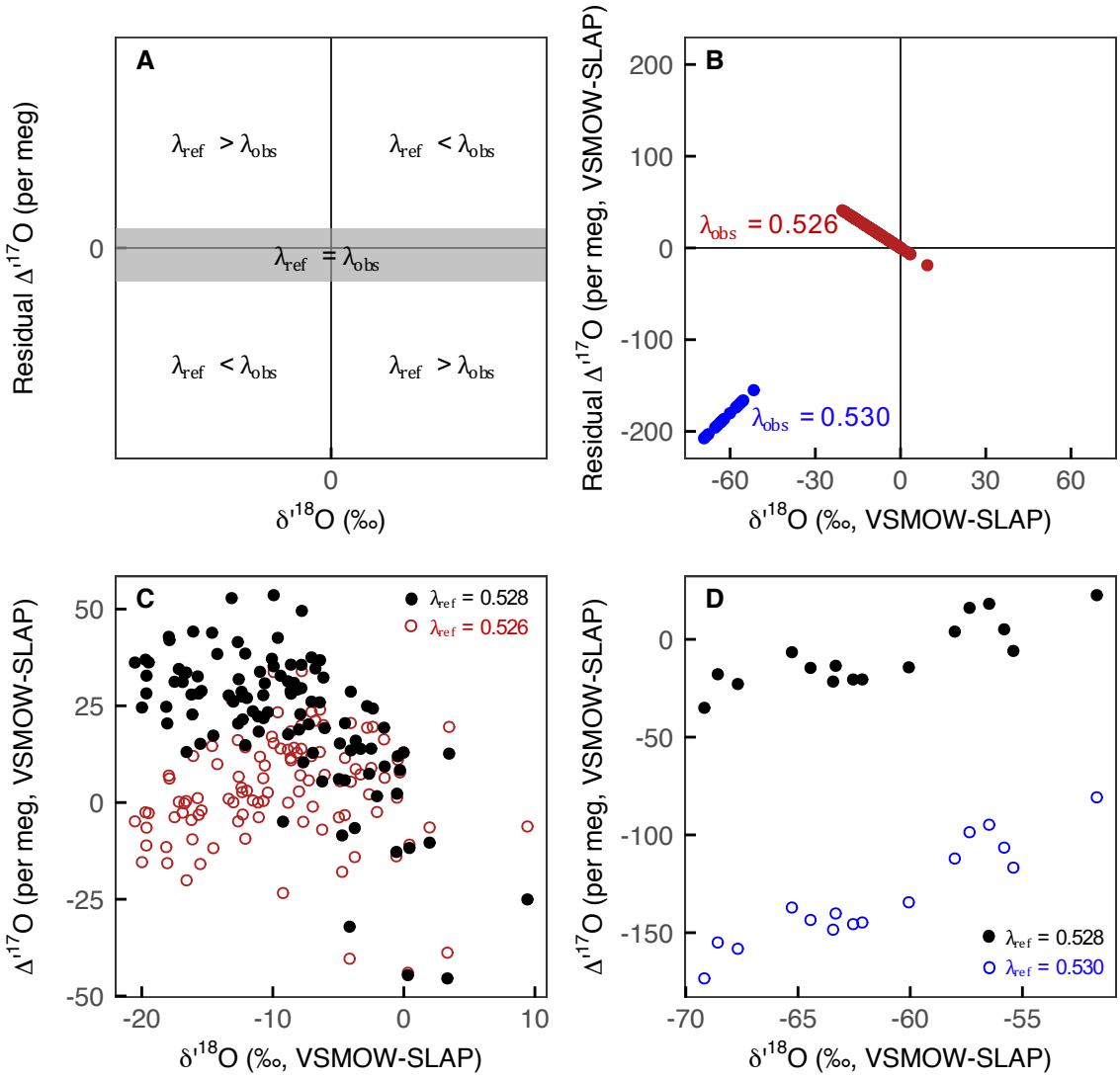

Figure 5.14 Schematic (A) and observations (B-D) showing the effect of reference slopes on $\Delta'^{17}O$ values. In each panel, λ_{ref} is equal to 0.528 and λ_{obs} is a theoretical (A) or observed (B-D) slope. Color (red and blue) distinguish datasets with different λ_{obs}. Data in red (λ_{obs} = 0.526) are from the surface water dataset newly compiled in this paper; data in blue (λ_{obs} = 0.530) are replotted from Landais et al. (2012b). In (B), the residual $\Delta'^{17}O$ is the difference between $\Delta'^{17}O_{0.528}$ and $\Delta'^{17}O_{\lambda obs}$ and is a linear function of $\delta'^{18}O$. Plots (C) and (D) show the effects on choice of λ_{ref} on $\Delta'^{17}O$ values. In these plots, $\Delta'^{17}O$ is calculated with λ_{ref} equal to 0.528 (filled black circles) and $\Delta'^{17}O$ calculated with (C) λ_{ref} equal to 0.526 (open red circles) or (D) λ_{ref} equal to 0.530 (open blue circles). Note that every panel has different axes.

Table 5.7 Observed λ (λ_{obs}) by water type. See Table 5.2 for references.

Sample subset	λ_{obs} ± standard error
All data	0.5276 ± 0.00006
Luz and Barkan (2010)	0.5282 ± 0.0003
Plant water	0.5188 ± 0.0003
Precipitation	0.5255 ± 0.0003
Ocean	0.528 ± 0.001
Snow and ice	0.5285 ± 0.00006
Surface and subsurface	0.5259 ± 0.0001

5.7 Analytical methods and considerations

5.7.1 Analytical methods

Triple oxygen isotope ratios are measured with dual inlet isotope ratio mass spectrometry or laser absorption spectrometry (Table 5.8). With careful analysis, both methods can achieve high quality $^{17}O/^{16}O$ measurements and similar (~10 per meg) precision for the $\Delta'^{17}O$ parameter. Typically, triple oxygen isotope data are measured in analytical sessions and data corrections (VSMOW-SLAP normalization, drift, etc.) are applied over a full session (Thompson, 2012; Werner and Brand, 2001). For IRMS systems, an analytical session is defined for each reactor (~200 analyses) and lasts approximately 2-4 weeks of near-constant analysis; for laser-based systems, an analytical session is typically defined as a batch or tray of samples or a 'calibration window' as in Schauer et al. (2016) that can span a few days to a few months.

Table 5.8 Water triple oxygen isotope analysis methods.

	IRMS	Picarro	Los Gatos Research (LGR)
Analysis method	Dual-inlet isotope ratio mass spectrometry (IRMS)	Cavity ring-down spectroscopy (CRDS, laser-based)	Cavity-enhanced laser absorption spectroscopy
Instrument	Various (Delta Plus, MAT 253, Nu Perspective)	L2140-i	Triple Water Isotope Analyzer (TWIA)
Sample preparation	CoF_3 reaction	$H_2O_{(l)} \rightarrow H_2O_{(g)}$	$H_2O_{(l)} \rightarrow H_2O_{(g)}$
Analyte	O_2 gas	Water vapor	Water vapor
Analysis time	2 to 3 hours	1.5 to 3 hours	< 1 hour to 7+ hours
$\Delta'^{17}O$ precision	~ 10 per meg	< 8 per meg	~ 10 per meg
Lab footprint	10s m^2	1-2 m^2	1-2 m^2
Method development	Barkan and Luz, 2005	Steig et al., 2014; Schauer et al., 2016	Berman et al., 2013

5.7.1.1 Dual inlet isotope ratio mass spectrometry

The IRMS cobalt(III) fluoride method was first described by Baker et al. (2002) and was later modified by Barkan and Luz (2005) to improve the precision of $\delta^{17}O$ and $\delta^{18}O$ measurements. In this process, water is fluorinated to convert liquid water to oxygen gas:

$$2H_2O_{(l)} + 4CoF_{3(s)} \rightarrow O_{2(g)} + 4HF_{(g)} + 4CoF_{2(s)}. \quad \text{Eq. 5.16}$$

Following fluorination, O_2 gas passes through a series of traps and molecular sieves to remove reaction byproducts and capture the purified sample. Triple oxygen isotope ratios are measured on O_2 gas using Thermo-Finnigan Delta Plus (e.g., Luz and Barkan, 2010), Thermo-Finnigan 253 (e.g., Schoenemann et al., 2014), or Nu Perspective (this study) mass spectrometers. In total, a measurement takes ~3 hours and samples are typically analyzed twice. Our methods and IRMS workflow are described in Section 5.8.

5.7.1.2 Laser absorption spectrometry

Because the fluorination and IRMS methods are complex and require significant laboratory infrastructure (Section 5.8), there is interest in using cavity ring-down spectroscopy (Picarro Inc.) or cavity-enhanced laser absorption (Los Gatos Research, LGR) to measure triple oxygen isotope ratios. These laser absorption spectrometers can achieve similar $\Delta'^{17}O$ precision as IRMS techniques, have a smaller laboratory footprint, are cheaper and more portable than mass spectrometers, and simultaneously measure $\delta^{18}O$, $\delta^{17}O$, and $\delta^{2}H$ (Berman et al., 2013; Schauer et al., 2016; Steig et al., 2014). Laser absorption spectrometry may also be faster than the IRMS method because laser-based analyzers do not require complex sample conversion (liquid water to gaseous O_2) and the absorption analysis only takes a few minutes. However, high-quality laser absorption isotope data require many injections of the same sample, which can cumulatively take longer than a single IRMS analysis (Berman et al., 2013), and additional work is needed to directly compare $\delta^{18}O$, $\delta^{17}O$, and $\Delta'^{17}O$ data from laser-based and IRMS systems. An example of the workflow required to achieve ~10 per meg $\Delta'^{17}O$ precision on a Picarro water isotope analyzer is described in Schauer et al. (2016).

5.7.2 Analytical recommendations and best practices

5.7.2.1 VSMOW-SLAP normalization

We recommend that triple oxygen isotope compositions be normalized to the VSMOW-SLAP scale following the approach described by Schoenemann et al. (2013). We provide code (Supplement 5.3) and an example data file (Supplement 5.4) to show how to do this normalization. This normalization technique improves the accuracy of isotope measurements, simplifies inter-lab data comparisons (Brand and Coplen, 2001; Coplen, 1988; Gonfiantini, 1978; Meijer et al., 2000; Paul et al., 2007; Schoenemann et al., 2013), and corrects for analytical inconsistencies such as pressure-baseline offsets (Yeung et al., 2018).

At a minimum, VSMOW and SLAP should be measured the beginning and end of every analytical session. Ideally, VSMOW and SLAP should also be analyzed within each session because instrument nonlinearities can evolve through time. Necessary isotopic compositions of VSMOW, VSMOW2, SLAP, and SLAP2 are reported in Table 5.9. We recommend that $\delta^{17}O_{SLAP}$ (–29.6968‰) be calculated directly from the defined values of $\delta^{18}O_{SLAP}$ (–55.5‰), $\Delta'^{17}O_{SLAP}$ (0.00‰), and λ_{ref} (0.528) (Gonfiantini, 1978; Schoenemann et al., 2013) because this approach results in excellent inter-lab $\Delta'^{17}O$ reproducibility and mathematically is the same approach that most labs already use to correct $\delta^{18}O$ data (Berman et al., 2013; Kaiser, 2009; Schoenemann et al., 2013).

Table 5.9 Isotopic composition of common standards and reference waters.

	$\delta^{18}O$ (‰)	$\delta^{17}O$ (‰)	$\delta^{2}H$ (‰)	$\Delta'^{17}O$ (per meg)
VSMOW [a], VSMOW2[b]	0	0	0	0
SLAP[a], SLAP2[b]	–55.5	–29.6968[c]	–428.0	0
GISP	−24.78 ± 0.09[e]	–13.16 ± 0.05[c] –13.12 ± 0.05[d] –13.5 ± 0.3[f]	−189.7 ± 1.0[e]	22 ± 11[c] 23 ± 10[d] 24 ± 12[f]
USGS 45	–2.238 ± 0.011[e]	–1.19 ± 0.3[d] –1.1 ± 0.3[f]	–10.3 ± 0.4[e]	12 ± 1[d] 13 ± 7[f]
USGS 46	–29.80 ±0.03 [e]	–15.85 ± 0.02[d] –15.7 ± 0.2 [f]	–235.8 ± 0.7[e]	20 ± 2[d] 19 ± 11[f]
USGS 47	–19.80 ± 0.02[e]	–10.47 ± 0.02[d] –10.4 ± 0.4[f]	–150.2 ± 0.5[e]	40 ± 1[d] 32 ± 9[f]
USGS 48	–2.224 ± 0.012[e]	–1.15 ± 0.01[d] –1.1 ± 0.2[f]	–2.0 ± 0.4[e]	26 ± 3[d] 31 ± 6[f]
USGS 49	–50.55 ± 0.04[e]	–27.8 ± 0.5[f]	–394.7 ± 0.4[e]	13 ± 8[f]
USGS 50	4.95 ± 0.02[e]	2.7 ± 0.2[f]	32.8 ± 0.4[e]	–10 ± 7[f]

Notes:
All isotopic data are normalized to the VSMOW-SLAP scale.
a) Gonfiantini, 1978; Barkan and Luz, 2005
b) Lin et al., 2010
c) Schoenemann et al., 2013
d) Berman et al., 2013 (isotopic data are weighted by the inverse of precision; uncertainties are the averages of three experimental methods weighted by the number of measurements)
e) USGS Reports of Stable Isotopic Composition Reference Materials (uncertainty is the 95% confidence interval)
f) this study (uncertainty is one unweighted standard deviation). The $\Delta'^{17}O$ of USGS47 reported in this study is substantially lower than the value from Berman et al. (2013). Our measured $\delta^{18}O$ and $\delta^{17}O$ values are nearly identical to the accepted (USGS) or previously published (Berman et al., 2013) values, and we do not have a compelling analytical explanation for this one low $\Delta'^{17}O$ value.

5.7.2.2 Secondary reference standards

We recommend regular analysis of commercially available secondary water standards (e.g., GISP and USGS reference waters, Table 5.9) to ensure proper calibration to the VSMOW-SLAP scale, confirm the accuracy of isotope ratio measurements, and monitor analytical drift. The $\delta^{18}O$ and $\delta^{2}H$ values of GISP and USGS reference water are readily available (Araguas-Araguas and Rozanski, 1995; Brand et al., 2014; Gonfiantini, 1984); presently, values of $\delta^{17}O$ and $\Delta'^{17}O$ are only reported by individual laboratories.

In our experience, ~5-10% of samples within an analytical session should be secondary reference waters. This proportion is necessary for a meaningful assessment of the accuracy and precision of data, although more USGS and/or GISP analyses may be necessary when unknown sample waters span a large (> 10‰) range in $\delta^{18}O$ or d-excess. Secondary reference analyses should be distributed evenly throughout every analytical session to monitor instrument drift.

Finally, the isotopic composition of standards and reference waters should bracket the expected isotopic composition of unknowns. This is typically not an issue for $\delta^{18}O$, $\delta^{17}O$, and $\delta^{2}H$ because USGS reference waters span the common range of natural waters (Figures 5.4a and 5.4c, Table 5.9). However, the range of $\Delta'^{17}O$ and d-excess of standards and reference waters (Table 5.9) is much smaller than observed $\Delta'^{17}O$ (Figure 5.3b) and d-excess (Figure 5.3e) variability. Therefore, we recommend that laboratories develop additional reference waters to expand isotopic ranges. New reference waters can be developed from evaporated snow (low $\delta^{18}O$, $\Delta'^{17}O$, and d-excess) or creative collections of combustion water (e.g., condensate from a home furnace) that have very low (< –350 per meg) $\Delta'^{17}O$ values that inherit oxygen from atmospheric O_2 ($\Delta'^{17}O \sim =$ –400 to –500 per meg) (Barkan and Luz, 2011; Wostbrock et al., 2020; Yeung et al., 2012; Young et al., 2014).

5.7.2.3 Analytical sanity checks

We recommend laboratories perform evaporation experiments and develop mixing curves to monitor analytical performance. Laboratory-controlled evaporation and mixing experiments can result in substantial isotopic variation (far above analytical precision) and are well-predicted by simple isotope models (Equations 5.6 and 5.7). These quality checks are relatively simple and should be included as part of regular analytical maintenance and upkeep. Templates to develop mixing curves and evaporation experiments are provided in Supplements 5.2 and 5.5, respectively.

5.7.2.4 How to calculate and report $\Delta'^{17}O$ precision

Typically, reported precision for $\Delta'^{17}O$ is approximately 10 per meg, orders of magnitude better than analytical errors in $\delta^{17}O$ and $\delta^{18}O$ (~0.1 to 1‰). One major source of analytical error in both IRMS and laser absorption spectrometers is physical fractionation of water vapor during sample handling (i.e., injection, sample conversion, and transport of the vapor to optical cavities or through O_2 prep lines). However, this fractionation is presumably mass-dependent such that the

errors for $\delta^{17}O$ and $\delta^{18}O$ are correlated and vary along a line with a slope close to 0.528, resulting in very precise $\Delta'^{17}O$ measurements (Barkan and Luz, 2007; Landais et al., 2006; Schoenemann et al., 2013). In other words, if $\delta^{17}O$ and $\delta^{18}O$ vary during sample handing, they do so along a line that is parallel to λ_{ref} and $\Delta'^{17}O$ errors are largely independent of the precision for $\delta^{17}O$ and $\delta^{18}O$. Errors on analyses made by laser absorption spectrometers do not cancel in exactly the same way in because the $H_2{}^{17}O$ and $H_2{}^{18}O$ absorption measurements do not necessarily covary. Instead, laser absorption spectrometers achieve low $\Delta'^{17}O$ error from incredibly precise $\delta^{17}O$ and $\delta^{18}O$ measurements. Using simple error propagation, the precision of $\delta^{17}O$ and $\delta^{18}O$ measurements must be better than 0.007‰ (assuming $\delta^{17}O$ and $\delta^{18}O$ errors are uncorrelated) in order to achieve 10 per meg precision on $\Delta'^{17}O$. Achieving such high precision can be challenging and frequently requires many (> 20) repeat analyses (e.g., Berman et al., 2013). If errors on $\delta^{17}O$ and $\delta^{18}O$ are not independently precise enough to get 10 per meg precision on $\Delta'^{17}O$, authors must show that errors in $\delta^{17}O$ and $\delta^{18}O$ values are correlated.

Currently, there is no universal way to calculate and report analytical triple oxygen isotope error. We recommend that authors calculate $\delta^{18}O$, $\delta^{17}O$, and $\Delta'^{17}O$ precision from secondary reference standards and report the pooled standard deviation to express to external reproducibility of replicate measurements. The pooled standard deviation (σ_p) is:

$$\sigma_p = \sqrt{\frac{\sum_{i=1}^{k}(n_i-1)s_i^2}{\sum_{i=1}^{k}(n_i-1)}} \qquad \text{Eq. 5.17}$$

where s_i is the standard deviation and n_i is the number of replicate measurements of the i-th sample and k is the total number of samples. In addition, we recommend that authors also report one standard deviation for replicate analyses of unknowns. It is important to report both measures of uncertainty because the pooled standard deviation represents the performance of the analytical system while the standard deviation of individual analyses represents error on each unknown.

5.7.2.5 Memory effects

Regardless of analytical method (IRMS or laser absorption spectroscopy), we recommend analyzing samples in order of increasing or decreasing $\delta^{18}O$ and using preparatory injections to minimize memory effects. As needed, USGS reference waters can help bridge large $\delta^{18}O$ gaps

between sequential samples. In Picarro and LGR analyzers, the isotopic compositions of water from preparatory injections are analyzed but the data are typically ignored (e.g., Bailey et al., 2013; Berman et al., 2013; Schauer et al., 2016; Steig et al., 2014; Tian et al., 2018). In IRMS systems, memory effects are concentrated in the CoF_3 reactor (Barkan and Luz, 2005) and can be cleared with preparatory injections. Product gases (O_2 and HF) from these injections should be pumped away without purification or analysis.

In our reactors at the University of Michigan, we use one preparatory injection when sequential $\delta^{18}O$ values are within 5‰, and two preparatory injections when sequential $\delta^{18}O$ values differ by more than 5‰. In our experience, typically no more than two preparatory injections are necessary to clear IRMS memory effects, but we encourage each lab to independently determine best practices to minimize memory effects from individual reactors.

5.7.2.6 Reporting recommendations

First and foremost, triple oxygen isotope data must be reported to three decimal places to facilitate data comparisons and enable $\Delta'^{17}O$ to be recalculated in various reference frames. Data can be reported as individual $\delta^{17}O$ and individual $\delta^{18}O$, both to three decimal places, or as average $\delta^{18}O$ and average $\Delta'^{17}O$, both to three decimal places. It is insufficient to provide average $\delta^{18}O$ and average $\delta^{17}O$ even when both are reported to three decimal places. Typically, these data are reported in supplementary files, but this is left to the discretion of each author. Supplements 5.6, 5.7, and 5.8 are included as templates to report unknown, standard, and reference water data.

Following precedent (Barkan and Luz, 2007; Luz and Barkan, 2010), we recommend that all triple oxygen isotope studies use a value of 0.528 for λ_{ref} and clearly report the value of λ_{ref} used. A value of 0.528 for λ_{ref} maintains consistency with earlier triple oxygen isotope studies (Table 5.2), clearly distinguishes equilibrium ($\theta_{eq} = 0.529$) and kinetic ($\theta_{diff} = 0.518$) fractionation effects (Figure 5.13), and removes most $\Delta'^{17}O$ effects from Rayleigh distillation.

Finally, we recommend that triple oxygen water isotope studies include both $\Delta'^{17}O$ and d-excess data when possible. Combining $\Delta'^{17}O$ and d-excess can reveal information about hydrologic cycling (Section 5.5) and the parameters (e.g., α, δ, and λ values) that drive isotope fractionation. Adding $\delta^{2}H$ measurements is straightforward for studies that use laser absorption spectrometers and is a worthwhile additional measurement for those that use IRMS techniques.

5.7.2.7 Sample selection

We recommend using existing $\delta^{18}O$ and d-excess data to select samples for triple oxygen isotope analysis. For example, at the University of Michigan, we use a Picarro water isotope analyzer to measure $\delta^{18}O$ and $\delta^{2}H$, and then systematically select a subset of samples for IRMS $\delta^{17}O$ and $\delta^{18}O$ analysis. Additional details on this process and our analytical methods are in Section 5.8.1. Initial $\delta^{18}O$ data should also be used to determine the requisite number of preparatory injections and arrange analytical order to minimize memory effects for triple oxygen isotope analysis.

Sample selection should also consider the expected range of $\Delta'^{17}O$ variation and be sure to select samples that are likely to result in statistically significant $\Delta'^{17}O$ variation (i.e., greater than ~10 per meg). For example, assuming non-steady-state evaporation, the maximum possible slope between d-excess and $\Delta'^{17}O$ is ~2 per meg $‰^{-1}$ (e.g., Barkan and Luz, 2007; Li et al., 2015). Therefore, statistically significant $\Delta'^{17}O$ variation is most probable in datasets that have >5‰ range in d-excess. Datasets with only a few per mil variability in $\delta^{18}O$ and/or d-excess typically result in $\Delta'^{17}O$ variation within analytical precision. We encourage researchers to explore the expected $\Delta'^{17}O$ variability on a case-by-case basis with code provided in Supplement 5.1.

5.8 New surface water data

As part of this review, we report a new, near-global dataset of surface water triple oxygen isotope data (Figures 5.2–5.4). Here, we explain our sample collection, analytical methods, and a brief summary of our results.

5.8.1 Sample collection and isotope analysis

We organized a crowdsource effort to collect over 1,600 water samples from around the world for isotope analysis. Water was collected in 2 dram glass vials (Ace Glass 8779-20) or 20 ml HDPE plastic vials (Wheaton 986716). Samples collected in plastic vials were transferred into glass vials within a few months of collection so we do not expect any fractionation with the sample containers (Spangenberg, 2012). Vials were capped with PolyCone caps to prevent leaks or evaporation, filtered (0.45 μm, VWR 28145-493), and then stored in a dark environment before isotope analysis.

We used a Picarro L2130-i cavity ringdown spectrometer with a high-precision vaporizer (A0211) and attached autosampler to measure the $\delta^{18}O$ and $\delta^{2}H$ values of every freshwater sample collected (over 1500 samples). The L2130-i does not measure $\delta^{17}O$. Each sample was analyzed nine times; we use the average of the last four analyses. We used the Picarro ChemCorrect software to monitor samples for organic contamination and normalized measured $\delta^{18}O$ and $\delta^{2}H$ to the VSMOW-SLAP scale with USGS reference waters (USGS45, 46, 49, and 50) and four in-house liquid standards. Isotopic drift and precision were monitored using the Picarro L2130-i Drift and Precision Test worksheet, which is available for download from the Picarro community support forum (https://www.picarro.com/support/community). Precision of repeat analyses of deionized water was better than 0.1‰ and 0.3‰ for $\delta^{18}O$ and $\delta^{2}H$, respectively.

Using the Picarro data, we selected 104 surface waters (rivers and lakes) from the crowdsourced dataset for triple oxygen isotope analysis. Samples were selected from 14 regions across 6 continents. To ensure a representative range of isotopic compositions, we selected samples that span 30‰ in $\delta^{18}O$ and 50‰ in d-excess.

Triple oxygen isotopes were analyzed with a dual inlet Nu Perspective isotope ratio mass spectrometer at the University of Michigan. We convert liquid water to O_2 gas with cobalt(III) fluoride and a custom-built fluorination line based on the method outlined by Baker et al. (2002) and refined by Luz and Barkan (2005). Our analytical methods have been described previously (Li et al., 2017, 2015; Passey et al., 2014), although these measurements were made with a different mass spectrometer (Thermo 253) and fluorination line previously at Johns Hopkins University. Our methods have changed only slightly since the laboratory was relocated to the University of Michigan.

Briefly, we inject ~2 μL of water through a septum port into a 360-370 ˚C CoF_3 nickel reactor to convert liquid water to O_2 gas and gaseous hydrofluoric acid (HF) (Equation 5.16). Helium gas carries O_2 gas through a nickel trap immersed in liquid nitrogen (−196 ˚C) to remove HF. We further purify the O_2 gas by passing it through a custom-built stainless steel column (~ 1 m, 1/8″ OD) that is packed with a 5 Å molecular sieve (Strem Chemicals, CAS#69912-79-4) and immersed in a methanol/dry ice slush (−80 ˚C). After purification, we collect the O_2 gas in a −196 ˚C trap that is packed with a 5 Å molecular sieve. This process takes ~ 15 minutes. After the O_2 is collected, helium gas is pumped away (14 minutes), liquid nitrogen is replaced by a −80 ˚C

methanol/dry ice slush, and the O_2 is transferred to a −180 ˚C cold finger (12 minutes) that is part of the dual inlet system of the Nu mass spectrometer. The cold finger has a few pellets of 5 Å molecular sieve to ensure the O_2 gas remains in the cold finger. Finally, the cold finger is heated (9 minutes) to 90 ˚C to release O_2 from the molecular sieve, and the sample is introduced to the mass spectrometer. In total, sample preparation takes just over an hour.

The O_2 gas is analyzed in dual inlet mode for *m/z* 32, 33, and 34. To minimize analytical error, each analysis consists of 40 cycles during which the ratio of sample to reference gas (99.999% compressed oxygen, with approximate values of $\delta^{17}O_{VSMOW}$ = 10.3‰, $\delta^{18}O_{VSMOW}$ = 20.3‰) is determined. Each cycle consists of 50 seconds of integration time on the sample gas or reference gas and 20 seconds of idle time between integrations. Resistances on the *m/z* 32, 33, and 34 Faraday cups are 2×10^8, 3×10^{11}, and 1×10^{11} Ω, respectively. Analysis in the mass spectrometer takes approximately two hours.

We normalize triple oxygen isotope data to the VSMOW-SLAP scale following the approach described by Schoenemann et al. (2013). We analyze VSMOW2 and SLAP2 in at least triplicate at the beginning, end, and middle of every reactor. The $\delta^{18}O$ and $\delta^{17}O$ values of VSMOW2 and SLAP2 are indistinguishable from those of VSMOW and SLAP (Lin et al., 2010). In addition, we routinely analyze six USGS reference waters (USGS45, 46, 47, 48, 49, 50) to determine long-term, external precision of our system, to monitor isotopic drift, and to ensure analytical accuracy. In our lab, the pooled standard deviation of replicate triple oxygen isotope analyses of USGS reference waters is 0.3‰ for $\delta^{17}O$, 0.5‰ for $\delta^{18}O$, and 8 per meg for $\Delta'^{17}O$.

5.8.2 Results

New triple oxygen isotope data are reported in Supplements 5.6-5.8 and plotted in Figures 5.2–5.4. For the full dataset, $\delta^{18}O$ ranges from –20.3 to 9.6‰, d-excess ranges from –31.8 to 21.1‰, and $\Delta'^{17}O$ ranges from –45 to 54 per meg. Most isotope compositions cluster between –14 to –5‰, 3 to 13‰, and 14 to 33 per meg ($\delta^{18}O$, d-excess, and $\Delta'^{17}O$, respectively), but have high standard deviations (6.1‰, 11.1‰, and 18 per meg, respectively) and are poorly described by average values. In this dataset, $\Delta'^{17}O$ values are moderately to strongly positively correlated with d-excess (r = 0.73) and are moderately to strongly negatively correlated with $\delta'^{18}O$ (r = –0.64). Both $\Delta'^{17}O$ and d-excess are very weakly correlated or uncorrelated with latitude, longitude, elevation, mean annual temperature, mean annual precipitation, and mean annual relative humidity

(all $r < \pm 0.3$). In general, rivers have lower $\delta^{18}O$, higher d-excess, and higher $\Delta'^{17}O$ than lakes, although some rivers and lakes in arid regions are isotopically similar (Supplement 5.6). The slope (λ) of the $\delta'^{18}O$–$\delta'^{17}O$ regression line through this dataset is 0.5260 ± 0.0002. Climate data (mean annual precipitation, temperature, and relative humidity) from the sampling locations of the new surface waters were extracted from the CRU 2.0 dataset (New et al., 2002) and are reported in Supplement 5.6.

5.9 Applications and directions of future work

5.9.1 Modern applications

Studies of $\Delta'^{17}O$ variation in the hydrosphere have two primary applications: as a complement to d-excess and as an analog to the geologic record. In modern hydrologic studies, $\Delta'^{17}O$ and d-excess can provide complementary information about moisture transport and moisture source conditions because $\Delta'^{17}O$ is less sensitive to temperature than d-excess (Figure 5.13). For example, a combination of $\Delta'^{17}O$ and d-excess can decouple equilibrium and kinetic fractionation effects and reconstruct both temperature and relative humidity at a moisture source (e.g., Landais et al., 2012; Uechi and Uemura, 2019).

It is also important that we understand modern meteoric water $\Delta'^{17}O$ variability in order to expand its use in hydrologic applications and to interpret $\Delta'^{17}O$ data in the geologic record. Currently, a number of important questions about the co-variability of $\delta^{18}O$, $\Delta'^{17}O$, and d-excess in modern meteoric waters remain, and should be the focus of future work. First, future hydrologic $\Delta'^{17}O$ studies should focus on rivers and/or amount-weighted monthly precipitation to evaluate the slopes and intercepts of $\delta'^{18}O$–$\delta'^{17}O$ regression lines across latitudinal gradients and a range of climate conditions. Second, a mechanistic explanation of the seasonal precipitation $\Delta'^{17}O$ variation (higher $\Delta'^{17}O$ in the winter, lower $\Delta'^{17}O$ in the summer) is still unknown. This cycle has been observed in multiple regions but is not fully explained (Affolter et al., 2015; Li et al., 2015; Tian et al., 2018; Uechi and Uemura, 2019). Third, follow-up work is necessary in lake systems to constrain the parameters in isotopic evaporation models (Equations 5.6 and 5.7). To date, most lake water triple oxygen isotope studies have focused on $\Delta'^{17}O$ in hyperarid climates where lakes are very evaporated (e.g., western US (Passey and Ji, 2019), Atacama Desert, and Sistant Basin in eastern Iran (Surma et al., 2018, 2015, respectively)), but additional lake water $\Delta'^{17}O$ observations

from less evaporated temperate and tropical regions would be helpful. Fourth, we encourage triple oxygen isotope data-model comparisons. Many state of the art isotope-enabled general circulation models now include $\delta^{17}O$ (e.g., Brady et al., 2019), but modeling kinetic fractionation effects is still a challenge and modeled $\Delta'^{17}O$ estimates must be evaluated with modern observations (Risi et al., 2013; Schoenemann and Steig, 2016; Wong et al., 2017).

Finally, future modern triple oxygen isotope studies should expand to include water types that have not yet been studied or are still poorly understood. These include, but are not limited to, water vapor; soil water, which frequently undergoes extensive fractionation in the upper soil layers (Barnes and Allison, 1984); groundwater, which can integrate information about seasonal recharge, local and regional water tables, and paleoclimate conditions (Jasechko, 2019); and seawater. Generally it is assumed that the isotopic composition of seawater is invariant and similar to that of SMOW (Luz and Barkan, 2010; Zakharov et al., 2019), but this idea is largely untested for triple oxygen isotopes.

5.9.2 Paleoclimate and geologic applications

The most appealing application of triple oxygen isotopes in the geologic record is the ability to track aridity and constrain the isotopic effects of evaporation. This has long been a challenge in isotope geochemistry because very few minerals contain both oxygen and hydrogen, and there is no d-excess equivalent in geologic materials. Now, the addition of $\Delta'^{17}O$ to $\delta^{18}O$ records can help identify effects of evaporation and aridity (Alexandre et al., 2019; Gázquez et al., 2018; Passey et al., 2014; Surma et al., 2018), add constraints on diagenesis and formation conditions of sedimentary records (Levin et al., 2014), and reconstruct the isotopic composition of ancient meteoric and ocean waters (e.g., Gehler et al., 2011; Herwartz et al., 2015; Liljestrand et al., 2020; Passey and Ji, 2019). For example, $\Delta'^{17}O$ and 'clumped isotopes' (Δ_{47}) in lake carbonates can be used to reconstruct the isotopic composition of unevaporated paleo-water (Passey and Ji, 2019). Similarly, $\Delta'^{17}O$ from gypsum hydration water offers new insights into changes in relative humidity across glacial-interglacial cycles that are impossible to discern with records of $\delta^{18}O$ alone (Gázquez et al., 2018).

To date, $\Delta'^{17}O$ has been measured in carbonates, sulfates, phosphates, nitrates, silicates, and oxides to answer an array of paleoclimate questions (Bao et al., 2016). Additional work is still needed to calibrate solid $\Delta'^{17}O$ standards (Barkan et al., 2019; Wostbrock et al., 2020), define

fractionation factors (Bergel et al., 2020; Cao and Liu, 2011; Guo and Zhou, 2019; Sharp et al., 2016; Voarintsoa et al., 2020), and refine analytical methods (Affek and Barkan, 2018; Fosu et al., 2020; Sakai et al., 2017), but the potential of triple oxygen isotopes to separate equilibrium and kinetic fractionation effects in paleoclimate applications is immense. Additional work to understand the modern variation in $\Delta'^{17}O$ in waters will also help expand triple oxygen isotopes as tool for paleoclimate reconstructions.

5.10 Summary

Measurements of small, mass-dependent triple oxygen isotope variations have come a long way in less than two decades. Deviations from a $\delta'^{18}O$–$\delta'^{17}O$ mass-dependent reference line (expressed as $\Delta'^{17}O$) that were once considered unimportant and too difficult to measure are now well characterized; these variations are statistically significant and explained by well-known equilibrium and kinetic fractionation effects. Values of $\Delta'^{17}O$ complement d-excess, can be used to reconstruct relative humidity at moisture sources and the isotopic composition of paleo-waters, and help discern isotopic effects of evaporation that are impossible to quantify with $\delta^{18}O$ alone.

In this review, we synthesize meteoric water isotope data to explain global variations of $\delta'^{18}O$, $\delta'^{17}O$, $\delta^{2}H$, $\Delta'^{17}O$, and d-excess. We explain the hydrologic processes that cause meteoric water $\Delta'^{17}O$ to vary, evaluate the established triple oxygen isotope global meteoric water line (Luz and Barkan, 2010), and present updated meteoric water lines (Equations 5.14 and 5.15) for polar or tropical and temperate regions. Although the slope of the meteoric water line for tropical and temperate waters deviates from 0.528, we recommend the continued use of 0.528 as λ_{ref} for all triple oxygen isotope studies. This value maintains consistency with earlier work, simplifies data comparisons, and is mechanistically useful because it is nearly identical to $\lambda_{Rayleigh}$. In addition, we recommend that all triple oxygen isotope studies normalize values of $\delta^{18}O$ and $\delta^{17}O$ to the VSMOW-SLAP scale, and encourage authors to include raw $\delta^{18}O$ and $\delta^{17}O$ data, reported to three decimal places, as supplementary material with every study. These analytical and reporting practices will streamline data comparisons and promote new understanding of triple oxygen isotope variability.

Currently only a handful of labs are able to make high quality $\Delta'^{17}O$ measurements, but small, portable laser absorption spectrometers are becoming popular and new datasets are rapidly emerging. Future triple oxygen isotope measurements should focus on surface waters and amount-

weighted monthly precipitation to continue to evaluate meteoric water lines. In addition, future isotope hydrology research should explore $\Delta'^{17}O$ variability in water vapor, ocean water, groundwater, and lakes to further trace modern water cycling and better reconstruct paleohydrological conditions. Taken together, modern meteoric water $\Delta'^{17}O$ variability serves as a baseline from which to answer an array of previously unquantifiable paleoclimate questions and offers new insights into modern water cycling.

Acknowledgements and funding

This work was supported by University of Michigan Rackham Predoctoral Fellowship support and Department of Earth and Environmental Sciences Turner Award (Aron), NSF Tectonics Program Award 1550101 (Poulsen), NSF-EAR Postdoctoral Fellowship Award 1725621 (Beverly), and start-up funds from the University of Michigan Department of Earth and Environmental Sciences (Levin, Passey). We thank Ryan Horwitz for assistant with water isotope analyses and the many individuals who participated in our crowdsourced sample collection.

5.11 References

Aemisegger, F., Pfahl, S., Sodemann, H., Lehner, I., Seneviratne, S.I., Wernli, H., 2014. Deuterium excess as a proxy for continental moisture recycling and plant transpiration. Atmos. Chem. Phys. 14, 4029–4054. https://doi.org/10.5194/acp-14-4029-2014

Affek, H.P., Barkan, E., 2018. A new method for high-precision measurements of $^{17}O/^{16}O$ ratios in H_2O. Rapid Commun. Mass Spectrom. 32, 2096–2097. https://doi.org/10.1002/rcm.8290

Affolter, S., Häuselmann, A.D., Fleitmann, D., Häuselmann, P., Leuenberger, M., 2015. Triple isotope (δD, $\delta^{17}O$, $\delta^{18}O$) study on precipitation, drip water and speleothem fluid inclusions for a Western Central European cave (NW Switzerland). Quat. Sci. Rev. 127, 73–89. https://doi.org/10.1016/j.quascirev.2015.08.030

Alexandre, A., Webb, E., Landais, A., Piel, C., Devidal, S., Sonzogni, C., Couapel, M., Mazur, J.-C., Pierre, M., Prié, F., Vallet-Coulomb, C., Roy, J., 2019. Effects of grass leaf anatomy, development and light/dark alternation on the triple oxygen isotope signature of leaf water and phytoliths: insights for a new proxy of continental atmospheric humidity. Biogeosciences 16, 4613–4625. https://doi.org/10.5194/bg-2019-73

Angert, A., Cappa, C.D., DePaolo, D.J., 2004. Kinetic ^{17}O effects in the hydrologic cycle: Indirect evidence and implications. Geochim. Cosmochim. Acta 68, 3487–3495. https://doi.org/10.1016/j.gca.2004.02.010

Araguas-Araguas, L., Rozanski, K., 1995. Interlaboratory comparison for deuterium and oxygen-

18 analysis of precipitation samples. Vienna.

Bailey, A., Toohey, D., Noone, D., 2013. Characterizing moisture exchange between the Hawaiian convective boundary layer and free troposphere using stable isotopes in water. J. Geophys. Res. Atmos. 118, 8208–8221. https://doi.org/10.1002/jgrd.50639

Baker, L., Franchi, I.A., Maynard, J., Wright, I.P., Pillinger, C.T., 2002. A Technique for the Determination of $^{18}O/^{16}O$ and $^{17}O/^{16}O$ Isotopic Ratios in Water from Small Liquid and Solid Samples. Anal. Chem. 74, 1665–1673. https://doi.org/10.1021/ac010509s

Bao, H., Cao, X., Hayles, J.A., 2016. Triple Oxygen Isotopes: Fundamental Relationships and Applications. Annu. Rev. Earth Planet. Sci. 44, 463–492. https://doi.org/10.1146/annurev-earth-060115-012340

Bao, H., Fairchild, I.J., Wynn, P.M., Spotl, C., 2009. Stretching the Envelope of Past Surface Environments: Neoproterozoic Glacial Lakes from Svalbard. Science (80-.). 323, 119–122.

Barkan, E., Affek, H., Luz, B., Bergel, S.J., Voarintsoa, N.R.G., Musan, I., 2019. Calibration of $\delta^{17}O$ and $^{17}O_{excess}$ values of three international standards: IAEA-603, NBS19 and NBS18. Rapid Commun. Mass Spectrom. 33, 737–740. https://doi.org/10.1002/rcm.8391

Barkan, E., Luz, B., 2011. The relationships among the three stable isotopes of oxygen in air, seawater and marine photosynthesis. Rapid Commun. Mass Spectrom. 25, 2367–2369. https://doi.org/10.1002/rcm.5125

Barkan, E., Luz, B., 2007. Diffusivity fractionations of $H_2{}^{16}O/H_2{}^{17}O$ and $H_2{}^{16}O/H_2{}^{18}O$ in air and their implications for isotope hydrology. Rapid Commun. Mass Spectrom. 21, 2999–3005. https://doi.org/10.1002/rcm.3180

Barkan, E., Luz, B., 2005. High precision measurements of $^{17}O/^{16}O$ and $^{18}O/^{16}O$ ratios in H_2O. Rapid Commun. Mass Spectrom. 19, 3737–3742. https://doi.org/10.1002/rcm.2250

Barnes, C.J., Allison, G.., 1984. The distribution of deuterium and ^{18}O in dry soils: 3. Theory for non-isothermal water movement. J. Hydrol. 74, 119–135. https://doi.org/10.1016/0022-1694(84)90144-6

Bergel, S.J., Barkan, E., Stein, M., Affek, H.P., 2020. Carbonate $^{17}O_{excess}$ as a paleo-hydrology proxy: Triple oxygen isotope fractionation between H_2O and biogenic aragonite, derived from freshwater mollusks. Geochim. Cosmochim. Acta. 275, 36–47. https://doi.org/10.1016/j.gca.2020.02.005

Berman, E.S.F., Levin, N.E., Landais, A., Li, S., Owano, T., 2013. Measurement of $\delta^{18}O$, $\delta^{17}O$, and ^{17}O-excess in Water by Off-Axis Integrated Cavity Output Spectroscopy and Isotope Ratio Mass Spectrometry. Anal. Chem. https://doi.org/10.1021/ac402366t

Bhattacharya, S.K., Savarino, J., Thiemens, M.H., 2000. A new class of oxygen isotopic

fractionation in photodissociation of carbon dioxide: Potential implications for atmospheres of Mars and Earth. Geophys. Res. Lett. 27, 1459–1462. https://doi.org/10.1029/1999GL010793

Blunier, T., Barnett, B., Bender, M.L., Hendricks, M.B., 2002. Biological oxygen productivity during the last 60,000 years from triple oxygen isotope measurements. Global Biogeochem. Cycles 16, 1–15. https://doi.org/10.1029/2001gb001460

Blunier, T., Bender, M.L., Barnett, B., Von Fischer, J.C., 2012. Planetary fertility during the past 400 ka based on the triple isotope composition of O_2 in trapped gases from the Vostok ice core. Clim. Past 8, 1509–1526. https://doi.org/10.5194/cp-8-1509-2012

Bowen, G.J., 2010. Isoscapes: Spatial Pattern in Isotopic Biogeochemistry. Annu. Rev. Earth Planet. Sci. 38, 161–187. https://doi.org/10.1146/annurev-earth-040809-152429

Bowen, G.J., Cai, Z., Fiorella, R.P., Putman, A.L., 2019. Isotopes in the Water Cycle: Regional- to Global-Scale Patterns and Applications. Annu. Rev. 47, 453–479. https://doi.org/10.1146/annurev-earth-053018- 060220

Bowen, G.J., Kennedy, C.D., Henne, P.D., Zhang, T., 2012. Footprint of recycled water subsidies downwind of Lake Michigan. Ecosphere 3, 1–16. https://doi.org/10.1890/ES12-00062.1

Brady, E., Stevenson, S., Bailey, D., Liu, Z., Noone, D., Nusbaumer, J., 2019. The Connected Isotopic Water Cycle in the Community Earth System Model Version 1. J. Adv. Model. Earth Syst. 11, 2547–2566. https://doi.org/10.1029/2019MS001663

Brand, W.A., Coplen, T.B., 2001. An interlaboratory study to test instrument performance of hydrogen dual-inlet isotope-ratio mass spectrometers. Fresenius J. Anal. Chem. 370, 358–362. https://doi.org/10.1007/s002160100814

Brand, W.A., Coplen, T.B., Vogl, J., Rosner, M., Prohaska, T., 2014. Assessment of international reference materials for isotope-ratio analysis (IUPAC technical report). Pure Appl. Chem. 86, 425–467. https://doi.org/10.1515/pac-2013-1023

Brooks, J.R., Barnard, H.R., Coulombe, R., McDonnell, J.J., 2010. Ecohydrologic separation of water between trees and streams in a Mediterranean climate. Nat. Geosci. 3, 100–104. https://doi.org/10.1038/NGEO722

Cao, X., Liu, Y., 2011. Equilibrium mass-dependent fractionation relationships for triple oxygen isotopes. Geochim. Cosmochim. Acta 75, 7435–7445. https://doi.org/10.1016/j.gca.2011.09.048

Cernusak, L.A., Barbour, M.M., Arndt, S.K., Cheesman, A.W., English, N.B., Feild, T.S., Helliker, B.R., Holloway-Phillips, M.M., Holtum, J.A.M., Kahmen, A., Mcinerney, F.A., Munksgaard, N.C., Simonin, K.A., Song, X., Stuart-Williams, H., West, J.B., Farquhar, G.D., 2016. Stable isotopes in leaf water of terrestrial plants. Plant Cell Environ. 39, 1087–1102.

https://doi.org/10.1111/pce.12703

Coplen, T.B., 1988. Normalization of oxygen and hydrogen isotope data. Chem. Geol. Isot. Geosci. Sect. 72, 293–297.

Craig, H., 1961. Isotopic Variations in Meteoric Waters. Science (80-.). 133, 1702–1703. https://doi.org/10.1126/science.133.3465.1702

Craig, H., Gordon, L.I., 1965. Deuterium and oxygen-18 variations in the ocean and the marine atmosphere, in: Tongiorgi, E. (Ed.), Proceedings of a Conference on Stable Isotopes in Oceanographic Studies and Paleotemperatures. Spoleto, Italy, pp. 9–130.

Criss, R.E., 1999. Principles of Stable Isotope Distribution. Oxford University Press, New York.

Criss, R.E., Farquhar, J., 2008. Abundance, Notation, and Fractionation of Light Stable Isotopes. Rev. Mineral. Geochemistry 68, 15–30. https://doi.org/10.2138/rmg.2008.68.3

Dansgaard, W., 1964. Stable isotopes in precipitation. Tellus 16, 436–468. https://doi.org/10.3402/tellusa.v16i4.8993

Dütsch, M., Pfahl, S., Sodemann, H., 2017. The impact of nonequilibrium and equilibrium fractionation on two different deuterium excess definitions. J. Geophys. Res. Atmos. 122, 12,732-12,746. https://doi.org/10.1002/2017JD027085

Farquhar, J., Thiemens, M.H., 2000. Oxygen cycle of the Martian atmosphere-regolith system: of secondary phases in Nakhla and Lafayette. J. Geophys. Res. 105, 991–997. https://doi.org/10.1029/1999je001194

Fosu, B.R., Subba, R., Peethambaran, R., Bhattacharya, S.K., Ghosh, P., 2020. Technical Note: Developments and Applications in Triple Oxygen Isotope Analysis of Carbonates. ACS Earth Sp. Chem. 4, 702–710. https://doi.org/10.1021/acsearthspacechem.9b00330

Franz, P., Röckmann, T., Franz, P., High-precision, T.R., 2005. High-precision isotope measurements of $H_2{}^{16}O$, $H_2{}^{17}O$, $H_2{}^{18}O$, and the $\Delta^{17}O$-anomaly of water vapor in the southern lowermost stratosphere. Atmos. Chem. Phys. 5, 5373–5403.

Galewsky, J., Steen-Larsen, H.C., Field, R.D., Worden, J., Risi, C., Schneider, M., 2016. Stable isotopes in atmospheric water vapor and applications to the hydrologic cycle. Rev. Geophys. 54, 809–865. https://doi.org/10.1002/2015RG000512

Gat, J., 1996. Oxygen and hydrogen isotopes in the hydrologic cycle. Annu. Rev. Earth Planet. Sci. 24, 225–262. https://doi.org/10.1146/annurev.earth.24.1.225

Gázquez, F., Morellón, M., Bauska, T., Herwartz, D., Surma, J., Moreno, A., Staubwasser, M., Valero-garcés, B., Delgado-huertas, A., Hodell, D.A., 2018. Triple oxygen and hydrogen isotopes of gypsum hydration water for quantitative paleo-humidity reconstruction. Earth

Planet. Sci. Lett. 481, 177–188. https://doi.org/10.1016/j.epsl.2017.10.020

Gehler, A., Tütken, T., Pack, A., 2011. Triple oxygen isotope analysis of bioapatite as tracer for diagenetic alteration of bones and teeth. Palaeogeogr. Palaeoclimatol. Palaeoecol. 310, 84–91. https://doi.org/10.1016/j.palaeo.2011.04.014

Gonfiantini, R., 1984. Advisory group meeting on stable isotope reference samples for geochemical and hydrochemical investigations. Vienna.

Gonfiantini, R., 1978. Standards for stable isotope measurements in natural compounds. Nature 271, 534–536. https://doi.org/10.1038/271534a0

Gonfiantini, R., Wassenaar, L.I., Araguas-Araguas, L., Aggarwal, P.K., 2018. A unified Craig-Gordon isotope model of stable hydrogen and oxygen isotope fractionation during fresh or saltwater evaporation. Geochim. Cosmochim. Acta 235, 224–236. https://doi.org/10.1016/j.gca.2018.05.020

Guo, W., Zhou, C., 2019. Triple oxygen isotope fractionation in the DIC-H_2O-CO_2 system: A numerical framework and its implications. Geochim. Cosmochim. Acta 246, 541–564. https://doi.org/10.1016/j.gca.2018.11.018

Herwartz, D., Pack, A., Krylov, D., Xiao, Y., Muehlenbachs, K., Sengupta, S., Di Rocco, T., 2015. Revealing the climate of snowball Earth from $\delta^{17}O$ systematics of hydrothermal rocks. Proc. Natl. Acad. Sci. U. S. A. 112, 5337–5341. https://doi.org/10.1073/pnas.1422887112

Horita, J., Wesolowski, D.J., 1994. Liquid-vapor fractionation of oxygen and hydrogen isotopes of water from the freezing to the critical temperature. Geochim. Cosmochim. Acta 58, 3425–3437.

Hulston, J.R., Thode, H.G., 1965. Variations in the S^{33}, S^{34}, and S^{36} Contents of Meteorites and Their Relation to Chemical and Nuclear Effects. J. Geophys. Res. 70, 3475–3484.

Jasechko, S., 2019. Global Isotope Hydrogeology—Review. Rev. Geophys. 57, 835–965. https://doi.org/10.1029/2018RG000627

Joussaume, S., Jouzel, J., Sadourny, R., 1984. A general circulation model of water isotope cycles in the atmosphere. Nature 311, 24–29. https://doi.org/10.1038/311680a0

Jouzel, J., Merlivat, L., 1984. Deuterium and Oxygen 18 in Precipitation: Modeling of the Isotopic Effects During Snow Formation. J. Geophys. Res. 89, 11749–11757. https://doi.org/10.1029/JD089iD07p11749

Kaiser, J., 2009. Reformulated ^{17}O correction of mass spectrometric stable isotope measurements in carbon dioxide and a critical appraisal of historic 'absolute' carbon and oxygen isotope ratios. Geochim. Cosmochim. Acta 72, 1312–1334. https://doi.org/10.1016/j.gca.2007.12.011

Kaseke, K.F., Wang, L., Wanke, H., Tian, C., Lanning, M., Jiao, W., 2018. Precipitation Origins and Key Drivers of Precipitation Isotope (^{18}O, ^{2}H, and ^{17}O) Compositions Over Windhoek. J. Geophys. Res. Atmos. 123, 7311–7330. https://doi.org/10.1029/2018JD028470

Kendall, C., Coplen, T.B., 2001. Distribution of oxygen-18 and deuteriun in river waters across the United States. Hydrol. Process. 15, 1363–1393. https://doi.org/10.1002/hyp.217

Landais, A., Barkan, E., Luz, B., 2008. Record of $\delta^{18}O$ and ^{17}O-excess in ice from Vostok Antarctica during the last 150,000 years. Geophys. Res. Lett. 35, 1–5. https://doi.org/10.1029/2007GL032096

Landais, A., Barkan, E., Yakir, D., Luz, B., 2006. The triple isotopic composition of oxygen in leaf water. Geochim. Cosmochim. Acta 70, 4105–4115. https://doi.org/10.1016/j.gca.2006.06.1545

Landais, A., Ekaykin, A., Barkan, E., Winkler, R., Luz, B., 2012a. Seasonal variations of ^{17}O-excess and d-excess in snow precipitation at Vostok station, East Antarctica. J. Glaciol. 58, 725–733. https://doi.org/10.3189/2012JoG11J237

Landais, A., Risi, C., Bony, S., Vimeux, F., Descroix, L., Falourd, S., Bouygues, A., 2010. Combined measurements of ^{17}O-excessand d-excess in African monsoon precipitation: Implications for evaluating convective parameterizations. Earth Planet. Sci. Lett. 298, 104–112. https://doi.org/10.1016/j.epsl.2010.07.033

Landais, A., Steen-Larsen, H.C., Guillevic, M., Masson-Delmotte, V., Vinther, B., Winkler, R., 2012b. Triple isotopic composition of oxygen in surface snow and water vapor at NEEM (Greenland). Geochim. Cosmochim. Acta 77, 304–316. https://doi.org/10.1016/j.gca.2011.11.022

Levin, N.E., Raub, T.D., Dauphas, N., Eiler, J.M., 2014. Triple oxygen isotope variations in sedimentary rocks. Geochim. Cosmochim. Acta 139, 173–189. https://doi.org/10.1016/j.gca.2014.04.034

Li, S., Levin, N.E., Chesson, L.A., 2015. Continental scale variation in ^{17}O-excess of meteoric waters in the United States. Geochim. Cosmochim. Acta 164, 110–126. https://doi.org/10.1016/j.gca.2015.04.047

Li, S., Levin, N.E., Soderberg, K., Dennis, K.J., Caylor, K.K., 2017. Triple oxygen isotope composition of leaf waters in Mpala, central Kenya. Earth Planet. Sci. Lett. 468, 38–50. https://doi.org/10.1016/j.epsl.2017.02.015

Lin, Y., Clayton, R.N., Groning, M., 2010. Calibration of $\delta^{17}O$ and $\delta^{18}O$ of international measurement standards – VSMOW, VSMOW2, SLAP, and SLAP2. Rapid Commun. Mass Spectrom. 24, 773–776. https://doi.org/10.1002/rcm.4449

Liljestrand, F.L., Knoll, A.H., Tosca, N.J., Cohen, P.A., Macdonald, F.A., Peng, Y., Johnston, D.T., 2020. The triple oxygen isotope composition of Precambrian chert. Earth Planet. Sci. Lett. 537, 1–10. https://doi.org/10.1016/J.EPSL.2020.116167

Luz, B., Barkan, E., 2010. Variations of $^{17}O/^{16}O$ and $^{18}O/^{16}O$ in meteoric waters. Geochim. Cosmochim. Acta 74, 6276–6286. https://doi.org/10.1016/j.gca.2010.08.016

Luz, B., Barkan, E., Yam, R., Shemesh, A., 2009. Fractionation of oxygen and hydrogen isotopes in evaporating water. Geochim. Cosmochim. Acta 73, 6697–6703. https://doi.org/10.1016/j.gca.2009.08.008

Majoube, M., 1971. Oxygen-18 and deuterium fractionation between water and steam. J. Chem. Phys. 68, 1432–1436.

Marrero, T.R., Mason, E.A., 1972. Gaseous Diffusion Coefficients. J. Phys. Chem. Ref. Data 1, 3–118. https://doi.org/10.1063/1.3253094

Martin, F.M., 2002. Isotopic fractionation and the quantification of ^{17}O anomalies in the oxygen three-isotope system: an appraisal and geochemical significance. Geochim. Cosmochim. Acta 66, 1881–1889.

Matsuhisa, Y., Goldsmith, J.R., Clayton, R.N., 1978. Mechanisms of hydrothermal crystallization of quartz at 250°C and 15 kbar. Geochim. Cosmochim. Acta 42, 173–182. https://doi.org/10.1016/0016-7037(78)90130-8

McKeegan, K.D., Leshin, L.A., 2001. Stable Isotope Variations in Extraterrestrial Materials. Rev. Mineral. Geochemistry 43, 279–318. https://doi.org/10.2138/gsrmg.43.1.279

McKinney, C.R., McCrea, J.M., Epstein, S., Allen, H.A., Urey, H.C., 1950. Improvements in mass spectrometers for the measurement of small differences in isotope abundance ratios. Rev. Sci. Instrum. 21, 724–730. https://doi.org/10.1063/1.1745698

Meijer, H.A.J., Li, W.J., 1998. The Use of Electrolysis for Accurate $\delta^{17}O$ and $\delta^{18}O$ Isotope Measurements in Water. Isot. Evironmental Heal. Stud. 34, 349–369. https://doi.org/10.1080/10256019808234072

Meijer, H.A.J., Neubert, R.E.M., Visser, G.H., 2000. Cross contamination in dual inlet isotope ratio mass spectrometers. Int. J. Mass Spectrom. 198, 45–61. https://doi.org/10.1016/s1387-3806(99)00266-3

Merlivat, L., 1978. Molecular diffusivities of $H_2{}^{16}O$, $HD^{16}O$, and $H_2{}^{18}O$ in gases. J. Chem. Phys. 69, 2864–2871. https://doi.org/10.1063/1.436884

Miller, M.F., 2018. Precipitation regime influence on oxygen triple-isotope distributions in Antarctic precipitation and ice cores. Earth Planet. Sci. Lett. 481, 316–327. https://doi.org/10.1016/j.epsl.2017.10.035

New, M., Lister, D., Hulme, M., Makin, I., 2002. A high-resolution data set of surface climate over global land areas. Clim. Res. 21, 1–25.

Noone, D., Risi, C., Bailey, A., Berkelhammer, M., Brown, D.P., Buenning, N., Gregory, S., Nusbaumer, J., Schneider, D., Sykes, J., Vanderwende, B., Wong, J., Meillier, Y., Wolfe, D., 2013. Determining water sources in the boundary layer from tall tower profiles of water vapor and surface water isotope ratios after a snowstorm in Colorado. Atmos. Chem. Phys. 13, 1607–1623. https://doi.org/10.5194/acp-13-1607-2013

Pack, A., Herwartz, D., 2014. The triple oxygen isotope composition of the Earth mantle and understanding $\Delta^{17}O$ variations in terrestrial rocks and minerals. Earth Planet. Sci. Lett. 390, 138–145. https://doi.org/10.1016/j.epsl.2014.01.017

Pang, H., Hou, S., Landais, A., Delmotte, V.M., Jouzel, J., 2019. Influence of Summer Sublimation on δD, $\delta^{18}O$, and $\delta^{17}O$ in Precipitation, East Antarctica, and Implications for Climate Reconstruction From Ice Cores. J. Geophys. Res. Atmos. 124, 7339–7358. https://doi.org/10.1029/2018JD030218

Pang, H., Hou, S., Landais, A., Masson-Delmotte, V., Prie, F., Steen-Larsen, H.C., Risi, C., Li, Y., Jouzel, J., Wang, Y., He, J., Minster, B., Falourd, S., 2015. Spatial distribution of ^{17}O-excess in surface snow along a traverse from Zhongshan station to Dome A, East Antarctica. Earth Planet. Sci. Lett. 414, 126–133. https://doi.org/10.1016/j.epsl.2015.01.014

Passey, B.H., Hu, H., Ji, H., Montanari, S., Li, S., Henkes, G.A., Levin, N.E., 2014. Triple oxygen isotopes in biogenic and sedimentary carbonates. Geochim. Cosmochim. Acta 141, 1–25. https://doi.org/10.1016/j.gca.2014.06.006

Passey, B.H., Ji, H., 2019. Triple oxygen isotope signatures of evaporation in lake waters and carbonates: A case study from the western United States. Earth Planet. Sci. Lett. 518, 1–12. https://doi.org/10.1016/j.epsl.2019.04.026

Paul, D., Skrzypek, G., Forizs, I., 2007. Normalization of measured stable isotopic compositions to isotope reference scales – a review. Rapid Commun. Mass Spectrom. 21, 3006–3014. https://doi.org/10.1002/rcm.3185

Poulsen, C.J., Ehlers, T.A., Insel, N., 2010. Onset of convective rainfall during gradual late miocene rise of the central andes. Science (80-.). 328, 490–493. https://doi.org/10.1126/science.1185078

Rech, J.A., Currie, B.S., Jordan, T.E., Riquelme, R., Lehmann, S.B., Kirk-Lawlor, N.E., Li, S., Gooley, J.T., 2019. Massive middle Miocene gypsic paleosols in the Atacama Desert and the formation of the Central Andean rain-shadow. Earth Planet. Sci. Lett. 506, 184–194. https://doi.org/10.1016/j.epsl.2018.10.040

Report of Stable Isotopic Composition Reference Material USGS45, 2014. Reston, VA.

https://isotopes.usgs.gov/lab/referencematerials/USGS45.pdf

Report of Stable Isotopic Composition Reference Material USGS46, 2014. Reston, VA. https://isotopes.usgs.gov/lab/referencematerials/USGS46.pdf

Report of Stable Isotopic Composition Reference Material USGS47, 2014. Reston, VA. https://isotopes.usgs.gov/lab/referencematerials/USGS47.pdf

Report of Stable Isotopic Composition Reference Material USGS48, 2014. Reston, VA. https://isotopes.usgs.gov/lab/referencematerials/USGS48.pdf

Report of Stable Isotopic Composition Reference Material USGS49, 2015. Reston, VA. https://isotopes.usgs.gov/lab/referencematerials/USGS49.pdf

Report of Stable Isotopic Composition Reference Material USGS50, 2015. Reston, VA. https://isotopes.usgs.gov/lab/referencematerials/USGS50.pdf

Risi, C., Bony, S., Vimeux, F., Descroix, L., Ibrahim, B., Lebreton, E., Mamadou, I., Sultan, B., 2008. What controls the isotopic composition of the African monsoon precipitation? Insights from event-based precipitation collected during the 2006 AMMA field campaign. Geophys. Res. Lett. 35, 1–6. https://doi.org/10.1029/2008GL035920

Risi, C., Landais, A., Bony, S., Jouzel, J., Masson-Delmotte, V., Vimeux, F., 2010. Understanding the ^{17}O excess glacial-interglacial variations in Vostok precipitation. J. Geophys. Res. Atmos. 115, 1–15. https://doi.org/10.1029/2008JD011535

Risi, C., Landais, A., Winkler, R., Vimeux, F., 2013. Can we determine what controls the spatio-temporal distribution of d-excess and ^{17}O-excess in precipitation using the LMDZ general circulation model? Clim. Past 9, 2173–2193. https://doi.org/10.5194/cp-9-2173-2013

Roscoe, H.K., Fowler, C.L., Shanklin, J.D., Hill, J.G.T., 2004. Possible long-term changes in stratospheric circulation: Evidence from total ozone measurements at the edge of the Antarctic vortex in early winter. Q. J. R. Meteorol. Soc. 130, 1123–1135. https://doi.org/10.1256/qj.03.70

Rowley, D.B., Garzione, C.N., 2007. Stable Isotope-Based Paleoaltimetry. Annu. Rev. Earth Planet. Sci. 35, 463–508. https://doi.org/10.1146/annurev.earth.35.031306.140155

Rozanski, K., Araguás-Araguás, L., Gonfiantini, R., 1993. Isotopic Patterns in Modern Global Precipitation, in: Swart, P.K., Lohmann, K.C., Mckenzie, J., Savin, S. (Eds.), Climate Change in Continental Isotopic Records Geophysical Monograph Series, (Vol. 78). American Geophysical Union, Washington, DC, pp. 1–36. https://doi.org/10.1029/GM078p0001

Rumble, D., Miller, M.F., Franchi, I.A., Greenwood, R.C., 2007. Oxygen three-isotope fractionation lines in terrestrial silicate minerals: An inter-laboratory comparison of hydrothermal quartz and eclogitic garnet. Geochim. Cosmochim. Acta 71, 3592–3600.

https://doi.org/10.1016/j.gca.2007.05.011

Sakai, S., Matsuda, S., Hikida, T., Shimono, A., Mcmanus, J.B., Zahniser, M., Nelson, D., Dettman, D.L., Yang, D., Ohkouchi, N., 2017. High-Precision Simultaneous $^{18}O/^{16}O$, $^{13}C/^{12}C$, and $^{17}O/^{16}O$ Analyses for Microgram Quantities of $CaCO_3$ by Tunable Infrared Laser Absorption Spectroscopy. Anal. Chem. 89, 11846–11852. https://doi.org/10.1021/acs.analchem.7b03582

Salati, E., Dall'Olio, A., Matsui, E., Gat, J.R., 1979. Recycling of water in the Amazon Basin: An isotopic study. Water Resour. Res. 15, 1250–1258. https://doi.org/10.1029/WR015i005p01250

Schauer, A.J., Schoenemann, S.W., Steig, E.J., 2016. Routine high-precision analysis of triple water-isotope ratios using cavity ring-down spectroscopy. Rapid Commun. Mass Spectrom. 30, 2059–2069. https://doi.org/10.1002/rcm.7682

Schoenemann, S.W., Schauer, A.J., Steig, E.J., 2013. Measurement of SLAP2 and GISP $\delta^{17}O$ and proposed VSMOW-SLAP normalization for $\delta^{17}O$ and $^{17}O_{excess}$. Rapid Commun. Mass Spectrom. 27, 582–590. https://doi.org/10.1002/rcm.6486

Schoenemann, S.W., Steig, E.J., 2016. Seasonal and spatial variations of $^{17}O_{excess}$ and d_{excess} in Antarctic precipitation: Insights from an intermediate complexity isotope model. J. Geophys. Res. Atmos. 121, 11215–11247. https://doi.org/10.1002/2016JD025117.Received

Schoenemann, S.W., Steig, E.J., Ding, Q., Markle, B.R., Schauer, A.J., 2014. Triple water-isotopologue record from WAIS Divide, Antarctica: Controls on glacial-interglacial changes in $^{17}O_{excess}$ of precipitation. J. Geophys. Res. Atmos. 119, 8741–8763. https://doi.org/10.1002/2014JD021770.Received

Sharp, Z.D., Gibbons, J.A., Maltsev, O., Atudorei, V., Pack, A., Sengupta, S., Shock, E.L., Knauth, L.P., 2016. A calibration of the triple oxygen isotope fractionation in the SiO_2-H_2O system and applications to natural samples. Geochim. Cosmochim. Acta 186, 105–119. https://doi.org/10.1016/j.gca.2016.04.047

Sharp, Z.D., Wostbrock, J.A.G., Pack, A., 2018. Mass-dependent triple oxygen isotope variations in terrestrial materials. Geochemical Perspect. Lett. 7, 27–31. https://doi.org/10.7185/geochemlet.1815

Spangenberg, J.E., 2012. Caution on the storage of waters and aqueous solutions in plastic containers for hydrogen and oxygen stable isotope analysis. Rapid Commun. Mass Spectrom. 26, 2627–2636. https://doi.org/10.1002/rcm.6386

Steig, E.J., Gkinis, V., Schauer, A.J., Schoenemann, S.W., Samek, K., Hoffnagle, J., Dennis, K.J., Tan, S.M., 2014. Calibrated high-precision ^{17}O-excess measurements using cavity ring-down spectroscopy with laser-current-tuned cavity resonance. Atmos. Meas. Tech. 7, 2421–2435. https://doi.org/10.5194/amt-7-2421-2014

Surma, J., Assonov, S., Bolourchi, M.J., Staubwasser, M., 2015. Triple oxygen isotope signatures in evaporated water bodies from the Sistan Oasis, Iran. Geophys. Res. Lett. 42, 8456–8462. https://doi.org/10.1002/2015GL066475

Surma, J., Assonov, S., Herwartz, D., Voigt, C., Staubwasser, M., 2018. The evolution of ^{17}O-excess in surface water of the arid environment during recharge and evaporation. Sci. Rep. 8, 1–10. https://doi.org/10.1038/s41598-018-23151-6

Thiemens, M.H., 2006. History and Applications of Mass-Independent Isotope Effects. Annu. Rev. Earth Planet. Sci. 34, 217–262. https://doi.org/10.1146/annurev.earth.34.031405.125026

Thiemens, M.H., Chakraborty, S., Dominguez, G., 2012. The Physical Chemistry of Mass-Independent Isotope Effects and Their Observation in Nature. Annu. Rev. Phys. Chem. 63, 155–177. https://doi.org/10.1146/annurev-physchem-032511-143657

Thiemens, M.H., Heidenreich, J.E., 1983. The mass-independent fractionation of oxygen: A novel isotope effect and its possible cosmochemical implications. Science (80-.). 219, 1073–1075. https://doi.org/10.1126/science.219.4588.1073

Thiemens, M.H., Jackson, T.L., Brenninkmeijer, C.A.M., 1995. Observation of a mass independent oxygen isotopic composition in terrestrial stratospheric CO_2, the link to ozone chemistry, and the possible occurrence in the Martian atmosphere. Geophys. Res. Lett. 22, 255–257. https://doi.org/10.1029/94GL02996

Thompson, M., 2012. Precision in chemical analysis: A critical survey of uses and abuses. Anal. Methods 4, 1598–1611. https://doi.org/10.1039/c2ay25083g

Tian, C., Wang, L., Kaseke, K.F., Bird, B.W., 2018. Stable isotope compositions (δ^2H, $\delta^{18}O$ and $\delta^{17}O$) of rainfall and snowfall in the central United States. Sci. Rep. 8, 1–15. https://doi.org/10.1038/s41598-018-25102-7

Tian, C., Wang, L., Tian, F., Zhao, S., Jiao, W., 2019. Spatial and temporal variations of tap water ^{17}O-excess in China. Geochim. Cosmochim. Acta 260, 1–14. https://doi.org/10.1016/j.gca.2019.06.015

Uechi, Y., Uemura, R., 2019. Dominant influence of the humidity in the moisture source region on the ^{17}O-excess in precipitation on a subtropical island. Earth Planet. Sci. Lett. 513, 20–28. https://doi.org/10.1016/j.epsl.2019.02.012

Uemura, R., Barkan, E., Abe, O., Luz, B., 2010. Triple isotope composition of oxygen in atmospheric water vapor. Geophys. Res. Lett. 37, 1–4. https://doi.org/10.1029/2009GL041960

Uemura, R., Masson-Delmotte, V., Jouzel, J., Landais, A., Motoyama, H., Stenni, B., 2012. Ranges of moisture-source temperature estimated from Antarctic ice cores stable isotope

records over glacial-interglacial cycles. Clim. Past 8, 1109–1125. https://doi.org/10.5194/cp-8-1109-2012

Vimeux, F., Tremoy, G., Risi, C., Gallaire, R., 2011. A strong control of the South American SeeSaw on the intra-seasonal variability of the isotopic composition of precipitation in the Bolivian Andes. Earth Planet. Sci. Lett. 307, 47–58. https://doi.org/10.1016/j.epsl.2011.04.031

Voarintsoa, N.R.G., Barkan, E., Bergel, S., Vieten, R., Affek, H.P., 2020. Triple oxygen isotope fractionation between $CaCO_3$ and H_2O in inorganically precipitated calcite and aragonite. Chem. Geol. 539, 119500. https://doi.org/10.1016/j.chemgeo.2020.119500

Werner, R.A., Brand, W.A., 2001. Referencing strategies and techniques in stable isotope ratio analysis. Rapid Commun. Mass Spectrom. 15, 501–519. https://doi.org/10.1002/rcm.258

Winkler, R., Landais, A., Sodemann, H., Dümbgen, L., Prié, F., Masson-Delmotte, V., Stenni, B., Jouzel, J., 2012. Deglaciation records of ^{17}O-excess in East Antarctica: Reliable reconstruction of oceanic normalized relative humidity from coastal sites. Clim. Past 8, 1–16. https://doi.org/10.5194/cp-8-1-2012

Wong, T.E., Nusbaumer, J., Noone, D.C., 2017. Evaluation of modeled land-atmosphere exchanges with a comprehensive water isotope fractionation scheme in version 4 of the Community Land Model. J. Adv. Model. Earth Syst. 9, 978–1001. https://doi.org/10.1002/2016MS000842

Wostbrock, J.A.G., Cano, E.J., Sharp, Z.D., 2020. An internally consistent triple oxygen isotope calibration of standards for silicates, carbonates and air relative to VSMOW2 and SLAP2. Chem. Geol. 533, 119432. https://doi.org/10.1016/j.chemgeo.2019.119432

Yeung, L.Y., Hayles, J.A., Hu, H., Ash, J.L., Sun, T., 2018. Scale distortion from pressure baselines as a source of inaccuracy in triple-isotope measurements. Rapid Commun. Mass Spectrom. 32, 1811–1821. https://doi.org/10.1002/rcm.8247

Yeung, L.Y., Young, E.D., Schauble, E.A., 2012. Measurements of $^{18}O^{18}O$ and $^{17}O^{18}O$ in the atmosphere and the role of isotope-exchange reactions. J. Geophys. Res. Atmos. 117, 1–20. https://doi.org/10.1029/2012JD017992

Young, E.D., Galy, A., 2004. The Isotope Geochemistry and Cosmochemistry of Magnesium. Re 55, 197–230. https://doi.org/10.2138/gsrmg.55.1.197

Young, E.D., Galy, A., Nagahara, H., 2002. Kinetic and equilibrium mass-dependent isotope fractionation laws in nature and their geochemical and cosmochemical significance. Geochim. Cosmochim. Acta 66, 1095–1104. https://doi.org/10.1016/S0016-7037(01)00832-8

Young, E.D., Yeung, L.Y., Kohl, I.E., 2014. On the $\delta^{17}O$ budget of atmospheric O_2. Geochim.

Cosmochim. Acta 135, 102–125. https://doi.org/10.1016/j.gca.2014.03.026

Zachos, J., 2001. Trends, Rhythms, and Aberrations in Global Climate 65 Ma to Present 292, 686–693. https://doi.org/10.1126/science.1059412

Zakharov, D.O., Bindeman, I.N., Tanaka, R., Friðleifsson, G.Ó., Reed, M.H., Hampton, R.L., 2019. Triple oxygen isotope systematics as a tracer of fluids in the crust: A study from modern geothermal systems of Iceland. Chem. Geol. 530, 119312. https://doi.org/10.1016/j.chemgeo.2019.119312

Chapter 6 Conclusion

This dissertation is a compilation of four chapters that use oxygen and hydrogen isotopes to trace how water is exchanged between the land and the atmosphere. Each of these chapters provides new insights and understanding about terrestrial hydrologic cycling that we did not or could not know without water isotopes. This concluding chapter highlights the most important findings and implications from my dissertation. I end with research questions that have emerged from this dissertation and available datasets that may guide future work.

6.1 Dissertation summary and key findings

Ratios of stable oxygen and hydrogen isotopes are among the most common isotopic measurements in Earth science and have been a cornerstone of climate and hydrologic research for over six decades. Initially, most isotope hydrologists associated the spatial variability of water isotopes with Rayleigh distillation and used water isotopes to trace rainout and condensation. However, recent technological and analytical developments (e.g., laser absorption spectrometers and high precision triple oxygen isotope measurements, both of which I use throughout my dissertation) have led to a proliferation of new datasets that probe questions about water cycling across a wide range of spatial and temporal scales. Together, these studies paint a nuanced picture of water cycling that is much more complex than a simple Rayleigh distillation model.

Hydrologic and climate research over the last two decades has coalesced into three primary applications of isotope hydrology. Each of these applications goes well beyond Rayleigh distillation and demonstrates the power of isotopes to study water cycling across space and time. First, water isotopes record information about remote oceanic moisture sources (e.g., Steen-Larsen et al., 2015) and water sources in surface and groundwater (e.g., Evaristo et al., 2015). For example, water isotopes can trace preferential moisture pathways in soil (e.g., Allen et al., 2019) to identify which sources of water are accessible to plants (e.g., Brooks et al., 2010). Second, water isotopes can separate or reveal hydrologic processes that may not be discernable with other methods. This is particularly important in ecohydrologic research because water isotopes can

distinguish evaporation and transpiration fluxes (Yakir and Sternberg, 2000) whereas traditional techniques such as eddy covariance only measure the bulk latent heat or evapotranspiration flux. Third, water isotope data integrates a record of hydrologic processes as water moves through the environment. For example, the isotopic composition of precipitation in the Amazon Basin reveals information about evaporative conditions above oceanic moisture sources, moisture recycling over land, and local condensation (Salati et al., 1979). This dissertation explores all three of these applications.

This dissertation leverages a comprehensive observational network I built and explores new applications and insights from stable water isotopes to trace spatial and temporal variability in the hydrologic cycle. Chapters 2 and 3 focus on forest ecohydrology and use water isotopes to quantify the role of trees in local and regional water budgets. Chapters 4 and 5 use the isotopic composition of precipitation and surface water to refine longstanding assumptions about isotope hydrology. All four of these chapters highlight processes other than Rayleigh distillation that drive water cycling.

The most important novel findings from this dissertation are that structural disturbances in forest canopies can alter land-atmosphere mixing and gas exchange between ecosystems and the atmosphere (Chapter 2) and that precipitation on the dry flank of the Western Cordillera in the central Andes is sourced from the Pacific Ocean (Chapter 4). Neither of these findings would have been possible without stable water isotopes. In Chapter 2, water isotopes offer insights into the evaporation, transpiration, and boundary layer mixing that drive land-atmosphere water exchange. This work helps ecohydrologists understand the biogeochemical response of forests following vegetation thinning management or rapid natural ecological succession. In Chapter 4, atmospheric moisture trajectories show that Pacific-sourced moisture is transported up the dry western flank; precipitation isotopes show that this water actually makes it to the land, which is important because raindrops can conceivably evaporate entirely as they fall through such dry air. This finding can help manage freshwater resources in a dry climate and has important implications for reconstructions of paleoaltimetry and paleoclimate in the central Andes.

The most important contributions from this dissertation are that stable water isotopes can help quantify the role of plants in land-atmosphere water exchange (Chapters 2 and 3) and the addition of substantial new datasets that constrain water cycling in the central Andes (Chapter 4) and hydrologic triple oxygen isotope variability (Chapter 5). Chapters 3 and 5 focus primarily on

method development and isotope systematics, respectively, and pave the way for future work on a variety of hydrologic and paleoclimate questions.

The conclusions and implications from this dissertation improve our understanding of the hydrologic processes that drive water cycling between the land and the atmosphere from ecosystem to global scales. Taken together, the chapters in this dissertation have a wide range of applications in hydrology, ecology, geology, and climate modeling and demonstrate the immense potential of stable water isotopes to better understand the water cycle.

6.2 Remaining questions

This work has also motivated a number of research questions. The questions listed below are among the most important unanswered questions that have emerged or are highlighted from my dissertation. I intend to work on the first three questions during my postdoctoral work.

1) **Why is precipitation $\Delta'^{17}O$ higher in the winter and lower in the summer?** Seasonal $\Delta'^{17}O_p$ variation is observed in many datasets (including Chapter 4), but a convincing explanation of this pattern remains unclear. In the hydrologic triple oxygen isotope literature, higher winter $\Delta'^{17}O_p$ values are often explained by more equilibrium fractionation, and lower summer $\Delta'^{17}O_p$ values are explained by more kinetic fractionation (e.g., Tian et al., 2018). However, this qualitative reasoning is not very satisfying and offers very little in terms of the processes or environmental controls that drive $\Delta'^{17}O_p$. Likely, seasonal $\Delta'^{17}O_p$ variation is due to small, possibly temperature dependent, deviations between observed $\delta'^{18}O$–$\delta'^{17}O$ slopes and the slope of the triple oxygen isotope reference relationship, but this is an active area of research.
2) **Do the laser-based $\delta^{17}O$ analyzers work well?** In other words: I just got my start-up funds! Should I buy the new $\delta^{17}O$-enabled Picarro? Interest in hydrologic $\Delta'^{17}O$ data is rapidly emerging, but the analytical steps to make these measurements have traditionally been quite complex. Recently, Picarro and LGR, another company that makes laser-based water isotope analyzers, developed technology that may simplify $\Delta'^{17}O$ measurements by using laser absorption spectroscopy to simultaneously analyze liquid or water vapor $\delta^{18}O$, $\delta^{17}O$, and $\delta^{2}H$. These analyzers are appealing because they have a small footprint and are field-portable, cost about a quarter of the price of an isotope ratio mass spectrometer (IRMS), operate automatically (with an autosampler), and can achieve similar $\Delta'^{17}O$

precision (~10 per meg) as traditional IRMS measurements. However, such high precision from Picarro and LGR data frequently requires optimistic statistics, and there has not yet been a rigorous comparison of Picarro, LGR, and IRMS $\Delta'^{17}O$ data. We are well positioned to do this comparison at the University of Michigan because we have both an IRMS (Levin/Passey Lab) and Picarro (Poulsen Lab) to measure $\delta^{18}O$ and $\delta^{17}O$. A more robust assessment of laser-based $\Delta'^{17}O$ data will inform the suite or types of questions that these analyzers can help answer.

3) **What are the values of X_E and α_{diff}?** The isotopic composition of water during evaporation is very sensitive to X_E, the volumetric ratio of water lost to evaporation relative to inflowing water, and α_{diff}, the kinetic fractionation factor (Criss, 1999; Gázquez et al., 2018; Passey and Ji, 2019; Surma et al., 2018). However, the values of X_E and α_{diff} are not well known. Theoretically, X_E can range from 0 (no evaporative loss) to 1 (all water loss is due to evaporation); α_{diff} can range from 1 (pure turbulent transport and no isotopic fractionation) to 1.0285 (pure molecular transport and lots of isotopic fractionation as vapor diffuses through the air; Merlivat, 1978). Typically, X_E is assumed to be ~ 0.5 (e.g., Passey and Ji, 2019) and α_{diff} is ~ 1.014 (e.g., Gat, 1996; Jasechko et al., 2013; Surma et al., 2018), but these values vary widely and can have a substantial impact on isotopic interpretations (e.g., Horita et al. 2008). I have done some initial analysis that suggests the typical values of X_E and α_{diff} are likely too high, and that the fractionation associated with evaporation may be overestimated in some instances (Aron et al. 2019). Still, additional work is needed to further constrain the values of X_E and α_{diff}.

4) **What contributes to the overall poor simulated d-excess in isotope-enabled climate models?** Isotope-enabled climate models simulate isotopic ratios in the atmosphere, ocean, ice, and land. Generally, observed and simulated $\delta^{18}O$ data agree very well, and isotope-enabled climate models are used for a number of modern and paleoclimate applications (Brady et al., 2019). However, the agreement between simulated and observed d-excess is quite poor, which means that modeled d-excess is rarely used in hydrologic or paleoclimate studies (Nusbaumer et al., 2017; Wong et al., 2017). As shown in every chapter of this dissertation, d-excess offers important and valuable insights into hydrologic processes and environmental conditions that are impossible to discern with $\delta^{18}O$ alone. Therefore,

additional work to improve the simulated d-excess in climate models would be a fruitful and worthwhile area of future study.

5) **Are there better ways to quantify ecosystem-atmosphere water exchange and quantify evaporation and transpiration fluxes?** Chapters 2 and 3 present new insight into ecosystem-atmosphere water exchange from water isotopes. However, scaling this type of work from the plot or ecosystem level to regional and global scales is not always straightforward because soil water is isotopically heterogeneous and the hydraulics of vegetation vary among species and environments. Therefore, it is important to evaluate new analytical techniques and combine multiple types of data to address ecohydrologic research questions. In the coming years, solar induced fluorescence (Shan et al., 2019), the carbonyl sulfide flux (Whelan et al., 2018), and terrestrial LiDAR (light detection and ranging; e.g., Atkins et al., 2018) data will provide a wealth of new data on vegetation structure and gas exchange between ecosystems and the atmosphere. Combining insights from water isotopes and some of these new data streams will improve our mechanistic understanding of land-atmosphere water interaction.
6) **What processes drive the isotopic composition of precipitation across the entire Andean orogen?** Water isotope studies in the Andes typically focus on observed variability at a single site (e.g., Ampuero et al., 2020), valley (e.g., Gonfiantini et al., 2001), or region (Chapter 2). To date, there has not yet been a comprehensive assessment of precipitation (or surface water) isotopes across the entire orogen. While the Andes and Amazon are by no means a data-rich region (Putman and Bowen, 2019), there are plenty of observations to explore continental-scale isotope patterns and compare regional or latitudinal hydrology. Compiled South American precipitation isotope data will also be a useful dataset to evaluate the performance of isotope-enabled climate models and a new technique to 'tag' source regions that can help identify and trace atmospheric moisture transport (e.g., Tabor et al., 2018).

6.3 Suggestions and data for future work

Throughout the course of my graduate studies I have compiled a number of datasets that did not make it into this dissertation. Here I briefly describe these datasets and explain how they can help address some of the remaining questions outlined above.

1) **Crowdsourced water samples.** This dataset includes $\delta^{18}O$ and $\delta^{2}H$ vales of over 1,600 water samples. These samples were collected from 49 countries and 6 continents through a crowdsourced effort and include precipitation, surface water, ground water, tap water, melted snow and ice, and ocean water. Isotopic data from 104 of these samples are included in Chapter 5, but the full dataset remains relatively unexplored. The dataset includes weekly timeseries from the Huron River in Ann Arbor and weekly precipitation samples collected in Ann Arbor and at UMBS in northern lower Michigan. These timeseries may be useful in explaining the high winter/low summer $\Delta'^{17}O_p$ pattern. These samples are properly stored (to prevent evaporation) should anyone want to do additional isotopic analyses in the future.
2) **Central Andes surface waters.** This dataset includes $\delta^{18}O$ and $\delta^{2}H$ data from 557 surface water samples collected in southern Peru. These samples were collected from 2016-2019 from the same region as the precipitation network in Chapter 4. Combined with published water isotope data from South America, this dataset can help explain the environmental controls on isotopic variability across the Andean orogen. In addition, this dataset can inform isotope-based interpretations of paleoelevation and paleoclimate in the Andes, which remains an area of ongoing work.
3) **University of Michigan Biological Station (UMBS) water vapor.** This dataset includes very high resolution (~0.1-1 Hz) water vapor $\delta^{18}O$ and $\delta^{2}H$ data from two UMBS forest sites during the 2015 and 2016 growing seasons. In Chapter 2, I analyzed the diurnal vapor isotope variability from the 2016 dataset, but did not focus in depth on synoptic, seasonal, or interannual vapor isotope signals. UMBS is located downwind of Lake Michigan, so this vapor isotope data has pronounced and distinct d-excess signatures that may be a helpful benchmark to evaluate regional isotope modeling or improve simulated d-excess in isotope-enabled climate models.

Finally, I want to end with an acknowledgement of the opportunistic and collaborative sample collection that buoyed my PhD. Nearly every sample I analyzed and discussed in Chapters 4 and 5 was collected through citizen science projects and crowdsourced efforts. These projects gave me an opportunity to work with non-scientists on rigorous research projects and constantly reminded me of the power of collaboration. None of the work in Chapter 4 would have been possible without

the Peruvian station managers who watch over the precipitation collection equipment and have been collecting rain samples for more than four years. I never could have collected all the crowdsource samples (Chapter 5) on my own. At a time of much skepticism about science and climate change in this country, this type of engagement helps to demystify the scientific process, promote communication, and generate interest in environmental science. Beyond these particular projects, this collaborative effort among a diverse group of individuals shows the power of working together towards a common goal.

6.4 References

Allen, S.T., Kirchner, J.W., Braun, S., Siegwolf, R.T.W., Goldsmith, G.R., 2019. Seasonal origins of soil water used by trees. Hydrol. Earth Syst. Sci. 23, 1199–1210. https://doi.org/10.5194/hess-23-1199-2019

Ampuero, A., Stríkis, N.M., Apaéstegui, J., Vuille, M., Novello, V.F., Espinoza, J.C., Cruz, F.W., Vonhof, H., Mayta, V.C., Martins, V.T.S., Cordeiro, R.C., Azevedo, V., Sifeddine, A., 2020. The Forest Effects on the Isotopic Composition of Rainfall in the Northwestern Amazon Basin. J. Geophys. Res. Atmos. 125. https://doi.org/10.1029/2019jd031445

Aron, P.G., Levin, N.E., Poulsen, C.J., Winkelstern, I.Z., Beverly, E.J., Yarian, D.A., 2019. Variability of Triple Oxygen Isotopes in Meteoric Waters, American Geophysical Union.

Atkins, J.W., Fahey, R.T., Hardiman, B.H., Gough, C.M., 2018. Forest Canopy Structural Complexity and Light Absorption Relationships at the Subcontinental Scale. J. Geophys. Res. Biogeosciences 123, 1387–1405. https://doi.org/10.1002/2017JG004256

Brady, E., Stevenson, S., Bailey, D., Liu, Z., Noone, D., Nusbaumer, J., 2019. The Connected Isotopic Water Cycle in the Community Earth System Model Version 1. J. Adv. Model. Earth Syst. 11, 2547–2566. https://doi.org/10.1029/2019MS001663

Brooks, J.R., Barnard, H.R., Coulombe, R., McDonnell, J.J., 2010. Ecohydrologic separation of water between trees and streams in a Mediterranean climate. Nat. Geosci. 3, 100–104. https://doi.org/10.1038/NGEO722

Criss, R.E., 1999. Principles of Stable Isotope Distribution. Oxford University Press, New York.

Evaristo, J., Jasechko, S., McDonnell, J.J., 2015. Global separation of plant transpiration from groundwater and streamflow. Nature 525, 91–94. https://doi.org/10.1038/nature14983

Gat, J., 1996. Oxygen and hydrogen isotopes in the hydrologic cycle. Annu. Rev. Earth Planet. Sci. 24, 225–262. https://doi.org/10.1146/annurev.earth.24.1.225

Gázquez, F., Morellón, M., Bauska, T., Herwartz, D., Surma, J., Moreno, A., Staubwasser, M., Valero-garcés, B., Delgado-huertas, A., Hodell, D.A., 2018. Triple oxygen and hydrogen isotopes of gypsum hydration water for quantitative paleo-humidity reconstruction. Earth Planet. Sci. Lett. 481, 177–188. https://doi.org/10.1016/j.epsl.2017.10.020

Gonfiantini, R., Roche, M.A., Olivry, J.C., Fontes, J.C., Zuppi, G.M., 2001. The altitude effect on the isotopic composition of tropical rains. Chem. Geol. 181, 147–167.

Horita, J., Rozanski, K., Cohen, S., 2008. Isotope effects in the evaporation of water: A status report of the Craig-Gordon model. Isotopes Environ. Health Stud. 44, 23–49. https://doi.org/10.1080/10256010801887174

Jasechko, S., Sharp, Z.D., Gibson, J.J., Birks, S.J., Yi, Y., Fawcett, P.J., 2013. Terrestrial water fluxes dominated by transpiration. Nature 496, 347–50. https://doi.org/10.1038/nature11983

Merlivat, L., 1978. Molecular diffusivities of $H_2{}^{16}O$, $HD^{16}O$, and $H_2{}^{18}O$ in gases. J. Chem. Phys. 69, 2864–2871. https://doi.org/10.1063/1.436884

Nusbaumer, J., Wong, T.E., Bardeen, C., Noone, D., 2017. Evaluating hydrological processes in the Community Atmosphere Model Version 5 (CAM5) using stable isotope ratios of water. J. Adv. Model. Earth Syst. 9, 949–977. https://doi.org/10.1002/2016MS000839

Passey, B.H., Ji, H., 2019. Triple oxygen isotope signatures of evaporation in lake waters and carbonates: A case study from the western United States. Earth Planet. Sci. Lett. 518, 1–12. https://doi.org/10.1016/j.epsl.2019.04.026

Putman, A.L., Bowen, G.J., 2019. Technical Note: A global database of the stable isotopic ratios of meteoric and terrestrial waters. Hydrol. Earth Syst. Sci. 23, 4389–4396. https://doi.org/10.5194/hess-23-4389-2019

Salati, E., Dall'Olio, A., Matsui, E., Gat, J.R., 1979. Recycling of water in the Amazon Basin: An isotopic study. Water Resour. Res. 15, 1250–1258. https://doi.org/10.1029/WR015i005p01250

Shan, N., Ju, W., Migliavacca, M., Martini, D., Guanter, L., Chen, J., Goulas, Y., Zhang, Y., 2019. Modeling canopy conductance and transpiration from solar-induced chlorophyll fluorescence. Agric. For. Meteorol. 268, 189–201. https://doi.org/10.1016/j.agrformet.2019.01.031

Steen-Larsen, H.C., Sveinbjörnsdottir, A.E., Jonsson, T., Ritter, F., Bonne, J., Sodemann, H., Blunier, T., Vinther, B.M., 2015. Moisture sources and synoptic to seasonal variability of North Atlantic water vapor isotopic composition. J. Geophys. Res. Atmos. 120, 5757–5774. https://doi.org/10.1002/2015JD023234

Surma, J., Assonov, S., Herwartz, D., Voigt, C., Staubwasser, M., 2018. The evolution of ^{17}O-excess in surface water of the arid environment during recharge and evaporation. Sci. Rep. 8, 4972. https://doi.org/10.1038/s41598-018-23151-6

Tabor, C.R., Otto-Bliesner, B.L., Brady, E.C., Nusbaumer, J., Zhu, J., Erb, M.P., Wong, T.E., Liu, Z., Noone, D., 2018. Interpreting Precession-Driven $\delta^{18}O$ Variability in the South Asian Monsoon Region. J. Geophys. Res. Atmos. 123, 5927–5946. https://doi.org/10.1029/2018JD028424

Tian, C., Wang, L., Kaseke, K.F., Bird, B.W., 2018. Stable isotope compositions (δ^2H, $\delta^{18}O$ and $\delta^{17}O$) of rainfall and snowfall in the central United States. Sci. Rep. 8, 1–15. https://doi.org/10.1038/s41598-018-25102-7

Whelan, M.E., Lennartz, S.T., Gimeno, T.E., Wehr, R., Wohlfahrt, G., Wang, Y., Kooijmans, L.M.J., Hilton, T.W., Belviso, S., Peylin, P., Commane, R., Sun, W., Chen, H., Kuai, L., Mammarella, I., Maseyk, K., Berkelhammer, M., Li, K.F., Yakir, D., Zumkehr, A., Katayama, Y., Oge, J., Spielmann, F.M., Kitz, F., Rastogi, B., Kesselmeier, J., Marshall, J., Erkkila, K.M., Wingate, L., Meredith, L.K., He, W., Bunk, R., Launois, T., Vesala, T., Schmidt, J.A., Fichot, C.G., Seibt, U., Saleska, S., Saltzman, E.S., Montzka, S.A., Berry, J.A., Elliott Campbell, J., 2018. Reviews and syntheses: Carbonyl sulfide as a multi-scale tracer for carbon and water cycles, Biogeosciences. https://doi.org/10.5194/bg-15-3625-2018

Wong, T.E., Nusbaumer, J., Noone, D.C., 2017. Evaluation of modeled land-atmosphere exchanges with a comprehensive water isotope fractionation scheme in version 4 of the Community Land Model. J. Adv. Model. Earth Syst. 9, 978–1001. https://doi.org/10.1002/2016MS000842

Yakir, D., Sternberg, S.L., 2000. The use of stable isotopes to study ecosystem gas exchange. Oecologia 123, 297–311.